Diss. ETH No. 20568

Investigations on the catalytic decomposition of guanidinium formate, ammonium formate and methanamide as NH$_3$-precursors for the selective catalytic reduction of NO$_x$

A dissertation submitted to

ETH ZURICH

for the degree of

Doctor of Sciences

presented by

DANIEL PEITZ

M.Sc., University of Erlangen-Nuremberg

born July 20th, 1983

citizen of Germany

accepted on the recommendation of

Prof. Dr. A. Wokaun, examiner

Prof. Dr. J. A. van Bokhoven, co-examiner

Dr. O. Kröcher, co-examiner

2012

Tempora mutantur, nos et mutamur in illis

Acknowledgements

Table of Contents

Summary

Since the late 1970s, engine control and exhaust gas aftertreatment achieved impressive reductions in the emission of legally regulated components. The introduction of the three-way catalyst for gasoline-fuelled engines provided a system suitable for the removal of all regulated compounds and its principle is still used today. Diesel-fuelled engines, however, need a combination of different dedicated catalysts to remove all critical emission components. Recent emission legislation focusses in particular on a strong reduction in the emission of nitrogen oxides (NO_x).

The most widespread technique for the removal of NO_x from Diesel exhaust is the selective catalytic reduction (SCR). In the process, a reducing agent, namely ammonia (NH_3), is needed to convert the toxic NO_x to harmless nitrogen and water. Due to safety concerns, an NH_3-precursor, rather than ammonia gas is employed in vehicles. Currently, a eutectic mixture of urea in water, known by the trade name AdBlue®, is adopted as a convenient NH_3-precursor for the SCR process in vehicles. However, alternative substances with advantageous temperature stability and/or higher storage stability of ammonia were proposed in the past years. The most promising of these alternative NH_3-precursor compounds are guanidinium formate, ammonium formate and methanamide, all of which were investigated in this work. So far, the reliable release of the stored ammonia without the production of undesired side products remains the largest obstacle in their wide adoption in commercial applications.

All the mentioned alternative NH_3-precursor compounds are formic acid derivatives, which becomes a significant disadvantage during hydrolysis, because formic acid, in addition to ammonia gas, is also produced in the

exhaust duct. Formic acid additionally causes the emission of the toxic side products methanamide and hydrogen cyanide, by condensing with some of the produced ammonia gas.

In the first part of this work a novel experimental setup for the investigation of NH_3-precursor solutions was developed. The previously available setups focused mainly on investigating the SCR reaction, and consequently substituted dosing of ammonia gas for the complicated spraying of NH_3-precursor solutions into the reactor. The spray pattern achieved was determined to be very homogeneous and suitable for the investigation of various NH_3-precursor solutions.

Temperature-programmed decomposition experiments, in combination with density functional theory (DFT) simulations, were performed to shed light onto the reaction pathways of guanidinium formate on a titanium dioxide hydrolysis catalyst. Guanidinium formate decomposition proceeds as parallel decomposition of neutral guanidine and formic acid on the catalyst surface. Guanidine decomposition starts either under the participation of water (hydrolysis) or without (elimination) to release one first molecule of ammonia. The remaining fragment can rearrange to yield urea, which decomposes according to the established reaction pathways via isocyanic acid to yield the remaining two molecules of ammonia and one equivalent of carbon dioxide. From a purely energetic perspective, formic acid could either decompose to carbon monoxide and water or to carbon dioxide and hydrogen with equal likelihood, however, experimentally only the decomposition to carbon monoxide was observed on titanium dioxide.

Noble metal doping of titanium dioxide was performed to enable the rapid decomposition of formic acid during the dosing of alternative NH_3-precursor compounds. Indeed, palladium and gold could be used for a

targeted decomposition of formic acid, but palladium also strongly oxidized the produced ammonia. Gold-doped titanium dioxide, however, showed no significant oxidation of ammonia, leading to a reliable decomposition of guanidinium formate, which yielded only ammonia and carbon dioxide. In fact, the good conversion of formic acid even facilitated guanidine decomposition, due to the suspended stabilization as a salt. Besides guanidinium formate, ammonium formate or methanamide solutions could also be converted to a gas mixture containing solely ammonia and carbon dioxide as reaction products on the gold-doped titanium dioxide catalyst.

The developed catalyst was further tested concerning its resistance against hydrothermal aging or sulfur poisoning. Both effects were performed under conditions representative of commercial operation. Hydrothermal aging barely affected the catalytic conversion of NH_3-precursors in the preferred operation range, even though the aging conditions (with up to 800°C) were significantly above the temperature range considered acceptable for gold-containing catalysts. Sulfur poisoning had a stronger influence on the catalytic conversion. Though ammonia yields were not reduced, formic acid decomposition declined, resulting in higher formic acid emissions and carbon monoxide, rather than carbon dioxide as decomposition product.

The extraordinary stability of the catalytic conversion of formic acid derived NH_3-precursor compounds by the gold-doped titanium dioxide catalyst, even after severe aging, could not be directly attributed to a certain active site. Implications from experiments and the catalyst characterization suggest the activity is due to sites which are less susceptible to hydrothermal aging than deposited gold, which sinters on the titanium dioxide catalyst surface.

Decomposition of NH_3-precursor solutions under high pressure conditions was investigated as a possibility to convert the compounds to ammonia. The pressures were chosen to be sufficiently high to keep the contained water in its liquid state, thereby always providing a large excess of reactant. Addition of a hydrolysis catalyst showed much less influence during the decomposition reaction than in the gas phase. Formic acid derived methanamide yielded not only ammonia and carbon dioxide but also hydrogen during conversion in the compact converter unit.

Recently proposed *enhanced-SCR*, utilizing a mixture of urea ammonium nitrate and water, was investigated in detail on commercial SCR catalysts. The supposed enhancement of the SCR reaction in the low temperature regime could not be observed to the degree proposed by previous works on this subject. In fact, the additional dosing of ammonium nitrate had a detrimental effect on the currently most promising SCR catalyst, i.e. Cu-exchanged zeolite. Besides the testing of the influence of ammonium nitrate dosing on the overall SCR performance, experiments aiming for the determination of the optimum ammonium nitrate to urea ratio provided clear indications that the currently considered SCR mechanism must be extended by additional reactions, or may not even be applicable to certain catalyst types.

Kurzfassung

Seit Ende der 1970er können Motorsteuerung und Abgasnachbehandlung eine beeindruckende Reduktion der Emission von gesetzlich limitierten Schadstoffen vorweisen. Die Einführung des Drei-Wege Katalysators für benzinbetriebene Motoren ermöglichte die Verringerung sämtlicher Schadstoffe mit einem einzigen System, das auch heute prinzipiell noch so weiterverwendet wird. Dieselmotoren dagegen benötigen die Kombination verschiedener spezifischer Katalysatoren, um alle Emissionskomponenten zu entfernen. Neuere Grenzwertverordnungen konzentrieren sich dabei ganz besonders auf die Verringerung der Emission von Stickoxiden (NO_x).

Die Selektive Katalytische Reduktion (SCR) ist gegenwärtig das am meisten verwendete Verfahren um NO_x aus Dieselabgas zu entfernen. In dem Prozess wird ein Reduktionsmittel, Ammoniak, benötigt, um die giftigen NO_x zu harmlosen Stickstoff und Wasser umzuwandeln. Aus Sicherheitsgründen wird ein Ammoniakvorläufer statt Ammoniakgas in Fahrzeugen eingesetzt. Zurzeit ist dies eine benutzerfreundliche eutektische Mischung aus Harnstoff und Wasser mit dem Handelsnamen AdBlue®. Jedoch wurden in den letzten Jahren auch alternative Substanzen mit besserer Temperaturstabilität und/oder höherer Ammoniakspeicherdichte vorgeschlagen. Die aussichtsreichsten dieser alternativen Ammoniakvorläufersubstanzen sind Guanidiniumformiat, Ammoniumformiat und Methanamid, welche in dieser Arbeit untersucht wurden. Die zuverlässige Freisetzung des gespeicherten Ammoniaks ohne unerwünschte Nebenprodukte stellt gegenwärtig die grösste Hürde zur kommerziellen Nutzung dar.

Die erwähnten alternativen Ammoniakvorläufersubstanzen sind alle Ameisensäurederivate, was während der Hydrolyse ein Nachteil ist, da

neben Ammoniakgas auch korrosive Ameisensäure produziert wird. Ameisensäure führt ausserdem durch die Kondensation mit einem Teil des produzierten Ammoniaks zur Emission der giftigen Nebenprodukte Methanamid und Blausäure.

Ein neuartiger Versuchsaufbau zur Untersuchung von Ammoniakvorläufersubstanzen wurde zunächst entwickelt, da bestehende Aufbauten sich vorwiegend auf die Untersuchung der SCR Reaktion konzentrierten und das komplizierte Eindüsen von Ammoniakvorläufersubstanzlösung mit der Dosierung von Ammoniakgas ersetzten. Im neuen Aufbau konnte ein sehr homogenes Sprühbild erreicht werden, das geeignet für die Untersuchung von verschiedenen Ammoniakvorläufersubstanzlösungen ist. Temperaturprogrammierte Zersetzungsversuche wurden zusammen mit dichtefunktionaltheoretischen (DFT) Simulationen durchgeführt, um die Reaktionspfade von Guanidiniumformiat auf Titandioxid Hydrolysekatalysatoren zu erforschen. Die Guanidiniumformiatzersetzung läuft als parallele Zersetzung von neutralem Guanidin und Ameisensäure auf der Katalysatoroberfläche ab. Die Guanidinzersetzung setzt zunächst ein Ammoniakmolekül frei, entweder durch Einfluss von Wasser (Hydrolyse) oder ohne Wasser (Eliminierung). Das verbleibende Fragment kann sich zu Harnstoff umlagern, der über die bekannten Reaktionspfade *via* Isocyansäure die verbliebenen zwei Ammoniakmoleküle und ein Äquivalent von Kohlendioxid freisetzt. In der energetischen Betrachtung kann sich die Ameisensäure gleichermassen entweder zu Kohlenmonoxid und Wasser oder zu Kohlendioxid und Wasserstoff zersetzen, experimentell wurde jedoch nur die Zersetzung zu Kohlenmonoxid auf Titandioxidkatalysatoren beobachtet.

Es wurden ausserdem Edelmetalldotierungen durchgeführt, um die schnelle Zersetzung von Ameisensäure während der Dosierung von alternativen

Ammoniakvorläufersubstanzen zu ermöglichen. Tatsächlich waren Palladium und Gold für eine gezielte Zersetzung der Ameisensäure geeignet, doch Palladium oxidierte auch den produzierten Ammoniak. Gold-dotiertes Titandioxid dagegen führte zur zuverlässigen Zersetzung von Guanidiniumformiat ohne Ammoniakoxidation, es wurde ausschliesslich Ammoniak und Kohlendioxid freigesetzt. Die gute Umsetzung der Ameisensäure führte sogar zur vereinfachten Guanidinzersetzung, da es nicht mehr als Salz stabilisiert wurde. Neben Guanidiniumformiat konnten auch Ammoniumformiat- und Methanamidlösungen zu einem Produktgas aus Ammoniak und Kohlendioxid umgesetzt werden.

Der entwickelte Katalysator wurde ausserdem auf seine Resistenz gegenüber hydrothermaler Alterung und der Vergiftung durch Schwefel getestet, jeweils unter Bedingungen, die realistisch für die kommerzielle Verwendung sind. Die hydrothermale Alterung zeigte kaum Einfluss auf die katalytische Zersetzung im Arbeitstemperaturbereich, obwohl die Alterungsbedingungen mit bis zu 800°C deutlich über den normalerweise empfohlenen Temperaturen für goldhaltige Katalysatoren lagen. Die Vergiftung mit Schwefel hatte einen stärkeren Einfluss auf die katalytische Umsetzung: Zwar wurde die Ammoniakausbeute nicht beeinflusst, die Zersetzung der Ameisensäure wurde jedoch reduziert, was zu höheren Ameisensäureemissionen und Kohlenmonoxid statt Kohlendioxid als Zersetzungsprodukt führte.

Die aussergewöhnlich stabile katalytische Zersetzung von Ameisensäure-verwandten Ammoniakvorläufersubstanzen durch den golddotierten Titandioxidkatalysator auch nach der heftigen Alterung konnte keinem eindeutigen aktiven Zentrum zugeordnet werden. Aus den Experimenten

und der Katalysatorcharakterisierung kann jedoch gefolgert werden, dass die Aktivität durch ein Zentrum verursacht ist, das weniger anfällig für die hydrothermale Alterung als das abgeschiedene Gold auf der Katalysatoroberfläche ist, welches nachweislich sintert.

Die Zersetzung von Ammoniakvorläufersubstanzen unter hohem Druck wurde als eine weitere Möglichkeit untersucht, die Verbindungen zu Ammoniak umzusetzen. Der hohe Druck wurde gewählt, um das enthaltene Wasser im flüssigen Zustand zu halten, so war stets ein grosser Überschuss an Edukt vorhanden. Die Zugabe eines Hydrolysekatalysators zeigte weit weniger Einfluss auf die Zersetzung als in der Gasphase. Das Ameisensäure-verwandte Methanamid produzierte neben Ammoniak und Kohlendioxid auch Wasserstoff während der Zersetzung in dem kompakten Reaktor.

Das kürzlich vorgestellte verbesserte-SCR Verfahren, das eine Mischung aus Harnstoff, Ammoniumnitrat und Wasser verwendet, wurde auf kommerziellen Katalysatoren untersucht. Die zu erwartende Verbesserung der SCR Reaktion im Tieftemperaturbereich konnte nicht in dem Ausmass beobachtet werden, wie es in vorhergehenden Arbeiten vorgeschlagen wurde. Tatsächlich hatte die zusätzliche Dosierung von Ammoniumnitrat für den interessantesten SCR Katalysator, ein Kupfer-ausgetauschter Zeolith, einen negativen Einfluss. Neben dem Einfluss von Ammonium-nitratdosierung auf die SCR Reaktion insgesamt, wurden auch Versuche zum optimalen Ammoniumnitrat zu Harnstoff Verhältnis durchgeführt. Dabei zeigte sich deutlich, dass der gegenwärtige Mechanismus zur Beschreibung der SCR erweitert werden muss oder sogar für einige Katalysatortypen nicht zutreffend ist.

1. Introduction

1.1. Automotive emissions

1.1.1. Classification of emissions

Combustion of hydrocarbon fuels not only produces CO_2 and H_2O as reaction products, but also a wide range of other compounds. While the amount of the additional compounds is very small compared to the two main products, their effect on human health and/or the environment is significant. [1,2,3]

The emissions of internal combustion engines (ICE) can be classified into the following categories: hydrocarbons (HC) or carbon monoxide (CO), particulate matter (PM), nitric oxides (NO_x), and sulfur oxides (SO_x). [4] Here, hydrocarbons are of almost any chemical nature including unburnt compounds such as alkanes, alkenes, aromatics, or could also consist of only partially burnt hydrocarbons ranging from small fragments, such as CO to oxidized hydrocarbons which agglomerated to form larger molecules up to aerosols. [5] However, as soon as the compounds are no longer gaseous (at a given temperature) they are considered as particulate matter (PM). The chosen type of PM measurement will greatly influence the proportion of PM or HC. [6,7] PM mostly consists of carbon compounds, but can also contain significant amounts of carbon-free matter, such as ash residues from burnt engine lubricant, or metal particles from engine wear. [8] Nitric oxides (NO_x) are formed from nitrogen and O_2 in the intake air due to the high temperatures during combustion. [9] Sulfur oxides in the exhaust gas originate from combustion of sulfur-containing hydrocarbon fuel and engine lubrication oil. [10]
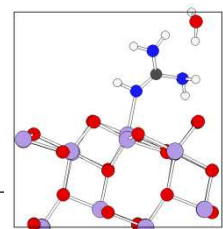
1.1.2. Gasoline and Diesel emissions

While gasoline and Diesel fuel are both based on mixtures of hydrocarbons, their combustion is conducted in a significantly different manner, resulting in different compositions of the exhaust gas.

Gasoline is combusted in the Otto engine using an amount of air containing just the right amount of O_2 to transform the hydrocarbon fuel to CO_2 and H_2O (stoichiometric amount) according to 1-1. [11]

$$H_xC_y + \left(\frac{x}{2} + y\right)O_2 \rightarrow y\,CO_2 + \frac{x}{2}H_2O \qquad \text{1-1}$$
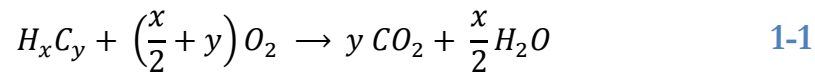
The ratio of dosed O_2 relative to the amount needed for combustion is referred to as λ, in case of gasoline engines it will fluctuate within no more than 2% from unity. [12]

In contrast, Diesel engines are operated under lean conditions, i.e. at $\lambda > 1$. This difference in the amount of O_2 provided during combustion will not only cause different emissions, but also fundamentally different conditions for the catalytic treatment of the emissions in exhaust gas aftertreatment systems. [13]

Another technical difference between gasoline and Diesel engines that has significant consequences on the observed emissions is that gasoline is traditionally vaporized before entering the cylinder, while Diesel is directly injected as a liquid. Direct injection is advantageous for fuel economy, [11] but due to unavoidable inhomogeneities of O_2 concentration in the combustion chamber, part of the fuel droplets will not be burnt but rather pyrolized and form soot particles. [14,15] In contrast, pre-vaporized gasoline vapor will be distributed as homogenously as the intake O_2, thereby forming significantly lower amounts of soot particles. [16]

It should be mentioned that recent developments in gasoline engine technology blur the historic distinction between the emissions from the two different engine types. The main reason for these developments is the increased pressure on fuel economy, leading to the implementation of characteristic Diesel techniques such as high-pressure direct injection or operation at λ >1 in gasoline engines. [17] In the near future the homogeneous charge compression ignition (HCCI) could also be realized commercially for both fuel types. [18] However, the advantages of these techniques are offset by well-known disadvantages which will drive new fields of activity in exhaust gas aftertreatment. [19,20]

In general, one has the possibility to try to avoid the formation of emissions *a priori* or to remove the emissions in the produced exhaust gas flow. Engine-based and fuel-based measurements try to minimize emissions at the source, while catalytic treatment of the exhaust gas is employed to reduce the produced emissions to acceptable levels. [21]

1.1.3. Emission control legislation

The amount of pollutants in automotive tailpipe emissions was first regulated in the State of California in the USA in 1966. [22] Emission control legislation has spread ever since to industrialized countries around the world. In the European Union, a compendium of emission control regulations was introduced for passenger cars and heavy duty trucks, starting to be put into effect from 1992, with regular amendments for decreasing the amount of permitted pollutants. [23,24,25,26] As the emission legislation in other regions like the USA or Japan evolved very similarly, [21] the development of emission guideline tightening can be
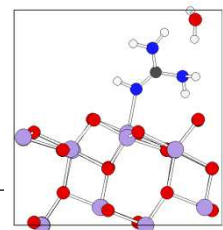
effectively shown using the EU-legislation for passenger cars and heavy-duty trucks.

In Table 1-1 the evolution of emission legislation for passenger cars starting from 1992 with Euro 1 is shown for gasoline and Diesel vehicles. The stated values need to be reached within the New European Driving Cycle (NEDC) chassis dynamometer procedure. Starting from 2000 (Euro 3) the test cycle was modified to also include the 40 s engine warm-up period which was previously omitted from sampling. The dates are valid for the approval of new types of vehicles, while new vehicles just need to comply with the regulation within one year of their introduction. [27]

Table 1-1: EU emission standards for passenger cars (category M).

Stage	Date	CO	HC	HC+NO$_x$	NO$_x$	PM	PN
				g/km			*#/km*
Compression Ignition (Diesel)							
Euro 1	01.07.1992	2.72	-	0.97	-	0.140	-
Euro 2	01.01.1996	1.00	-	0.70	-	0.080	-
Euro 3	01.01.2000	0.64	-	0.56	0.50	0.050	-
Euro 4	01.01.2005	0.50	-	0.30	0.25	0.025	-
Euro 5a	01.09.2009	0.50	-	0.23	0.18	0.005	-
Euro 5b	01.09.2011	0.50	-	0.23	0.18	0.005	$6.0 \cdot 10^{11}$
Euro 6	01.09.2014	0.50	-	0.17	0.08	0.005	$6.0 \cdot 10^{11}$
Positive Ignition (Gasoline)							
Euro 1	01.07.1992	2.72	-	0.97	-	-	-
Euro 2	01.01.1996	2.20	-	0.50	-	-	-
Euro 3	01.01.2000	2.30	0.20	-	0.15	-	-
Euro 4	01.01.2005	1.00	0.10	-	0.08	-	-
Euro 5	01.09.2009	1.00	0.10[†]	-	0.06	0.005	-
Euro 6a	01.09.2014	1.00	0.10[†]	-	0.06	0.005	$6.0 \cdot 10^{12}$ [‡]
Euro 6b	01.09.2017	1.00	0.10[†]	-	0.06	0.005	$6.0 \cdot 10^{11}$ [‡]

† *non-methane hydrocarbons (NMHC) = 0.068 g/km.*

‡ *only applicable to vehicles with direct-injection (DI) engines.*

One can easily see that the reduction of pollutants in the exhaust gas achieved in the past decades is tremendous: The amount of pollutants in Diesel exhaust, for example, was reduced from Euro 1 to Euro 6 for each component by at least 82%. Also the reductions achieved in reducing gasoline exhaust pollutants are significant, though values remained largely unchanged since Euro 4 (2005).
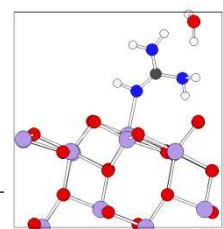
In Table 1-2 also the evolution of heavy-duty Diesel engine emission legislation is presented. The introduction of Euro III also changed the test cycle from the ECE R-49 steady-state engine test to the European Stationary Cycle (ESC) and the European Transient Cycle (ETC) if the engines were equipped with a Diesel Particulate Filter (DPF) or a NO_x aftertreatment system. [27]

Table 1-2: EU emission standards for heavy-duty Diesel engines.

Stage	Date	Test cycle	CO	HC	NO_x	PM
					g/kWh	
Euro I*	01.10.1992		4.5	1.10	8.0	0.36
Euro II	01.10.1996	ECE R-49	4.0	1.10	7.0	0.25
	01.10.1998		4.0	1.10	7.0	0.15
Euro III	01.10.2000		2.1	0.66	5.0	0.10
Euro IV	01.10.2005	ESC + ETC	1.5	0.46	3.5	0.02
Euro V	01.10.2008		1.5	0.46	2.0	0.02
Euro VI	01.01.2013		1.5	0.13	0.4	0.01

* for engines above 85 kW rated power.

Here, the reductions are even more impressive, with up to 97% decrease for NO_x emissions from 1992 to 2013. Considering that, prior to the Euro I emission guidelines, even higher values were observed, in terms of practical applications, NO_x emissions are almost eliminated in Euro VI engine exhaust compared to pre-Euro I vehicles.

These requirements could only be fulfilled by a huge effort in both, engine-based emission control and exhaust gas aftertreatment. [28] The technical solutions which were developed are introduced in the next two sections.

1.1.4. Engine-based emission control

As the emissions of HC, CO and soot point towards an incomplete and, therefore, inefficient combustion process, not only environmental considerations or legislative pressure were the driving forces in avoiding these emissions. In other words, development of engine technology not only improved engine efficiency but also reduced the amounts of produced HC, CO and soot. [21] Most prominently the continuing development of higher pressures for high-pressure injection and optimizations on the injections intervals led to significant improvements of the emission of HC, CO and soot. [29]

Charging the engine with exhaust-driven turbines (turbochargers) was mainly motivated by an increase in engine performance, but it also improved exhaust composition by providing a large excess of O_2 for the combustion of hydrocarbons. [13]

Engine-based methods to reduce NO_x formation are less attractive, as they often incur a fuel penalty, in contrast to efficient lean combustion which promotes NO_x formation. The introduction of exhaust gas recirculation (EGR) helped to lower emissions of NO_x by recycling some of the cooled exhaust gas into the engine, thereby lowering the O_2 partial pressure and reducing the maximum temperatures during combustion due to the increased amount of inert gas. [21]

For large marine Diesel engines water injection into the cylinder of the Diesel engine is also an option to lower peak temperatures, which can reduce NO_x formation by up to 70%. [30] This method, however, can only be applied to the robust Diesel engines used in maritime applications, not so much in today's sophisticated automotive Diesel engines. Besides, one
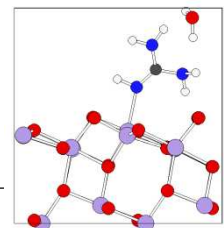
would need to transport not only Diesel fuel but also deionized water in the vehicle for reliable operation.

However, there are certain tradeoffs one faces when employing the mentioned technical issues, as on one hand excess O_2 and high cylinder pressures reduce the hydrocarbon, CO and soot emissions, but favor the formation of NO_x during the combustion process. EGR, on the other hand, reduces NO_x formation, but will also cause an increase in hydrocarbon, CO and soot emissions, due to the reduced amount of O_2 present during combustion. [21,31] This tradeoff can be visualized by plotting the range of possible operation points of an engine with their corresponding PM formation and NO_x emissions as shown in Figure 1-1.
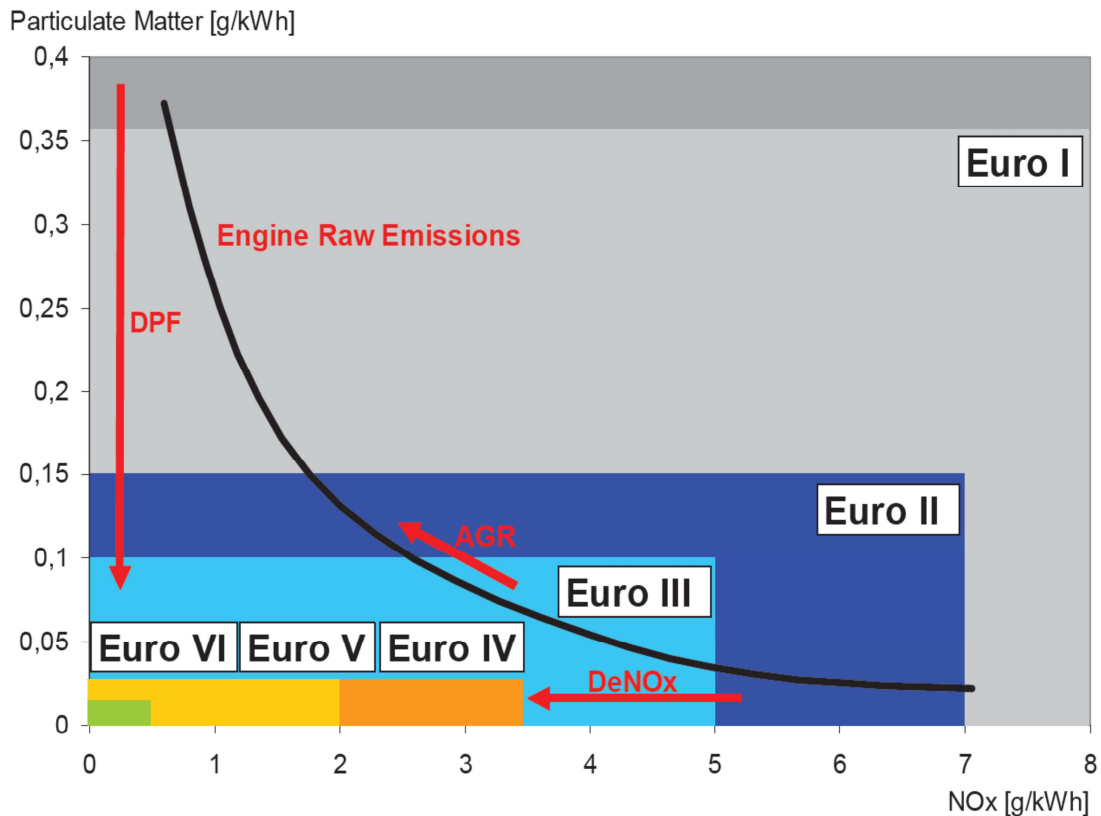
Figure 1-1: Trade-off between PM formation and NO$_x$ emissions for heavy-duty Diesel engines. (Figure reprinted from [32])

As can be seen in the figure, an engine may technically be operated to fulfill strict requirements concerning PM formation or concerning NO$_x$ emissions, while most other operation modes will fall short of reaching the requirements, even though they are more balanced concerning the emissions. In practical applications, engine-based emission control must therefore be combined with catalytic exhaust aftertreatment to reach the legal requirements.

1.1.5. Exhaust gas aftertreatment

Catalytic emission control systems, as chemical measures of transforming certain components in the exhaust gas, are very specific to the reaction
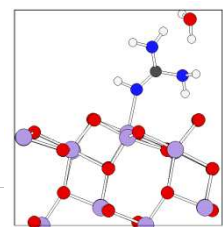
conditions. Here one needs to first distinguish between the exhaust gas aftertreatment of gasoline exhaust, and the exhaust of Diesel engines.

Due to the combustion around $\lambda = 1$ there are alternately traces of O_2 or slightly reducing conditions in the gasoline exhaust. [4] This enables running oxidation and reduction reactions using just one catalytic converter. The system was dubbed "three-way catalyst", due to the three chemical reactions 1-2 to 1-4 occurring on the catalyst.

$$H_x C_y + \left(\frac{x}{2} + y\right) O_2 \rightarrow y\ CO_2 + \frac{x}{2} H_2 O \qquad \text{1-2}$$

$$2\ CO\ +\ O_2 \rightarrow 2\ CO_2 \qquad \text{1-3}$$

$$2\ NO_x\ +\ 2x\ CO \rightarrow N_2 + 2x\ CO_2 \qquad \text{1-4}$$
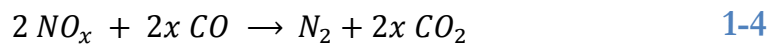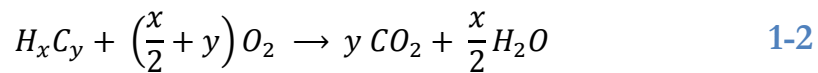
The catalytic converters usually consist of a γ-Al_2O_3 washcoat often mixed with CeO_2 for O_2 storage during lean combustion, and the active noble metal component. [12] There is no fixed composition of commercially employed catalysts. Depending on the producer, the intended application and noble metal price, different mixtures, or single noble metal catalysts are used, but exact details remain the secret of the producers. [4] Rhodium is necessary for high activity in reaction 1-4, while the other two reactions can be catalyzed by any platinum group metal. [33] However, the substitution of platinum by the (in recent years) less expensive palladium [34] is problematic, due to the formation of palladium-rhodium alloys, which will deter the catalytic properties compared to the isolated materials. [35]

Three-way catalysts with O_2 sensor for operation at $\lambda = 1$ were first sold in the USA built into the Volvo 264 in 1976. [36] Since then, catalytic converters have been optimized tremendously, as the amount of noble metals could be significantly reduced while performance remained constant or, even increased. [37] The basic concept, however, has remained the same, and even the latest emission regulations for Otto engines are fulfilled

using a three-way catalytic converter as the sole exhaust gas aftertreatment system component. [29]

In contrast, exhaust gas aftertreatment for Diesel engines requires a series of several dedicated catalytic converters to reduce the different emission components, because the three-way catalyst may not be used due to its operation at $\lambda = 1$. In addition to the emission components found in gasoline exhaust, the particulate matter contained in Diesel engine exhaust also needs to be eliminated.

First, HC and CO are removed by the Diesel oxidation catalyst (DOC) using a noble metal-based catalyst. The DOC is constructed similarly to a three-way catalyst – a γ-Al$_2$O$_3$ washcoat with deposited noble metal is used. As there is no requirement for NO$_x$ reduction activity, the DOC does not contain rhodium. Instead, platinum or palladium (and mixtures thereof) are used for the oxidation activity. [29] As platinum is more resistant to sulfur poisoning, it is usually used at least partly, even though it is more expensive (in past years). [38] Due to the lower temperatures of Diesel exhaust, the DOC is mounted closer to the engine than for the three-way catalyst on gasoline engines. [39] Besides the two oxidation reactions 1-5 and 1-6, the oxidation of NO to NO$_2$ (1-7) with the excess O$_2$ contained in Diesel exhaust is also catalyzed by the DOC. However, in contrast to the other reactions, the chemical equilibrium of this reaction has a strong dependence on temperature and is not as clearly on one side as it is the case for the previous reactions.

$$H_xC_y + \left(\frac{x}{2}+y\right)O_2 \rightarrow y\,CO_2 + \frac{x}{2}H_2O \qquad \text{1-5}$$

$$CO + O_2 \rightarrow 2\,CO_2 \qquad \text{1-6}$$

$$2\,NO + O_2 \rightleftharpoons 2\,NO_2 \qquad \text{1-7}$$
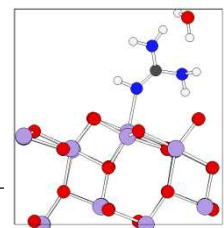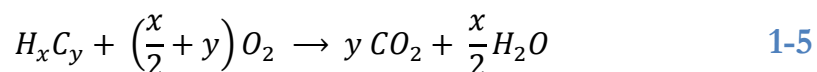
In heavy duty applications, the DOC is usually combined with a Diesel particulate filter (DPF) for the removal of particulate matter (PM). [40,41] The NO_2 produced by the upstream DOC is used as an oxidation agent for the carbon-based soot on the DPF. This approach has became known as continuously regenerating trap (CRT®). [42] For heavy duty applications with engines operating regularly at high load the NO_2 produced by the DOC suffices for the constant removal of carbonaceous PM. [5] In applications which do not provide exhaust gas temperatures sufficiently high for soot oxidation by NO_2 generated by the DOC, the DPF is also coated with a noble metal catalyst in order to constantly regenerate NO_2. The DPF is then referred to as a catalyzed continuously regenerating trap (CCRT®). [43] As NO_2 is a stronger oxidation agent than O_2, its regeneration from NO provides a good opportunity to constantly remove the collected soot in the DPF. The removal of PM in automotive applications cannot rely exclusively on the oxidation of soot by NO_2 (1-8), because the exhaust temperatures are too low most of the time. However, in order to also use the oxidation of soot with O_2 (1-9), higher temperatures in the DPF are needed.

$$C_{soot} + 2\,NO_2 \rightarrow CO_2 + 2\,NO \qquad\qquad \textbf{1-8}$$

$$C_{soot} + O_2 \rightarrow CO_2 \qquad\qquad \textbf{1-9}$$
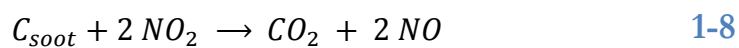
Measures to increase temperature in the DPF, besides electric heating [44], include the regular operation of the engine in a fuel-rich mode to create large amounts of HC that will be oxidized by the upstream DOC and the noble-metal coated DPF, thereby releasing heat, or the combination of DOC and DPF into one system that will be mounted closer to the engine. [45,46] In both systems reactions 1-5 through 1-7 also occur on the DPF.

Catalytic NO_x removal can be achieved by two principle techniques, one being the NO_x storage reduction (NSR) catalyst, and the other being the selective catalytic reduction (SCR) of NO_x using a reducing agent. In commercial applications, usually only one of the two systems is used for exhaust gas aftertreatment.

NSR needs the engine to operate under alternating conditions, i.e. the lean combustion must be disrupted in regular intervals by fuel-rich combustion with $\lambda < 1$. During O_2-rich operation, NO is oxidized by a noble metal, typically platinum to form NO_2. The NO_2 is stored as an alkaline earth nitrate species such as $BaNO_3$ in the NSR catalyst (reactions 1-10 and 1-11). The decomposition of $BaNO_3$ by NO via equilibrium 1-12 is avoided by the deposition of platinum next to barium, so the NO produced in 1-11 is reacted via 1-10.

$$2\,NO \,+\, O_2 \,\rightleftharpoons\, 2\,NO_2 \qquad\qquad \textbf{1-10}$$

$$BaCO_3 \,+\, 3\,NO_2 \,\longrightarrow\, Ba(NO_3)_2 \,+\, NO \,+\, CO_2 \qquad \textbf{1-11}$$

$$Ba(NO_3)_2 \,+\, NO \,\rightleftharpoons\, BaO \,+\, 3\,NO_2 \qquad \textbf{1-12}$$
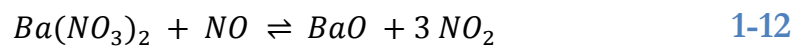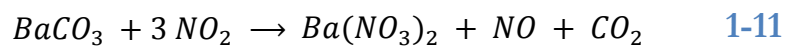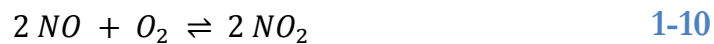
During fuel-rich conditions, HC and CO, which cannot be oxidized by the upstream DOC due to a lack of O_2, will be used to reduce the stored nitrate to nitrogen (reactions 1-13 to 1-15). [47]

$$2\,Ba(NO_3)_2 \,\longrightarrow\, 2\,BaO \,+\, 4\,NO \,+\, 3\,O_2 \qquad \textbf{1-13}$$

$$BaO \,+\, CO_2 \,\longrightarrow\, BaCO_3 \qquad\qquad \textbf{1-14}$$

$$2\,NO \,+\, 2\,CO \,\longrightarrow\, N_2 \,+\, 2\,CO_2 \qquad\qquad \textbf{1-15}$$
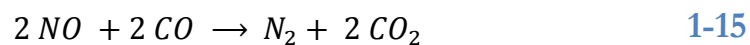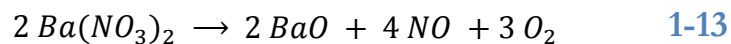
As the reduction of NO_x is not performed during their emission, but rather during the fuel-rich operation of the engine, the system needs to be well tuned in order to adjust the operating temperature windows for the consecutive reactions. NO_x storage, for example, already works efficiently at low temperatures, but the NO oxidation to NO_2, which is needed for
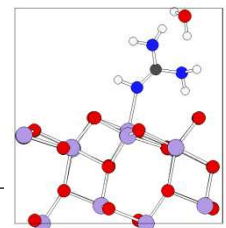
storage and reduction of the stored nitrates using HC and CO, needs higher temperatures for rapid reaction. [48] In contrast, if temperatures are too high, NO_x storage efficiency decreases. The regular operation of the engine without excess O_2 causes a fuel consumption penalty of approximately 2-5%. [49] NSR catalyst may only be used if the Diesel fuel being used contains low amounts of sulfur (ultra-low sulfur Diesel = ULSD, with less than 10 ppm S by volume), as otherwise the Ba and emitted sulfur oxides will form inactive $BaSO_4$, which is thermodynamically more stable than $BaNO_3$. [50,51] However, even with ULSD, the catalyst will need to be regenerated in regular intervals by thermally decomposing the $BaSO_4$ to regenerate NO_x storage capacity. [52,53] As the catalyst requires noble metals, and the size of the NSR-unit is scaled with the amount of NO_x, the system becomes expensive for large engines. [29,21]

SCR on the other hand can be operated constantly during lean combustion. It selectively reduces the formed NO_x in excess O_2 by a catalytic reaction with an additionally dosed reducing agent, such as HC, H_2 or NH_3. The reducing agent is oxidized to yield CO_2 and H_2O, just H_2O, or N_2 and H_2O, respectively.

Reaction with HC was the first method for NO_x removal, patented in 1957 to reduce NO_x emissions from nitric acid production [54], and modified in 1957 for the operation in O_2 containing gases [55]. While the utilization of HC seems very attractive due to the convenience of using Diesel fuel or other easily available liquid hydrocarbons, such as ethanol, as the reducing agent, it shows only low selectivity for the reduction of NO_x to N_2. The efficiency of the reducing agent is low, because most of the HC are oxidized to yield CO_2 and H_2O. In addition, HC side products are often formed from the dosed HC, and NH_3 or N_2O emissions are observed from

transformation of NO_x. [56] There are only few commercial systems utilizing HC-SCR today, because the achieved efficiencies are low compared to other techniques. As a consequence, the applications are not covered by automotive or other on-road legislation, but rather by technical guidelines specific for the application. [29] Most advanced systems reach up to 70% NO_x conversion, however only within a very small temperature range, [57] with deviations of as little as 75 K causing a decrease down to 20%. [58] In real engine operation, efficiencies below 15% for all operation points have also been observed. [59] In recent years, only the possibility of using E85 gasoline (gasoline containing 85% ethanol) as a temperature stable, and possibly widely distributed fuel mixture in the near future as source of ethanol for HC-SCR, has motivated further research. [60,61]

H_2-SCR requires H_2, which is proposed to be produced by reforming of Diesel fuel onboard, rather than being stored in a dedicated tank. Even though there is detailed knowledge about fuel reforming in stationary systems, start-stop operation in a vehicle is not yet fully resolved. [33] Once H_2 is produced, it reduces NO_x on H_2-SCR catalysts containing noble metals deposited on metal oxide support. [62] The reactivity for H_2-SCR is highest for Pt/Al_2O_3, other noble metals such as Pd or Rh on Al_2O_3 support follow [63]. The high price of these noble metals is another drawback of this technique. Even with noble metals being used, their activity below 300°C is unsatisfactory and reduction of NO_x is often rather selective towards N_2O formation, rather than to N_2. [64,65] The addition of H_2 to NH_3 during NH_3-SCR caused a significant enhancement over Ag/Al_2O_3 SCR catalysts in a temperature range of 200-550°C. [66,67] This could also be confirmed for urea-based SCR [68] and could, therefore, become interesting in the future, [69] provided there is a ready supply of H_2
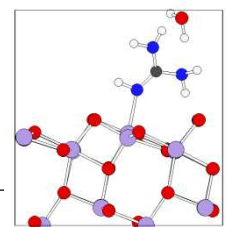
onboard. Interestingly, urea along with aqueous NH_3 [70] and NH_3 derivatives, [71] was also proposed as a H_2 storage compound that could be decomposed in mobile applications. [72]

NH_3-SCR requires NH_3, which also needs to be produced onboard; due to safety issues NH_3-precursor compounds such as urea are used as a substitute. [33] The compounds are dosed into the hot exhaust, where they are decomposed to release NH_3. When NH_3 is produced, the reaction with NO_x on dedicated NH_3-SCR catalysts is unrivalled in selectivity and low temperature activity. [73] These catalysts are either metaloxide-based catalysts or metal-exchanged zeolites. [31] Vanadiumoxide is most often used as an active component in metaloxide-based catalysts, but vanadium-free metal-oxide based catalysts are being developed, because there have been concerns about vanadium emissions under hydrothermal conditions. [74,75] Recent measurements showed 40 times higher emission of vanadium for vehicles equipped with a vanadia-based SCR system. X-ray absorption near edge structure (XANES) spectroscopy detected V_2O_5 as the most abundant vanadium species in the emitted PM. [76] However, as the amount of emitted vanadium is very low, proper testing of the catalysts remains an issue. [77]

The metals used for exchange in the zeolite framework are either iron or copper. Several other metals have been tested, but only these two were finally commercialized due to their superior performance. [78] There are several zeolite structures employed in commercial systems today, depending on the exchanged metal. In the past, a wide range of synthetic and natural zeolites were investigated, such as ZSM-5, beta zeolite (BEA), mordenite (MOR), heulandite–clinoptilolite (HEU), ferrierite (FER) and chabazite (CHA). [79]

Today, the BEA framework seems to be the best suited for Fe-exchanged zeolites, [80] while the Cu-exchanged chabazite developed in recent years was found to be the best system containing Cu. [81] The low temperature activity of Cu-chabazite and the high hydrothermal durability led to the widespread implementation in automotive SCR applications. [82] However, metal-oxide based SCR catalysts remain the most frequent solution for industrial applications of NH_3-SCR in power plants, large Diesel engines in ships, or other heavy-duty applications. This is mainly due to their lower price, but also due to their robustness against high concentrations of SO_2 and HC in the exhaust gas. [81,83,84]

The reactions leading to the reduction of NO_x depend on the relative amounts of NO and NO_2 in the exhaust gas. Exhaust gas mainly consists of NO, but due to the upstream DOC, some of the NO is converted to NO_2. [85] The oxidation of NO is very advantageous, because, with pure NO, only the *standard-SCR* (1-16) reaction proceeds, but when NO_2 is also present, the much quicker *fast-SCR* (1-17) is possible. [86] Pure NO_2 needs to be converted via reaction 1-18, which consumes one third more NH_3 than the other two routes. [87]

$$4\,NO + O_2 + 4\,NH_3 \;\rightarrow\; 4\,N_2 + 6\,H_2O \qquad \textbf{1-16}$$

$$2\,NO + 2\,NO_2 + 4\,NH_3 \;\rightarrow\; 4\,N_2 + 6\,H_2O \qquad \textbf{1-17}$$

$$6\,NO_2 + 8\,NH_3 \;\rightarrow\; 7\,N_2 + 12\,H_2O \qquad \textbf{1-18}$$
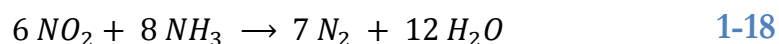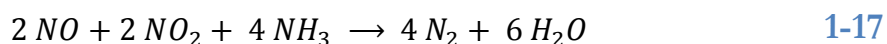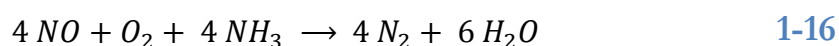
Drawbacks of NH_3-SCR include the formation of NH_4NO_3, which can fill up catalyst pores at temperatures below 200°C. [87] $(NH_4)_2SO_4$ can form at even higher temperatures, if sufficient amounts of SO_3 are formed by SO_2 oxidation on the upstream DOC. [88] Another issue is the emission of unreacted NH_3 ("NH_3-slip"), which needs to be avoided because of the corrosiveness of NH_3 and the low odor threshold. [21] Solutions to resolve
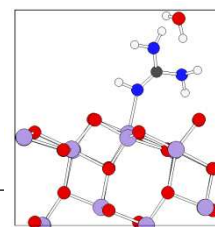
this issue are either the sub-stoichiometric dosing of NH_3, or the addition of a NH_3-slip oxidation catalyst for reaction with the excess O_2. [89] The NH_3-slip catalyst can be designed to be very small compared to the remaining catalytic converters, since the emissions of NH_3 are very low and the oxidation is very fast. For the NH_3-slip catalyst, Pt or Pd coatings are used, because only very small quantities are needed. [90]

NH_3-SCR became the method of choice for the reduction of NO_x emissions in mobile applications, and is today also considered to be the most promising technique to reach upcoming emission guidelines. [29] Since its introduction in heavy-duty trucks in 2004, it has grown into other Diesel engine markets, such as buses, maritime applications, passenger cars or off-road. [91]

1.2. Ammonia precursor compounds for NH₃-SCR

1.2.1. NH₃ gas or solution

NH_3-SCR was first tested in fossil fuel power plants in Japan in 1975 by the Electric Power Development Company, Ltd. [92] Commercial operation in coal power plants (>250 MW) started around 1980 [93]. As there were few concerns with handling NH_3 gas at industrial installations, compressed NH_3 gas was used as the most convenient source for NH_3. [94] The NO_x reduction rates achieved in the first commercial systems were already between 80 to 90%, and the technique was soon widely adopted. [95] One issue with NH_3-SCR was poisoning of the active V_2O_5 in vanadia-based SCR catalysts by arsenic, if present in large amounts (up to 40 ppm [93]) in the coal. Modifying the catalyst by addition of MoO_3 improved the situation significantly. [96] Another problem can be the blockage of catalyst pores by sulfate salts, such as $CaSO_4$ formed from sulfur and metals

contained in the coal. Choosing low sulfur coal avoids this issue, but is often not feasible due to economic considerations. Hindering $CaSO_4$ formation by reducing the content of calcium has not proved advantageous in commercial power plants. In fact, Ca or lignite is actually added to coal containing less than 2% Ca, as it represents an economic method to mitigate arsenic poisoning of the vanadia-based catalyst. [93] Catalyst deactivation due to blockage by ash is most effectively avoided by sonic horns, which can even be combined with soot blowers to physically hinder the deposition of particles on the catalyst. [97] Still, during the regular inspections of the furnace, the catalyst is inspected and cleaned. [93]

Even though TiO_2 is not easily sulfated, long-term operation in coal exhaust containing high amounts of sulfur oxide can lead to the formation of sulfates. The addition of WO_3 was able to increase the sulfation resistance of TiO_2 by increasing its acidity. [98]

Overall, SCR with NH_3 either as anhydrous gas or as 19.5% or 29% aqueous solution has successfully spread to fossil plants worldwide since its introduction in Japan, reducing today on average 90% of NO_x emissions with typically just 5 ppm of NH_3 slip [93]. However, local communities, especially in urban surroundings, try to push for the substitution of NH_3-gas or aqueous NH_3 solution by less harmful substances like urea. [97]

1.2.2. Cyanuric acid

As far back as 1977, a Japanese patent mentions the possibility of replacing NH_3 in power plant exhaust gas aftertreatment with inorganic ammonium salts, urea or cyanuric acid granules of 0.1-10 mm diameter. [99] However, almost one decade later, in 1986, the publication of Perry and Siebers on high NO conversion, when directing a Diesel engine exhaust flow through
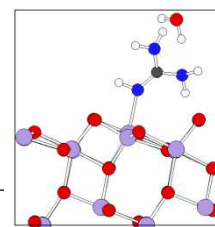
a heated bed of cyanuric acid, still received much attention. [100] Their intention in using cyanuric acid was to release isocyanic acid upon heating above 330°C. They believed the evolved HNCO to be the active reactant in reduction of NO. [101] Indeed, they were able to reliably decompose cyanuric acid to HNCO. NO was converted to N_2 in their setup when flowing through a stainless steel beads bed with the produced HNCO. These results led to several patents on the utilization of cyanuric acid in mobile exhaust gas aftertreatment – a process that became known as RAPRENO$_x$ (RAPid REduction of NO$_x$). [102,103,104] However, it was later shown that the stainless steel beads used as reactor filling material actually catalyzed the decomposition of HNCO, [105] leading to the production of NH_3, which was the actual reducing agent. During this time, first experiments were conducted with solid urea as NH_3-storage compound, and a direct comparison showed urea to be advantageous for multiple applications. [106]

1.2.3. Urea

After the invention of HC-SCR for mobile NO$_x$ sources, to avoid handling NH_3, [107] and the discovery of cyanuric acid as a safe NH_3-storage compound, [100] urea was proposed as a storage material for NH_3 in 1988 [108]. By then, urea was already known to work as an NH_3-precursor for SCR in stationary applications for three years [109]. First results on mobile urea-based SCR were publically presented in 1990, already showing NO$_x$ conversions above 90% from 250°C at gas hourly space velocities (GHSV) of 12,900 h^{-1} [110]. The first patented mobile applications of urea solutions for SCR were registered in 1990 [111].

There are numerous advantages in using urea, ranging from its chemical properties to its low price. Urea is a non-toxic, non-corrosive solid, which is hygroscopic and well-soluble in water.

Due to the large-scale production of urea as a bulk commodity, it is readily available in large quantities. Since the involved reactants CO_2 and NH_3 needed for urea synthesis are bulk chemicals that are produced directly from air and natural gas, using the well-known industrial Haber-Bosch process, urea can be produced at a low price. [112]

Each urea molecule can be decomposed to yield two molecules of NH_3 and one molecule of CO_2, with the overall reaction requiring one molecule of H_2O. Decomposition of urea can be split into two reactions, the first one being a thermolysis of urea to isocyanic acid (HNCO), and the second being the hydrolysis of HNCO (reactions 1-19 and 1-20). [85]

$$H_2NCONH_2 \rightarrow NH_3 + HNCO \qquad \textbf{1-19}$$

$$HNCO + H_2O \rightarrow NH_3 + CO_2 \qquad \textbf{1-20}$$
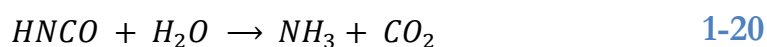
In contrast to the HNCO hydrolysis, the urea thermolysis was, so far, considered to proceed without catalytic enhancement, but recent investigations at PSI provided evidence that urea thermolysis is actually also catalyzed. [113]

The NH_3 storage density of solid urea (gravimetric and volumetric) is very high, but the dosing is technically challenging. In order to release all the stored NH_3, urea needs to be contacted with a catalyst, and this is quite difficult to achieve during dynamic operation of a vehicle. [114] In order to dose solid urea, urea is pressed into spherical pellets of defined diameter. The pellets are then dispensed from the storage tank by a star feeder [115] and shot onto a hydrolysis catalyst-coated heated plate using pressurized air. [116] The catalyst-coated plate constituted an external reactor in a
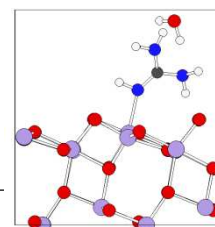
bypass flow of the main exhaust for the conversion of solid urea to NH_3 gas. [117] Later modifications of the reactor place the unit in the main exhaust duct, downstream of an oxidation catalyst, in order to harvest heat from the exhaust gas for the decomposition of the dosed urea, rather than using solely electric heating. [118]

Still, the handling and dosing of solid urea in mobile SCR systems remains complicated, as small amounts of solids are hard to dose as dynamically as the NO_x emissions from the engine varied. [114] Handling is made even more difficult by the high deliquescence of solid urea, which easily transforms the single solid urea pellets into larger aggregates of solid urea that no longer passed the solid transfer sections. [119]

In order to simplify the dosage of urea into the main exhaust duct, aqueous solutions of urea were introduced. A concentration of 32.5% (by mass) urea in H_2O was chosen for mobile applications as a standardized solution due to the eutectic nature with a melting point of -11°C. The trade name AdBlue® was introduced in many countries, in others the solution became known as Diesel Exhaust Fluid (DEF) or as Aqueous Urea Solution (AUS). [120] For the exhaust gas aftertreatment of Diesel engines in large ships a more concentrated solution of 40% urea is used, as the stored urea solution is not exposed to low temperatures in the ship's engine room. As the temperature in many parts of the world falls regularly below -11°C in winter, the AdBlue® tank of vehicles must be equipped with a heating system. Most frequently the heating system is a combination of electric heating and a heat exchanger drawing off-heat from the engine cooling fluid. [121]

High-temperature stability of AdBlue® is also restricted, as urea in the aqueous solution will start decomposing, thereby building up pressure in

the storage tank. AdBlue® containments and transport lines are not generally built to withstand pressures higher than 50 mbar relative to ambient pressure. However, AdBlue® in a sealed vessel will build-up a pressure of 70 mbar under storage at 40°C. The shelf life when stored between 30-35°C is reduced to just 6 months. [122]

The easy release of NH_3 from the precursor compound clearly becomes a disadvantage for the application of AdBlue® in Mediterranean up to tropic areas.

The NH_3 storage potential of AdBlue® amounts to 0.201 kg/L (0.184 kg/kg) NH_3/solution [120] compared to solid urea with 0.567 kg/kg (0.749 kg/L solid block or 0.42 kg/L pellets).

Since the commercial introduction of AdBlue® in 2004, [123] it has been adopted worldwide for heavy-duty applications of Diesel engines equipped with SCR systems, and is considered the most promising system for the Diesel-engine passenger car market. [33]

1.2.4. Ammonium formate

In the course of optimizing the low-temperature stability of aqueous urea solution, various anti-freeze additives were tested. For example typical engine coolant antifreeze additives such as ethanol [124], propylene glycol or methanol [125] were added to aqueous urea. However, the freezing point depression was not very significant (< 10 K) and the emission of the additionally introduced hydrocarbons in the exhaust was not acceptable. [125] In contrast, ammonium formate addition to aqueous urea solution caused a depression of the freezing point down to -30°C, and it could even contribute to the NH_3-storage capacity. [126] Inorganic ammonium salts have already been proposed for application in fossil fuel power plant SCR
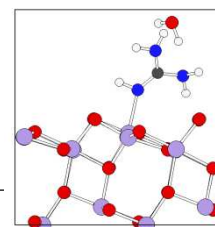
systems [99], but ammonium formate was only mentioned in previous disclosures concerning the selective non-catalytic reduction (SNCR) of NO_x in these units. [127] The use of ammonium formate as an additive to urea solution has brought the benefit of decreasing the melting point, [128] and yet increased the amount of stored NH_3 in the solution. [129] Depending on the application, high NH_3-containing solutions could also be prepared that showed comparable low-temperature stability to AdBlue®. [130] The most preferable solutions are named Denoxium-20 or Denoxium-30 with freezing points around -20°C and -30°C, respectively. The NH_3-releasing capacity amounts to 0.207 kg/kg (0.232 kg/L) for Denoxium-30 and to 0.205 kg/kg (0.228 kg/L) for Denoxium-20. Denoxium-20 is only advantageous to Denoxium-30 in so far that it contains less of the more expensive ammonium formate, while containing approximately the same amount of stored NH_3. The melting point of Denoxium-30 is actually not exactly -30°C – the solution shows a hysteresis of freezing as low as -31°C and melting as high as -26°C. [131] Until now, only the Denoxium-30 solution has been commercially employed, either under the name Denoxium®, or, in Canada, the USA and Mexico, under the name TerraCairPlus®, due to a license agreement between Denoxium® owner Kemira Oyj with Terra Environmental Technologies Inc. [132]

There is already interest in modeling the evaporation of ammonium formate urea solution droplets in the exhaust gas duct. [133] Ammonium formate will split into ammonia and formic acid in the hot exhaust. [129] While ammonia is the desired product that is consumed in the SCR reaction, formic acid constitutes an undesired emission. In fact, formic acid is the most corrosive halogen-free organic acid, and its corrosive effect on metals is further enhanced by O_2. [134] The corrosion of steel by formic

acid is a function of the acid concentration and the temperature [135], but in contrast to inorganic acids, formic acid does not form a passivating film on the metals during corrosion. [136] In the past, the corrosive effect on various types of steel was investigated (type 304 [137], type 430 [138], SUS 329J1 [139], AISI-316 [140]), however the experiments did not include corrosion by hot formic acid vapors.

In addition to the immediate corrosive effect of formic acid, there is an additional danger of forming undesired side products from the reaction of formic acid with compounds in the exhaust gas. One possible side reaction is the formation of methanamide by a condensation with NH_3. [141] Methanamide is considered to be teratogenic [142], though it must be noted that while some animal studies did show teratogenic effects, [143] others (with different application doses) did not observe a teratogenic effect [144].

From methanamide hydrogen cyanide (HCN) can also be formed by the removal of another water molecule. As HCN is a very toxic compound, its emissions must be avoided, even though there is no immediate legal regulation on the concentration of HCN in internal combustion engine exhaust gas. The formation of HCN from methanamide will be discussed in more detail later.

In practical applications the emission of side products are either not known to the commercial producers, reduced by controlling decomposition parameters, or seem to be accepted, possibly also due to the policy of the companies selling ammonium formate solution not publically mentioning the side product formation. [131]
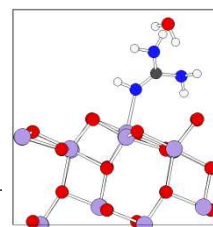
1.2.5. Ammonium carbamate

In order to avoid freezing issues altogether, solid precursor compounds are a good substitute for solutions of NH_3-precursor compounds. However, the handling of solid NH_3-precursors are more complicated, especially if they also need to be contacted with a decomposition catalyst like solid urea (as discussed in section "1.2.3. Urea").

There are, however, also solid substances which do not need a catalyst to yield NH_3, and only need to be heated for NH_3 release. One compound in this category is ammonium carbamate. Ammonium carbamate is the ammonium salt of the instable carbamic acid, and it can be transformed to urea by a condensation of the salt. [145] Another compound which can be decomposed to yield NH_3 without a catalyst is ammonium carbonate. [146] However, ammonium carbonate stores less NH_3 per mass and volume, because it contains an additional molecule of water with respect to ammonium carbamate. In detail, ammonium carbamate stores 0.436 kg NH_3/kg (0.698 kg/L), while ammonium carbonate stores 0.354 kg NH_3/kg (0.531 kg/L).

The decomposition of ammonium carbamate or ammonium carbonate in order to yield NH_3 are both thought to proceed via a two-step reaction. For ammonium carbamate the reaction proceeds according to 1-21 and 1-22 via the instable carbamic acid. [145]

$$NH_4COONH_2 \rightarrow NH_3 + HCOONH_2 \qquad \text{1-21}$$
$$HCOONH_2 \rightarrow NH_3 + CO_2 \qquad \text{1-22}$$
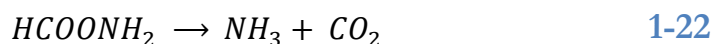
The decomposition of ammonium carbonate is considered to proceed via the stable ammonium bicarbonate intermediate. [146]

$$(NH_4)_2CO_3 \longrightarrow NH_3 + (NH_4)HCO_3 \qquad \text{1-23}$$

$$(NH_4)HCO_3 \longrightarrow NH_3 + CO_2 + H_2O \qquad \text{1-24}$$
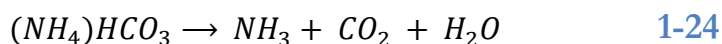
In addition, the condensation of ammonium carbamate to yield urea and water can occur as the following side reaction. [147]

$$NH_4COONH_2 \longrightarrow NH_2CONH_2 + H_2O \qquad \text{1-25}$$

As all the above reactions are also reversible, the repeated cycling between heating and cooling during the operation can lead to the presence of all the compounds in the storage tank. This can become an issue if H_2O condenses during cooling inside the tank, because it can lead to an uncontrolled production of NH_3 from ammonium carbamate and with it a sudden pressure increase in the storage tank. [141]. This becomes relevant for the decomposition of ammonium carbonate, because H_2O is released, but commercial ammonium carbonate usually also contains ammonium carbamate as well [148].

As ammonium carbamate stores more NH_3, does not produce H_2O during decomposition and needs less heat for decomposition, it is preferred over ammonium carbonate. Despite the difficulties associated with the dynamically controlled decomposition of ammonium carbamate, the system was tested for commercial applications. [149,150] Recently, a light-duty application on a 5.9 L Diesel engine was presented and the use of ammonium carbamate was protected by the name Solid SCR®. [151]

However, until now, ammonium carbamate does not seem to be commercially applied as NH_3-precursor in any mobile application.

1.2.6. Metal ammine chlorides

A completely different approach in storing NH_3 is the reversible coordination of NH_3 as a ligand to metal atoms. [152] Since the absorption
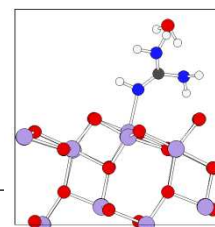
of ammonia as a ligand is exothermic, and its release is endothermic, the idea is to first store NH_3 in metal ammine chlorides, so it can be later released by heating the salt. Salts of particular interest for NH_3 release are $Mg(NH_3)_6Cl_2$, $Ca(NH_3)_8Cl_2$ and $Sr(NH_3)_8Cl_2$, due to the high amount of NH_3 they can store. [128] Even though $CaCl_2$ and $SrCl_2$ would be advantageous compared to $MgCl_2$ because of their higher NH_3 storage capacity, these compounds are less attractive for practical applications. This is not because of economic considerations, but because of the high NH_3 vapor pressure exhibited by $Ca(NH_3)_8Cl_2$ and $Sr(NH_3)_8Cl_2$. The NH_3 vapor pressure of $Ca(NH_3)_8Cl_2$ at 25°C is 630 mbar, and that of $Sr(NH_3)_8Cl_2$ is 550 mbar [153], both of which are rather high for handling or even storing in a sealed container, as there would be significant leakage of NH_3 in the case of a container rupture in an accident. [154] The storage and release of NH_3 into or from these salts is proceeding successively, with decreasing enthalpies of adsorpition or desorption as the amount of coordinated NH_3 increases. The individual reactions for $MgCl_2$ are given in 1-26 to 1-28.

$$MgCl_{2\,(s)} + NH_{3\,(g)} \rightleftharpoons Mg(NH_3)Cl_{2\,(s)} \quad \Delta H_r = -87.0 \frac{kJ}{mol} \quad \text{1-26}$$

$$Mg(NH_3)Cl_{2\,(s)} + NH_{3\,(g)} \rightleftharpoons Mg(NH_3)_2Cl_{2\,(s)} \quad \Delta H_r = -74.9 \frac{kJ}{mol} \quad \text{1-27}$$

$$Mg(NH_3)_2Cl_{2\,(s)} + 4\,NH_{3\,(g)} \rightleftharpoons Mg(NH_3)_6Cl_{2\,(s)} \quad \Delta H_r = -55.6 \frac{kJ}{mol} \quad \text{1-28}$$
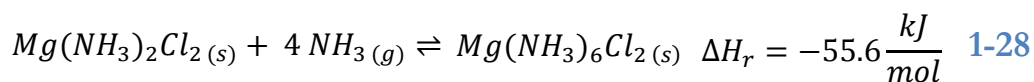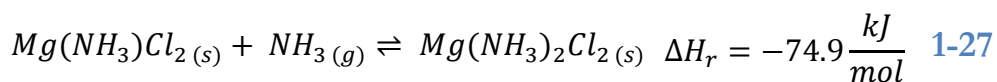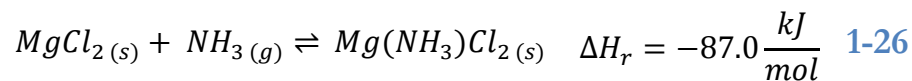
All reactions are exothermic, but reaction enthalpies are different. [155] Using the Van't Hoff equation (1-29), the releasing temperature for NH_3 at a constant reservoir pressure of 1.5 bar can be calculated.

$$\ln P_{NH_3,eq} = \frac{-\Delta H_{r,k}}{RT} + \frac{\Delta S_{r,k}}{R} \qquad \text{1-29}$$

In 1-29 the index k identifies the reaction of the NH_3 absorption or desorption process, R is the gas constant, T the temperature, $\Delta H_{r,k}$ the

corresponding desorption enthalpy per mole NH_3 and $\Delta S_{r,k}$ the corresponding desorption entropy of the reaction. The calculated temperatures for release of the last 4 absorbed NH_3 molecules are 150°C, 298°C for the second, and 387°C for the first molecule. From these calculated values the full release of all six stored NH_3 molecules is impractical because of the high temperatures needed. This reduces the amount of practically stored NH_3 to two thirds of the theoretical value. Another factor that reduces the amount of stored NH_3 is that a powder, and not a single crystal, is used. Typically void fraction of 45-50% are present in the storage container, which not only decreases NH_3-storage capacity but also reduces heat transfer. [154] Since heat transfer is crucial for the dynamic release of NH_3 gas from the salt, the powder is compacted under high pressure. [156] Bulk densities of 97% of the solid density can be achieved, approaching 93% of the volumetric NH_3 storage capacity of liquefied NH_3. [154] As the ammine salt releases NH_3 gas, its density is reduced and NH_3 gas diffusion is not hindered. When the salts are exhausted of NH_3, they can be recharged with NH_3. During absorption, the pressurized cylinders are first heated so that the NH_3 evenly distributes within the bulk material. [157]

Recently, the Danish company Amminex announced the launch of a production part approval process for exchangeable cylinders filled with metal ammine salts for NH_3 storage, the total investment amounted to 50 million €. [158] Also, the US-based Navistar and French Faurecia invested in Amminex's technology, promising rapid utilization in mobile applications. [159] Interestingly, Amminex is using $SrCl_2$ rather than $MgCl_2$ as NH_3 absorbant, because it has the advantage of requiring only 80°C for the release of 7 molecules of NH_3. [160] This can be achieved by using the
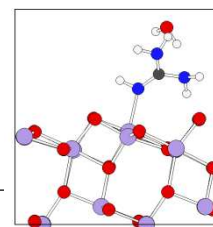
engine coolant as heat source. The cartridges filled with charged $Sr(NH_3)_8Cl_2$ are not classified as dangerous goods, in spite of the 550 mbar of NH_3 vapor pressure present at 25°C. During the operation, pressures of 6 bar are achieved in the cartridge, so there is a need for robust containers. So far, no comments have been made regarding the possibility of transporting the storage salt during NH_3 dosage onto the SCR catalyst. In this case the SCR catalyst could be deactivated due to its sensitivity towards earth-alkaline metals. [161,162] In addition to the application as a NH_3 source for SCR, the cartridges are proposed as storage cylinders for NH_3 which will be converted to H_2 and used to power a fuel cell. [163]

1.2.7. Methanamide

Analogous to urea being the condensation product of ammonium carbamate, methanamide (formamide) is the condensation product of ammonium formate. At ambient conditions (20°C, 1 atm), methanamide is a liquid with a vapor pressure of 30 mbar and a melting point of 2°C. [164] However, if mixed with water, an aqueous 80% methanamide solution has a melting point of -28°C, and remains stable at temperatures up to 100°C. [141] This solution is known as Admide® and is also proposed as an NH_3-precursor for mobile applications. In addition to the excellent temperature stability, the solution with 0.30 kg/kg (0.33 kg/L) also stores more than 50% more NH_3 than AdBlue®. [165] In contrast to urea, methanamide will molecularly vaporize without decomposition. Admide® was further determined to be biodegradable, but was also found to correlate with teratogenic effects in some animal tests [143], though not in all. [144] As the general perception of methanamide was that it indeed causes defects to the unborn child, the introduction of Admide® to the

automotive market was cancelled. [142] Today's gasoline fuel contains up to 1% (by volume) of benzene [166] also due to the substitution of lead-based anti-knocking agents, even though benzene is known as a teratogenic substance. [167] Therefore, the handling of Admide® solution by trained personnel during the regular service of a vehicle should be acceptable, considering the great advantages of using the solution.

Under certain disadvantageous conditions, such as overdosage of the reducing agent at low temperature, emissions of molecular methanamide, rather than the decomposition products, can occur. However, during decomposition methanamide also yields upon hydrolysis formic acid which, as previously mentioned, is a corrosive compound. Decomposition of formic acid may either lead to CO and H_2O, or to CO_2 and H_2. Unfortunately, the preferred latter decomposition reaction products are not the main products, but rather CO and H_2O. Another possible reaction that occurs at very high temperatures during methanamide decomposition is the removal of water to yield HCN. As previously mentioned, there is no immediate legal regulation on the emission of HCN in exhaust gas, but due to the toxicity of the compound it should be avoided.

Currently, the use of Admide® as a NH_3-precursor is protected by MAN Truck & Bus, [168] but seems not commercially used, due to a lack of acceptance for handling of the substance or the associated side products.

1.2.8. Guanidinium salts

In urea, two amine groups are attached to a carbonyl moiety. If the carbonyl is replaced by an imine function, one obtains guanidine. Guanidine is an instable compound with one of the highest basicities for organic compounds. Both properties are driven by the stabilization of the
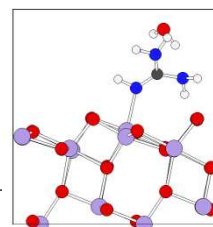
guanidinium cation by three amine functions connected to the central carbon atom. Due to the symmetric structure, the guanidinium cation is a very stable compound in combination with an anion. [169] For the utilization of guanidinium salts in exhaust gas aftertreatment, small organic anions are preferred which decompose completely to gaseous products. The most promising compounds are therefore guanidinium carbonate, guanidinium hydrogencarbonate, guanidinium formate and guanidinium oxalate. Besides the preference of CO_2 as decomposition product for the anion, the solubility of the salt in water is also an essential factor which needs to be observed. Here, the solubility of guanidinium formate, with up to 6.19 kg dissolving in 1 L of water is unrivaled. [170] However, in order to achieve good thermal stability, significantly less salt is dissolved in water. An aqueous 60% guanidinium formate solution can be stored for several months at a temperature of 60°C, and can be supercooled to a temperature of -30°C without freezing. [171] The low amount of water contained in the solution compared to AdBlue® is an advantage, because significantly less water needs to be evaporated by the hot exhaust gas. [172] In this solution, again, approximately 1.5 times the amount of NH_3 is stored compared to AdBlue®. However, due to the high stability of the compound, its catalytic decomposition below 200°C is incomplete. [165] The decomposition of guanidinium carbonate and guanidinium bicarbonate is occurring at lower temperatures, but the solubility of the salt is much lower – not even the NH_3-storage capacity of AdBlue® is achieved, which makes it largely irrelevant. [165].

The decomposition of guanidinium formate is best achieved on a dedicated hydrolysis catalyst, and since higher temperatures than those found in the exhaust gas duct are needed, the decomposition in a side stream reactor

with the possibility of external heating is preferred. [**165**] The conditions for the catalytic decomposition of guanidinium formate, including the necessary temperature, space velocity and catalyst material, are determined in the presented work. This represents one part of an industrial research project aimed at the commercial utilization of guanidinium formate as NH_3-precursor compound in exhaust gas aftertreatment.

1.3. Background to presented work

1.3.1. Guanidine and its uses

Guanidine was first obtained by Strecker in 1861 by the oxidative degradation of guanine. [**173**] Guanine is one component in naturally occurring guano, which was generally applied nitrogen fertilizer, prior to the discovery of industrial NH_3 synthesis by the Haber-Bosch process. Synthetic approaches for guanidine also exist, and these can be from urea [**174**], from cyanamide [**175,176**], from dicyanodiamide [**177,178**], from dicyanodiamidine [**179,180**], from ammonium thiocyanate [**181,182**] or from other compounds [**183,184**]. Industrially, only the synthesis from dicyandiamide, cyanamide and urea are used for large-scale production of guanidine and its salts. The dicyandiamide route being by far the most important. [**169**]

Even though guanidine is structurally very similar to urea, and a small organic compound, the molecule is not well characterized. For example, the crystal structure of solid guanidine (melting point 48-49°C [**185**] or approximately 50°C [**186**]) was only determined in 2009, [**187**] although the crystal structure of urea has been known since 1923. [**188**]

The use of guanidine has been motivated by its high basicity with a pK_a value of 13.6 for the corresponding guanidinium cation. [**189**] In water,
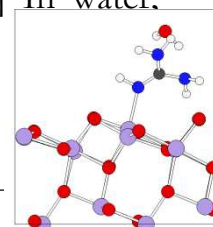
guanidine is, therefore, more basic than NH_3. This can be attributed to the resonance stabilization of the guanidinium cation. [190] In the gas phase the basicity is comparable to triethylamine. [191]

The exact symmetry of the guanidinium ion has been a matter of discussion. While the CN_3 moiety has been determined as planar with identical lengths for the CN bonds [192], the symmetry of the entire ion in different salts was proposed to be either D_{3h}, [193,194,195] C_{3h} [196] or C_{3v} [190]. Due to experimental difficulties of determining the position of hydrogen atoms by x-ray crystallography, [197] and as there are only measurements of guanidinium derivatives using neutron diffraction, [198,199,200] the exact symmetry remains unclear. Molecular simulations give varying results, depending on the used level of theory. [201,202,203]

The 3-fold symmetry of the guanidinium ion with six equivalent hydrogen atoms provides excellent conditions for hydrogen bonding. [192] This property is exploited in protein denaturation, where the multiple hydrogen bonds donated from guanidine are used to disturb the secondary structure of proteins. [204] This effect is most conveniently utilized with guanidinium chloride, which is still one of the strongest known denaturants for protein folding [205,206] even though it's discovery dates to 1938. [207]

Besides the utilization in biochemistry, guanidinium compounds are also used as propellants and explosives. [169] Automobile airbag systems contain guanidinium nitrate, which is ignited in the case of a collision to inflate the airbag within 40 ms of the impact. [208] The salt is extruded into small cylinders, with variations in shape and size influencing the progressive gas output. [209,210] Other applications of guanidinium nitrate or nitroguanidine are in gun propellant formulations, [211,212] as additives in rocket propellants [213] or as explosives. [214]

The decomposition of guanidinum compounds prior to the research project associated with this thesis has mainly been of interest for propellant applications. There are, therefore, some works on guanidinium nitrate decomposition, [215,216,217] but not for other guanidinium salts that are of interest for exhaust gas aftertreatment. Only one previous work is found for the hydrolysis of a guanidinium salt, i.e. guanidinium carbonate, but only because of its implications on the synthesis of guanidinium compounds. [218] Literature about guanidinium formate is even scarcer, and less related. There are some theoretical works on the interaction between the ions as model systems, because the bonding pattern between guanidinium and formate can occur in protein denaturation. [219,220]

There are a few patents which actually disclosed in some way the use of guanidinium salts as NH_3-storage compounds prior to the research project. [221] The motivation varied from producing NH_3 to be burnt for propulsion, [222] to actually using guanidinium compounds for NH_3-SCR. [223] However, it must be noted that these disclosures contain a list of several N-rich compounds for NH_3-storage and release, so one cannot be certain about the sincerity of mentioning guanidinium compounds for NH_3-SCR.

So far all publications dedicated to guanidinium salts for the applications as NH_3-precursor compounds in NH_3-SCR, which included also experimental data, were associated with the industrial research project which initiated also this thesis. Consequently, the experiments associated with the catalytic decomposition of guanidinium salts are truly novel. However, as a consequence of this originality a comparison with similar measurements outside our laboratory can not be performed.
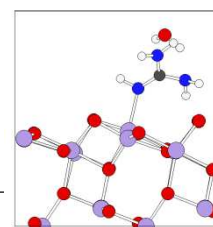
1.3.2. Hydrolysis catalysts

The hydrolysis catalyst's purpose is to decompose the NH_3-precursor compound so that the stored NH_3 is released and becomes available as a reactant for the SCR reaction. The decomposition of the precursor is assisted by the reaction with water contained in the exhaust and the NH_3-precursor solution, hence the name hydrolysis. As the hydrolysis of guanidinium formate is a new topic, one needs to look at the hydrolysis catalysts employed for the decomposition of other NH_3-precursor compounds.

As urea is the standard NH_3-precursor compound, its decomposition should be briefly discussed. The release of two molecules of NH_3 from urea consists of two consecutive reactions, with the stable intermediate isocyanic acid (HNCO). The thermolysis of urea to HNCO occurs at elevated temperatures also without the presence of a catalyst. However, recent investigations at PSI also found that the reaction is catalytically enhanced as well. [113] The second step, the hydrolysis of HNCO, does not occur without a catalyst being present. If HNCO is not decomposed, the corresponding quantity of NH_3 would be mostly lost, because HNCO does not reduce NO_x as efficienct as NH_3. Also, HNCO can easily polymerize to form higher molecular compounds such as the trimer cyanuric acid. [224,225] Therefore, the catalytic hydrolysis of HNCO must be conducted in the exhaust gas aftertreatment system.

There has been previous work on determining the most active catalyst materials for the decomposition of HNCO. From the results, ZrO_2 showed the highest activity for HNCO hydrolysis, followed by TiO_2 (anatase) and Al_2O_3. [226] TiO_2 (rutile) is less active in the catalytic decomposition. However, as ZrO_2 is more susceptible to poisoning by sulfur than TiO_2,

and SO_2 emissions remain a component in Diesel exhaust gas, TiO_2, rather than ZrO_2, is the preferred material. In real applications, many commercial exhaust gas aftertreatment systems do not feature a dedicated hydrolysis catalyst for the conversion of HNCO, due to the limited available space for the exhaust gas aftertreatment system and/or cost issues.

Luckily, the SCR catalysts used in mobile applications are not only catalytically active in reducing NO_x, but also for the hydrolysis of HNCO. The hydrolysis of HNCO – and as recently shown the catalyzed thermolysis of urea – comes as a highly appreciated side-effect of these catalysts, as it also effectively prevents the polymerization of HNCO. This would otherwise be a significant threat to the catalyst, because the polymers could block the pores on the catalytic surface.

The different commercially relevant SCR catalysts and comments about their hydrolysis activity are presented here. The two main categories of metal-oxide based catalysts and metal-exchanged zeolites should be split into vanadiumoxide containing or vanadiumoxide-free catalysts and Fe-exchanged zeolites or Cu-exchanged zeolites, respectively.

Vanadiumoxide containing catalysts are the oldest amongst those used in mobile applications, but remain state-of-the-art especially in heavy-duty applications such as ship diesel engines and trucks. Typically, they contain around 2% of vanadium in the form of vanadia (V_2O_5) as an active component, with a support material of high-surface TiO_2 (anatase). In order to stabilize the TiO_2 (anatase) surface against rearrangements at high operation temperatures, SiO_2 and WO_3 are added. [227] WO_3 also increases acidity, which is advantageous for NH_3 absorption and reduces sulfation of the TiO_2 support. SiO_2 acts as a stuctural stabilizer on all length scales, ranging from the creation of a silicate network for structural stability up to
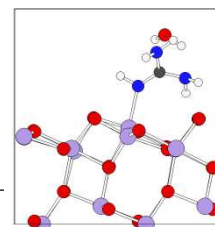
glass fibers which are added to increase physical stability of the usually extruded pure catalyst honeycomb structures. Vanadia-based catalyst are very attractive due to their low cost and robustness against high operation temperatures and sulfur poisoning. However, they show little activity in the low-temperature range present in automobile exhaust under real driving conditions. [228] Additionally, at high temperatures, NH_3 can be oxidized to N_2O, which has a greenhouse gas warming potential of 310 CO_2 equivalents. [229] Also, there have been concerns about the emission of vanadium compounds during operation at high temperatures due to volatile vanadium species. [74,75]

Consequently, research on vanadium-free metal oxide based SCR catalysts was initialized. [230,231,232] Some of the catalysts utilized in the first years of SCR in power plants contained iron-, [233] manganese- or nickel oxides [234] as the active component, but their activity in the temperature window for mobile SCR applications is much worse than those of vanadia-based catalysts. Also, these early vanadium-free catalysts had problems in maintaining a high selectivity of NO_x reduction to N_2. Novel vanadia-free SCR catalysts are based on rare-earth metal-oxides and transition metal oxides. In particular, ceria-zirconia mixed oxides seem to be very promising catalyst systems, [235] but also Fe_2O_3/ZrO_2 with WO_3 doping [236] and hybrid systems with commercial SCR catalysts were proposed. [237] Currently, there is active research and development on this topic in industry, but little information is publically shared.

The other branch of vanadia-free catalysts are metal exchanged zeolites. Many different transition metals were tested in various zeolite structures, but finally only a few are commercially utilized. Until a few years ago, Fe-exchanged zeolites of the type Fe-ZSM-5 were the preferred choice, and

still remain one of the most attractive catalyst types, due to their good hydrothermal stability and small production of N_2O emissions from NH_3 oxidation at high temperatures, compared to vanadia-based catalysts. [238] However, recently Cu-exchanged zeolites came back into discussion, mainly as Cu^{2+} exchanged ZSM-5. Cu-exchanged beta zeolites were also previously in competition with Fe-ZSM-5 catalysts, but were inferior in performance at elevated temperatures, produced N_2O emissions and were suspected to show the formation of toxic dioxin formation under certain operation conditions, as deduced by the dioxin formation from Cu-containing DPF additives. [239,240] Recent experiments performed by the US Environmental Protection Agency (EPA) with different exhaust gas aftertreatment systems incorporating Cu-exchanged zeolites, however, did not show any production of polychlorinated dibenzo-p-dioxins, although there actually was a small decrease measured. [241,242,243]

The latest generation of Cu-exchanged zeolites that were introduced to the market by industrial companies are based on the SSZ-13 zeolite with a chabazite (CHA) structure. [244,245,246] The peculiar chabazite structure features relatively small pores (radius ~3.8 Å) in eight-membered rings, which provide sites for isolated Cu atoms. [247] These isolated Cu^{2+} ions are the active sites for the SCR of NO. [248] Due to the ideal dispersion of the active centers, and their structural stabilization, these new generation of Cu-chabazite catalysts perform not only better at low temperature SCR than any other metal-exchanged zeolite or metal-oxide catalyst, but also offer a hydrothermal stability practically only limited by the bulk stability of the chabazite framework. This new catalyst material was quickly transferred into commercial applications, and its propagation is currently mainly limited by the high raw material price of the SSZ-13 zeolite, which is synthesized
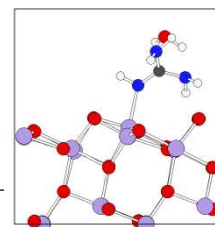
using expensive templates. Not even deactivation of Cu-chabazite by hydrocarbons seems to be a serious issue for state-of-the-art catalyst, in contrast to the effects observed for previous systems. [249]

As already mentioned, all these commercially employed catalysts are not only active in SCR of NO_x, but show also good catalytic activity for the hydrolysis of urea. In the case of vanadia-based SCR catalysts, the main component TiO_2 (anatase) is actually known to be the best dedicated hydrolysis catalyst for HNCO, apart from ZrO_2. Even the metal-exchanged zeolites show good hydrolysis activity, which is independent on the exchanged metal species, but rather on the zeolite framework. For all catalysts, the space velocities needed for the SCR reaction (up to 50,000 h^{-1}) are more than enough for the much faster hydrolysis of HNCO, which works up to around 150,000 h^{-1}, provided the temperature is around 180°C. For guanidinium formate, decomposition was probed on a selection of the previously presented catalysts, including Fe-ZSM-5 zeolite, and dedicated hydrolysis catalysts like TiO_2 (anatase), ZrO_2 and γ-Al_2O_3. [165] Decomposition could in principle be achieved on all the tested catalyst materials, but in comparison to urea, guanidinium formate decomposition required much higher operation temperatures. In detail, at 400°C Fe-ZSM-5 and Al_2O_3 showed a conversion above 90%. However, in the case of Fe-ZSM-5 the gas feed had to be O_2-free – already with only 10% O_2 30% of the NH_3 was oxidized. At 400°C, ZrO_2 showed a conversion of just below 60%. Only TiO_2 (anatase) showed already an NH_3 yield of above 90% at 300°C and a tested gas hourly space velocity of up to 30,000 h^{-1}. During the decomposition at high temperatures traces of the side products methanamide and HCN could also be detected in the gas phase.

These investigations led to the conclusion that guanidinium formate decomposition would not be feasible in the main exhaust duct. Instead, a side-stream decomposition reactor connected to a bypass of the main exhaust duct, and equipped with an additional electric heating, was planned to accommodate a dedicated guanidinium formate decomposition catalyst. This reactor should then decompose guanidinium formate to NH_3 and dose the produced gas flow into the main exhaust duct, thereby providing gaseous NH_3 at temperatures the SCR will start to light-off. At these temperatures, which are around 150°C for the latest generation of Cu-chabazite SCR catalysts, even AdBlue® could not be sprayed into the main exhaust duct due to incomplete decomposition that would cause the deposition of solid urea or higher-molecular side products in the SCR catalyst, which ultimately leads to its deactivation.

The side-stream NH_3-generator developed in the industrial research project framework of this thesis could, therefore, be used with both, guanidinium formate and regular AdBlue® as NH_3-precursor solution. AdBlue® has the advantage that during most of the operation time the electric heating would not be necessary.

1.3.3. Supported Au catalysis

Since an Au-doped TiO_2 (anatase) catalyst was found to decompose guanidinium formate most effectively, while avoiding the formation of undesired side products, a brief introduction to supported Au catalysis should also be given.

Historically, gold was considered to be a catalytically inert material. Even though there were some early indications for the catalytic activity of gold in hydrogenation reactions back in 1973, [250] it was not until a decade later
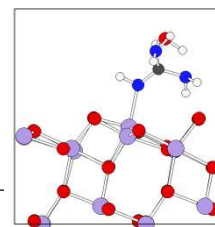
that research was attracted to a completely new field of catalysis. In 1987 Haruta and coworkers presented the extraordinary CO oxidation activity of nanometer-sized gold particles supported on TiO_2. [251] The activity was even maintained at a temperature of just -77°C, making for the first time an Au-based catalyst the most active one for a specific chemical reaction. It was realized that the fine dispersion of Au is responsible for the catalytic activity which could not be observed for bulk material. In 1988 supported Au was also shown to catalyze the hydrochlorination of ethyne to form vinyl chloride, which is needed for polyvinyl chloride (PVC) production. [252]

These two research highlights opened the door to a research field featuring more than 1,000 publications annually. Even though research on supported Au catalyst has been conducted with great efforts in the meantime, there still remain many open questions, and intense discussion on the details of Au catalysis. In general, the preparation of the supported catalyst, with the size distribution of the dispersed Au, and the support used has strong consequences on the observed catalytic activity. [253] As catalytic activity is also heavily influenced by the presence of O_2 and water, [254] the comparison of results from different research groups can become controversial. Things become even more complicated when pinpointing the active site for the catalytic reaction on a supported Au-catalyst. For most reactions, any possible site of activity is proposed as the active center by competing research groups. [255] In recent years, the discussion is further enhanced by novel analytical techniques in high-resolution electron microscopy which are now able to detect even isolated Au atoms. [256] These new observations causes a re-evaluation of previous theories and even some additional possibilities for the active site in catalysis.

The situation is briefly illustrated by the fact that, ever since the discovery in 1988, researchers worldwide were and still are looking at the highly interesting CO oxidation on supported Au, [257] this means that today any possible active site is advocated by a certain group of experimentalists and molecular modeling reseachers, arguing the active site causing catalytic activity has finally been determined. [255]

Within the Au catalysis community there was also the interesting observation that formic acid is decomposed on supported Au to H_2 and CO_2 more efficiently than on any other supported noble-metal catalyst, including Pt. [258] This is proposed as a step towards the utilization of formic acid as a high-density H_2-precursor compound that can be utilized for hydrogen fuel cells. [259] However, the concept of targeted formic acid decomposition sounds very attractive, and led to the doping of TiO_2 with Au to facilitate guanidinium formate decomposition.

The details on the preparation and use of Au/TiO_2 for the decomposition are given in the corresponding chapter of this thesis.

1.4. Scope of the presented thesis

As mentioned, this work was initiated by the start of an industrial research project titled "NO_x Reduktion im motorischem Abgas von Dieselmotoren mit Guanidinsalzen". The project was led by AlzChem AG, a chemical company from Germany working in the field of carbon-nitrogen compounds such as guanidinium salts. The direct project partners included also the chemical company NIGU Chemie (Germany) which, as an AlzChem subsidiary, is specialized in the synthesis of guanidinium derivatives.
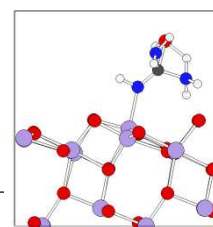
Moreover, the Technical University of Munich was represented by two groups, one being from the chair of thermodynamics led by Prof. Sattelmayer, the other from the chair of internal combustion engines led by Prof. Wachtmeister.

Also, the former exhaust gas aftertreatment group (today: catalysis for energy) led by Dr. Oliver Kröcher from the Paul Scherrer Institute. Various other companies contributed to the project by supplying catalyst samples or other materials or by discussion on the obtained results.

The set goal of the research project is to demonstrate the successful operation of a guanidinium formate based exhaust gas aftertreatment system on a Diesel engine at the TU Munich. The project tasks were assigned according to the competences of the respective parterns, with

- NIGU Chemie working on the synthesis of guanidinium formate and formulation of the aqueous solutions which could also contain urea,

- AlzChem working on the characterization of the guanidinium formate solutions and testing for corrosivity and toxicity,

- the group at PSI working on the development of a decomposition catalyst for guanidinium formate, the elucidation of guanidinium formate decomposition pathways and the characterization of the operation parameters for a decomposition reactor,

- the chair for thermodynamics working on the upscaling of the reactor proposed by PSI, engineering the reactor to account for the conditions defined for decomposition and producing a prototype which could be operated on a Diesel test stand,

- the chair for internal combustion engines which integrated the provided prototype into the exhaust gas aftertreatment system of a Diesel engine, including integration into the engine control unit and dosing of the produced NH_3-gas from the decomposition reactor uniformly into the main exhaust duct.

In order to fulfill the assigned tasks of (i) developing a good decomposition catalyst, (ii) investigating the reaction networks, and (iii) defining reaction parameters, a novel experimental setup was constructed which included the dosage of solutions of NH_3-precursor solutions in a laboratory-based setup for the first time. The development of this setup is described in the third chapter, along with some experiments demonstrating its powerful capabilities. The chapter is based on a corresponding publication in "Review of scientific instruments". [260]

The following two chapters are dedicated to investigating decomposition of guanidinium formate, first towards the elucidation of the involved reactions during decomposition, and then to the development of an ideal decomposition catalyst. This includes its preparation, testing for catalytic performance and aging resistance and, finally, its transfer to the prototype stage. The chapter about the reaction mechanism forms the basis for a publication in the "Journal of Physical Chemistry". [261] A European patent application (EP12152814) was also registered for the newly-developed hydrolysis catalyst.

The next chapter presents the decomposition of aqueous solutions of NH_3-precursor compounds in the liquid phase under elevated pressures. Besides commercial catalyst materials, the newly developed Au-doped hydrolysis catalyst is also tested. The chapter is a combination of a
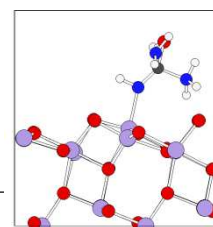
manuscript for publication in "Topics in Catalysis" and the European and international patent applications EP11153417 and 2011P01935WO.

In the final chapter, the proposed utilization of NH_4NO_3/urea solutions as NH_3-precursor solutions for *enhanced-SCR* are presented and discussed, using the results obtained on common commercial SCR catalysts.

2. Methods and experimental setup

2.1. Experimental setups and computational methods

2.1.1. Setup for investigations on NH_3-precursor solutions

In order to investigate the decomposition of liquid NH_3-precursor compound solutions, a dedicated experimental setup first had to be designed and constructed. The new setup was necessary, as even though there have been investigations in exhaust gas aftertreatment for several years, so far no lab-scaled setup for dosing liquid solutions of NH_3-precursor compounds was available at the institute. The reason for the lack of experimental setups is that urea decomposition is usually considered to work well on SCR catalysts whenever NO_x reduction occurs. Therefore, lab-based experiments designed to investigate SCR prefer to use the decomposition products NH_3 and CO_2, because these gases can be dosed more easily, and so experimental setups can be constructed in a less complicated manner.

The new experimental setup contains a reactor in which solutions of NH_3-precursor compounds can be sprayed onto hydrolysis or SCR catalysts. The gas feed flowing through the reactor is analyzed by gas phase FTIR spectroscopy for the detection of gaseous decomposition products and liquid-quenched by a gas absorption unit for the quantification of aerosols or high-molecular decomposition products.

A custom-made two-fluid spraying nozzle was used to nebulize 10-200 µL/min of NH_3-precursor solutions in a full spraying cone. Different catalyst-coated support structures such as ceramic honeycombs, metallic honeycombs or ceramic foams could be inserted into the reactor,
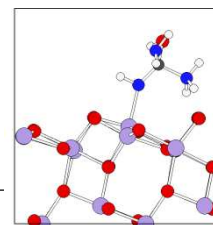
which was built in two diameters to enable experiments at different gas velocity regimes, in the range of 3,000-40,000 h^{-1} or 25,000-200,000 h^{-1}. The model exhaust gas entering the reactor was mixed from individual gas components and was heated to temperatures of up to 450°C in a heat exchanger mounted to the reactor inlet. The product gas from the catalytic decomposition was transported through heated lines into the gas cell of a Thermo Scientific Antaris IGS FTIR spectrometer. The spectrometer was operated using the software Quantpad, in which a multi-component gas analysis method was developed, including a correction for cross-sensitivities of measured components. Alternatively, some of the product gas was liquid-quenched using a gas absorption unit previously developed at PSI. The collected solutions from steady-state operation at a certain operation temperature were quantified using high-pressure liquid chromatography. The relevant high molecular compounds evolved during decomposition of guanidinium salts, or other NH_3-precursor compounds, were previously included in the HPLC method, which later allowed the reliable assignment of all the components found. As it constituted a significant part of the overall project, Chapter 3 provides more details on the analytics, and the development and construction of the experimental setup.

## 2.1.2. Tubular quartz reactor for TPD experiments

Temperature-programmed decomposition (TPD) experiments were performed in a different experimental setup than the investigations on NH_3-precursor solutions. Here, no spraying of liquid was necessary, but catalyst-coated ceramic cordierites were shortly dipped into solutions of NH_3-precursor compounds and placed into the reactor. The deposited

NH_3-precursors on the catalyst-coated cordierite were then subjected to a heating ramp while the decomposition products were quantified using a similar analytics system as for the spraying experiments: an FTIR gas phase spectroscopy and a liquid-quench unit providing samples for HPLC analysis.

Cordierite monoliths (400 cpsi, 9 x 13 cells, $L = 20$ mm, $V = 4.4$ cm^3) were coated with commercial TiO_2-anatase catalyst (Millenium Chemicals DT51; loading 119 g/L), according to the method described in the preparation section. For each experiment, a TiO_2-coated monolith was dipped into an aqueous solution of guanidinium formate (GuFo) and dried to evenly deposit a 50 mg amount of solid GuFo on the catalyst. In the temperature-controlled quartz reactor a second, untreated TiO_2-coated monolith was placed directly downstream of the first at a gas hourly space velocity (GHSV) of 95,500 h^{-1} for each. Nitrogen, containing 10% O_2 and 5% water vapor, was used as the base feed [262]. The gases were dosed by electronic mass flow controllers and water by a heated gas washing bottle. The product gas was pumped in trace-heated tubes at a flow of 150 L/h at STP through a heated gas-measuring cell (180°C) with a volume of 200 mL and 2 m path length, built into an FTIR spectrometer (Thermo Electron Nexus).

A multi-component method for the correction of non-linear responses and cross-sensitivities, facilitated the quantification of the possible gas components NO, NO_2, N_2O, NH_3, H_2O, CO, CO_2, isocyanic acid (HNCO), nitric acid (HNO_3), formic acid (HCOOH), formaldehyde (H_2CO), methanamide ($HCONH_2$) and hydrocyanic acid (HCN) with an accuracy of $\pm$ 1% and a detection limit of 1-3 ppm. In addition to the direct analysis of gaseous species, 220 L/h at STP of the product gas were
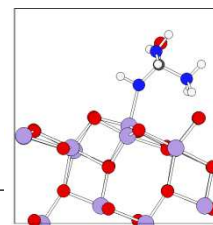
quenched with an absorbing solution in order to wash aerosols [263] out of the gas and to dissolve higher molecular compounds by an HPLC eluent (aqueous solution of NaH_2PO_4). The absorbing solution was periodically replaced and all parts were flushed with an excess of eluent. The collected samples were evaluated by HPLC analysis (Dionex UltiMate 3000, 197 nm detector wavelength, Waters IC-Pak anion exchange column), and compared to a library of previously recorded reference compounds (urea, biuret, triuret, cyanuric acid, ammeline, ammelide, melamine, formoguanamine, formylguanidine). For the experiments, the dry monoliths were slowly heated at a rate of 10 °C/min from room temperature to 400 °C. During this process, the evolution of product gases was recorded as a function of the monolith's temperature. The FTIR analysis has a time resolution of 7.4 s, while the HPLC analysis exhibited a temporal resolution of 2.5 min, due to the long sampling intervals.

2.1.3. DFT molecular modeling

The experiments to determine the decomposition reactions were supported by theoretical modeling of guanidinium formate decomposition in the gas phase and on a TiO_2 model surface. From this work, insights into the energetics of the decomposition reaction were gained that could be used to indicate the possible reaction routes occurring on the catalyst surface.

Quantum mechanical energies were calculated using density functional theory (DFT). The PBE functional was used, as it is a well-tested functional for solids, surfaces and molecules [264], and a functional of the computationally efficient and non-problematic generalized gradient approximation type. To solve the DFT equations, the DMol³ local orbital method [265,266] was used, because of its general applicability and

expediency for gas phase, surface and bulk compounds. The default basis set DND, with its element dependent cutoff radius, was used together with other default settings for integration and tolerances on self-consistent field (SCF) and geometry optimization convergence. For the Ti atoms of the TiO_2 substrate, a DSPP [267] effective core potential was adopted. The (101) TiO_2-anatase surface was modeled by a 12 layer 2 x 3 supercell slab, containing 66 atoms. The lower 30 atoms were fixed at their DFT bulk positions, the other near surface atoms were free to geometrically relax during interaction with adsorbates. The in plane k-space integration was done on a 2 x 2 unshifted mesh. In order to cope with level crossings, all calculations were done within an electronic thermal ensemble of 5 mHartree, which implied formally electronic free energies instead of the usual total energies (the energy difference to the total energy is small, and the zero temperature limits are the total energy).

Adsorption conformations for hypothetical and known intermediate species in the reaction were determined by geometry optimization procedures. Saddle points marking the transition states between two basins with chemically different species were then surveyed. Starting from the geometries of the adsorbed intermediate species, tentative geometries of reactant and product were prepared by adding the required reactant like H_2O or product like NH_3 or CO_2 in a suitable geometry. Afterwards, the saddle point for each reaction step was located using the search method of Govind [268] and its recent refinements. It was observed that if the reaction path between the prepared reactant and product was too contorted, then convergence was not achieved, because the saddle point optimization was distracted repeatedly to a spurious maximum along the contorted path. With the current method, a new search endpoint was
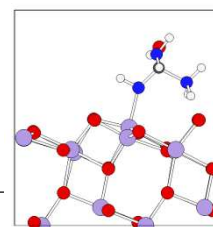
extracted from a scan across the supposed real saddle point, but with an inaccurate and tentative geometry. After such a revision of the endpoint, all real saddle points were found. The endpoints for each reaction step were found by intrinsic reaction coordinate (IRC) [269] searches using a method similar to that for molecules [270]. This yielded a clear picture of breaking and formation of bonds during each reaction step, representing an ensemble average path along a valley with steep walls. These IRC ended naturally at a local minimum. Due to the corrugation of the energy surface, this may not be the global minimum for the adsorption of the intermediate species. Moreover, the IRC endpoint often involved an adsorbed educt H_2O or product NH_3. The minor barriers between the IRC endpoint and the global minimum for the adsorbate were of less interest, as these did not constitute the rate determining step. Moreover, the IRC over a shallow barrier may not represent the ensemble average in a realistic fashion. However, the adsorption and desorption energies for H_2O and NH_3 that are essential for the reaction energetics could be calculated easily.

2.1.4. High-pressure reactor

The decomposition of the NH_3-precursor solutions was intended to proceed in the liquid phase. As the aqueous solutions would boil under atmospheric pressure, a pressure valve with a set pressure of 50 bar was positioned downstream of the stainless steel reactor tube. The catalyst bed was fixed inside the reactor by a porous metal frit with 60 μm pores. A thermocouple placed inside the catalytic bed was used to record the reaction temperature and for feedback control of the heating wire wrapped around the reactor tube, while a pressure sensor was installed upstream of the reactor to guarantee constant pressure of 50 bar inside the reactor. The

NH_3-precursor solutions were fed using a high pressure liquid chromatography (HPLC) pump with a constant flow rate of 5 mL/min.
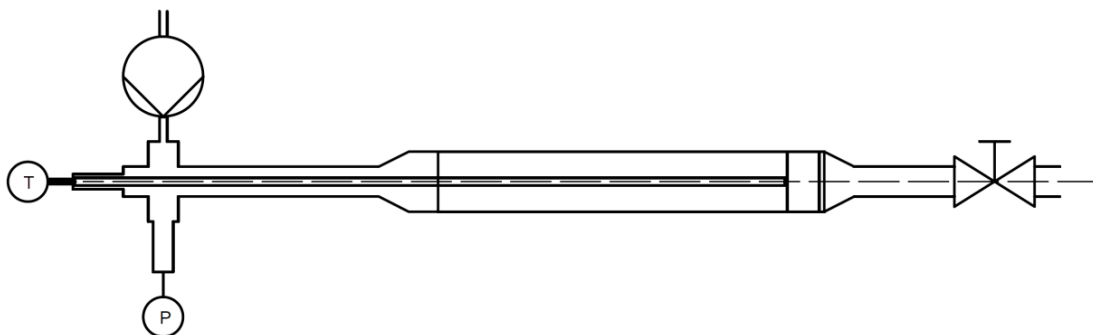

Figure 2-1: Scheme of the high-pressure NH_3-generator used to convert NH_3-precursor compound solutions into gaseous NH_3.

Before the pressure was released by the outlet valve, the gases were cooled so they could be quantitatively quenched in water. The mass of collected sample and the corresponding amount of consumed NH_3-precursor solution per sampling interval was recorded and used for the evaluation.

The nitrogen balance of the decomposition reactions was evaluated by photometric quantification of the main product NH_3, whereas side products or undecomposed NH_3-precursor compounds were determined by HPLC analysis.

The photometric measurement of NH_3 was adopted from the indophenol method for the quantification of NH_3 in solution according to the VDI method 2461. [271] By the addition of phenol and sodium hypochlorite, sodium nitroprusside catalytically transformed NH_3 into the blue indophenol dye. The quantification was performed by UV/vis spectroscopy at 630 nm. Calibration solutions were prepared using ammonium chloride, while the blank value was determined from de-ionized water. As the method is extremely sensitive the collected samples needed to be diluted depending on the amount of contained NH_3.
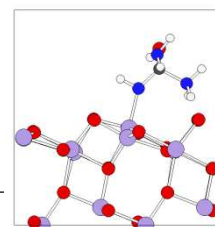
The liquid samples obtained from the quenched product gases were diluted with 5 mM phosphate buffer (adjusted to pH 7 with NaOH) in order to prepare them for HPLC analysis. [263] Typical side products including isocyanic acid (HNCO), biuret, cyanuric acid, ammeline, ammelide or melamine could be quantified, [272] however, only HNCO and biuret were found in the course of the presented experiments. The undecomposed NH_3-precursor compounds urea and methanamide could also be determined quantitatively and were found to represent more than 97% of the molar amount of nitrogen not emitted as NH_3 in all experiments.

In addition to analysis of the gas quenching solution, the gaseous reaction products of methanamide decomposition on Au/TiO_2 at 150°C, which were not soluble in water were captured in a gas collecting tube and subsequently analyzed by feeding them into a quadrupole mass spectrometer. By this measure, it was intended to capture eventually formed CO or H_2, which could evolve during decomposition of methanamide. [273] The analysis provided only a crude quantitative result, as CO_2 was also contained in the gas sample even though it was mostly quenched in the solution due to the high amount of dissolved NH_3.

2.2. Preparation of catalysts and NH_3-precursor solutions

2.2.1. Guanidinium salt solutions

Guanidinium salts were provided by NIGU Chemie as commercial samples, or synthesized by NIGU Chemie as research materials exchanged in the framework of the research project. Guanidinium salt solutions were either prepared in the laboratory using the provided guanidinium salts and de-ionized water, or provided by NIGU Chemie as a ready-to use solution. In particular, the solutions intended for the use at the engine test stand

were prepared by NIGU Chemie using a standardized method and sent to PSI. In case of guanidinium formate, the 60% guanidinium formate aqueous solution (GuFo 60) was prepared by dissolving 60% by mass of guanidinium formate in distilled water, and adjusting the pH to 7 by using formic acid. Guanidinium formate/urea mixtures were also adjusted to pH 7 using formic acid. The labeling of aqueous guanidinium formate solution is built up by specifying the salt guanidinium formate (GuFo), its mass-percentage in the solution, and, if present, then the mass percentage of urea. As an example, GuFo 38/15 was used in some experiments as a NH_3-precursor solution, because it was considered to show good temperature stability while, compared to GuFo 60, contained less of the more expensive GuFo, while showing an equally high NH_3-storage capacity.

2.2.2. Other NH_3-precursor solutions

Other NH_3-precursor solutions were prepared by diluting the pure NH_3-precursor compounds as purchased from Sigma-Aldrich in de-ionized water. Solutions of the following precursor compounds were prepared: NH_4NO_3/urea mixtures, ammonium formate solution and methanamide solution. The densities needed for the conversion of volumetric flow rates to mass flow rates were determined by using thermostatted volumetric flasks filled with the solution and a balance (Mettler-Toledo). All the prepared solutions, including their density, are given in Table 2-1.
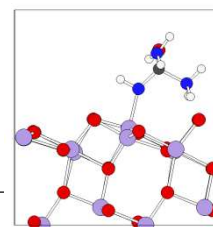
Table 2-1: GuFo-free NH₃-precursor solutions used in this work.

Solution	Composition					Density
	NH_4NO_3	urea	Ammonium formate	Methanamide	water	g/mL
NH_4NO_3/urea	43.3	32.5	-	-	24.2	1.30
Forzatti-sltn.	29.4	32.5	-	-	38.1	1.23
20% NH_4NO_3	20	-	-	-	80	1.08
AmFo 40	-	-	40	-	60	1.09
Admide®	-	-	-	80	20	1.11

2.2.3. Hydrolysis catalysts materials

Hydrolysis catalyst materials were provided by industrial companies in order to enable rapid transfer of catalyst formulations to the prototype scale for the engine test stand. The hydrolysis catalysts were usually provided as powders, but some of the catalyst samples were already coated on metallic catalyst supports.

In detail, Cristal Global provided TiO_2 (anatase) and TiO_2 (rutile) of different particle size and with different surface areas. Also doped TiO_2 catalyst materials were prepared to increase stabilization of the crystal phase or to modify the acidity. The doped samples included TiO_2 with SiO_2 and WO_3 to increase stabilization of the TiO_2 (anatase) catalysts against a phase transition or rearrangement resulting in a decrease of surface area. WO_3 also increased surface acidity, which could be beneficial for the adsorption of basic molecules such as guanidine. On the other hand, La_2O_3-doped TiO_2 decreased the surface acidity, thereby increasing interaction of the catalyst with acidic compounds such as formic acid. The intention behind changing the acidity is to increase the residence time of selected

compounds on the catalyst surface, in order to provide more time for their decomposition. An overview on the catalyst samples and their surface areas and particle diameters is given in Table 2-2:

Table 2-2: Hydrolysis catalysts provided by Cristal Global with composition and basic characterization concerning surface area and particle size.

Name	TiO$_2$ structure	Dopants (mass%)			BET surface	Particle diameter
		WO_3	SiO_2	La_2O_3	m^2/g	μm
DT-51	anatase	-	-	-	90.1	1.7
DT-52	anatase	10	-	-	94.2	2.2
DT-57	anatase	-	-	10	113.3	1.9
DT-58	anatase	9	10	-	120.0	1.9
DT-60	anatase	5	10	-	92.3	1.8
DT-S10	anatase	-	10	-	118.1	1.8
AT1	anatase	-	-	-	11.6	0.4
G-5	anatase	-	-	-	355.3	2.0
UP100	rutile	-	-	-	72.6	0.3

The hydrolysis catalysts already coated on metallic catalyst support were based on TiO$_2$ (anatase), but the exact composition was not disclosed by the catalyst coaters. The metallic honeycomb support structures were provided by Emitec and were either sent to Interkat for a TiO$_2$ (anatase)-based hydrolysis catalyst coating, or coated at PSI using the hydrolysis catalysts provided by Cristal Global. In addition, hydrolysis catalyst-coated metallic foam structures were also provided, in this case the metallic catalyst support was prepared by Alantum, while the coating was done at Süd-Chemie.
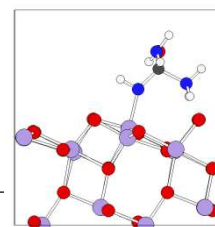
2.2.4. Preparation of noble metal-doped catalysts

Noble metal-doped hydrolysis catalysts were prepared by two different techniques, depending on the noble metal doping. For palladium doping, the incipient wetness impregnation method was used, while gold doping was performed by the deposition-precipitation method.

The incipient wetness impregnation of TiO_2 with Pd was performed using the commercial TiO_2 (anatase) and Palladium(II) acetylacetonate, abbreviated Pd(acac), as Pd precursor compound. Prior to the preparation of Pd-doped TiO_2 powder, the desired amount of TiO_2 powder was first dried in an oven at 200°C for 12 h and the pore volume was determined using N_2-physisorption. To achieve a certain amount of mass% Pd-doping, the calculated amount of Pd(acac) was dissolved in the volume of isopropanol corresponding to the pore volume of the TiO_2 powder. The wet powder was intensely mixed during the slow addition of the Pd-precursor solution, afterwards it was left to dry over night. The dry powder was mechanically mixed and ground using a mortar and pistil, then it could be sintered at 400°C for 5 h in order to decompose the Pd-precursor compound to leave only Pd on the TiO_2 (anastase) catalyst surface.

The Au/TiO_2 catalyst was prepared by deposition-precipitation following published methods [274] with some variations: commercial TiO_2-anatase (DT51, produced by Cristal Global; BET surface 90 m^2/g, $D_{50} = 1.7$ μm) was suspended and adjusted to pH 9 at 80°C using 0.2 M NaOH. A 0.005 M solution of $HAuCl_4$ (Sigma) was also heated to 80°C and adjusted to pH 9 using 0.2 M NaOH. Thereafter, it was added dropwise to the suspension of TiO_2. After complete addition, the resulting mixture was readjusted to pH 9 using 0.2 M NaOH. The mixture was left stirring at 80°C for 16 h. The catalyst was recovered by centrifugation, washed several

times with H_2O for chloride removal and dried at 80°C for 12 h. After drying, the catalyst was sintered in air at 400°C for 5 h.

### 2.2.5. Coating of catalyst supports

Catalyst powders were coated on support structures so that they could be inserted into the reactors. Ceramic cordierite honeycomb structures were preferred, as the structures could be cut out of large 10.5" honeycomb samples provided by Corning. The catalyst support could be fit into any shape needed for investigations. Another advantage of ceramic cordierite supports is their easy coating with catalyst suspensions, using previously described procedures. [275,228]. The cordierite ceramic material itself is not catalytically active, it is a compound described by the formula $2\,MgO \cdot 2\,Al_2O_3 \cdot 5\,SiO_2$. [276]

In detail, ceramic cordierite honeycomb substrates (400 cpsi, Corning) of the desired shape were dip-coated with an aqueous suspension of the catalyst powder containing commercial inorganic binder (Ludox AS-40). To increase the pH, a small amount of NH_3 was added so the powder could be well dispersed as the solution was not close to the isoelectric point of the TiO_2 (anastase) particles. After drying, the procedure was repeated until the desired amount of material was deposited. Finally, the catalyst coating was calcined at the support structure by heating to 550°C for 5 h, or in the case of some particularly sensitive coatings only to 400°C for 5 h.

2.3. Catalyst characterization techniques

2.3.1. BET surface area determination

Provided catalyst materials and in-house prepared catalysts were characterized for their specific surface area according to the theory of
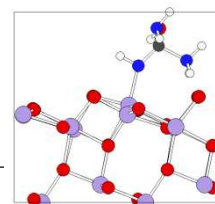
Brunauer, Emmett and Teller (BET-theory). [277] For the measurements, N_2-adsorption at -196°C was performed with a Quantachrome Autosorb instrument. All samples were outgassed at 200°C for a minimum of 12 h prior to the measurement. Relative pressures (p/p_0) between 0.05 to 0.30 were used to derive the active surface area from the isotherms.

2.3.2. Particle size determination

Particle analysis was performed using a Horiba LA-950 laser diffraction particle analyzer utilizing Mie-theory for size determination. The samples were dispersed in water by means of ultrasonication. A small amount of NH_3 was added to the water in order to shift the pH away from the isoelectric point. For the particle size calculation the diffraction index of TiO_2 (anatase) in water was inserted.

2.3.3. Powder X-ray diffraction spectroscopy

Powder X-ray diffraction (XRD) characterization of the catalysts was performed using a D8 Advance Bruker AXS diffractometer with Cu-K$_\alpha$ radiation and a 2θ range from 10-80°. The obtained diffraction peaks were compared with reference data for the pure substances.

2.3.4. Scanning electron microscopy

SEM images were obtained on a Carl Zeiss FE-SEM Ultra 55 scanning electron microscope using either secondary electrons or in lens detection. Au- and Pd-doped catalysts were analyzed after complete preparation including sintering at 400°C, but before coating on the monolith. Quantification of the Au content in the sample was performed by energy-dispersive X-ray spectroscopy (EDS) using an AMETEK EDAX TSL detector coupled to the electron microscope.

2.3.5. Transmission electron microscopy

Abberation corrected high angle annular dark field scanning transmission electron microscope (HAADF-STEM) images were obtained on a Hitachi HD-2700 at 200 kV acceleration voltage. The samples were prepared by deposition of freshly prepared Au/TiO_2 catalyst powder on copper TEM grids.

2.4. Data evaluation

2.4.1. FTIR-Quantification of gas phase components

The results from the quantification of gas phase compounds by the FTIR spectrometer were automatically imported into Microsoft Excel. In the Excel spreadsheet, the measured concentrations of decomposition products from NH_3-precursor compound decomposition were converted to yields obtained from the amount of inserted NH_3-precursor compounds. In the calculation the overall gas feed rate, the feed rate of NH_3-precursor solution and the composition of the NH_3-precursor solution were taken into account. Also, the change in overall gas flow due to the decomposition of the NH_3-precursor compound and the consumption of H_2O during the hydrolysis reaction were accounted. Finally, the measured concentration was set in relation to the maximum concentration that could be achieved for the component. All components containing nitrogen or carbon were summed up separately to obtain an element-based balance.

2.4.2. HPLC-Quantification of aerosols

First, aerosols quantified by HPLC in the liquid-quench solution were converted to the concentration in the product gas. For this reason, the
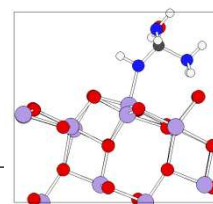
amount of quenched gas was calculated first, using the gas temperature, the atmospheric pressure, the saturation vapor pressure of water and the volume recorded by the gas meter. Then, the yields of the measured side reaction products could be calculated by using again the data gathered for the gas phase quantification, by including the stoichiometry factors, as the high-molecular compounds were formed from multiple smaller molecules. Also in the elemental balances the number of atoms per high-molecular side product needed to be included in the calculation for correct referencing of the inserted and collected material.

2.4.3. Formulae used to define reaction conditions

In this work several relations are used to describe reaction conditions.

The dosing ratio α describes the amount of added NH_3 relative to the contained NO_x-components. In the case of the *fast-SCR* or *standard-SCR* reaction, a value of unity provides enough NH_3 for perfect conversion.

$$\alpha = \frac{NH_{3\,(in)}}{NO_{x\,(in)}}$$

2-1

For the efficiency of the SCR reaction, $DeNO_x$ values are usually reported. The values are computed from the amount of NO_x in the exhaust gas entering the SCR system, and the amount of NO_x remaining after SCR treatment.

$$DeNO_x = \frac{NO_{x\,(in)} - NO_{x\,(out)}}{NO_{x\,(in)}}$$

2-2

As the formula only includes NO_x concentrations, it is representative of the conversion efficiency, but does not provide information about the selectivity. As the production of N_2O from NO_x must be avoided, it is usually accompanied by information about the observed selectivity.

The ratio between catalyst size and flow through the catalyst is expressed by the Gas Hourly Space Velocity (GHSV). It enables the comparison of experiments performed on different scales, or can be used to determine the catalyst size needed for a given exhaust gas flux when scaling a process.

$$GHSV = \frac{\dot{V}_{gas}}{V_{catalyst}} \qquad \text{2-3}$$

The Reynolds number gives an indication about the flow pattern for a specific system and can be used to distinguish between laminar and turbulent flow. [278,279] As a dimensionless number it can also be compared for different experimental setups and used to describe kinematic similarity.

$$Re = \frac{v_m \cdot d}{\nu} \qquad \text{2-4}$$

In the formula 2-4, v_m denotes the mean velocity of flow, d the diameter of the flow tube, and ν the kinematic viscosity of the fluid (in the case of model exhaust gas, the value for pure nitrogen is inserted).
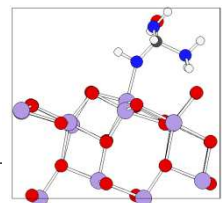
3. Setup for investigations on NH$_3$-precursors[*]

3.1. Introduction

As mentioned in the first chapter, the investigation of NH$_3$-precursor solutions for the SCR process required the construction of a novel experimental setup to provide the possibility to spray the solutions on hydrolysis catalysts.

Commercial SCR systems in cars and heavy-duty vehicles are based on aqueous 32.5% urea solution (AdBlue®), which releases ammonia in the hot exhaust gas system. [85] The released ammonia reduces the NO$_x$ on the SCR catalyst to form nitrogen and water. The decomposition of urea to ammonia is most effectively achieved using a separate hydrolysis catalyst, but may also be performed on the SCR catalyst. [280]

There are several issues associated with the involved reactions. One of the most critical problems in commercial applications is the incomplete decomposition of urea, which causes deposits in the exhaust gas aftertreatment system [281]. Researchers have also been working on replacing AdBlue® with other liquid reducing agents to improve temperature stability, ammonia releasing potential and/or deposit formation. [165]

There are only a few experimental setups in academic research laboratories to investigate the chemical processes involved in the SCR process utilizing urea solutions instead of the typically employed ammonia gas. [282,283]
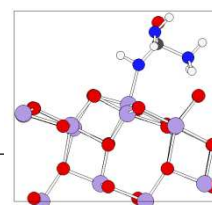
This is likely the main reason why spraying liquid reducing solution on a catalyst and the decomposition of urea or other ammonia precursor compounds is not well understood and cannot be properly modeled. [284,285] Our novel setup overcomes this deficiency by utilizing a miniature two-component nozzle, which produces a fine spray of liquid reducing agents directed onto a catalyst in a laboratory test reactor. Ceramic monoliths, metallic monoliths, ceramic foams or metallic foams may be used as substrates for catalyst coatings. Alternatively, catalyst pellets or packed beds can also be employed. A broad range of space velocities are covered by utilizing two interchangeable reactors with different internal diameters.

The reaction progress or catalyst activity may be determined using the comprehensive analysis of the reactor product gas stream. Low-molecular weight gas phase components are quantified using a multi-component gas analysis method on an FTIR spectrometer. Higher molecular weight compounds or aerosols may be determined using liquid quench gas absorption with subsequent HPLC analysis.

3.2. Background on development and construction

Laboratory-scale test reactors are still crucial for research on automotive catalysis as there are many factors that influence the composition of the emitted exhaust gas on an engine test rig. Some of the factors are easily controlled, such as the geometry of the exhaust gas aftertreatment system, fuel, engine oil or engine operation temperature. Other factors, such as exhaust gas temperature, engine wear, turbulence, particle formation, and adsorption and desorption phenomena of gases in transport pipes or on

soot included in the combustion effluent, may be much harder to reproduce. [286]

However, it is common for SCR test reactors in the laboratory to simplify the process for the sake of easier construction, easier operation and higher reliability. These simplifications include the replacement of aqueous urea solution with ammonia gas and carbon dioxide. These experimental setups are highly versatile in how they may be operated and used to study chemical reactions. [287] To the best of our knowledge, there is currently no experimental setup capable of directly spraying liquid reducing agents onto a catalyst in the presence of a model exhaust gas that includes a detailed analysis of the product gas stream.

The presented experimental setup bridges the gap between simple yet versatile, laboratory model gas test reactors, and engine test systems, which are too complex to allowing monitoring of the small changes caused by alternating parameters of the catalyst. During construction and the performance test, a uniform spray distribution was maintained at the catalyst front surface, which was necessary to produce reliable and reproducible data.

The model gases used for the investigations were mixed from single components using mass flow controllers, while water was dosed, pulsation-free, through oxidation of H$_2$. The gas mixture was passed through a heated ceramic bead bed to mix all of the components and to heat the gas mixture to the desired temperature before entering the reactor.

Correct tuning of the heating zones on the reactor and the surrounding components was of particular interest, as the temperature could heavily influence the kinetics of the chemical reactions. Multiple thermocouple
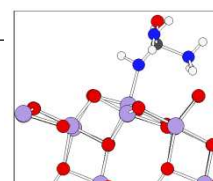
accesses on the reactor, in combination with a suitable heating procedure, were utilized to resolve this crucial issue.

After passing through the catalyst zone in the reactor, the gas stream was transferred through trace-heated tubes into the optical cell of an FTIR spectrometer using a heated gas pump. With the aid of a specially developed, multi-component gas analysis method, gas phase components were quantified. Simultaneously, higher-molecular weight compounds that could not be detected by FTIR spectroscopy were extracted from the reactor product gas stream using a gas absorption apparatus. The extracted gas was quenched using a HPLC eluent and the mixture was pumped to the absorption unit. At the absorption unit, the two phases were forced to mix thoroughly, thus solubilizing the aerosols contained in the gas phase. At regular intervals, samples were taken to be analyzed by HPLC.

3.3. Gas dosing and mixing

The use of real engine exhaust gas was not an option for this laboratory setup; therefore, the proxy exhaust gas needed for our investigations needed to be prepared. Typical exhaust gas components, such as: N_2, O_2, H_2O, CO_2, CO, NO, NO_2 and N_2O, were mixed homogeneously at varying compositions. It was decided to dose all non-condensing gases as pure gases or binary mixtures thereof in N_2 using thermal mass flow controllers (*Brooks 5850S*). For H_2O, no direct gaseous dosing could be used. Available commercial techniques for liquid water dosage with subsequent evaporation have the inherit drawback of water vapor concentration pulsations due to the irregular boiling of water. Therefore, a water dosing system based on the metering of gases was developed. Two 32-mm long platinum-covered (*OM Group*, Pt-loading: 90 g/ft^3) ceramic cordierite

monoliths (*NGK*, 400 cpsi) were utilized for the catalytic combustion of H$_2$ with an excess of O$_2$ in a 25-mm internal diameter tubular reactor. A metallic catalyst support (*Emitec*, 200 cpsi) was positioned in front of the Pt-catalyst to avoid the ignition of the gas mixture upstream of the catalyst (see Figure 3-1). To lower the catalyst temperature, the flow of the two reactants was diluted using the dosed N$_2$ needed in the exhaust gas. Quartz wool was used to fix the position of the catalyst-coated monoliths, followed by a blank ceramic cordierite monolith at the exit to prevent the transport of quartz fibers or catalyst dust into the remaining experimental setup. Furthermore, a pressure relief valve (threshold = 1.7 bar) was positioned downstream of the water vapor reactor so that, in the event of a large pressure increase, the pressure would release into the fume hood rather than into the experimental setup.

As the desired exhaust gas always contained O$_2$ in the percent range, an excess of O$_2$ was present at all times for H$_2$ oxidation. If experiments including the presence of water under the strict exclusion of O$_2$ were desired, a 5% excess of H$_2$ was used (ratio H$_2$ to O$_2$ of 2.1 : 1).

Figure 3-1: Scheme of the reactor for the pulsation-free formation of water vapor by the reaction of H$_2$ with O$_2$ in N$_2$. (A, E) glass wool, (B) flame arrester, (C, D) catalyst-coated monoliths and (F) uncoated cordierite monolith to retain the glass wool.

The nitrogen mass flow controller was capable of flow rates between 0-750 L/h at STP. The O$_2$ range was set between 0-100 L/h at STP and the H$_2$ range from 0-75 L/h at STP. All remaining gases were set below a maximum of 50 L/h at STP. Nitrogen, O$_2$ and H$_2$ were used as pure gases
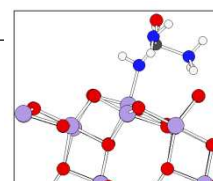
(5.0), while all other components were dosed as binary mixtures in nitrogen with concentrations ranging from 500 ppm to 14% in gas bottles.

From the exit of the water vapor reactor, all stainless steel tubes were trace-heated using proportional integral derivative (PID) heating controllers (*Omron E5CN*) to a temperature of 170 °C to avoid the condensation of water on the tube walls. The remaining gas components were added to the $N_2/O_2/H_2O$ base feed before entering the heat exchanger.

3.4. NH$_3$-precursor solution spray

Obtaining a reproducible, evenly distributed fine spray of liquid reducing agent in the reactor imposed the greatest design challenge. An ICP-MS (inductively coupled plasma mass spectrometry) spare parts manufacturer (*e-pond*) was able to supply us with a special two-component spraying nozzle adapted to our needs. In general, ICP-MS spraying nozzles are designed to not only nebulize relatively small amounts of liquids using gas flow, but to also tolerate high salt content and operate at elevated temperatures. Due to the chosen de Laval-type nozzle at the tip of the nebulizer, even highly concentrated reducing agent solutions could be sprayed into fine droplets. [288] The entire nozzle was made of borosilicate glass; giving it the same thermal stability and expansion coefficient ($3.3 \cdot 10^{-6}$/K at 20 °C) as the reactor in which it was integrated. In Figure 3-2, the dimensions and a picture showing colored liquid in the inner capillary can be seen. In comparison to conventional two-component spraying nozzles, the liquid uptake of ICP-MS nebulizers is extremely small. However, for our experiments, dosing rates of only a few mL/h were desired, which is in good agreement with the range specified for ICP-MS nebulizers.
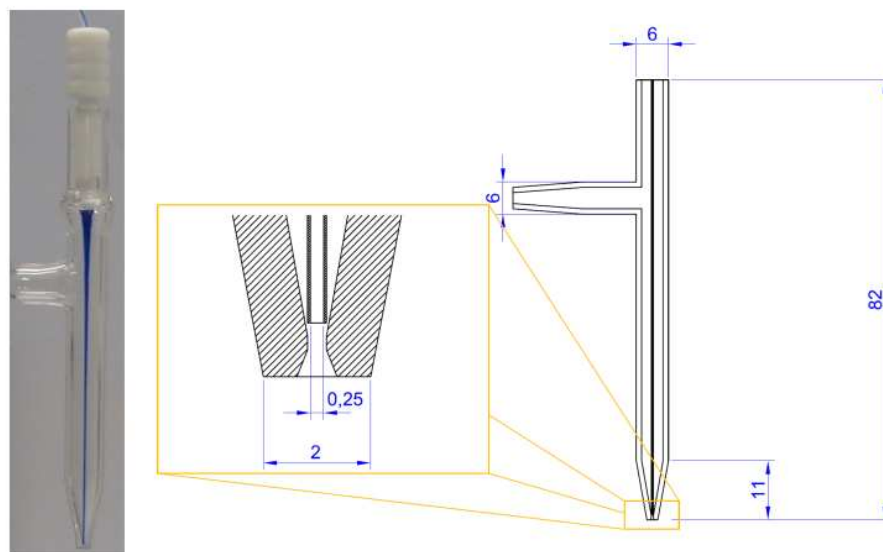
Figure 3-2: Left: Picture of the two-fluid nebulizer used for the spraying of liquid reducing agents into the catalytic reactor. The two-fluid nebulizer was originally designed for producing fine liquid sprays in ICP-MS instruments. Right: nebulizer dimensions in mm (right).

While the nitrogen gas flow for spraying was provided by a mass flow controller (50 L/h at STP), the dosing of the liquid to the nebulizer required more detailed consideration. The small volume flows needed to be provided precisely, with as few pulsations as possible. In principle, syringe pumps are ideally suited for this profile, but the volume which can be pumped is limited once the dosing has initialized. Because an increase in the syringe volume would cause a decrease in dosing precision, and syringe exchanges during operation would cause significant pulsations, a pump was chosen to convey liquid from a refillable reservoir to the nebulizer. Given the small volume flow range, HPLC pumps were evaluated. A small diameter steel capillary, acting as a flow restrictor, was used to connect the HPLC pump to the nebulizer, because the nebulizer aspirated liquid as the gas flow was turned on. This capillary increased the pressure drop, which prevented the nebulizer from taking up liquid without control, and ensured that all the high pressure-designed check valves of the HPLC pump were
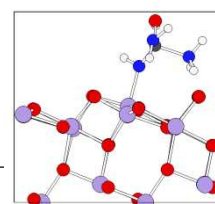
tight. A *Shimadzu LC-20AD* HPLC pump with two consecutive pistons – one to create the necessary pump pressure, the other to reduce pulsations – was chosen in combination with a *Shimadzu DGU-20A³* degasser unit, to remove contained gases in the reducing agent solution before pumping.

The combined dosing system was capable of spraying 10-200 µL/min of liquid into the reactor using a constant flow of nitrogen as the nebulizer gas (50 L/h at STP). The gas and liquid connectors are located outside the heating zone. Due to the concentric construction, the gas between the inner and outer capillary insulated the liquid from the hot temperatures inside the reactor. The tip of the nebulizer was completely immersed in the reactor, but only upon nebulization was the liquid at the tip no longer protected by a gas layer (see Figure 3-3).
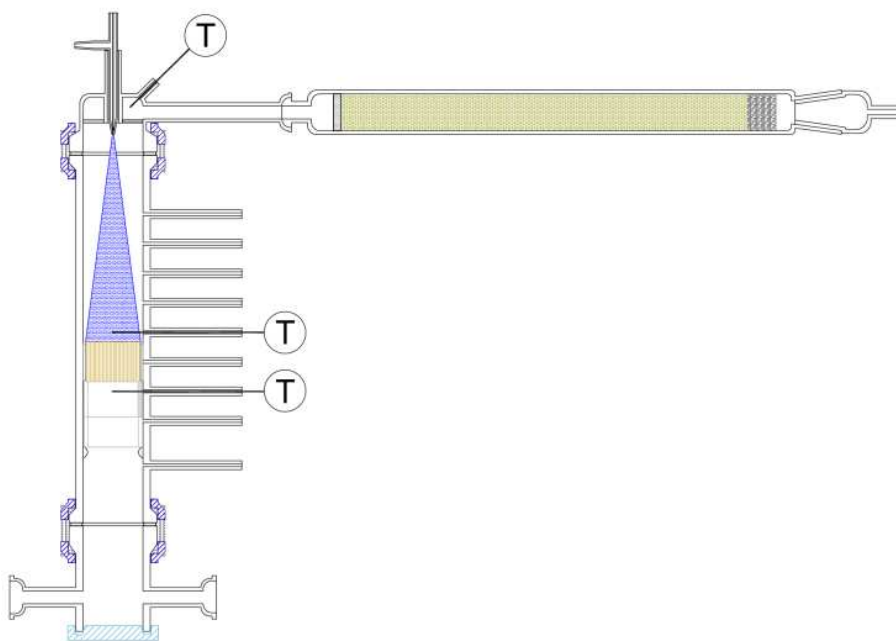

Figure 3-3: Technical drawing of the catalytic reactor for the investigation of liquid reducing agents with the attached heat exchanger for preheating the gas feed. The liquid reducing agents are dosed from the top of the reactor with a two-fluid nebulizer, shown in detail in Figure 3-2. The spray cone formed by the nebulizer is illustrated in blue. T: thermocouples in the reactor head, upstream and downstream of the catalyst.

3.5. Heating system and reactor

Temperature control of the model exhaust gas was necessary to enable experimentation at various temperatures of interest. The individual gases were dosed from the previously described setup along with the condensable water vapor. To prevent condensation of water and other components, e.g., NH_4NO_3 when dosing NH_3 and NO_x, all steel tubes were already trace-heated to 170 °C before they were merged into the heat exchanger. The transition from the 6-mm outer diameter steel tubing to the glass tubing at the entrance of the heat exchanger was fixed using a silicone hose. The heat exchanger itself was a 25-mm internal diameter borosilicate glass tube that could be opened via a build-in ground joint. The exit, however, was connected to the reactor entrance via a spherical ground joint (DIN-12 244 KS 19/9) to allow frequent removal of the reactor entrance. Close to the exit of the heat exchanger, a frit (25 mm, *P250*) was fused in the glass tube as a support for a ceramic steatite pellet (4-mm diameter and length) bed. The turbulent flow pattern created by the ceramic pellets helped to ensure good mixing and rapid heat transfer from the heat exchanger walls to the gas within the 250-mm length of the packed bed. The heating wires wrapped around the heat exchanger could be heated up to 450 °C, which is also the temperature limit of the borosilicate glass. The heat exchanger was operated using a feedback-controlled heater system and consisted of a single heating zone with a *K*-type thermocouple. Details of this heating zone and all the others can be found in Table 3-1. A *LabView* software routine was created in-house and used to read out and program the controllers for the various heating zones. The controllers were exclusively programmable PID controllers (*Omron E5CN*) used to achieve the desired temperatures with minimal undershoot and overshoot.
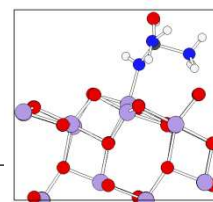
Table 3-1: Power rating and set temperatures of the heating zones.

No.	Heating zone	Set temperature °C	Power rating watt
1	heat exchanger	270 (adjusted)	600
2	reactor entrance	270 (adjusted)	220
3	reactor	230 (as desired)	710
4	reactor exit	220 (constant)	220
5	extraction capillary	190 (constant)	50
6	glass wool condenser	120 (constant)	50
7	spray temperature	230 (as reactor)	-
8	transfer to FTIR spectrometer + gas filter	170 (constant)	710
9	transfer to heat exchanger	170 (constant)	820
10	gas pump	180 (constant)	140
11	FTIR cell	180 (constant)	n/a

The reactor design was based upon a vertically mounted exhaust line, in two different diameter sizes (20.4 mm or 40 mm) with the catalyst resting upon a small neck (Figure 3-3) in the case of the larger reactor tube. A lead-in glass tube that contained the nebulizer was fused into the reactor entrance. The nozzle was positioned inside the hot reactor, to spray the reducing agent vertically onto the catalyst, while its connectors were located outside the heated reactor zone. The model exhaust gas from the heat exchanger entered the reactor entrance section perpendicular to the nebulizer and made a 90° turn into the reactor tube.

A porous glass frit (40 mm, *P250*), through which the model gas was passed, was fused horizontally into the reactor entrance to establish a laminar flow. The laminar flow results from a pressure drop across the frit and the cavities, which act as a flow straightener. The corresponding Reynolds numbers for operation at typical temperatures in the two reactors

are given in Table 3-2. The entire reactor entrance section was heated independently and could be removed to change the catalyst.

Table 3-2: Reynolds numbers in the tubular reactors under experimental conditions.

Temperature	Reynolds number	
°C	*20.4 mm reactor*	*40 mm reactor*
200	248	127
300	180	92
400	138	70

The flow inside the reactors was laminar in the entire temperature range, because the Reynolds numbers were significantly below 2,400, the transition to turbulent flow. [289] Since the reducing agent was sprayed into a laminar gas flow, a symmetric spray cone was formed that covered a circular area at the front surface of the catalyst. By choosing a suitable distance between the nebulizer and the catalyst, the spray cone was enlarged to cover the entire cross section of the catalyst. Glass rings of various heights were placed onto the neck to raise the catalyst in the tubular reactor. Openings in these rings provided access for thermocouples. The inserted catalysts were coated onto metallic or ceramic supports and consisted of extruded catalyst structures, or of packed beds. Catalyst supports were wrapped with ceramic fiber ribbon to prevent the gas flow from by-passing the catalyst. The temperature of the gas flow before entering and upon leaving the catalyst was measured using thermocouples, which could be inserted into the reactor every 20 mm along its length. This tubular section of the reactor was a second heating zone; the temperature of the gases leaving the catalyst was used as actuating variable for the temperature controller. The temperature of the gases entering the catalyst
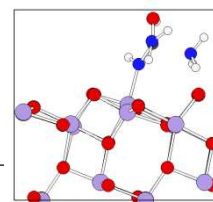
was tuned to the identical value as the temperature of the gases at the catalyst exit by re-adjusting the heat exchanger and reactor entrance heating zones. Thus, the cooling effect of nebulization was compensated for and the reaction temperature on the catalyst could be controlled accurately. Large reaction enthalpies, whether exothermic or endothermic, could additionally alter the gas temperature during passage through the catalyst but these were also compensated for by employing the described heating strategy.

Two reactors were used, one with 40 mm and one with 20.4 mm inner diameter. While the large diameter reactor was used for space velocities of 3,000-40,000 h^{-1}, the small diameter was suited for the range of 25,000-200,000 h^{-1}. Both reactors were constructed in a very similar design. Minor changes were made to ensure interchangeable reactor sections at the entrance and exit. In the 20.4 mm reactor, the catalyst did not need to be supported by a neck in the reactor tube, and instead could be placed on top of an inserted thermocouple.

The reactor exit, which was also independently heated, was composed of a tubular extension of the main part with two side arms with spherical joints at the end. The spherical joints allowed the arms to be easily disconnected even after heating to high temperatures. The main tube was closed using a PTFE-stopper, which was removed to push the catalyst out of the reactor tube. The two opposing side arms were used to connect the FTIR gas analysis and gas absorption apparatus. As the entire reactor setup was situated in a fume hood, the excess gas not needed for analysis was simply vented out of the reactor via the side arms. An experimental setup flow scheme is shown in Figure 3-4. The thermocouples for the heating zones are labeled according to the numbering introduced in Table 3-1.
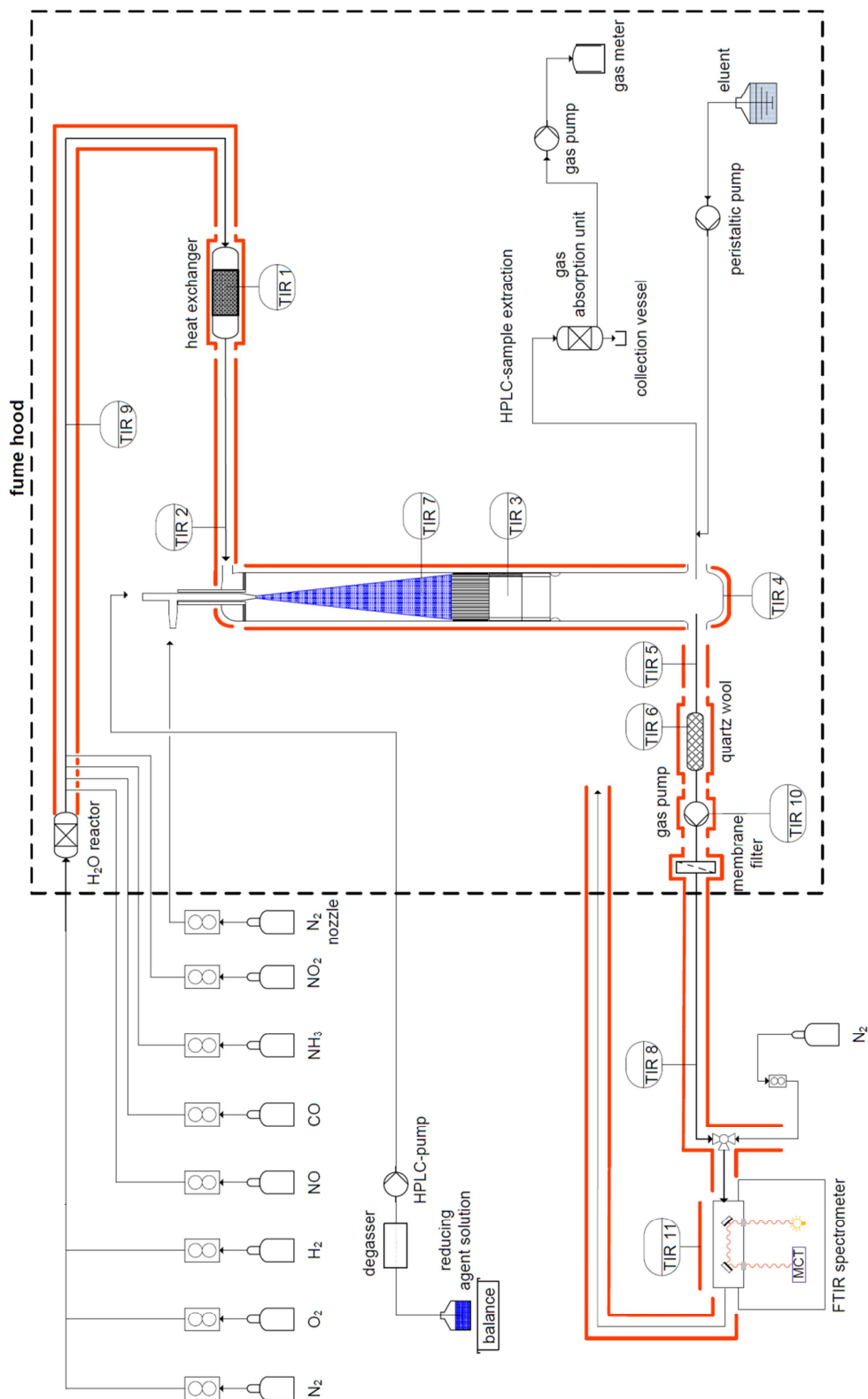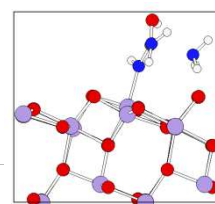
Figure 3-4: Process scheme depicting gas dosing system, heating zones of experimental setup, integration of the spray reactor with connections and analytics.

All reactor sections were first wrapped with glass silk heating cable (*isopad IS-SP*) with a power rating of 150 W/m, followed by insulation with glass silk, glass wool and aluminum. *K*-type thermocouples were used to measure temperatures, and as input signals for the heating controller feedback loops. Connection between the individual reactor sections was made using glass flanges (60 mm diameter) with graphite gasket seals (10 mm wide), which were compressed using aluminum muffles.

3.6. FTIR spectroscopy gas analysis

To quantify gaseous species in the gas stream from the reactor, a constant flow of 180 L/h at STP was pumped through a heated gas cell of an FTIR instrument. The gas was sucked from one of the side arms at the reactor exit and passed through a 10 mm internal diameter heated transfer tube filled with glass wool at 120 °C to remove catalyst particles, large aerosols and high molecular compounds. After passing through the heated PTFE-membrane gas pump (*KNF Neuberger N 012 ST.26 E*) at 180 °C, the gases were additionally filtered through a 5 μm pore diameter PTFE membrane (*Sartorius*) to remove remaining aerosols. A stainless steel tube heated to 170°C was then used to transfer the gases into an FTIR gas cell of an *Antaris IGS* (*ThermoFisher*) spectrometer. The cell was kept at a constant temperature of 180°C, and was equipped with ZnSe windows. ZnSe rather than KBr windows were chosen due to their resistance to water vapor and acidic gases like NO_2. A liquid nitrogen-cooled mercury cadmium telluride (MCT) detector was used to measure the beam intensity after passing through the cell. The IR beam path length in the cell was 2 m and the cell volume was 240 mL, resulting in a gas exchange rate of 5 s. After passing through the cell, the gases were sent, without pressure drop, through a wide

tube into the fume hood. Therefore, the measurements in the gas cell were performed at atmospheric pressure and corrected for daily variations. To quantify the gaseous compounds in the exhaust gas, a multi-component gas analysis method, including a correction for cross-sensitivities, was developed in *Quantpad* (Version 6.1, *ThermoNicolet*), and afterwards implemented into *Omnic* (Version 8.0, *ThermoFisher*), which was the software included with the spectrometer. Calibration was performed by taking spectra (32 scans) of certified reference gas standards, followed by the extension of the calibration by dosing gas mixtures of different concentrations, using the previously calibrated mass flow controllers. For liquid components that were not commercially available as gas in nitrogen, a nitrogen gas flow was saturated with the compound by passing it through temperature-controlled gas wash bottles, followed by wet chemical analysis. Each calibration consisted of up to 25 logarithmically equidistant points fitted with polymeric functions that were forced through the zero intercept point. The concentration ranges for the individual gas components, including the detection limits and limits of quantification, can be found in Table 3-3. The stated limits of detection and quantification were statistically determined from the noise of a series of nitrogen background measurements (8 scans per spectrum). [290] The detection limits may be higher if the components are to be measured in complex gas mixtures instead of nitrogen, even though the determined cross-corrections will reduce gas matrix effects. In contrast, increasing the number of scans will significantly improve the detection of individual components. The given figures should therefore provide a good estimate of the lower experimental limits.
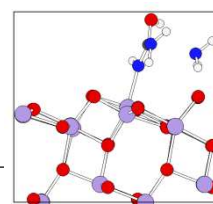
Table 3-3: Calibration of the FTIR spectrometer for quantification of gaseous compounds.

Component	Detection limit	Limit of quantification	Calibration range
	ppm	*ppm*	*ppm*
CO	0.4	1.2	40-1,600
CO_2	0.9	2.6	63-2,500
NO	1.1	3.8	25-1,000
NO_2	0.2	0.8	16-1,000
N_2O	0.1	0.5	10-200
H_2O	241	796	4,000-160,000
NH_3	1.3	2.2	40-6,300
HNO_3	0.2	0.9	300
HNCO	0.1	0.2	10-800
HCN	0.5	1.8	50-400
formic acid	0.1	0.4	100-2,000
formaldehyde	0.8	2.5	120
methanamide	1.8	4.9	35

For analysis, a 0.5 cm^{-1} resolution was chosen with one scan per second; however, eight or more scans were always averaged to obtain one spectrum. The recorded spectra were automatically evaluated and the determined concentrations plotted. If stationary experiments were performed, a mathematical average of the value during the period of interest was calculated for the measured components. All measured values were also exported to *Microsoft Excel* to be plotted in real time. The individual recorded spectra were saved in a compressed file but could be extracted individually for later evaluation.
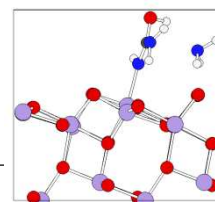
3.7. Aerosol quench apparatus

In addition to the low-molecular gas components, higher-molecular weight compounds and aerosols were also present in the product gas stream.

Because these compounds can be deposited in the FTIR cell, they can deteriorate the reflectivity of the enclosed mirrors and transparency of the windows. Additionally, many of the compounds would be difficult to measure quantitatively using FTIR spectroscopy, because they exhibit complex features in the IR spectrum that could not be used for quantification.

Instead of gas spectroscopy, an alternative analytical method was chosen, namely high pressure liquid chromatography (HPLC). Before analysis by HPLC, the gases and aerosols needed to be condensed into the liquid phase. For this, a liquid quench apparatus was mounted to the second side arm on the reactor exit.

The liquid quench was performed using a peristaltic pump (*Ismatec ISM852*) to transfer gas absorption solution into a capillary where a second PTFE capillary was concentrically inserted. The two-phase mixture of gas and absorbing solution was sucked through the PTFE capillary by a membrane pump (*KNF Neuberger HN79 KN.18*) at a flow rate of about 130 L/h at STP. 5 mM sodium phosphate (*Fluka p.a.*) buffered to pH 7 or pH 10.4, depending on the analysis needs, by the addition of NaOH (*Merck p.a.*) was used as the absorbing solution. In this way, gaseous and reactive isocyanic acid (HNCO) was immediately absorbed and stabilized as dissolved NaOCN salt. The absorption of aerosols occurred on the large wet surface of two fritted glass filters (30 mm, *P100* and 60 mm, *P40*) that were located between the liquid quench probe and the gas pump. The exit of the gas pump was connected to a gas meter (*Wohlgroth G-4 (C-0)*) equipped with a thermometer (see Figure 3-5). From the measured gas flow, the gas temperature, the atmospheric pressure, and the saturation vapor pressure of water, the actual flow of consumed reactor product gas was calculated.
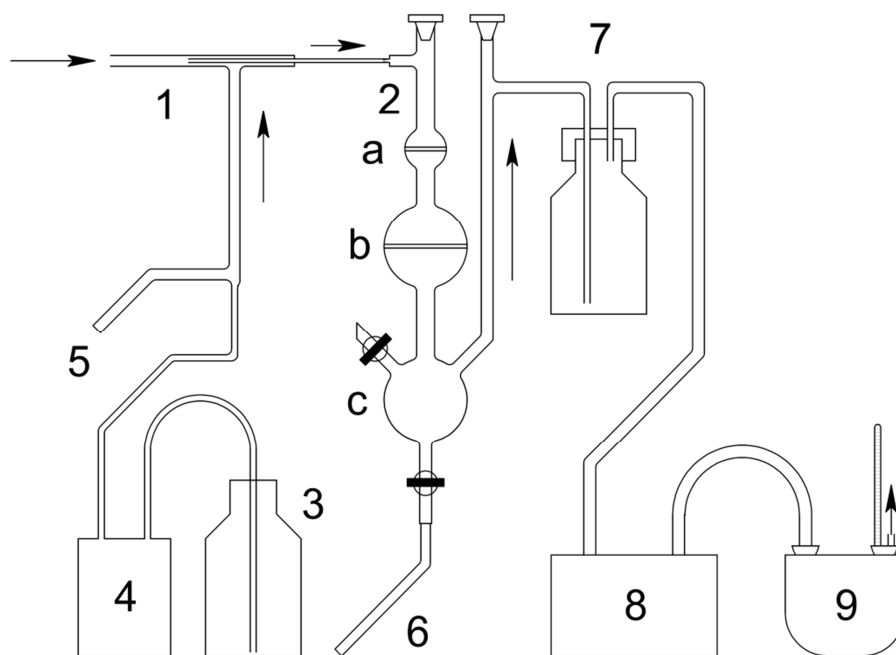
Figure 3-5: Aerosol quench and absorption apparatus for HPLC analysis of the reaction products: liquid quench of product gas (1), aerosol solubilizer (2), eluent reservoir (3), peristaltic pump (4), access for flushing (5), access to withdraw samples (6), water trap (7), gas pump (8), gas meter (9), glass frit P100 with a pore size of 40-100 µm (a), glass frit P40 with a pore size of 16-40 µm (b), and collection vessel (c).

The liquid samples were analyzed by HPLC using an anion exchange column and UV detection at 197 nm. A 5 mM sodium phosphate (*Fluka p.a.*) buffer with an identical pH to the absorbing solution was used as the eluent. The pH 7 buffer was used for measuring urea and HNCO. The pH 10.4 buffer was used for the analysis of higher molecular byproducts from ammonia precursor compounds.

The aerosol quench apparatus, based on a concept that was previously developed at the PSI laboratory, [263] and the HPLC method, in particular, were refined over the years. An updated description of the HPLC method, including a list of all compounds that may be detected and quantified, has been recently published. [272]

3.8. Performance in AdBlue®-SCR

A suitable and reliable experiment to evaluate our setup was to compare the SCR conversion using a urea solution to the conversion achieved with ammonia gas. With this approach, the reducing agent dosing, the spraying characteristics and the catalyst arrangement were all tested in a single experiment.

For the experiments, a 2.5% V$_2$O$_5$-based extruded catalyst (300 cpsi) was employed with a space velocity of 19,700 h^{-1} at a temperature of 230 °C. A feed gas mixture consisting of 1,000 ppm NO, 5% H$_2$O and 10% O$_2$ in N$_2$ was dosed at a rate of 500 L/h at STP. If NH$_3$ gas was added, the N$_2$ flow was adjusted to keep an overall flow of 500 L/h at STP. The liquid dosing of 32.5% urea in deionized water (AdBlue®) was varied from 10-40 µL/min, resulting in ammonia concentrations of 315-1,260 ppm given perfect urea hydrolysis according to reaction 3-1.

$$H_2NCONH_2 + H_2O \rightarrow 2\,NH_3 + CO_2 \qquad \textbf{3-1}$$
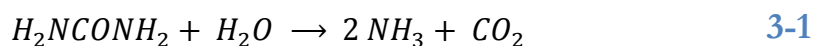
To obtain a reference SCR conversion, NO was dosed together with the gaseous reducing agent NH$_3$. The mixture reacted on the SCR catalyst according to reaction 3-2 in the *standard-SCR* reaction, and the exact conversion was monitored by FTIR analysis.

$$4\,NH_3 + 4\,NO + O_2 \rightarrow 4\,N_2 + 6\,H_2O \qquad \textbf{3-2}$$
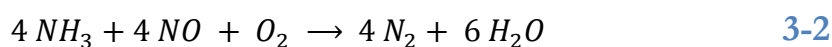
The remaining concentrations of NO and NH$_3$ in the product gas were measured at different reducing agent dosing rates. These measured concentrations were used to plot the NH$_3$ slip in the reactor product gas stream versus DeNO$_x$, as shown in Figure 3-6 and Figure 3-7. Because added NH$_3$ gas was completely mixed with the model exhaust gas by the heat exchanger, the deviation of the observed conversion from 100% is explained by the reaction kinetics.
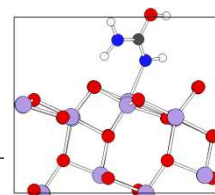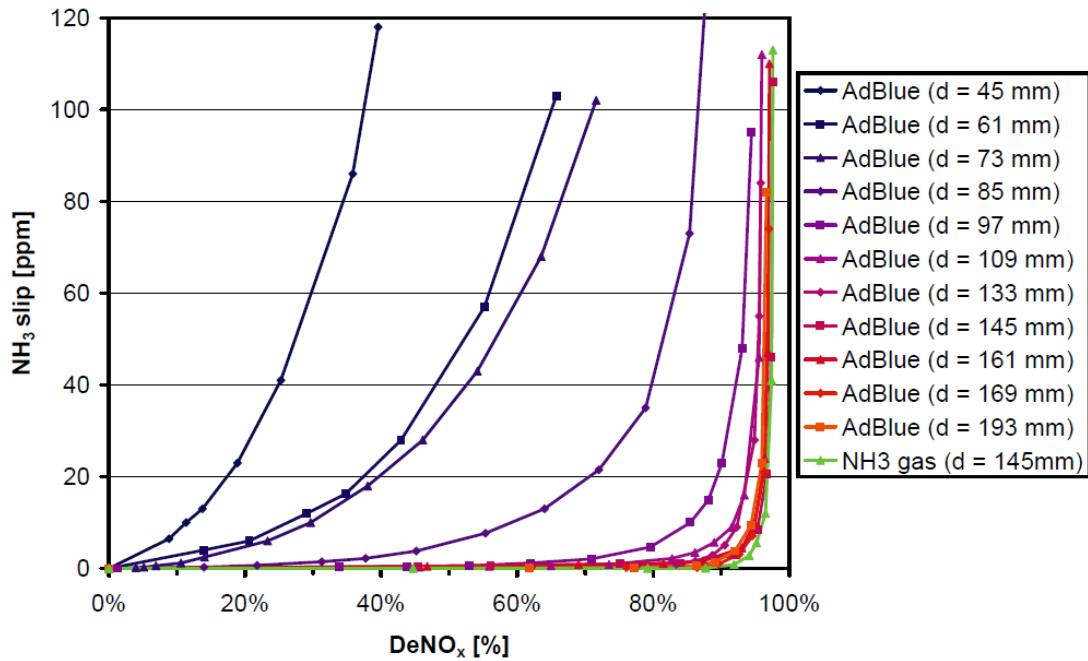
Figure 3-6: Test of the catalytic reactor for the SCR reaction. The influence of distance between the two-fluid nebulizer for urea solution (AdBlue®) injection and catalyst frontal area on ammonia slip through the catalyst is shown in correspondence to the achieved NO_x reduction ($DeNO_x$) rates. Urea decomposes to ammonia in the hot reactor and on the catalyst surface. The more homogeneous the spray on the frontal area of the catalyst, the less ammonia slip is observed. The optimum result is obtained with NH_3 gas, which is shown as reference. Catalyst: 2.5% V_2O_5-containing extruded catalyst (300 cpsi). T = 230°C. GHSV = 19,700 h^{-1}. Feed gas: 1,000 ppm NO, 5% H_2O and 10% O_2 in N_2. AdBlue® was varied from 10-40 µL/min, resulting in ammonia concentrations of 315-1,260 ppm.
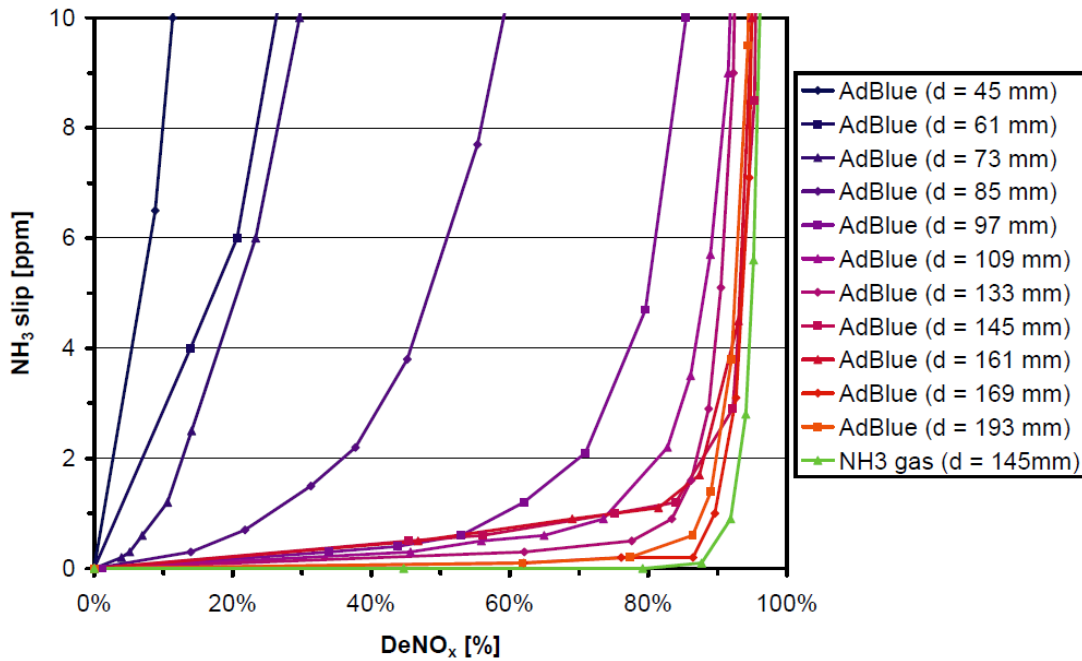
Figure 3-7: Excerpt from Figure 6 of distance-dependent NH$_3$ slip/NO$_x$ reduction (DeNO$_x$) plots at ammonia slip rates of up to 10 ppm.

To evaluate the distribution of the reducing agent spray, dosing of gaseous NH$_3$ was stopped and the aqueous urea solution was sprayed onto the catalyst. The inserted catalyst is known to catalyze both of the above processes, urea hydrolysis to NH$_3$, and its reaction with the dosed NO gas. [**280**] Because urea hydrolysis is much faster than NO reduction, we assumed the SCR reaction to be the rate determining process. [**280**] Hence, a lower DeNO$_x$ value at a similar NH$_3$ slip, when using urea solutions, indicated an inhomogeneous spray distribution among the catalyst channels. The optimum distance between injection nozzle and catalyst was determined by making several SCR experiments with various distances. The NO conversions and NH$_3$ slip values were determined for different liquid flow rates at each distance, yielding the plots of Figure 3-6 and Figure 3-7. At short distances, DeNO$_x$ values of less than 30% at a maximum NH$_3$ slip of 10 ppm were observed. With increased distance between the nebulizer
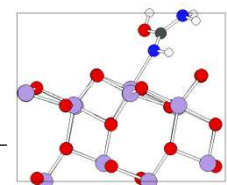
and catalyst, the NO conversion strongly increased. There was a limit beyond which an increase in the distance caused no further increase in NO conversion. At distances exceeding this determined limit, the circular area covered by the spraying cone was larger than the catalyst frontal area. Thus, the spray also reached the heated reactor walls. Nonetheless, due to the possibility of urea evaporation and/or decomposition without forming a large amount of deposits, no significant decline in NO conversion was monitored. At the optimum distance between the injection nozzle and the catalyst, a $DeNO_x$ value of 96.0% at 10 ppm NH_3 slip was obtained. This $DeNO_x$ value of 96.0% is only slightly below the corresponding value for gaseous NH_3 as the reducing agent, which was 96.1% $DeNO_x$ at 10 ppm NH_3 slip. The very small difference between NH_3-SCR and urea-SCR indicates a homogeneous distribution of the reducing agent in all of the catalyst channels.

The optimum distance resulted in a spray distribution almost identical to the experiment with gaseous ammonia. The percentage of homogeneous distribution at any distance could be calculated. Assuming a relatively sharp separation between the spray cone and the surrounding gas, the catalyst area covered by the spray was estimated. From this value the circular area and its diameter and radius were all derived and compared with the catalyst radius (Figure 3-8).
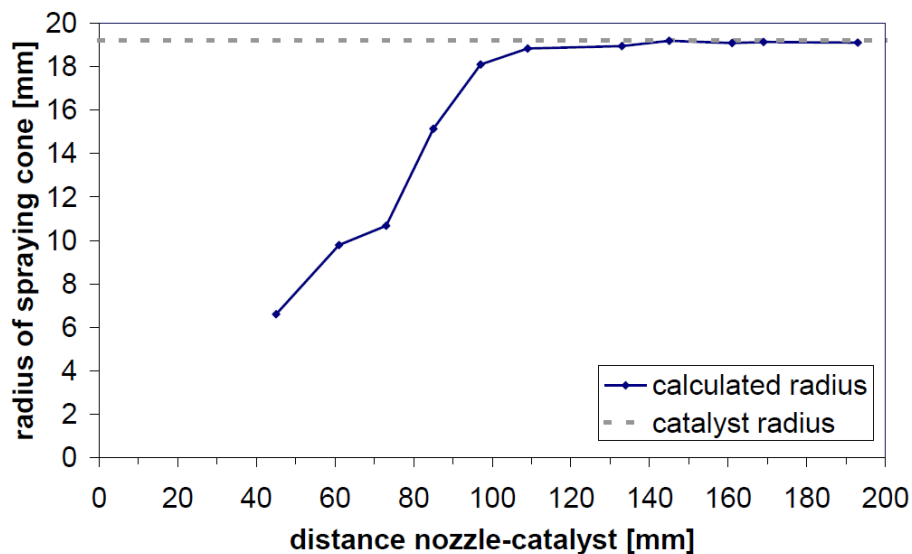
Figure 3-8: Spray cone radii at various distances derived from evaluation of NO$_x$ reduction rates (DeNO$_x$) with urea solution (AdBlue®). DeNO$_x$ values at 10 ppm NH$_3$-slip could be related to the covered catalyst frontal area, since a relatively sharp separation between the spray cone and the surrounding gas could be assumed.

3.9. Conclusion

The goal of our experimental setup was to investigate liquid reducing agents for the SCR process under laboratory conditions. Previous setups exclusively focused on either the nebulization process, the mixing of spray and gases, or the SCR reaction on the catalyst. In the presented setup, however, all these processes can be explored using a combination of analytic techniques.

One of the most critical steps was the homogenous nebulization of the liquid reducing agent and its homogenous distribution across all catalyst channels. This was achieved through suitable design of the reactor and a careful selection of the components used to construct the setup. The custom-made glass nebulizer with the HPLC dosing were the most essential components.
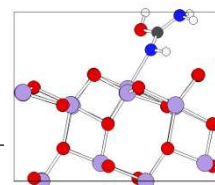
The SCR experiments with ammonia gas and urea solution proved that, when a proper distance between injection nozzle and catalyst was chosen, a homogeneous distribution of the liquid reducing agent can be achieved over the catalyst frontal area with our setup. The results from these experiments could also be used to calculate the quality of urea distribution, relative to the ideal case with ammonia gas, for different distances between the nebulizer and the catalyst. Moreover, the spray cone diameter at the catalyst's frontal area could be estimated in dependency on the injection distance.

With the new setup, it was possible to examine the processes occurring with the combination of reducing agent spraying, its decomposition, and the subsequent SCR reaction. The temperature necessary for decomposition of the reducing agent solution could be determined, or side products from incomplete decomposition could be quantitatively analyzed. Thus, nitrogen-containing substances that release ammonia upon decomposition could be investigated.

Processes not related to SCR, or exhaust gas aftertreatment in general, could be investigated in this novel setup, provided they involve three-phase reactions with gases, liquids and a catalyst.

4. Elucidation of the decomposition of GuFo[*]

4.1. Introduction

Guanidinium formate is considered a promising new ammonia precursor compound, which might be used as an alternative to urea solution in the selective catalytic reduction (SCR) process aboard of diesel vehicles [165]. Unlike urea solutions, guanidinium formate solutions do not tend to slowly decompose under hot weather conditions and do not freeze even in extremely cold winters. Guanidinium formate should be catalytically decomposable in a three-step reaction releasing ammonia. In the first step, guanidinium formate splits to guanidine and formic acid, then guanidine decomposes to ammonia and carbon dioxide by smooth hydrolysis while the formic acid decomposes independently. These reactions are feasible over a TiO_2 catalyst surface.

The aim of this chapter was to find the minimum energy reaction path for the decomposition of guanidinium formate on the (101) TiO_2-anatase catalyst surface using density functional theory (DFT), and verifying the proposed reaction pathways in temperature programmed decomposition (TPD) experiments. In the DFT calculations, local minima, saddlepoints and connecting intrinsic reaction paths on the basis of energy surfaces were derived to obtain the overall reaction pathways.

Predominant among the TiO_2 polymorphs is the anatase phase, because of its stability under hydrotreating conditions. Arrouvel et al. [291] determined
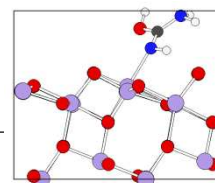
using DFT calculations the hydration state of four crystallographic planes of TiO_2-anatase ((101), (001), (100) and (110)) for a wide range of temperatures and water pressures prevailing under real hydrodesulfurization working conditions (600 < T < 700 K, low pH_2O/p_O, with p_O = standard vapor pressure). They found that the (110) and (100) surfaces dehydrate at low temperatures, while the (001) and (101) remain partially hydrated at high temperatures. Furthermore, the equilibrium crystal shape was mostly dominated by the very stable (101) surface. Semiempirical [292], Hartree-Fock [293] and DFT [294] calculations all came to the conclusion that water adsorbs dissociatively on the (001) surface. In contrast, on the (101) surface, molecular water adsorption is energetically more favorable when compared to the dissociative mechanism [295,296,297]. Very recently, Posternak et al. [298] questioned the high reactivity of the (101) surface and showed that hydroxyl formation is significantly increased on the ridges delimited by (101) TiO_2-anatase surfaces of different orientations.

The beneficial molecular water adsorption suggests that other molecules with polar hydrogen bonds, such as isocyanic acid (HNCO), might also adsorb non-dissociatively on the (101) TiO_2 surface. The co-adsorption of isocyanic acid and water, and their reaction to ammonia and carbon dioxide on the (101) TiO_2-anatase surface, were studied with *in situ* DRIFTS investigations and kinetic experiments [299] and were simulated in DFT calculations. It was calculated that isocyanic acid might adsorb in both ways, molecularly and dissociatively, on the (101) TiO_2-anatase surface. The instant at which water gets involved in the isocyanic acid adsorption on the surface is vital for determining the further course of the surface reaction. In the absence of water, it was found that HNCO can adsorb in molecular form on the catalyst surface [300]. In the presence of water, only

dissociative adsorption is relevant, leading to –NCO groups at the surface, which are immediately attacked to yield a carbamic acid complex. This carbamic acid complex is further transformed into a carbamate complex. After decarboxylation, an NH_2 group remains on the surface. At the end, NH_3 is formed by a proton transfer from the molecularly adsorbed water and the hydrolysis reaction is completed.

The decomposition of isocyanic acid by water on the (101) TiO_2-anatase catalyst surface was investigated in detail, but the decomposition of larger molecules, like urea and GuFo, which are precursor compounds for the SCR process, have not been theoretically studied. The competitive reaction pathways for urea decomposition, i.e., hydrolysis and NH_3 elimination, were simulated in the gas phase and in aqueous solutions [301]. The intramolecular ammonia elimination was calculated to have a lower activation energy when compared to the hydrolysis reaction. Guanidinium formate was theoretically studied in its role as a protein-salt bridge in enzymatic reactions [302,303], but so far it has not been studied as a precursor compound for the SCR process. Sagarik and Chaiyapongs investigated the structures and stabilities of salt-bridges in aqueous solutions, while Zheng and Ornstein concentrated on the stabilization of enzymes in nonaqueous solvents.

An ideal (101) TiO_2-anatase crystal lattice was chosen as a surface model, as this is the most prominent surface in commercial TiO_2-anatase hydrolysis catalysts [11]. Guanidinium formate was assumed to be adsorbed on the surface as guanidine and formic acid (Figure 4-1).
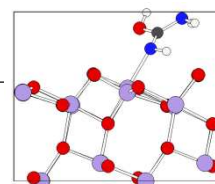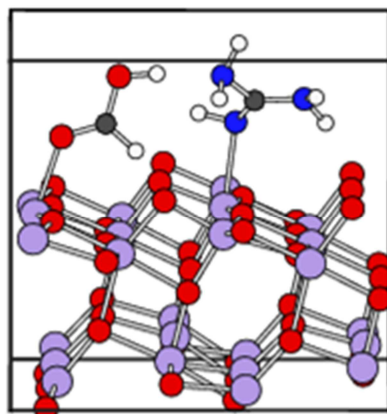
Figure 4-1: Guanidinium formate decomposition on the (101) TiO$_2$–anatase catalyst surface: Guanidine and formic acid adsorbed on two neighboring five-coordinated Ti surface sites. The box represents the computational cell. Oxygen atoms are red, titanium atoms violet, hydrogen atoms white, carbon atoms grey and nitrogen atoms blue.

For comparison, the reaction barriers and energies of reaction in the gas phase were also calculated. The guanidine decomposition to ammonia and carbon dioxide was then studied separately from the decomposition of formic acid to water and CO, or to H$_2$ and carbon dioxide. Along the proposed reaction paths, the intermediate compounds were identified (local minima on the potential energy surface). The competing reactions in most of the cases were based on the proton transfer towards the desired products (e.g. urea elimination/urea hydrolysis).

The theoretical results were compared with temperature-programmed decomposition experiments, in order to record the product distribution and to identify intermediate compounds in the course of the decomposition processes. From the quantified reaction products, and the onset temperatures of their emission, conclusions about the reactions occurring on the catalyst were drawn.

From the combination of theoretical and experimental results, it was concluded that the moment in which water enters the decomposition of guanidine is crucial and determines its course. In particular, the

temperature-programmed decomposition experiments propose a decomposition of guanidine to urea and subsequent decomposition to isocyanic acid. Followed by its rapid hydrolysis to ammonia as the main reaction pathway, which is in agreement with the theoretical calculations.

4.2. Computational method

The computational method is described in the chapter "2. Methods and experimental setup".

In short, the DMol^3 local orbital method [265,266] in combination with the PBE functional was used, with the default basis set DND. The element dependent cutoff radius together with other default settings for integration and tolerances on self-consistent field (SCF) and geometry optimization convergence were chosen for the individual calculations.

Starting from the geometries of the adsorbed intermediate species, tentative geometries of reactant and product were prepared by adding the required reactant like H_2O or product like NH_3 or CO_2 in a suitable geometry. Then, the saddle point for each reaction step was located using the search method of Govind [268] and recent refinements of this method.

If the reaction path between the prepared reactant and product was too contorted, then convergence was not achieved, as the saddle point optimization was led repeatedly to a spurious maximum along the contorted path. Thus, a new search endpoint was extracted from a scan across the supposed real saddle point, but with inaccurate tentative geometry. After such a revision of the endpoint, all real saddle points were found.
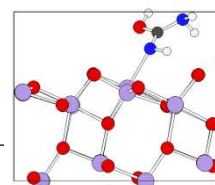
The endpoints for each reaction step were found by intrinsic reaction coordinate (IRC) [269] searches using a method similar to the one for molecules [270].

4.3. Experimental setup

The experimental setup used for the temperature-programmed decomposition experiments was described in section "2.1.2. Tubular quartz reactor for TPD experiments".

Instead of spraying the GuFo-solution on the catalytic material, catalyst-coated cordierite honeycombs were dipped into aqueous solution of GuFo. The GuFo impregnated catalyst samples were then subjected to a programmed heat ramp while the produced reaction products were quantified using FTIR spectroscopy and a liquid-quench followed by HPLC-analysis of the absorption solution.

4.4. Results

4.4.1. Guanidine decomposition via hydrolysis

All reactions with their corresponding energy barriers and reaction enthalpies are summarized in Figure 4-2, while Figure 4-3 shows the energetics of all intermediates and the reactions pathways connecting them.
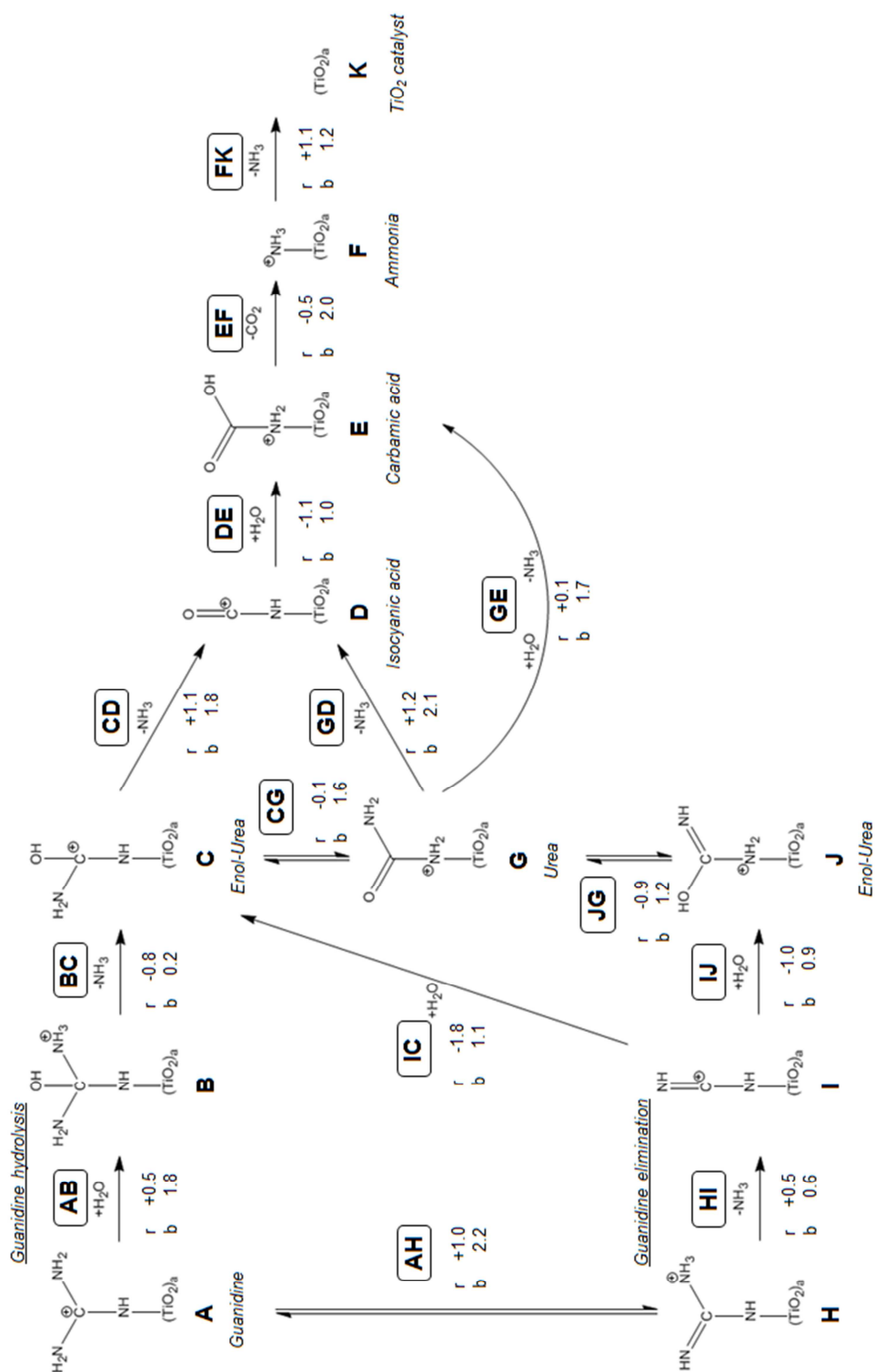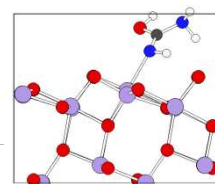
Figure 4-2: Decomposition reaction pathways for guanidine on the TiO₂ catalyst surface including the calculated energies of reaction and reaction energy barriers for the individual steps.
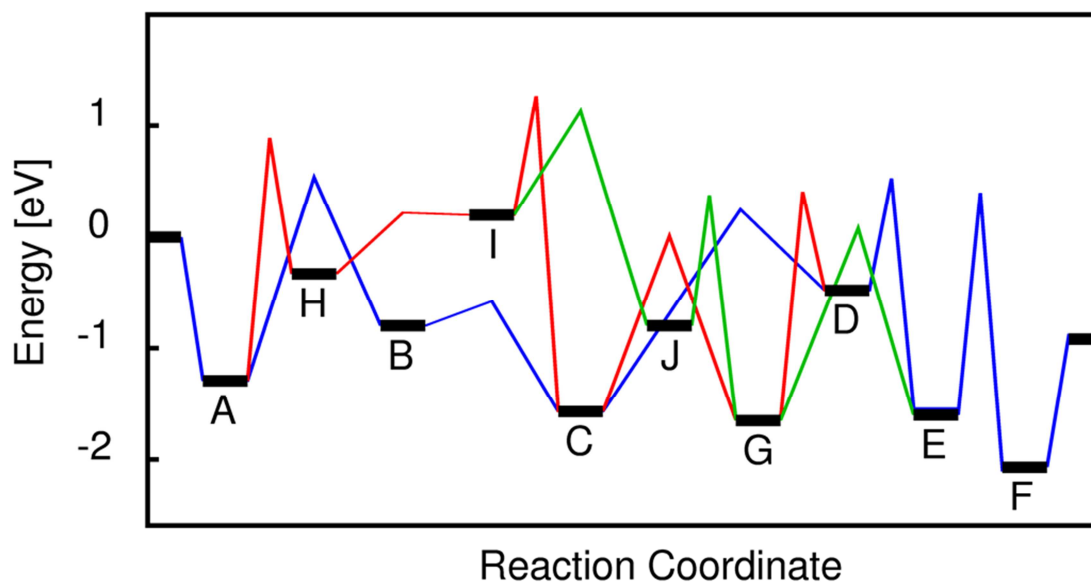
Figure 4-3: Energetics for adsorbates and reaction barriers on the catalyst surface along the reaction path determined from the intrinsic reaction pathway calculations.

The starting point for the calculations was guanidine adsorbed on a five-coordinated surface Ti atom (**A**). In reaction step **AB** of Figure 4-2, water from the gas phase dissociated to donate a proton to one of the NH_2 groups (forming loosely bound ammonia) and bind to the carbon atom of the guanidine as OH group (**B**). This reaction is endothermic with an energy change of 0.5 eV and an energy barrier of 1.8 eV for the water dissociation (**AB**). Step **AB** in Figure 4-4 shows the energy along the intrinsic reaction path. To the reactant side (left) the path ends in a local minimum with H_2O and guanidine co-adsorbed on the surface. The water molecule can be simply removed from the calculation or explicitly forced to the gas phase. Either method yields the same desorption energy starting from the co-adsorbed state with guanidine.
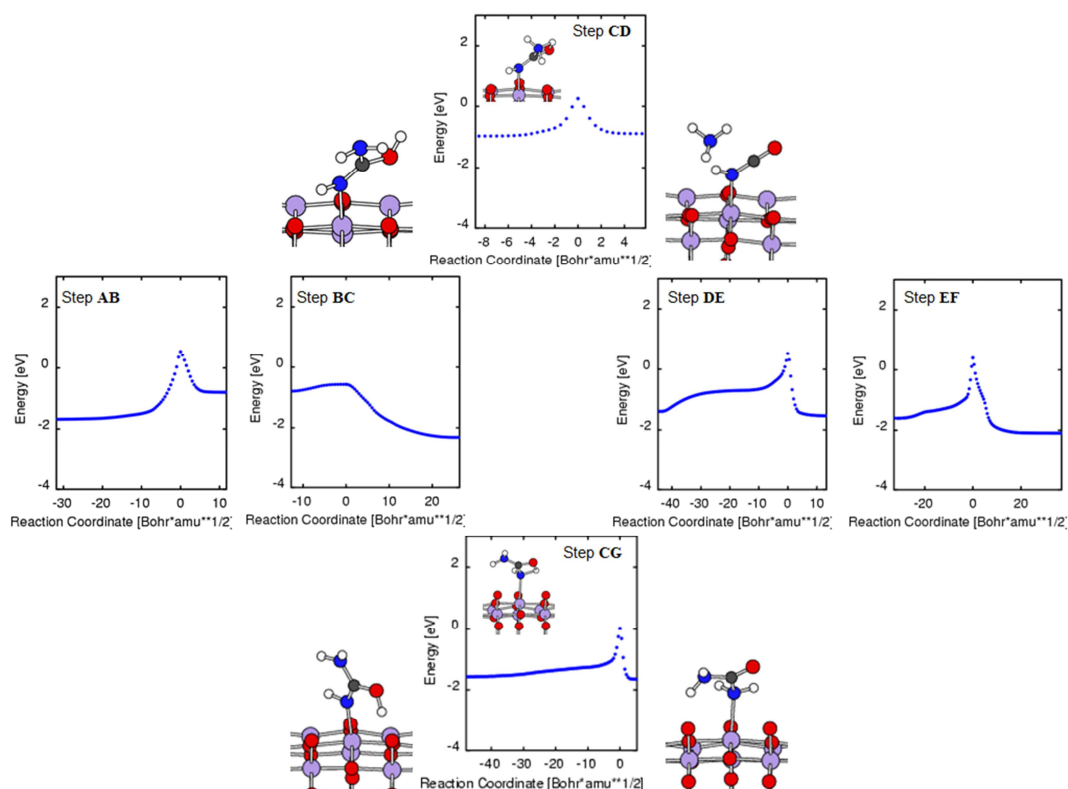
Figure 4-4: Intrinsic reaction pathway calculations for isocyanic acid and ammonia formation (top) or urea formation (bottom) following guanidine hydrolysis – one of the two principal decomposition routes for guanidine.

Typically, the molecule of main interest, here guanidine, stays in the basin of attraction of the local minimum. Often this minimum is not coincident with the global minimum for adsorption. The barriers between the local minima of adsorption tend to be shallow and are dictated by the surface roughness at atomic resolution. The existence of the co-adsorbed species and the local minima often causes the intrinsic reaction path graphs for subsequent reaction steps to not join at the same energy for the same adsorbed intermediate species. The passage across the low adsorption barriers is not determining the rate for the major barrier in a reaction step. In contrast, desorption of reaction products can be important steps involving energies of up to about 1 eV. Due to the relative unimportance of
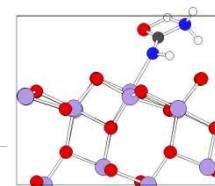
the various local minima for the adsorption of an intermediate species, the intermediate energies in Figure 4-2 and Figure 4-3 were generalized to the global adsorption minimum in question for the respective intermediate species.

The next step was ammonia release, which leads to an exothermic reaction (E_r = -0.8 eV) with a very low energy barrier of 0.2 eV (**BC**). To summarize, the hydrolysis of guanidine is an exothermic reaction (E_r = -0.3 eV) resulting in ammonia desorption from the catalyst surface and a $-N(H)-C^+(OH)-NH_2$ species (**C** = tautomeric enol structure of urea) retained on the catalyst surface. The rate-determining step was determined to be the water dissociation. Once water was split and NH_3 was formed, ammonia was easily released from the surface. The next reaction step involved a proton transfer by two different possibilities: (**CG**) the proton could move to the $-NH$ group and form the standard keto tautomeric structure of urea (**G**), or (**CD**) it could be transferred to the NH_2 group to form ammonia and desorb from the surface, leaving isocyanic acid (**D**). Energy profiles along the intrinsic reaction paths for these reaction steps are also shown in Figure 4-4. The reactions are either strongly endothermic (**CD**: E_r = 1.1 eV) or just weakly exothermic (**CG**: E_r = -0.1 eV). Based on the difference in reaction energy barriers, urea formation is preferred (E_b = 1.6 eV, Figure 4-4 on bottom) over isocyanic acid formation and ammonia desorption (E_b = 1.8 eV, Figure 4-4 on top). The intrinsic reaction path calculations were performed to understand how transition structures were linked to the reactants and products. In both cases, the reactions were determined by a proton transfer. In the transition state structures, the hydrogen atom was bound to the oxygen atom and either the nitrogen atom of the $-NH$ group (leading to urea formation) or the

nitrogen atom of the $-NH_2$ group (precursor state for NH_3 formation and desorption). On top in Figure 4-4 the intrinsic reaction path for isocyanic acid formation and ammonia desorption from the surface is shown.

If isocyanic acid is formed, another water molecule enters the reaction to hydrolyze the isocyanic acid to carbamic acid (**DE**). This reaction was found to be exothermic ($E_r = -1.1$ eV) but with an energy barrier of $E_b = 1.0$ eV for the reaction. Once carbamic acid (**E**) was formed, it dissociated to CO_2 and ammonia in a single reaction step with an energy barrier of 2.0 eV (**EF**). This reaction was exothermic ($E_r = -0.5$ eV) and resulted in ammonia bound to Ti (**F**), while CO_2 was desorbed from the surface.

If urea was formed, there were two possibilities for the course of the reaction. Either urea eliminated ammonia (**GD**) or water entered the reaction to hydrolyze the urea (**GE**). The simple unimolecular pathway involved a proton transfer from one of the $-NH_2$ groups to the other, followed by a cleavage of the C–N bond and elimination of NH_3. This process yielded isocyanic acid (**D**), which has been experimentally observed as a product of urea decomposition. The reaction was determined to be endothermic ($E_r = 1.2$ eV) with an energy barrier of 2.1 eV.

If urea hydrolyzed to carbamic acid (**E**) and ammonia, the reaction was slightly endothermic ($E_r = 0.1$ eV) and the energy barrier for the water dissociation was 1.7 eV. Regarding the calculated energy barriers, the two reactions of urea elimination and urea hydrolysis were, therefore, equally likely to occur. A nucleophilic attack of a water molecule on the carbonyl carbon atom and a protonation of the carbonyl oxygen atom were observed to occur in the first step of the hydrolysis reaction. In the resultant tetrahedral intermediate, a proton was transferred from a hydroxyl group to
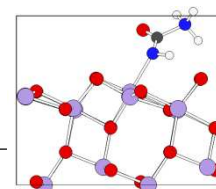
an amino group, and the corresponding C–N bond cleaved, releasing ammonia and carbamic acid.

4.4.2. Guanidine decomposition via elimination

Parallel to the hydrolysis pathway, there was a second possibility for guanidine decomposition, i.e. *via* ammonia elimination. The first step for this process was the proton transfer from one of the $-NH_2$ groups of guanidine to the second (**AH**). This reaction was determined to be endothermic (E_r = 1.0 eV) and the energy barrier for the proton transfer was 2.2 eV, as calculated in similar reactions. Ammonia was then formed and released (**HI**). This reaction was endothermic with an energy of 0.5 eV. After the first ammonia release, water entered the reaction and attacks the carbon atom of the remaining $-NH-C^+=NH$ species (**IJ**). Water splits on the $-N(H)-C^+=NH$ species (**I**, E_r = -1.0 eV, E_b = 0.9 eV) and forms a $-N(H)_2-C(OH)=NH$ species (**J**), which is another tautomeric enol structure of urea. The tautomerization to urea (**G**) was an exothermic reaction with E_r = -0.9 eV and E_b = 1.2 eV (**JG**). After the formation of urea, the reaction might proceed *via* urea elimination (**GD**) or urea hydrolysis (**GE**), as indicated in Figure 4-2. Intrinsic reaction path calculations were employed to understand how the transition structures were linked to the reactants and products. However, as the detailed intrinsic reaction pathways of the guanidine decomposition via hydrolysis were already presented exemplarily, the energy profile of guanidine decomposition via elimination are only shown in the energy profile overview Figure 4-3.

4.4.3. Formic acid decomposition

The most stable configuration of formic acid on a (101) TiO_2-anatase surface was molecularly adsorbed formic acid bonded by its oxygen atom to one five-coordinated surface Ti atom. According to the simulations, formic acid might decompose either to water and CO, or to carbon dioxide and H_2. Figure 4-5 shows the intrinsic reaction path calculations for these reactions.
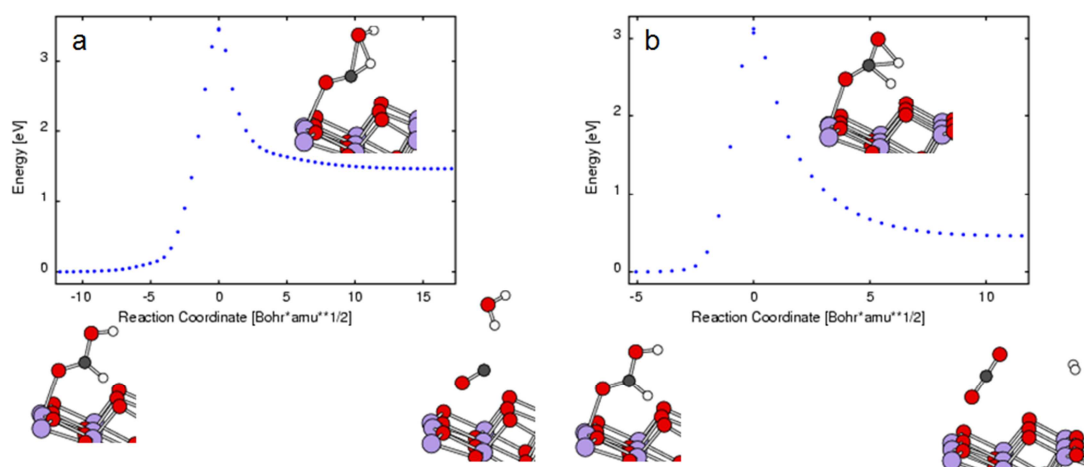

Figure 4-5: Intrinsic reaction pathway calculations for the decomposition of formic acid leading to (a) water and CO or (b) H_2 and carbon dioxide as products of the decomposition.

In the first case (a), which leads to H_2O and CO, the reaction was endothermic with a reaction energy of 1.5 eV and a energy barrier of 3.5 eV. In the second case (b), which leads to CO_2 and H_2, the reaction was endothermic as well ($E_r = 0.5$ eV) with a similar energy barrier ($E_b = 3.1$ eV). Based on these calculations, both reactions were feasible and equally likely to occur.
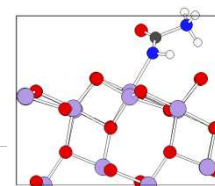
4.4.4. Comparison of the decomposition reactions

The theoretical calculations of the GuFo decomposition could be separated into the following steps: GuFo is bound to the TiO_2 catalyst surface as guanidine and formic acid. The decomposition of these two compounds is proceeding separately. While formic acid may decompose in two different reactions to yield two different final products, guanidine may take several different routes that have identical final products. The formic acid decomposition is of clearly lesser interest, as it does not yield the target compound NH_3, but merely coproducts. The guanidine decomposition on the contrary, is essential as its final product, the released NH_3, is the desired reducing agent for the SCR process in diesel exhaust cleanup systems. The two main pathways for guanidine are either decomposition via hydrolysis or decomposition via elimination. Both pathways have similar activation energies for the first step. Further along the path several barriers of similar height occur. None of the barriers stands out as a clearly rate determining step. Figure 4-2 gives an overview of the calculated reaction path steps in guanidine decomposition on the TiO_2 catalyst surface. It shows all the intermediate compounds and provides estimates for the reaction energy (r) and reaction energy barrier (b) of the individual reaction steps. Figure 4-3 is a conceptional sketch of the energetics for the adsorbates and barriers, with the intermediate species ordered schematically along the reaction path. The energies for most intermediate species can take several values because of adsorption in different local minima, for Figure 4-2 and Figure 4-3 the global minimum energy is used. All energies are with reference to the bare (101) surface and all molecular species in the gas phase. The energy difference all across Figure 4-3 is the calculated overall reaction energy for guanidine hydrolysis according to 4-1.

$$CN_3H_5 + 2\,H_2O \rightarrow 3\,NH_3 + CO_2 \qquad \text{4-1}$$
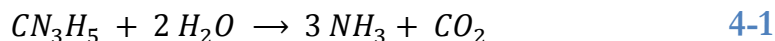
The intermediates are labeled according to the letters underneath the corresponding structures in Figure 4-2. The energies of the local minima are shown as horizontal bars, the barriers are shown as peaks between two local minima. The coincidence of a barrier with a local minimum does not imply that both refer to the same intermediate species. Rather, this indicates a saddle point between the previous and following minimum, therefore, bypassing the minimum in between. The energy levels of the minima are the lowest adsorbate conformational energy found without additional co-adsorbed species.

4.4.5. Experimental results

In general, the measurements showed that the products of the guanidinium formate (GuFo) decomposition on the TiO_2 catalyst surface were mainly ammonia, CO, formic acid and carbon dioxide. From the experimental results, the formation of NH_3 from GuFo was proposed to proceed in three reaction steps: (i) decomposition of GuFo to guanidine and formic acid, (ii) hydrolysis of guanidine to NH_3 and CO_2 *via* urea and HNCO intermediates and (iii) decomposition of formic acid to water and CO.

Figure 4-6 shows the concentration profiles that were determined by FTIR spectroscopy as a function of the monolith's temperature.
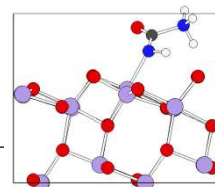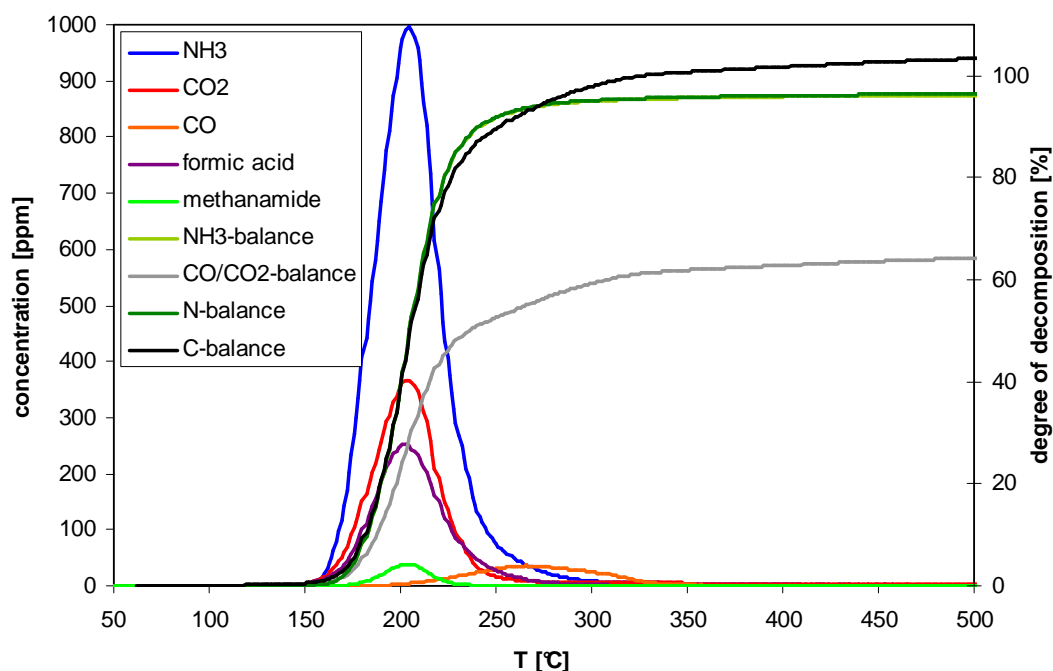
Figure 4-6: Product gas composition as a function of monolith temperature during the decomposition of coated GuFo in an 85% N_2, 10% O_2, and 5% H_2O atmosphere, as measured by FTIR spectroscopy.

All gaseous compounds included in the previously described method have been measured, but only those plotted were detected. The most striking feature is a maximum in the ammonia evolution at 205 °C. It overlapped with the maxima in formic acid, methanamide and CO_2 evolution. The maximum in HNCO evolution (~ 1 ppm, curve not shown in Figure 4-6) was situated at the slightly lower temperature of 200°C, while the very broad maximum in CO evolution occurred at 270°C. The symbols indicate the degree of decomposition as calculated from the initial weight of inserted GuFo and the concentrations of compounds measured by FTIR spectroscopy in the product gas. The degree of decomposition to ammonia was of special interest, but the values relating to all the measured nitrogen compounds were also very useful. CO and CO_2 were the thermodynamically most stable forms of carbon to leave the system, but

the values relating to all the measured carbon compounds also needed to be considered.

In Figure 4-7, the concentration profiles of higher molecular weight compounds are depicted, in addition to the nitrogen and carbon balance, which was deduced from both FTIR and HPLC analysis.
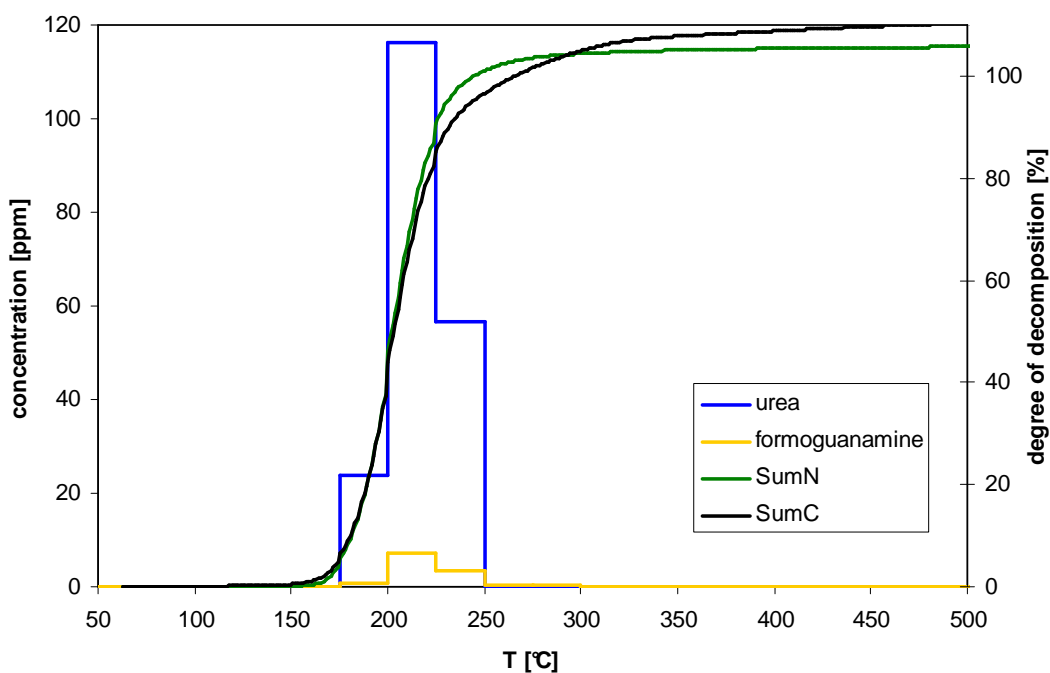

Figure 4-7: HPLC analysis of the product gas composition as a function of monolith temperature during the decomposition of coated GuFo in an 85% N_2, 10% O_2, and 5% H_2O atmosphere, as measured in absorption solution samples by HPLC.

The reason for the step-wise changes in concentration of the higher molecular weight compounds was due to the experimental procedure. Samples were restricted to sampling at regular intervals, unlike the continuous measurement in the FTIR gas cell. In spite of the sharp jumps in the concentration profile, the maxima for urea and formoguanamine emission, situated around 200°C can be resolved. The emissions of both compounds begins in the temperature window of 175–200°C, peak in the interval of 200–225°C and level off from 225–250°C. Melamine reached a
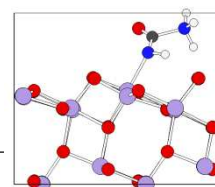
maximum concentration 150 times lower than the maximum of formoguanamine. It is not shown in the plot, although it could be reliably detected.

4.5. Discussion

4.5.1. Comparison of gas phase reactions and surface reactions

Table 4-1 shows a comparison of the reaction energies and energy barriers for the proposed reactions.

Table 4-1: Detailed comparision of the reaction barriers and reaction energies in the gas phase and on the catalyst surface for important decomposition reactions.

process	label	Reaction barrier [eV]		Reaction energy [eV]	
		gas phase	catalyst	gas phase	catalyst
guanidine hydrolysis	ABC[†]	2.0	1.8	-0.2	-0.3
guanidine elimination	AHI[†]	2.0	2.2	0.8	1.5
urea hydrolysis	GE	1.8	1.7	0.2	0.1
urea elimination	GD	1.9	2.1	0.9	1.2
isocyanic acid hydrolysis	DE	1.2	1.0	-0.7	-1.1
carbamic acid decomp.	EF	1.3	2.0	-0.2	-0.5
formic acid decomp. (a)	$CO+H_2O$	2.8	3.5	0.6	1.5
formic acid decomp. (b)	CO_2+H_2	2.7	3.1	-0.3	0.5

† *For the reaction on the catalyst surface, the reaction energies of both steps have been combined and the higher of the two barriers is reported*

In the search of local minima, the starting configurations took into account molecularly adsorbed species. The real minima were found by geometry optimization, and were taken as connecting points (reactant or products) on the potential energy surface when searching the transition states and minimum energy reaction pathways. Analogous to Figure 4-2 and Figure 4-3 for the reaction pathways and energetics on the catalyst surface, Figure

4-8 and Figure 4-9 depict the reaction pathways and energetics of the guanidine decomposition in the gas phase.
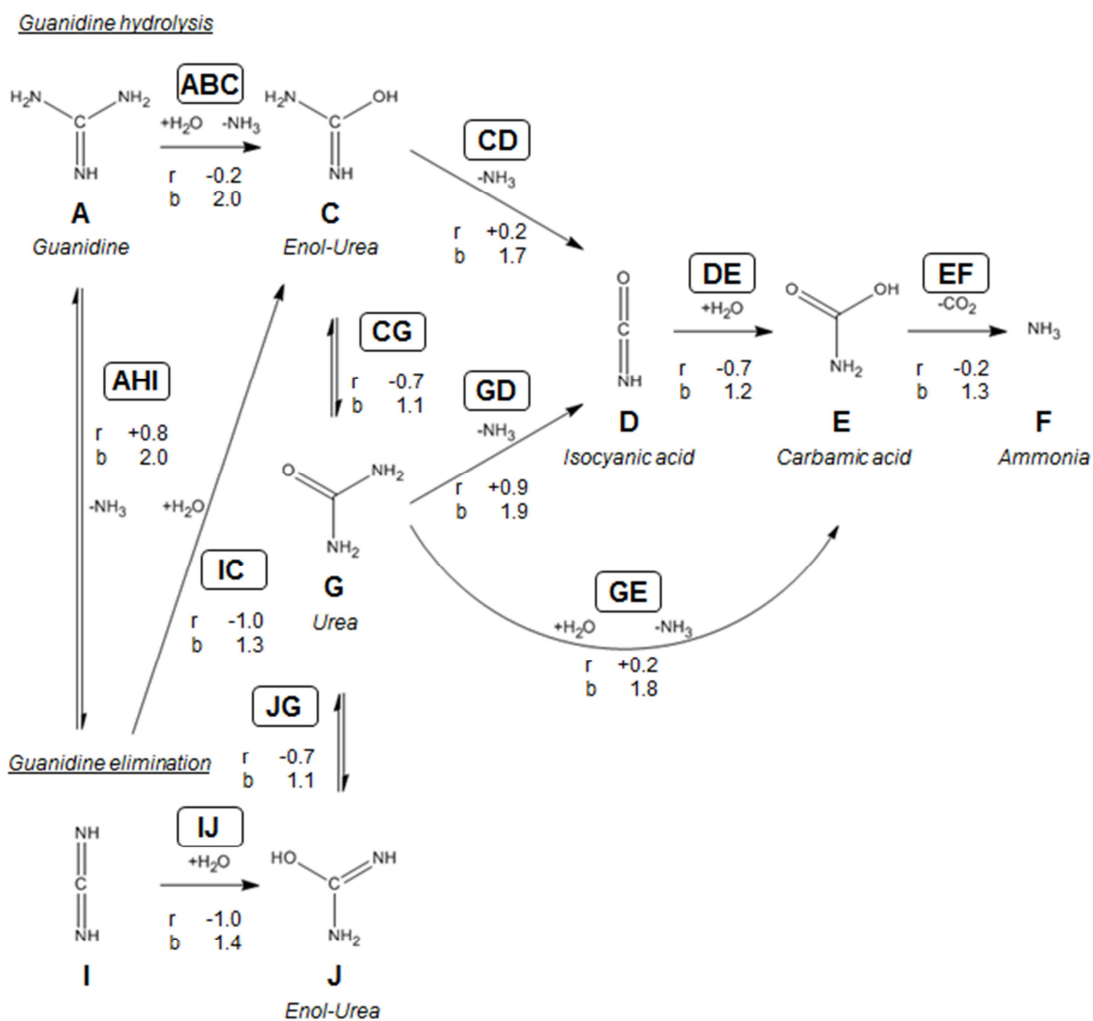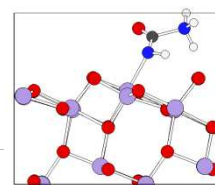

Figure 4-8: Decomposition reaction pathways for guanidine in the gas phase including the calculated energies of reaction and reaction energy barriers for the individual steps.
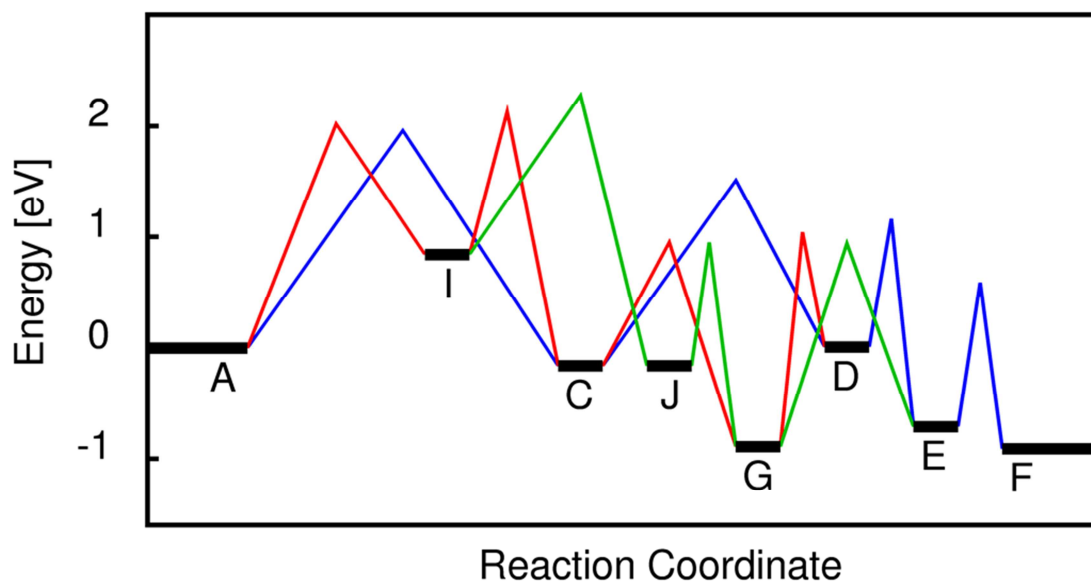
Figure 4-9: Energetics for adsorbates and reaction barriers in the gas phase along the reaction path determined from the intrinsic reaction pathway calculations.

This study does not cover the vibrational aspects of the free energies. However, it is expected that the vibrational entropy contributions along the reaction path vary relatively little, and so their inclusion should not alter the results qualitatively.

In the gas phase, guanidine hydrolysis as well as guanidine elimination proceeded in a single reaction step without intermediate. Therefore, the reaction steps were called **ABC** and **AHI** for guanidine hydrolysis and guanidine elimination, respectively. Their reaction energy can be compared to the corresponding sum of the two reaction energies on the catalyst surface, i.e. **AB** + **BC** and **AH** + **HI**. Guanidine hydrolysis is weakly exothermic in both, gas phase (-0.2 eV) and on the catalyst surface (-0.3 eV). Guanidine elimination on the other hand is endothermic in the gas phase (0.8 eV) and even more so on the catalyst surface (1.5 eV). The reaction barriers of the gas phase were compared to the higher barrier of the corresponding two reaction steps on the catalyst surface. For both, guanidine hydrolysis and guanidine elimination the reaction barriers in the

gas phase (2.0 eV and 2.0 eV) were quite similar to those on the catalyst surface (1.8 eV and 2.2 eV). The intermediates **C** and **J**, which were differently bound to the catalyst surface in Scheme 1, became identical in the gas phase Figure 4-8. Therefore, reactions **IC** & **IJ** and **CG** & **JG** became identical as well, which could be confirmed by the calculated values.

Urea elimination (**GD**, E_r = 0.9 eV, E_b = 1.9 eV) and urea hydrolysis (**GE**, E_r = 0.2 eV, E_b = 1.8 eV) were equally likely in the gas phase. On the TiO_2 catalyst surface, however, the activation energy was altered to 2.1 eV and 1.7 eV, respectively. The energies of the two reactions differed in that urea elimination was a strongly endothermic reaction (1.2 eV), while urea hydrolysis was a barely endothermic reaction (0.1 eV).

Isocyanic acid decomposition showed a slightly higher barrier in the gas phase (1.2 eV) compared to the one on the catalyst surface (1.0 eV). The reaction energy of the reaction on the catalyst surface was determined to be more exothermic than in the gas phase (-1.1 eV vs. -0.7 eV).

Carbamic acid decomposition was easier in the gas phase than on the catalyst surface. The reaction energies were determined to be -0.2 eV for the gas phase and -0.5 eV on the surface. While the reaction energies were the same, the activation energies differed from 1.3 eV in the gas phase to 2.0 eV on the catalyst surface.

The activation energies obtained for the gas phase and catalyst surface suggest quite similar activities for the GuFo decomposition. However, on the catalyst surface the reactants are forced into vicinity, thereby increasing the kinetics of the reaction significantly compared to the diluted gas phase reaction. So far, theoretical studies have neglected this effect, as there were no simulations of heterogeneously catalyzed reactions with similarly
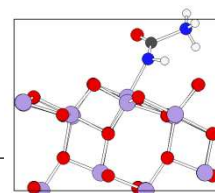
complex molecules. Therefore, this subject is going to be investigated in more details in future works, as it constitutes an important aspect of simulations of catalytic processes and will be certainly of great interest in anticipated works on comparably complex systems.

Formic acid, like carbamic acid, showed a tendency for gas phase decomposition. There were two possibilities for this decomposition: (i) decomposition to water and CO (experimentally found) or (ii) decomposition to carbon dioxide and H_2 (not confirmed by experiments). The gas phase reaction calculations gave similar activation energies for both reactions with 2.8 eV and 2.7 eV, respectively. The reaction leading to water and CO was endothermic (E_r = 0.6 eV) while the reaction yielding H_2 and carbon dioxide was exothermic (E_r = -0.3 eV). On the catalyst surface, both reactions were endothermic with reaction energies of 1.5 eV and 0.5 eV, respectively. The energy barriers were slightly higher, with values of 3.5 eV and 3.1 eV respectively. Therefore, judging from the theoretical investigations, the decomposition of formic acid and carbamic acid most likely occurred in the gas phase.

4.5.2. Summary of the proposed reaction pathways

Figure 4-2 gives an overview of the proposed reaction pathways for guanidinium formate decomposition on the TiO_2 catalyst surface. The first step was the guanidine hydrolysis reaction (**AB** and **BC**). Urea formation (**CG**) was preferred over the formation of isocyanic acid (**CD**), but once urea was formed, the hydrolysis to carbamic acid (**GE**) and elimination to isocyanic acid (**GD**) were equally possible. If isocyanic acid was formed, it was hydrolyzed to carbamic acid (**DE**) as intermediate before the release of ammonia and carbon dioxide (**EF**). If carbamic acid was formed (**GE**),

isocyanic acid was not observed at all and the reaction path had one step less. Therefore, two possibilities were feasible depending on whether isocyanic acid was observed or not:

Guanidine → Urea → Carbamic acid → NH_3 and CO_2

or

Guanidine → Urea → Isocyanic acid → Carbamic acid → NH_3 and CO_2.
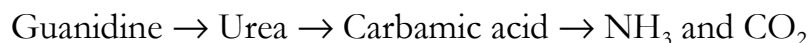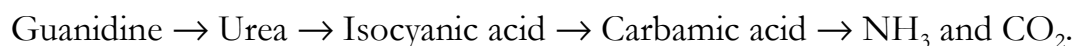
These two reaction paths were independent of the first reaction step, i.e., whether guanidine was hydrolyzed (water entered the reaction) or guanidine eliminated ammonia (in the absence of water). However, from experiments, guanidine decomposition was know to proceed insufficiently when water concentrations were low.

At the end of the reaction, guanidine and two H_2O molecules were consumed while one CO_2 and three NH_3 molecules were released to the gas phase. The released molecules were removed from the computational model upon their evolution. The overall reaction was calculated to be exothermic with $E_r = -0.92$ eV. In comparison, a value of $E_r = -0.9 \pm 0.5$ eV can be calculated using values obtained from experiments: $\Delta H_f^{\circ}{}_{solid}$(guanidine) = -56 kJ/mol [304], $\Delta_{sublimation}H^{\circ}$(urea) = 99 kJ/mol [305], $\Delta H_f^{\circ}{}_{gas}$(water) = -242 kJ/mol [306], $\Delta H_f^{\circ}{}_{gas}$(ammonia) = -46 kJ/mol [28] and $\Delta H_f^{\circ}{}_{gas}$(carbon dioxide) = -394 kJ/mol [28]. As the enthalpy of sublimation for guanidine is unknown, the value for urea was used with an approximated error of 50%.

4.5.3. Combined results from experiments and calculations

The TPD experiments, in combination with FTIR spectroscopy and HPLC analysis, provided valuable experimental data to verify the results of the theoretical study. The catalytic decomposition of GuFo on TiO_2-anatase
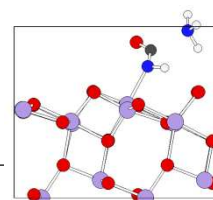
was observed to work quite well in this fundamental experiment, as more than 90% of the inserted nitrogen compounds exited the quartz reactor as gaseous ammonia. Along with the ammonia, most of the carbon stemming from the guanidinium cation left the reactor as CO_2, while the formate anion was only weakly affected by the catalyst, as it exited the reactor as formic acid. The combination of high ammonia and formic acid concentrations in the gas phase at these elevated temperatures resulted in their condensation to methanamide, which was therefore concurrent with the maximum of the ammonia evolution. Interestingly, HCN – the dehydration product of methanamide – was not observed. The sharp and matching maxima of ammonia, CO_2 and formic acid indicated a sudden dissociation of GuFo to instable guanidine, releasing formic acid. Only at elevated temperatures this released formic acid could be decomposed to CO. The relatively high abundance of urea as an aerosol could be attributed to a decomposition pathway of guanidine *via* urea and HNCO to ammonia. The extremely low concentration of HNCO should not be taken contradictory to the stated decomposition pathway, as HNCO is a rapidly reacting intermediate under these hydrothermal catalytic decomposition conditions. The formation of formoguanamine, as detected by HPLC analysis, was a side reaction during decomposition rather than an inherent reaction to this intermediate in a decomposition pathway. The origin of formoguanamine could have been a direct condensation of guanidine with formic acid to yield formylguanidine, followed by condensation with another guanidine molecule (reaction 4-2 and 4-3). The resulting compound formoguanamine is a very stable triazine compound that can be easily detected by its characteristic UV absorption during HPLC analysis. The intermediate of this condensation reaction, formylguanidine, unfortunately

could not be detected as an intermediate.

guanidine   formic acid   formylguanidine   **4-2**

formylguanidine   guanidine   formoguanamine   **4-3**
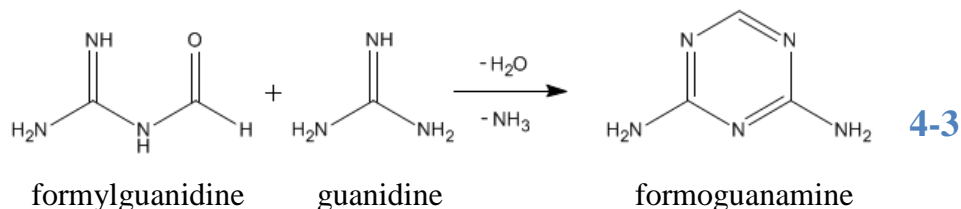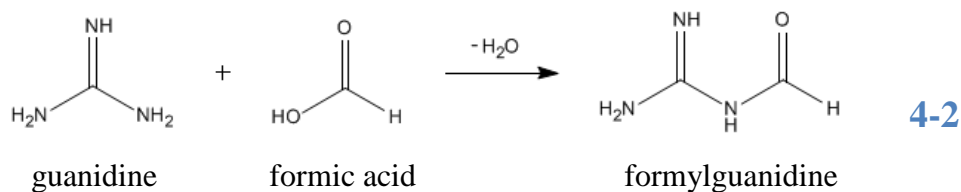
Formylguanidine is known to slowly hydrate in water to form aqueous guanidinium formate. Therefore, the reverse reaction – a condensation of guanidinium formate to yield formylguanidine – would be favoured by the high temperatures in this experiment. The reaction of formylguanidine to formoguanamine was favored by the driving force of creating an aromatic system, which could eventually explain why no formylguanidine could be found in the analysis.

4.6. Conclusion

A minimum energy reaction path for guanidinium formate decomposition on the (101) TiO_2-anatase surface is proposed from density functional theory calculations and temperature-programmed decomposition experiments. The initial step towards ammonia and carbon dioxide formation was the separate adsorption of guanidine and formic acid on five-coordinated Ti active sites on the surface. Several reaction paths have been calculated and compared to find the energetically preferred one. Water was always present in the gas phase above the catalyst surface in the calculations. There was no previous quantum mechanical study yielding
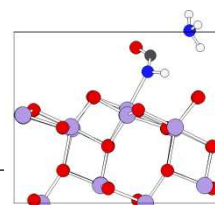
reaction barriers and reaction energies of a heterogeneously catalyzed reaction with similarly complex chemical compounds.

The first reaction in the calculations was found to be either the hydrolysis of guanidine or the elimination of ammonia by guanidine. Both reactions had similar reaction energy barriers for the formation of urea. Experimental results indicated that urea is an intermediate in guanidine hydrolysis. Once a urea-like structure was formed in the calculations, thermolysis and hydrolysis were equally possible.

A critical issue in the calculations was at which moment water entered the decomposition of guanidine, which would in the end determine the course of the reaction. In contrast to the results for the guanidine decomposition, the formic acid decomposition occurred in a single step. From theory, there were two equally possible reaction paths leading to different decomposition products: water and CO, or H_2 and carbon dioxide. From the experiments, however, the latter could not be confirmed.

Calculations of the reactions in the gas phase were performed and compared to the calculations of the reactions on the catalyst surface. The initial barriers for guanidine and urea hydrolysis or elimination relative to their reactant local minima were found to be similar on the catalyst surface and in the gas phase. For formic acid and carbamic acid decomposition the gas phase barrier from the local minimum of the intermediate reactant is somewhat lower in the gas phase. This appears to be contrary to the basic concept of catalysis where the catalyst lowers the barrier.

The present study suggests that the significant enhancement of the reaction rate due to the catalyst surface is due to the high concentration of reactants at the surface as a consequence of chemisorption. The (101) TiO_2-anatase

surface offers a good balance of barrier energies and adsorption energies relative to the gas potential.

Concerning a particular decomposition pathway, the following conclusions could be drawn from the experimental data: GuFo decomposition, in general, seems to take place as the separate decomposition of guanidine and formic acid. The dissociation is driven by the decomposition of guanidine, releasing formic acid at the instant of guanidine decomposition (i.e., 205°C in the measurements). Only at elevated temperatures formic acid decomposes to yield CO, however, not affecting the decomposition of guanidine at this temperature. During the peak emission of ammonia, considerable amounts of urea could also be detected as aerosol, as it was relatively easily evaporated in this temperature range. Moreover, compared to HNCO, which could only be measured in trace amounts, urea needed a longer residence time on the catalyst to decompose. Therefore, a pathway of decomposition from guanidine to urea, and consequent decomposition to HNCO and its rapid hydrolysis to ammonia, were proposed from the experiments.
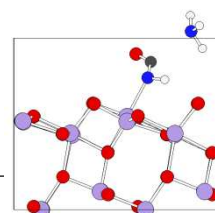
# 5. Decomposition of GuFo on noble metal-doped catalysts

5.1. Introduction

Combustion of fossil fuels or biomass leads to the emission of nitrogen oxides (NO_x), which are some of the most critical pollutants in metropolitan areas. NO_x (NO and NO_2) are not only harmful substances by themselves, but they also catalyze the formation of near-surface ozone, thereby increasing smog. [307]

Since the late 1960s, selective catalytic reduction (SCR) has been used in power plants to reduce NO_x emissions by enabling their reaction with ammonia (NH_3).

For mobile sources, such as passenger cars or heavy duty trucks, aqueous urea solution was found to be a safe precursor solution for NH_3. [123] The solution is sprayed on a decomposition catalyst in the hot exhaust to produce NH_3 according to reactions 1-19 and 1-20.

Ever since the commercialization of aqueous urea solution, its widespread utilization was frequently hampered by its limited temperature stability or the regular refill intervals for the mobile application. This initiated the development of several alternative ammonia storage materials as mobile precursors for on-board generation of the ammonia gas necessary in the SCR of NO_x. Several solutions of nitrogen-containing compounds were tested; amongst the most promising were methanamide, ammonium formate and guanidinium formate. [165] In particular, guanidinium formate, with its high ammonia storage potential and excellent solubility in water, seems promising as an alternative to urea. Guanidine shows structural
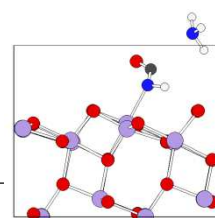
similarity to the urea molecule, and can be hydrolyzed under the release of NH_3 to form urea, as shown in reaction 4-3.

$$H_2N - C(NH) - NH_2 + H_2O \rightarrow H_2N - CO - NH_2 + NH_3 \qquad \textbf{5-1}$$
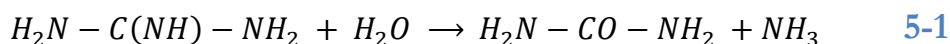
Formic acid stabilizes guanidine by forming the salt guanidinium formate (GuFo), which has a uniquely high solubility in water. The high solubility of GuFo, along with one additional NH_3 release from guanidine compared to urea, directly affects the amount of NH_3 stored per unit volume of the solution, thereby extending refill intervals.

Catalytic decomposition of GuFo was tested on pure TiO_2 (anatase) and on WO_3- or La_2O_3-doped TiO_2 (anatase). While the catalytic decomposition of guanidine to release NH_3 works quite smoothly on these catalysts, formic acid does not decompose easily. Changing the acidity of the catalyst using WO_3 or La_2O_3 even leads to higher formic acid concentrations in the product gas mixtures.

As formic acid corrodes the materials typically used in exhaust gas aftertreatment systems, its emission is a technical concern. Formic acid could also easily condensate with the released NH_3 to form methanamide, a relatively stable and harmful substance (reaction 5-2). Finally, the elevated temperatures in the exhaust gas can lead to water release from methanamide, thereby forming highly toxic HCN (reaction 4-3). [**273**] The emission of these side products from GuFo decomposition inhibited its adoption as an NH_3-precursor solution so far.

$$HCOOH + NH_3 \rightarrow HCONH_2 + H_2O \qquad \textbf{5-2}$$

$$HCONH_2 \rightarrow HCN + H_2O \qquad \textbf{5-3}$$
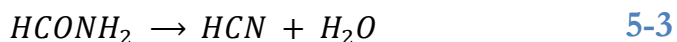
The slow decomposition of formic acid on hydrolysis catalysts can be regarded as the underlying reason for the side product formation. Consequently, there is a challenge to find a hydrolysis catalyst, which would

also show high activity in formic acid decomposition. Dedicated formic acid decomposition catalysts gained much attention recently, [308,309,310] due to the fact that formic acid is considered to be a convenient H_2-precursor compound for fuel cells. Ideally, the formic acid decomposition to H_2 and CO_2, according to reaction 5-4, is substantially preferred over the decomposition to CO and water (reaction 5-5). Otherwise the produced CO would poison the catalyst used in polymer electrolyte fuel cells to generate electricity from H_2.

$$HCOOH \rightarrow H_2 + CO_2 \qquad \text{5-4}$$

$$HCOOH \rightarrow H_2O + CO \qquad \text{5-5}$$
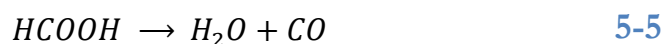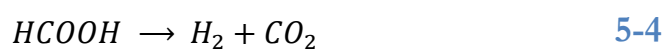
Alternatively, selective CO oxidation within the H_2 gas flow is considered to be an option for gas cleaning prior to insertion into fuel cells. Supported gold catalysts were found to be the best choice for this task, due to their excellent CO oxidation even at low temperatures. [311] Interestingly, supported Au catalysts were also determined to be the most active and selective material for the conversion of formic acid to H_2 and CO_2, outperforming other noble metals. [258] Given the relatively short period in which gold has been considered to be a heterogeneous catalyst, [251] these examples point to a huge potential of applications.

The commercial utilization of Au in catalysis currently lags behind these promising developments in research. Certainly, one of the main causes constitutes the "durability of the catalysts under real conditions" (Graham Hutchings). [257] In contrast, an example of a supported Au catalyst, which not only outperforms other noble metals in activity and selectivity, but also shows unmatched thermal stability under realistic conditions for exhaust gas aftertreatment, is presented.
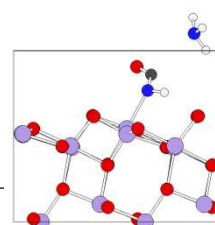
Exhaust gas aftertreatment is a highly demanding field for the application of catalysts, requiring low catalyst light-off temperatures, dealing with highly dynamic feedstock composition, temperature fluctuations and variations in space velocity, while demanding hydrothermal durability for the entire application lifetime. Additionally, poisoning by sulfur can be a very pronounced deactivation mechanism, depending on the combustion fuel used. In automotive and heavy duty transport applications, ultra-low sulfur Diesel has become the standard fuel in recent years, lowering the amount of sulfur in Diesel fuel to 10 ppm or less. Still, the accumulated amount of stored sulfates on catalysts during the entire lifetime can become significant and may impede catalyst performance.

Regeneration of Diesel particulate traps causes severe hydrothermal aging conditions, which may cause massive sintering of downstream catalysts. Temperatures of 500°C can easily be exceeded, while H_2O concentrations are in the range of 5-10%.

Stabilizing supported Au catalysts has been the object of several studies in the last years. As deposited gold is a requirement, the main parameter to influence stability is the support material. Examples include the preparation of a TiO_2 support, which was surface-modified with Al_2O_3 by a surface sol-gel process, and later used as Au support for the deposition-precipitation method. The resulting catalyst showed high activity for CO oxidation even after thermal aging at 500°C for 2.5 h in the presence of 8% O_2. [312] SiO_2 was also proposed as support material. [313] If SiO_2 is partially substituted with TiO_2 either as a thin film [314] or as particles [315] it was shown to be a good support material for Au, which showed advantageous thermal stability at 577°C or 400°C, respectively. More recently, Au deposited on yttrium-doped TiO_2 was presented as a long-term stable CO oxidation

catalyst. It showed only a 7% drop in conversion during a 48 h experiment compared to a 90% loss of Au/TiO_2 (P25). [**316**]

The objective of our investigation was to find a catalyst suitable for the decomposition of guanidinium formate, i.e. hydrolyzing guanidine as well as the commercial TiO_2 hydrolysis catalysts used for urea decomposition, while at the same time decomposing formic acid to harmless reaction products. Another requirement for the catalyst is to withstand the harsh aging conditions that are representative of long-term operation in automotive exhaust gas systems.

5.2. Experimental section

5.2.1. Catalyst preparation

Preparation of the noble-metal doped catalysts is described in detail in section "2.2.4. Preparation of noble metal-doped catalysts". While an incipient wetness impregnation was used for the Pd-doping, a deposition-precipitation procedure was chosen for the Au-doping.

For all experiments, the Pd/TiO_2 and Au/TiO_2 catalysts were coated on ceramic cordierite honeycomb substrates (400 cpsi, Corning) using a commercial inorganic binder (Ludox AS-40, Sigma), according to the procedure described in section "2.2.5 Coating of catalyst supports".

Thermal or hydrothermal catalyst aging was performed by placing the coated honeycomb into an oven, which could be connected to a water vaporizer in order to produce an atmosphere of air containing 10% H_2O. For thermal aging, the catalyst was heated to 750°C for 5 h, tested in the experimental setup and placed again in the oven at 750°C for 5 h. Hydrothermal aging consisted of a first aging procedure at 750°C for 5 h in
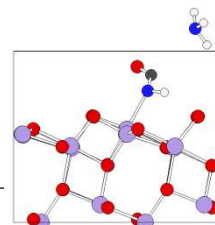
air containing 10% H_2O, testing the catalyst, and then another aging procedure at 800°C for 5 h in air containing 10% H_2O.

SO_2 poisoning was performed by fixing the catalyst into a plug-flow reactor at 400°C and flushing the catalyst with a gas flow containing 10% O_2, 5% H_2O, 200 ppm SO_2 and balance N_2 for 6 h.

5.2.2. Characterization

Catalyst characterization was performed by surface area determination, particle size measurement, powder X-ray diffraction and scanning electron microscopy coupled with energy-dispersive X-ray spectroscopy. Abberation corrected high angle annular dark field scanning transmission electron microscope (HAADF-STEM) images were used to monitor sintering of deposited noble metal particles. The experimental details concerning the characterization techniques can be found in section "2.3 Catalyst characterization techniques".

5.2.3. Catalytic activity measurements

The catalytic decomposition of guanidinium formate was investigated in the dedicated experimental setup for the investigation of liquid reducing agent solutions in the SCR process described in Chapter 3 "Setup for investigations on NH_3-precursor". [260] The carrier gas typically contained N_2, O_2 and H_2O, in which the H_2O was produced by the reaction of dosed H_2 with excess O_2. In the case of O_2-free carrier gas, a 5% excess of H_2 (H_2:O_2 = 2.1 : 1) was used to generate the H_2O for the gas mixture. The liquid reducing agent was sprayed onto the coated catalyst with a set flow rate of 3 mL/h into a heated gas flux of 500 L_N/h. Under ideal conditions, complete decomposition of guanidinium formate leads to a concentration

of 2,661 ppm NH_3 and 1,774 ppm CO_2 in the gas mixture. In the case of 40% ammonium formate aqueous solution (AmFo 40) a concentration of 931 ppm of both NH_3 and CO_2 is obtained while 80% methanamide aqueous solution (Admide®) leads to 2,636 ppm of NH_3 and CO_2.

Product gases were divided – one part was quantified by a multi-component gas analysis method using a ThermoFisher Antaris IGS FTIR spectrometer with 32 scans/spectrum at a resolution of 0.5 cm^{-1}, while the other part was directed to a liquid quench gas absorption setup, in order to collect high molecular compounds and aerosols for sequential high-pressure liquid chromatography (HPLC). Detected components were referenced to the amount of inserted ammonia precursor compounds, as calculated from the concentration and measured gravimetric flow of the solution used, in order to obtain the product yields. The temperature was varied in multiples of 10 K steps in the range of 180-320°C. Stationary conditions at every set temperature were ensured by waiting for at least 30 min. For HPLC analysis, three independent samples of the gas absorption fluid taken during stationary conditions at a set temperature were analyzed, and the mean value plotted. In one measurement, a quadrupole mass spectrometer was added to the analytics in order to quantify evolved H_2. The instrument was an InProcess GAM 400 mass spectrometer, equipped for the measurement of complex gas mixtures.

5.3. Results and discussion

5.3.1. Catalyst characterization

As for the catalyst support, a commercially available material was selected that had been known in literature for several years, only a basic characterization was performed. It was confirmed by XRD that the material
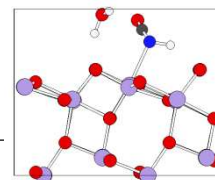
consisted of pure TiO_2 anatase crystalline phases without any detectable signals of rutile. A monodisperse particle size distribution with a D_{50} value of 1.7 μm was found by laser diffraction, which is rather large compared to the usually employed Degussa P-25 which has primary particles smaller than 100 nm. SEM images confirmed the average particle size, suggesting the absence of agglomerates, i.e. the D_{50} value measured by laser diffraction corresponds to the primary particles. The surface area as determined by N_2 physisorption and calculated using the BET theory, was 90 m^2/g. This implied a high corrugation of the particle surface, which was confirmed by the recorded SEM images.

After deposition of Au or Pd on the support, the resulting catalyst powders were characterized by multiple techniques. XRD spectra showed no additional signals to the deposited Au or Pd, which was expected due to the low concentration and the detection limit of nanodispersed noble metals below 5 nm. The particle diameter as determined by laser diffraction remained unchanged, as expected for nanometer-sized clusters deposited on micrometer-sized particles. The BET surface area determined after the deposition of Au or Pd on the TiO_2 support did not seem to be influenced, because no significant change within the measurement accuracy could be determined. Analysis by SEM provided images of the TiO_2 primary particles, but failed to depict Au or Pd clusters on the support. While the highly corrugated support surface was clearly visible, nanodispersed Au or Pd could not be detected, because the high-resolution images were blurred due to the electrostatic charging of the semiconductor TiO_2. Figure 5-1 shows SEM images of the 1.5% Au/TiO_2 catalyst – all other catalysts gave similar images.

With energy dispersive X-ray spectroscopy (EDX) the amount of deposited Au on the catalyst was determined to be roughly 1.3%, corroborating the quantitative deposition of gold with a theoretical loading of 1.5%. The spatial resolution during SEM-EDX spectra acquisition was too low to monitor the exact distribution of Au on the TiO_2 support surface. Instead, only a spatial average of the elemental distribution across an area of approximately 2 μm diameter could be measured.
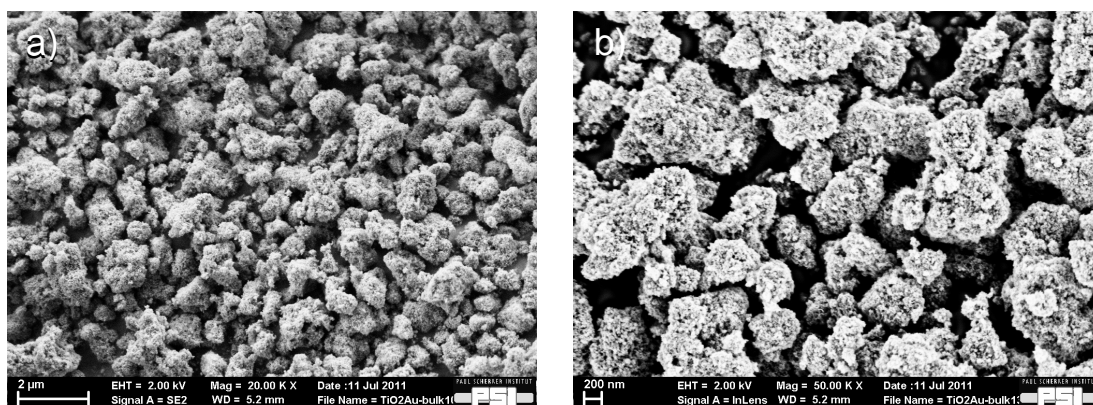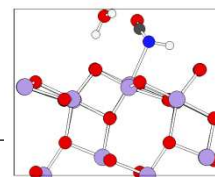

Figure 5-1: SEM images of the 1.5% Au/TiO₂ catalyst at (a) 20,000x magnification and (b) 50,000x magnification.

Energy dispersive X-ray spectroscopy (EDX) could not be applied to the Pd-doped TiO_2 catalyst, as the doping with 0.10% or 0.05% of Pd was below the detection limit of quantitative analysis.

Aberration corrected HAADF-STEM images visualized the distribution of Au on the support surface. In the fresh catalyst, the average particle size of the deposited Au was determined to be 4.1 nm, with a maximum particle size of 12 nm.
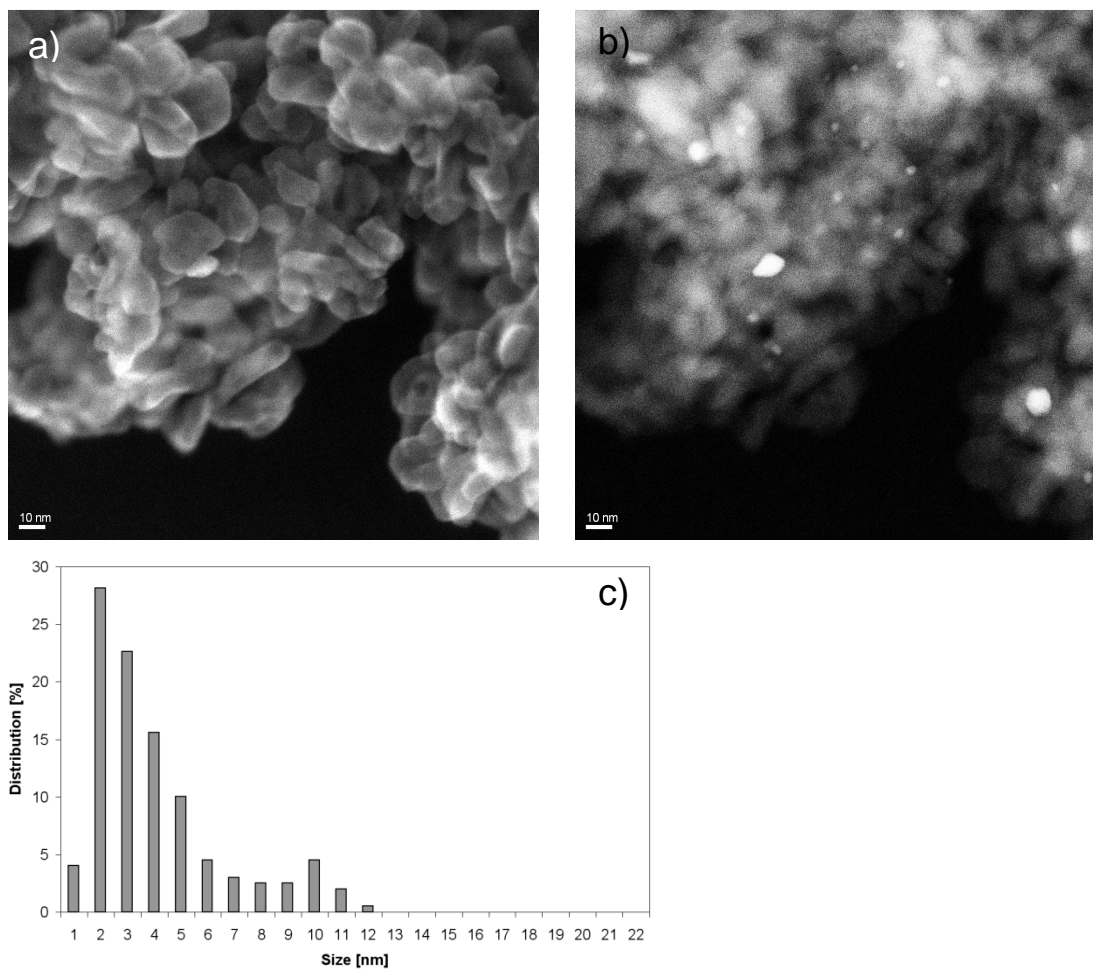
Chapter 5

Figure 5-2: HAADF-STEM images of the freshly prepared Au/TiO₂ catalyst with the corresponding particle size distribution for 250 Au clusters plotted in (c).

After hydrothermal aging of the catalyst, Au particles up to 22 nm could be detected on the catalyst surface, with the average particle size shifted to 11.1 nm.
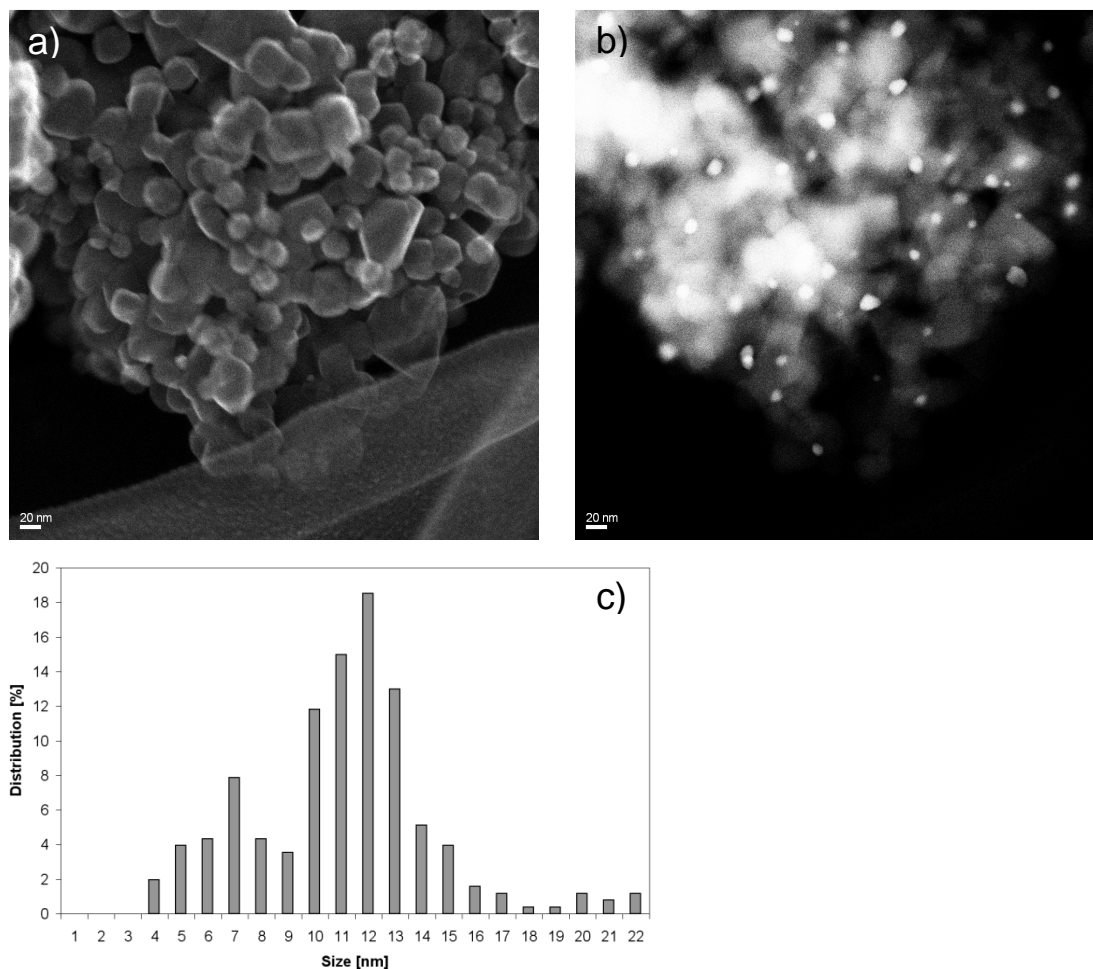
Figure 5-3: HAADF-STEM images of the hydrothermally aged (5 h at 750°C and 5 h at 800°C with 10% H_2O) Au/TiO$_2$ catalyst with the corresponding particle size distribution for 250 Au clusters plotted in (c).

The STEM images therefore indicated Au particle sintering during hydrothermal aging. The extent of sintering and its consequences will be discussed in detail during description of the obtained results of the catalytic testing after the hydrothermal aging procedure.

HAADF-STEM images of the Pd-doped catalyst were not recorded.

5.3.2. Catalytic activity of prepared catalyst

The purpose of the catalysts was to efficiently decompose guanidinium formate or other formate-derived NH_3-precursor compounds. While
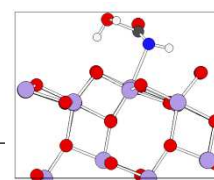
guanidinium is decomposed by the TiO_2, [261] the formate was intended to be decomposed by the deposited noble metal on the TiO_2. Consequently, first experiments were made to compare formic acid decomposition on pure TiO_2 and on Au-doped TiO_2. Figure 5-4 shows the decomposition of 1,000 ppm formic acid sprayed onto TiO_2 coated on ceramic cordierite support, and also the same amount of formic acid dosed on 1.5% Au/TiO_2 under identical conditions. Note the small difference in the space velocities applied in the following experiments is not significant for the reactions, and did not influence the observed yields and product distributions.
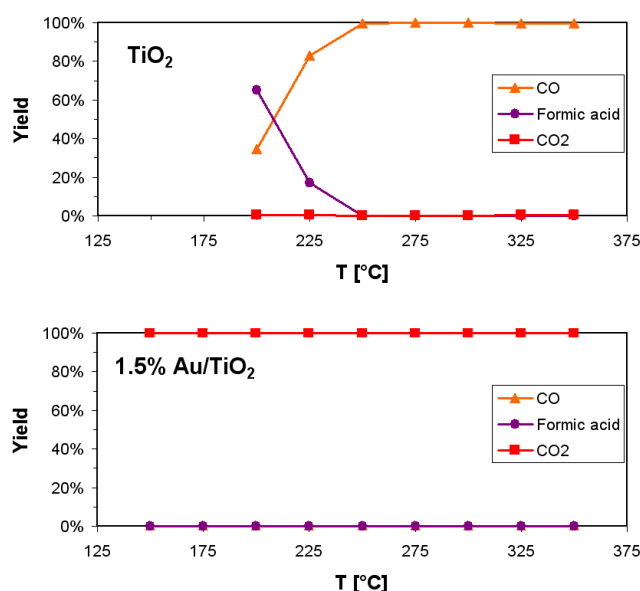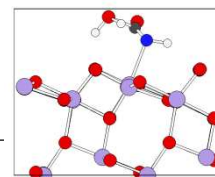

Figure 5-4: Formic acid decomposition on pure TiO_2 and on 1.5% Au/TiO_2 under comparable conditions (1,000 ppm Formic acid, 5% H_2O, 10% O_2, balance N_2, GHSV$_{TiO2}$ = 16,000 h^{-1} / GHSV$_{Au/ TiO2}$ = 14,900h^{-1}).

From 150-350°C, formic acid was efficiently decomposed to CO_2 on the Au/TiO_2 catalyst, while the pure TiO_2 catalyst showed the previously known opposing trends in CO and formic acid concentration, with formic acid being replaced by CO at increased temperatures. [317] As the gas analytics were based on FTIR spectroscopy, the H_2 evolved from formic

acid decomposition on Au/TiO_2, according to reaction 5-4, could not be detected.

Obviously, formic acid decomposition worked well on Au/TiO_2, but it would also work well on many other noble-metal doped TiO_2. However, in the desired application, formic acid should be decomposed, while the catalyst should not oxidize the main product ammonia. In order to see to what degree ammonia oxidation is relevant during formic acid decomposition, an experiment was performed at a constant temperature of 300°C with a constant dosage of 1,000 ppm formic acid, plus varying amounts of ammonia. These results are presented in Figure 5-5.
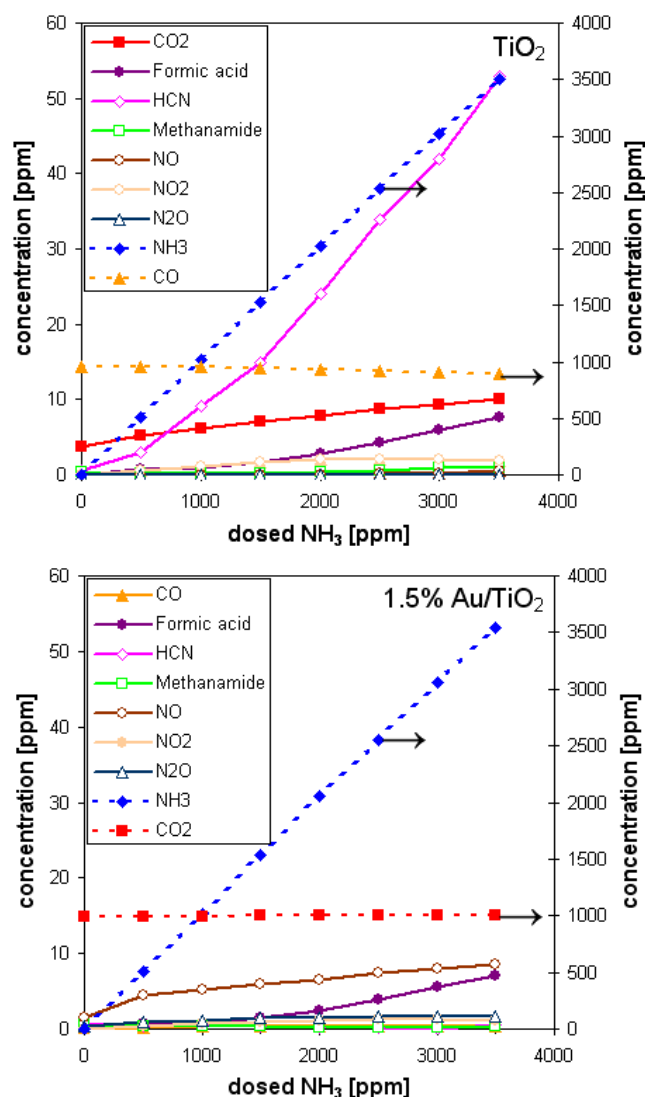
Figure 5-5: Formic acid decomposition with varying dosage of ammonia gas (1,000 ppm formic acid, 5% H_2O, 10% O_2, 0-3,500 ppm NH_3, balance N_2, 300°C, $GHSV_{TiO2}$ = 16,000 h^{-1} / $GHSV_{Au/TiO2}$ = 14,900 h^{-1}).

Figure 5-5 clearly shows that formic acid was decomposed by Au/TiO_2, independent of the concentration of dosed ammonia. The other important result is that dosed NH_3 was not oxidized in any significant amount, i.e. almost all the NH_3 that was fed into the system was detected as NH_3 in the gas phase at the reactor outlet. The possible oxidation products NO, NO_2 and N_2O only increased in negligible amounts compared to pure TiO_2. Note that due to the detection of reaction products by FTIR, the possible

oxidation product N_2 could not be detected. However, in this experiment the N-balance could be closed nonetheless with all remaining compounds.

It should be pointed out that both, pure TiO_2 and Au/TiO_2 showed increasing formic acid emissions with increasing ammonia dosage. However, with pure TiO_2, increasing emissions of HCN were also observed as ammonia dosage was raised. As HCN is formed from ammonia and formic acid via methanamide (which was not found in the product gas) it seems that the Au/TiO_2 catalyst indeed suppresses the formation of HCN by quickly decomposing formic acid as intended before it reacted with NH_3.

As the preliminary experiments concerning formic acid decomposition, or formic acid decomposition during ammonia dosage, showed complete formic acid decomposition on the Au/TiO_2 catalyst, the decomposition of guanidinium formate solution could be examined. For this reason, an aqueous 60% guanidinium formate solution was sprayed on the catalyst-coated monolith positioned in the reactor. For the purpose of comparison, the decomposition of 60% guanidinium formate aqueous solution on pure TiO_2 is shown on in Figure 5-6 (a) as a reference.
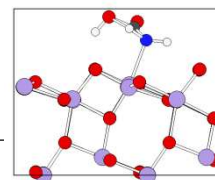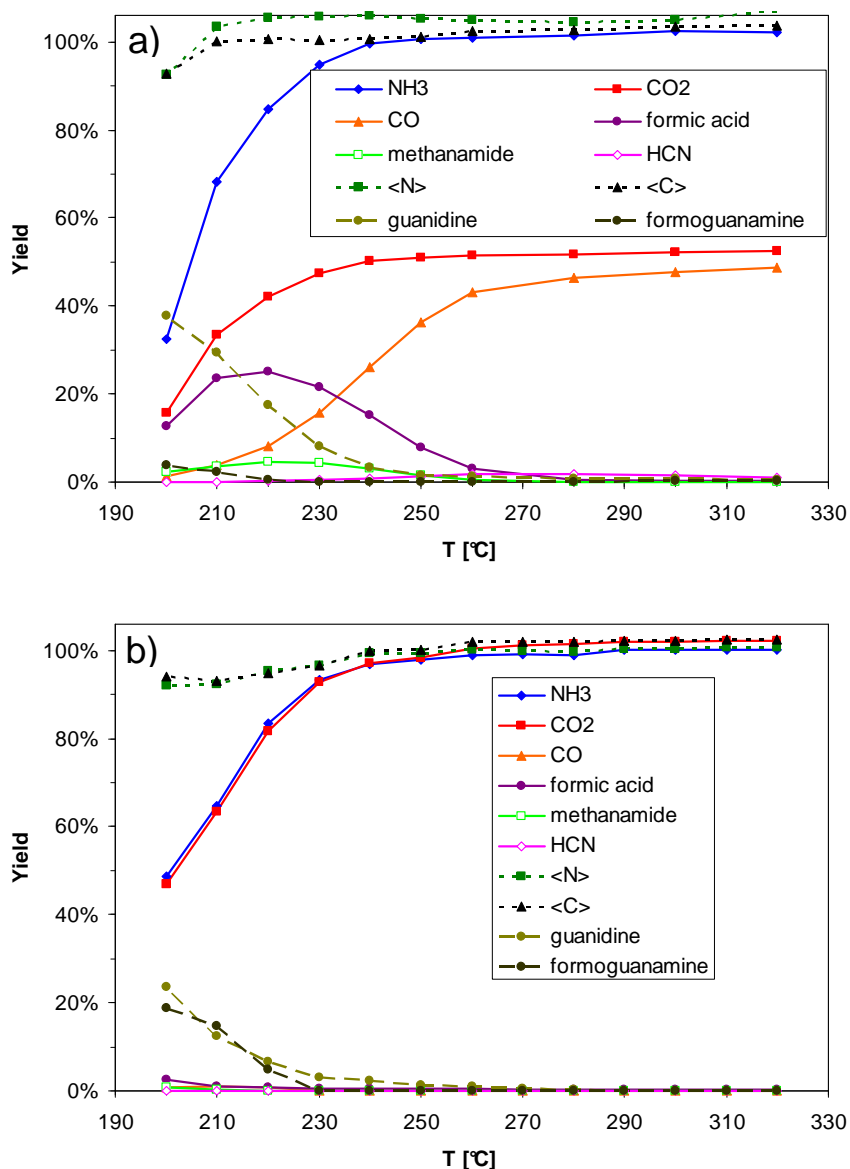
Figure 5-6: Decomposition of 60% guanidinium formate solution on a) pure TiO$_2$ (GHSV = 15,900 h^{-1}) and b) 1.5% Au/TiO$_2$ anatase (GHSV = 16,200 h^{-1}). Feed gas: 5% H$_2$O, 10% O$_2$, balance N$_2$.

The yields are plotted corresponding to the dosed amount of carbon or nitrogen, as no clear differentiation could always be made between carbon atoms derived from guanidinium or formate decomposition. The results, however, can be interpreted straightforwardly in accordance with previous results. [**165**] After initial dissociation of guanidinium formate into
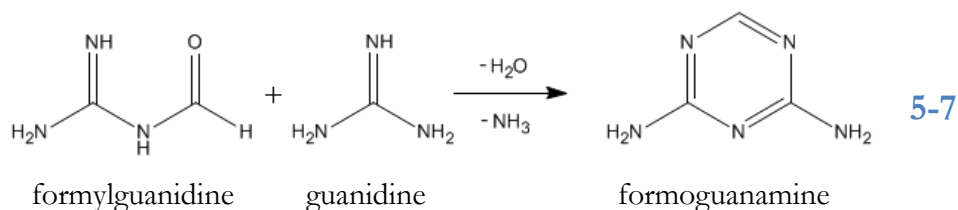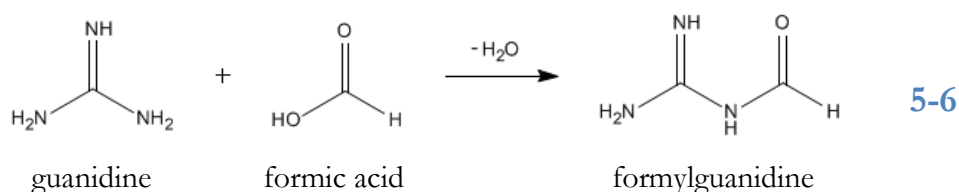
guanidine and formic acid, guanidine is readily decomposed to ammonia and CO_2 at temperatures around 250°C. At, or above, these temperatures, formic acid decomposes mainly to CO, and below these temperatures it can also simply remain in the gas phase. Formic acid partially reacted with the released ammonia to yield methanamide. The emission of methanamide is, therefore, accompanied by the emission of formic acid. Also, after removal of another water molecule, HCN can form from methanamide. The yield of HCN can be as high as 2% of the dosed amount of nitrogen, resulting in concentrations of 50 ppm in our experiments. Methanamide emissions gradually increased with formic acid concentrations in the gas phase. At temperatures below 240°C, formic acid amounted for at least 14% of all carbon emissions, while methanamide accounted for at least 1.4%. At elevated temperatures, the formation of the undesired side products of formic acid, methanamide and HCN declined, and were replaced with CO.

Deposition of Au on the TiO_2 catalyst was supposed to act to quickly decompose formic acid, such that side products like methanamide or HCN would not be able to form. Additionally, CO_2 rather than CO would be preferred as a decomposition product evolving from the dosed carbon. Figure 5-6 (b) shows the decomposition of 60% guanidinium formate aqueous solution on 1.5% Au/TiO_2. In comparison to Figure 5-6 (a), it is evident that the undesired compounds of formic acid, methanamide, HCN and also CO are not emitted above 210°C. The ammonia yields, on the other hand, are not influenced by the presence of Au. Actually, the release of ammonia might even be facilitated by the presence of Au, as suggested by the slightly steeper increase in NH_3 yields. This effect could be due to rapid formic acid decomposition, because formic acid is no longer able to stabilize NH_3 on the catalyst surface. Certainly, at 250°C or above there are
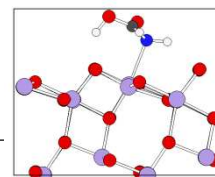
no side products formed from incomplete formic acid decomposition, while the ammonia yield remains above 98%. All the nitrogen is released as ammonia, and all carbon contained in the precursor compound is converted to CO_2, at identical yields. This not only includes the carbon of guanidine, which would also yield CO_2 on pure TiO_2, but also the carbon atom contained in formic acid. It is not yet clear whether formic acid was directly converted to CO_2 and H_2 or whether it was converted to CO and H_2O, followed by a subsequent oxidation of CO, or a water gas shift reaction yielding CO_2. A quadrupole mass spectrometer (MS) was connected to the reactor exit and samples were taken. No H_2 was detected by the MS during the decomposition experiments. As initially formed H_2 might also be oxidized by the catalyst and, not detected, 1,000 ppm of H_2 gas was added to the model exhaust gas. Of the additionally dosed 1,000 ppm, more than 90% could still be detected at the reactor exit by the MS. This indicates that H_2 in the gas phase could still be detected, if it was formed during the reaction. Unless formic acid was decomposed to CO_2 with only an intermediate structure of H_2 on the catalyst surface, which rapidly continued to be oxidized to H_2O, the decomposition pathway 5-4 to yield CO_2 and H_2 could be excluded. Formic acid would then be decomposed to CO and H_2O, with a subsequent oxidation of CO to CO_2. Water gas shift would again be possible, if the formed H_2 was consumed in an intermediate state. Otherwise, gas phase H_2 would at least be detected in traces.

The Au/TiO_2 catalyst actually fulfilled all the requirements concerning formic acid decomposition while not oxidizing NH_3. Thus, the guanidinium formate decomposition was no longer limited by side product formation, but by the temperature needed for decomposition of guanidine.

As can be seen in Figure 5-6 (b), at low temperatures guanidine was found in the gas phase. Along with guanidine, formoguanamine aerosols could also be detected, using the liquid quench gas absorption analysis. Formoguanamine is a condensation product originating from the reaction of formic acid with two molecules of guanidine, according to reaction 5-6 and 5-7. The emission of guanidine aerosols as the only side product above 230°C indicated the Au/TiO$_2$ catalyst was decomposing formic acid effectively – otherwise formoguanamine would be formed as well.

$$\text{guanidine} \quad + \quad \text{formic acid} \quad \xrightarrow{-H_2O} \quad \text{formylguanidine} \qquad \textbf{5-6}$$

$$\text{formylguanidine} \quad + \quad \text{guanidine} \quad \xrightarrow[-NH_3]{-H_2O} \quad \text{formoguanamine} \qquad \textbf{5-7}$$

Guanidinium formate decomposition was also tested on 0.05% Pd/TiO$_2$, with the results shown in Figure 5-7.
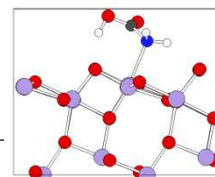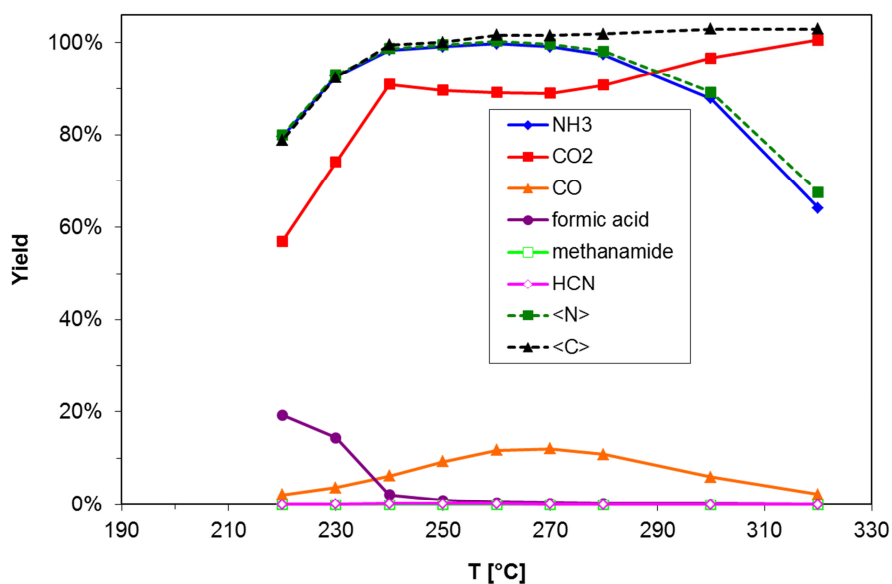
Figure 5-7: Decomposition of 60% guanidinium formate solution on 0.1% Pd/TiO$_2$ anatase (GHSV = 14,800 h^{-1}). Feed gas: 5% H$_2$O, 10% O$_2$, balance N$_2$.

Pd-doping also suppressed the formation of the side products methanamide and HCN during GuFo decomposition. However, not all the formic acid was converted to CO$_2$. Up to 25% of the formic acid was emitted as CO around 270°C. At temperatures below 240°C, formic acid could not even be decomposed to CO anymore. Instead, formic acid was emitted in the gas phase, with 40% of the overall formic acid at 220°C. However, all these minor issues could be accepted, if it was not for the significant NH$_3$ oxidation that starts from 270°C. At 320°C, 36% of the produced NH$_3$ were oxidized to N$_2$, as indicated from the N-balance. Losing such a high percentage of the stored NH$_3$ during NH$_3$-precursor decomposition is considered unacceptable. Reducing the amount of Pd-doping to 0.01% results in a catalyst that did not show NH$_3$-oxidation up to 320°C. However, side product formation increased, yielding up to 1% of HCN emissions from NH$_3$. This either rendered Pd-doping to cause NH$_3$ oxidation or to insufficiently suppress side product formation. Thus, the

experiments using Pd-doped catalysts were of lower relevance for practical applications, compared to those with Au-doped catalysts.

For the Au-doped TiO_2-catalyst, not only GuFo decomposition, but also ammonium formate and methanamide decomposition, were tried.

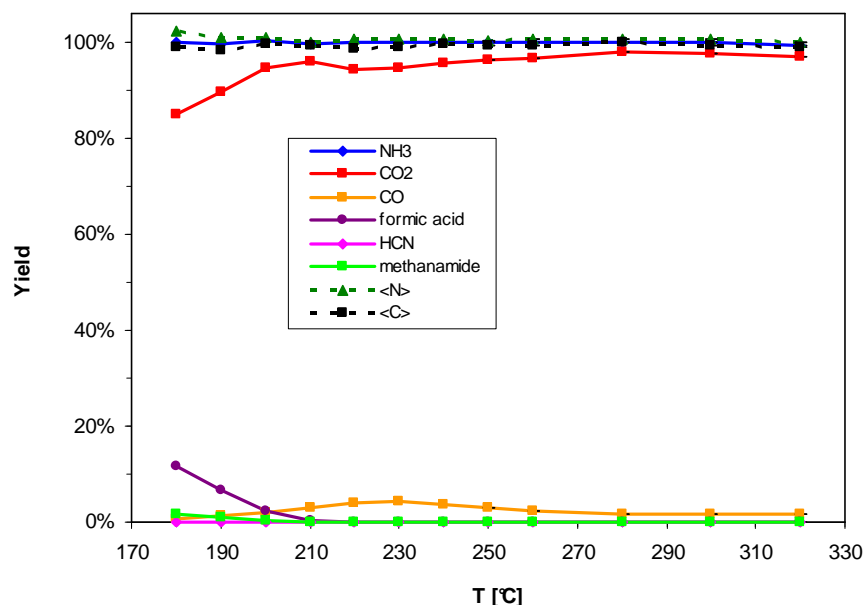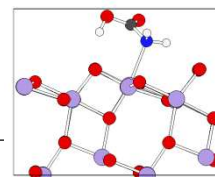The results for 40% ammonium formate solution are shown in Figure 5-8.

Figure 5-8: Decomposition of 40% ammonium formate solution on 1.0% Au/TiO₂ (Gas feed: 5% H₂O, 10% O₂ and 85% N₂. GHSV = 19,900 h⁻¹).

Decomposition of ammonium formate on the Au-doped catalyst caused no side product formation of methanamide or HCN above 200°C. NH_3 and CO_2 were the exclusive decomposition products, apart from a small amount of CO, peaking at 4% of the inserted carbon.

Compared to GuFo decomposition, AmFo decomposition did not require active hydrolysis of a NH_3-precursor for NH_3 generation. Instead, AmFo salt, which dissociated into NH_3 and formic acid, needed to be stopped from re-forming the salt by quickly decomposing the released formic acid. Rapid removal of formic acid was also required to avoid the formation of

toxic methanamide or HCN. As shown in the previous experiments, the Au/TiO_2 could fulfill this task well, without oxidizing NH_3 in significant amounts. In contrast, Figure 5-9 shows the decomposition of AmFo on a Pd-doped catalyst, and its consequent large activity in NH_3-oxidation. Even though side products were avoided in this case as well, the catalyst can not be considered viable for applications, because of the strong NH_3-oxidation.
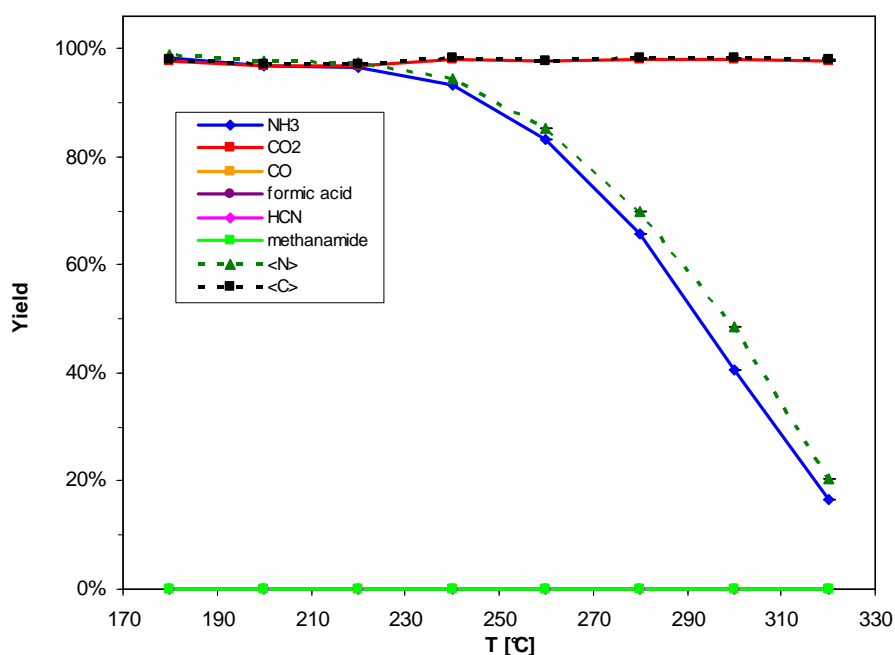

Figure 5-9: Decomposition of 40% ammonium formate solution on 0.1% Pd/TiO₂ (Gas feed: 5% H₂O, 10% O₂ and 85% N₂. GHSV = 14,800 h⁻¹).

Methanamide, as the condensation product of NH_3 and formic acid, was also tested as a NH_3-precursor compound. The decomposition of an 80% methanamide solution on Au/TiO_2 is shown in Figure 5-10.
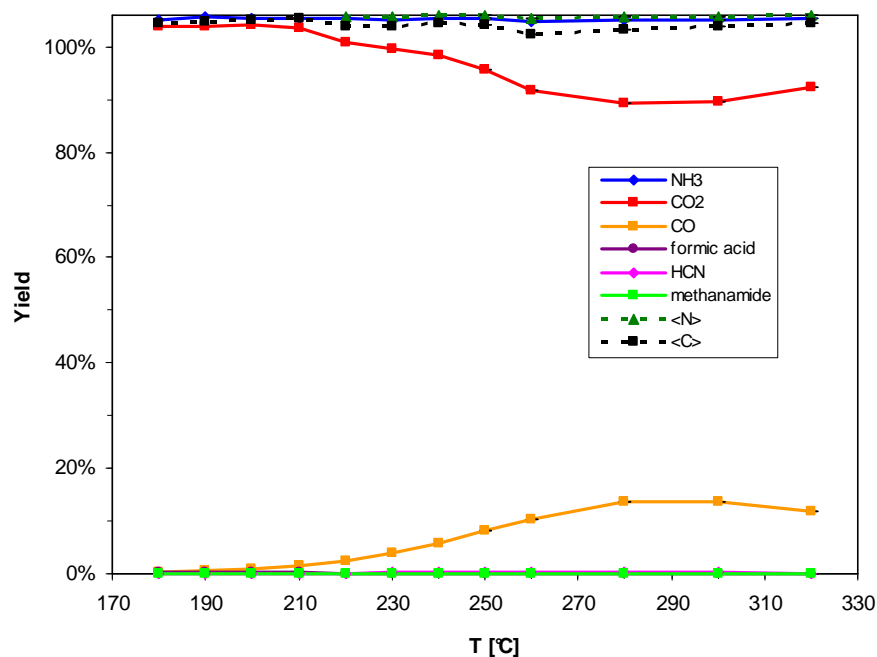
Figure 5-10: Decomposition of 80% methanamide solution on 1.0% Au/TiO₂ (Gas feed: 5% H₂O, 10% O₂ and 85% N₂. GHSV = 19,900 h⁻¹).

The decomposition products above 145°C are exclusively NH_3, CO_2 and a maximum of 14% CO. Only below 145°C could methanamide slip be monitored. This sets a minimum temperature required for complete decomposition to NH_3 which is not even met by low-temperature SCR catalysts for light-off.

Methanamide decomposition was also tried on a Pd-doped catalyst, and the results from the measurement are shown in Figure 5-11.
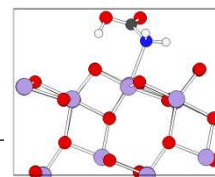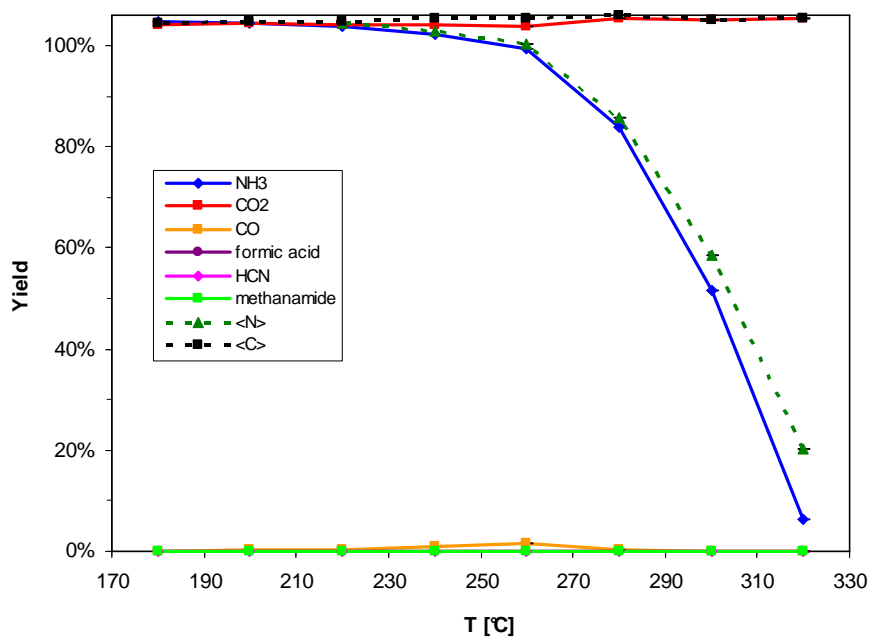
Figure 5-11 Decomposition of 80% methanamide solution on 0.1% Pd/TiO$_2$ (Gas feed: 5% H$_2$O, 10% O$_2$ and 85% N$_2$. GHSV = 14,800 h^{-1}).

The Pd-doping efficiently suppressed methanamide slip or emission of HCN, but again caused a significant conversion of NH$_3$ to N$_2$. Interestingly, traces of CO were only detected at intermediate temperatures around 260°C, below and above this temperature range only CO$_2$ was formed.

In total, the stationary yields with the Au/TiO$_2$ catalyst were virtually 100% at operation temperatures above 250°C (GuFo), 210°C (AmFo) or 145°C (methanamide). However, the question remained whether the conversion and selectivity would also be maintained after hydrothermal aging from representative exhaust gas aftertreatment conditions.

Pd-doping did suppress the formation of the undesired side products of formic acid, methanamide and HCN during decomposition of GuFo, AmFo and methanamide, but it also caused the oxidation of NH$_3$ to N$_2$. As NH$_3$ oxidation is highly undesirable in the case of a hydrolysis catalyst, and

renders Pd-doping irrelevant for commercial use, only few experiments were performed to investigate hydrothermal aging of a Pd-doped catalyst.

5.3.3. Catalytic activity after aging

First, thermal aging in air at 750°C for 5 h, followed by a second aging treatment of 750°C for 5 h was performed. In between the two aging procedures and at the end, catalytic tests were made to compare the change in catalytic activity.

Figure 5-12 shows how CO oxidation activity was affected at catalyst temperature of 150°C or at 250°C. At catalyst temperature of 150°C, virtually all activity was lost after 10 h of aging, and CO was no longer oxidized. At 250°C, the first aging procedure had only a small influence, but after the second aging for 5 h at 750°C the catalytic conversion dropped below 20%.
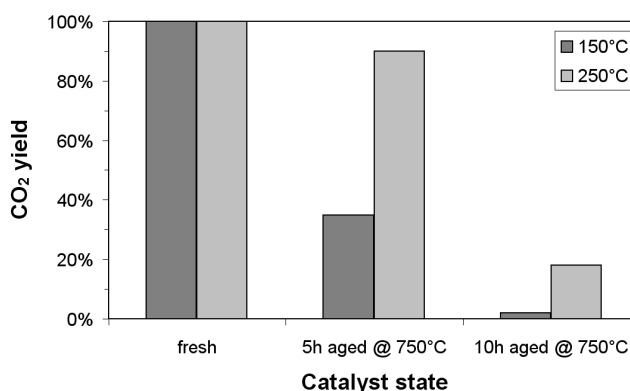
Figure 5-12: CO oxidation activity of 1.5% Au/TiO$_2$ in fresh state, after thermal aging for 5 h at 750°C and after thermal aging for 10 h at 750°C.

These results are in good agreement with the perceived low temperature-stability of supported Au catalysts. Although for application only the catalytic activity at T ≥ 250°C is of immediate interest, the remaining activity for CO oxidation at 250°C is insufficient after 10 h of aging at 750°C.
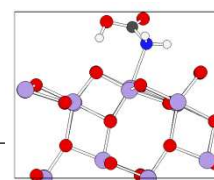
In contrast to the drop in CO oxidation activity after hydrothermal aging, the decomposition of guanidinium formate was not significantly affected by aging (Figure 5-13). On first sight, the fresh Au/TiO$_2$ catalyst, the catalyst aged for 5 h at 750°C and the catalyst aged for 10 h all yielded the identical product distribution. Only very small amounts of NO indicated the presence of Au on the catalyst, but the oxidation products N$_2$O and NO$_2$ were not formed, and NH$_3$ did not decrease, which would have indicated NH$_3$ oxidation to N$_2$. Similar results were obtained at 280°C and 320°C. In all cases, the performance of even the most aged catalyst was far better than that of the pure TiO$_2$ catalyst, and actually almost the same as with the fresh catalyst.
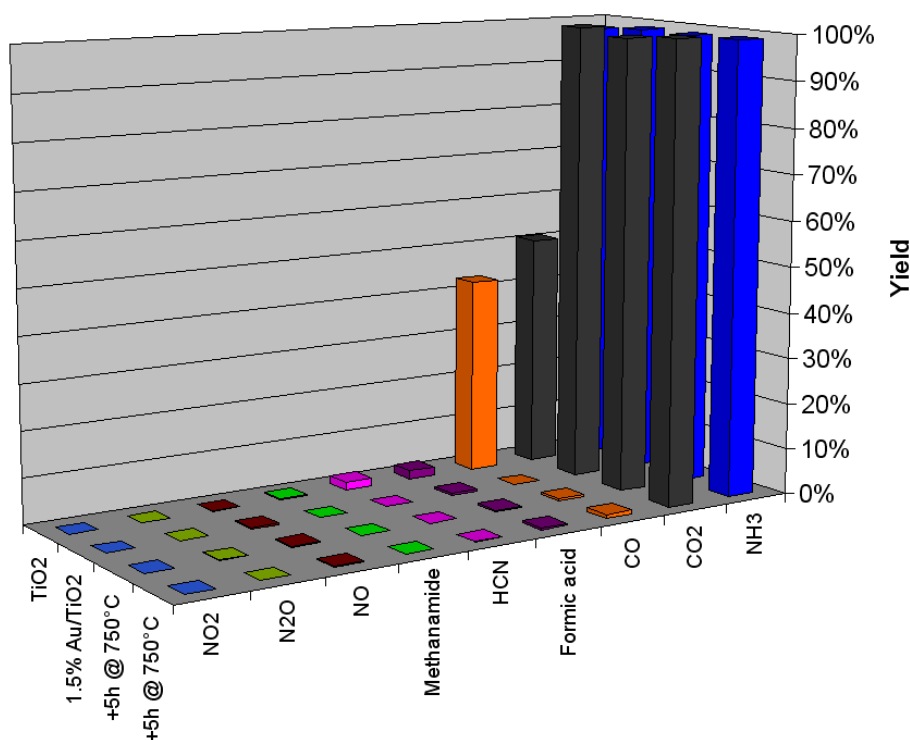

Figure 5-13: Product yields at 260°C from decomposition of 60% guanidinium formate on pure TiO₂, the fresh 1.5% Au/TiO₂ catalyst and the aged catalyst after 5 h of 750°C or after 10 h of 750°C.

In addition to basic thermal aging, a more severe hydrothermal aging process was also applied to the Au/TiO$_2$ catalyst, which better simulates

several years of catalyst operation in real exhaust gas, with its high water vapor content. The exact conditions for hydrothermal aging were 5 h at 750°C with 10% H_2O in air followed by 5 h at 800°C with 10% H_2O in air. The hydrothermal treatment at 800°C is equivalent to the aging a catalyst experiences over its lifetime in today's exhaust gas aftertreatment systems.

In analogy to Figure 5-13, Figure 5-14 shows the product distribution during decomposition of guanidinium formate solution at 250°C on pure TiO_2, fresh 1.5% Au/TiO_2, Au/TiO_2 hydrothermally aged for 5 h at 750°C with 10% H_2O and Au/TiO_2 additionally aged for 5 h at 800°C with 10% H_2O.

Figure 5-14: Product distribution during decomposition of guanidinium formate at 250°C on pure TiO₂, 1.5% Au/TiO₂, Au/TiO₂ aged 5 h at 750°C with 10% H₂O and Au/TiO₂ additionally aged for 5 h at 800°C with 10% H₂O.

At 250°C, the influence of hydrothermal aging on the performance of guanidinium decomposition was hardly noticeable. The NH_3 and CO_2 yields virtually remained at 100% and the traces of CO and formic acid
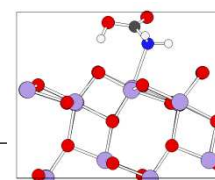
detected with the fresh catalyst did not increase. The same results were obtained up to 320°C, which was the highest temperature in our study. This observation was remarkable, because the CO oxidation activity dropped upon thermal aging alone. Formic acid decomposition to H_2 and CO_2 seemed to be unlikely but decomposition to CO and H_2O with subsequent oxidation of CO to CO_2 plausible. In order to match with the observed decreased oxidation activity for gas phase CO, a reaction mechanism proceeding from adsorbed formic acid via a release of H_2O to adsorbed CO is proposed. The adsorbed CO can be oxidized quantitatively to CO_2 instead of gaseous CO, which would then no longer be oxidized completely by the aged catalyst.

At this point it should be mentioned that the hydrothermal aging procedure did in fact also cause changes to the product gas composition. If the operation temperature was below 250°C, markedly 230°C or below, the aging procedure had a significant effect on the NH_3 and CO_2 yields (Figure 5-15). However, the aging did not affect the yields of formic acid, CO, methanamide or HCN, which indicates a decrease in guanidine decomposition, but constant conversion of formic acid.
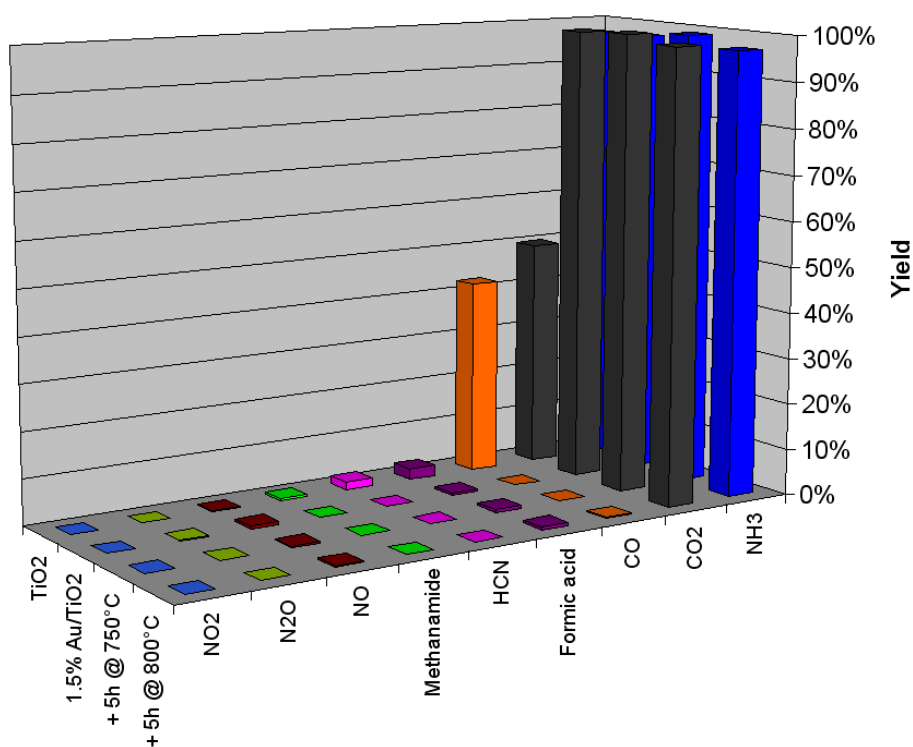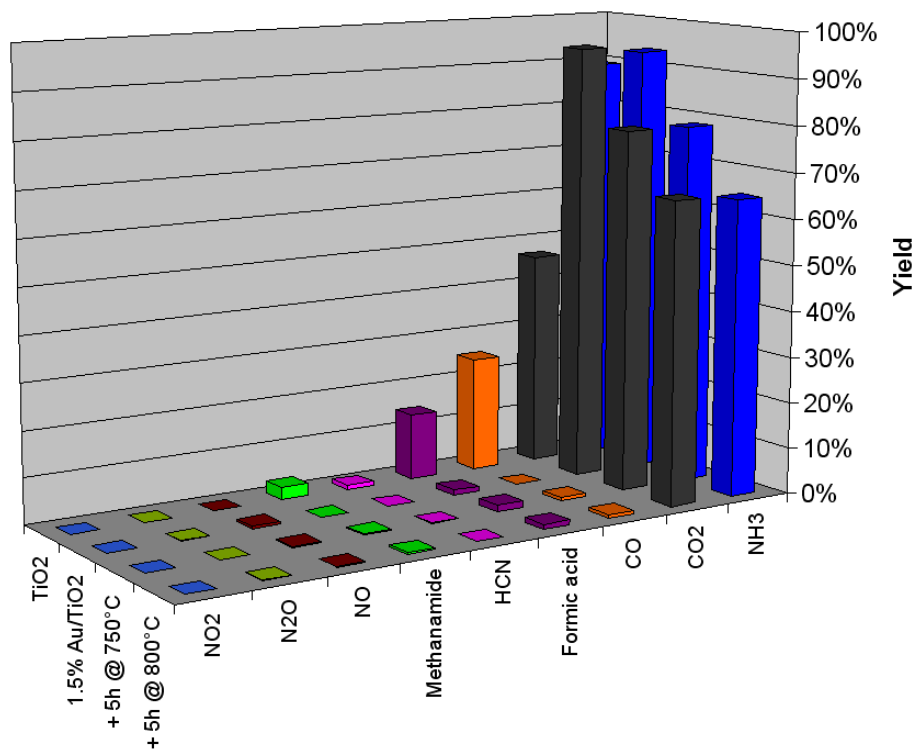
Figure 5-15: Product distribution during decomposition of guanidinium formate at 230°C on pure TiO₂, 1.5% Au/TiO₂, Au/TiO₂ aged 5 h at 750°C with 10% H₂O and Au/TiO₂ additionally aged for 5 h at 800°C with 10% H₂O.

In a dedicated control experiment, pure TiO_2 was subjected to the identical hydrothermal aging conditions as 1.5% Au/TiO_2. In the measurements at 230°C performed after aging, the NH_3 and CO_2 yields decreased to a comparable extent as the yields did for 1.5% Au/TiO_2 (Figure 5-16).
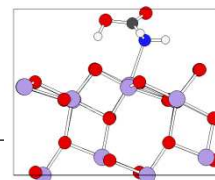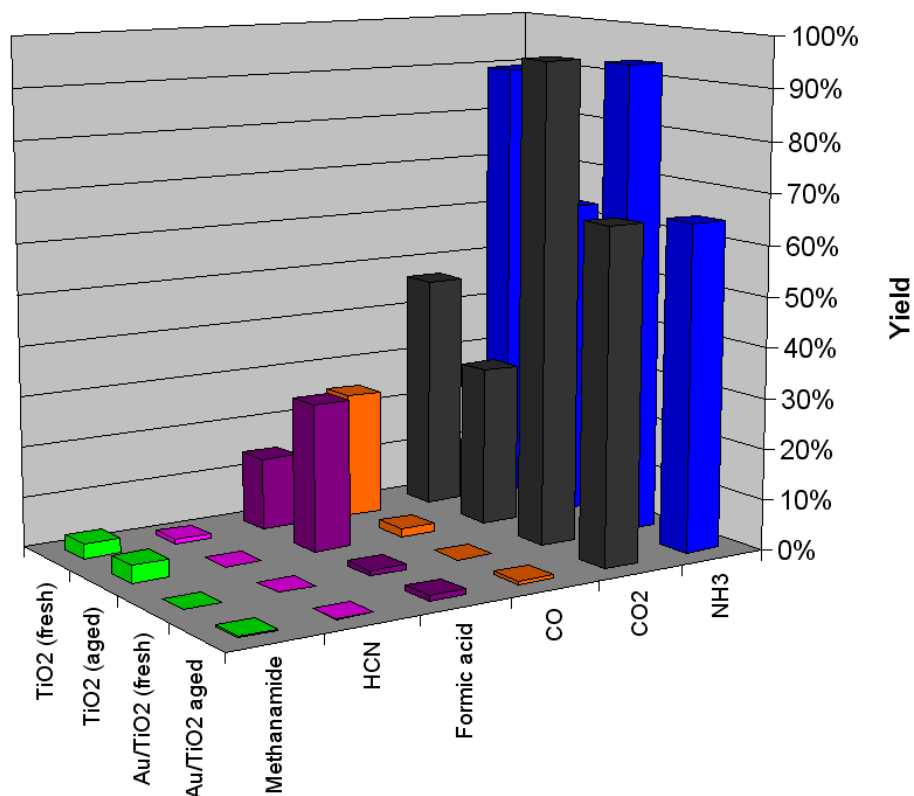
Figure 5-16: Product distribution during decomposition of guanidinium formate at 230°C on pure TiO$_2$ or 1.5% Au/TiO$_2$, either in their fresh state or after hydrothermal aging consisting of 5 h at 750°C and 5 h at 800°C with 10% H$_2$O in each case.

Thus, it could be proved that aging of the TiO$_2$ support rather than aging of the deposited Au caused this observable change. BET surface determination indicated that the active surface area of the support significantly decreased due to the hydrothermal treatment. However, a significant phase transition of the bulk TiO$_2$ from anatase to rutile could not be detected by XRD measurements (Figure 5-17).
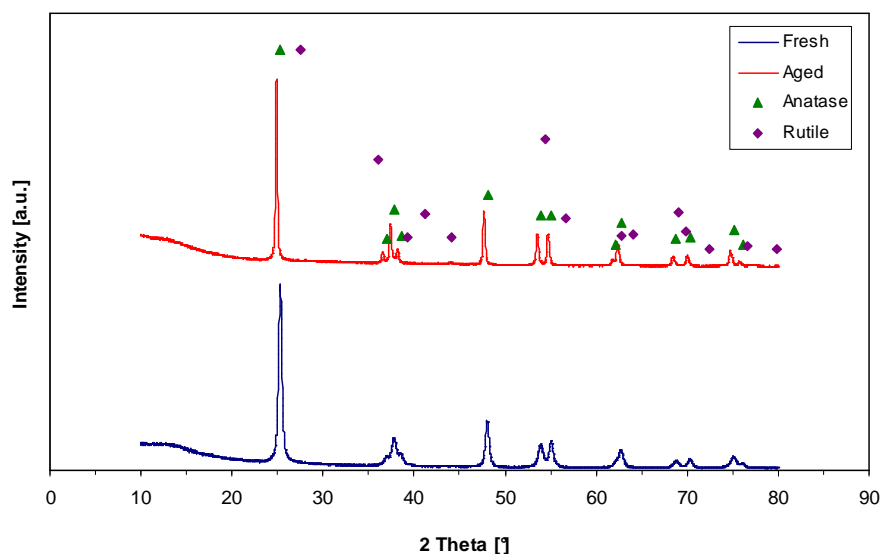
Figure 5-17: XRD spectra showing Au/TiO₂ in its fresh and hydrothermally aged state (5 h at 750°C and 5 h at 800°C with 10% H₂O). The positions of TiO₂ anatase and TiO₂ rutile reflexes are marked in the spectrum.

Only minute evolutions of a few rutile diffraction peaks could be detected, pointing towards a very small proportion of the bulk TiO_2 anatase making a phase transition. However, sintering of the surface, possibly accompanied by the partial formation of rutile at the accessible TiO_2 surface, might have caused the significant decrease in catalytic activity for the conversion of guanidinium formate to NH_3 and CO_2. Either effect is known to cause a decline in catalytic activity for the hydrolysis of guanidinium formate[23] or NH_3-precursor compounds [**280**] in general. From the decrease of NH_3 production and the subtle changes in the XRD, it can be concluded that the hydrothermal durability of the catalyst is limited by the stability of TiO_2 at the applied aging conditions, and it is this that impedes the hydrolysis of guanidine.

Although the TiO_2 support structure is deteriorated, this did not cause a decline in formic acid decomposition on the supported Au. This catalytic result was in apparent contrast to HAADF-STEM images, which clearly
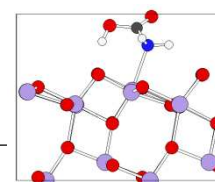
also indicated aging of the supported Au – the mean particle diameter shifted from 4.1 nm prior to the aging to 11.1 nm after the aging procedure. The observed decrease in CO oxidation activity also pointed towards a structural change of the active site. Nonetheless, the decomposition of formic acid during the hydrolysis of guanidinium formate remained sufficiently active to suppress the formation of side products, even after the hydrothermal aging procedure. These results suggest there could be actually two different catalytically active sites involved in CO oxidation and formic acid decomposition.

The size distribution of the supported Au before and after aging indicates that after the aging procedure no more than 10% of all Au particles were smaller than 7 nm, while 85% of all particles fell into this category before the aging. This caused a large shift in the average particle size, although the maximum particle size did not change proportionally. The particles of the fresh catalyst were already rather large due to their calcination at 400°C, when compared to the size of similar published catalysts. [318] Therefore, the growth in particle size had a much smaller effect on the number of interface sites between supported Au and TiO_2, which have been considered in other studies to be possibly the active site in Au catalysis. [319,320] Alternatively, the catalytic reaction could be mainly due to intrinsically more active large Au clusters, which are present in both, the fresh and the aged sample, even though they are usually not considered to be the active species in catalysis due to their lower surface area.

In general, there has been a large dispute about the active site in Au catalysis, focusing on the CO oxidation reaction. Size of the Au clusters, however, is generally accepted to be of crucial importance for the catalytic reaction. [255] While some claim small Au clusters or even individual atoms

only detectable by HAADF-STEM to be the active species, [**256**] others denied the requirement of Au being dispersed into isolated atoms or clusters of just a few atoms. [**321**] Formic acid decomposition to H_2 and CO_2 in He was claimed to require extremely fine-dispersed Au smaller than 1 nm for high catalytic activity, as the approx. 4 nm particles obtained upon thermal aging showed less activity.[9]

As previously mentioned, only a brief experiment was performed to investigate the hydrothermal aging resistance of a Pd-doped catalyst. A 0.05% Pd/TiO_2 catalyst was subjected to 850°C with 10% water vapor for a period of 8 h, then the experiment from Figure 5-7 was repeated.
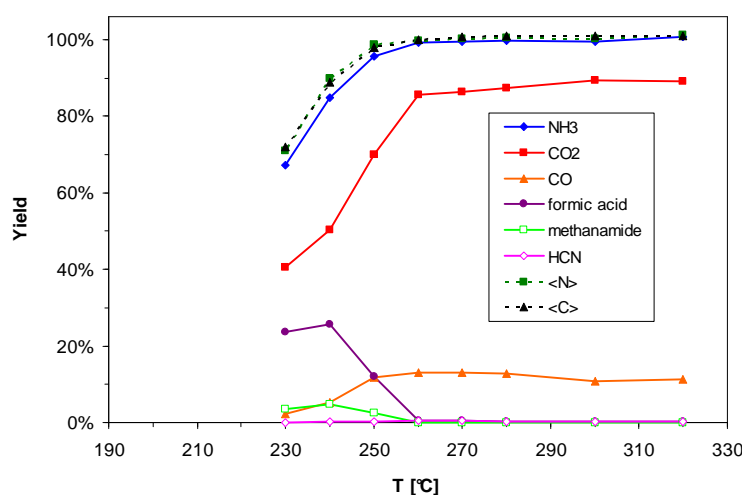
Figure 5-18: Decomposition of 60% guanidinium formate solution on 0.05% Pd/TiO₂ anatase (GHSV = 14,900 h⁻¹) after 8 h of hydrothermal aging at 850°C with 10% H₂O vapor. Feed gas: 5% H₂O, 10% O₂, balance N₂.

Aging of the Pd-doped catalyst had positive and negative aspects. While the NH_3-oxidation at high temperatures was so low that it could not be resolved, emission of formic acid increased and was shifted to higher temperatures. Moreover, concerning the negative aspects, methanamide emissions were also detected after the aging procedure, although they were
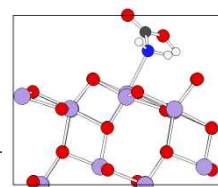
suppressed for the fresh catalyst. CO emission was higher than for the fresh catalyst, and the temperature window for emission was also wider. Concerning the emission of the side products, the aged Pd-doped catalyst was comparable to pure-TiO_2 (anatase), except for the still partially active CO oxidation. Significant sintering of deposited Pd on the catalyst surface was suspected of causing the decrease in activity. The larger Pd particles were then no longer active in the rapid catalytic decomposition of formic acid, as suggested from the emission of gaseous formic acid identical to experiments using pure TiO_2 (anatase).

Besides hydrothermal aging, the poisoning of catalysts by SO_2 poses another important challenge for automotive catalysts. Even though the sulfur content was significantly reduced in recent years, the catalyst had to be exposed to 200 ppm SO_2 at 400°C for 6 h to simulate within a short timespan the sulfur poisoning a catalyst experiences in an automotive exhaust gas system during an operation for approximately 400,000 km with ultra-low sulfur diesel fuel (ULSD). [322] After this treatment, decomposition of 60% guanidinium formate aqueous solution was tested using the aged catalyst. Since the catalyst used for the aging experiment was operated at slightly higher space velocities and was prepared by depositing only 1% instead of 1.5% Au by mass on the TiO_2 support, which increases the catalyst sensitivity towards aging, in Figure 5-19 the performance of this catalyst is compared before and after aging.
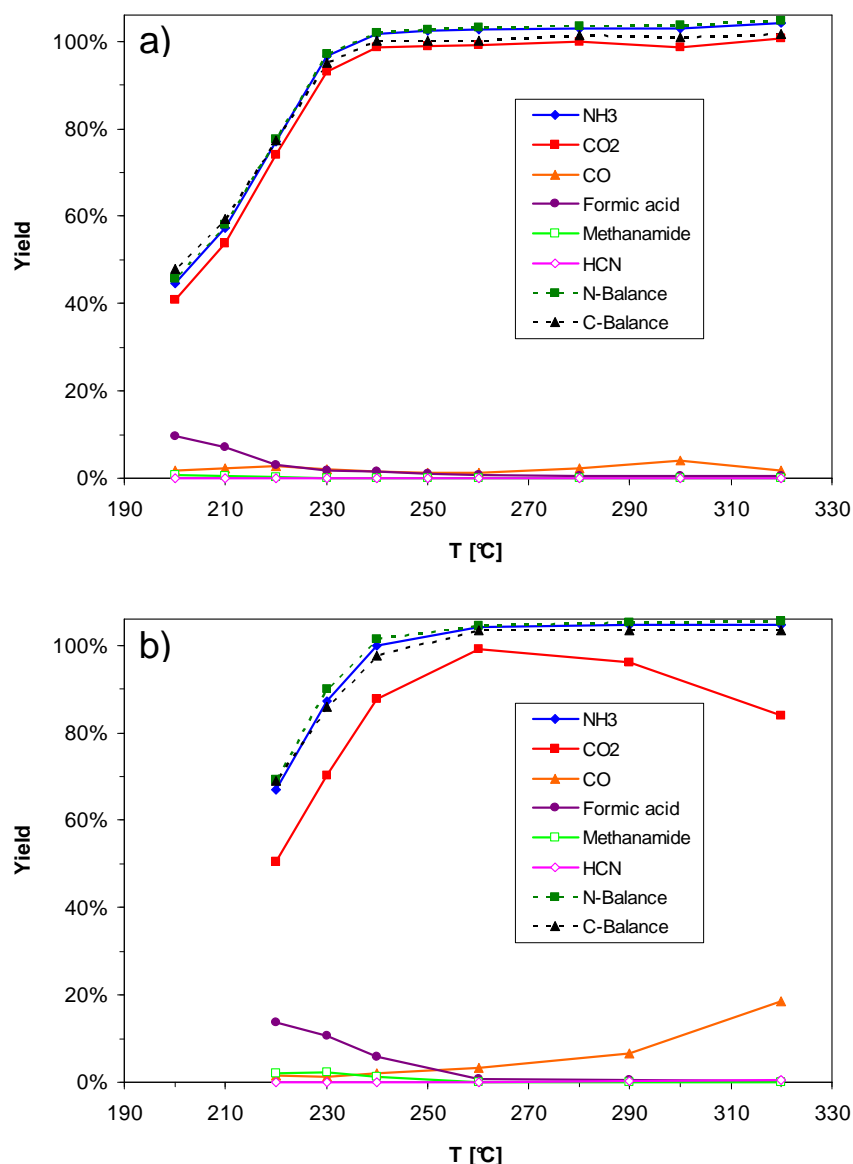
Figure 5-19: GuFo 60 decomposition before (top) and after (bottom) SO$_2$ aging (200 ppm at 400°C for 6 h) on 1.0% Au/TiO$_2$. Gas feed: 5% H$_2$O, 10% O$_2$ and 85% N$_2$. GHSV = 19,900 h^{-1}.

In this experiment, the aging procedure had a significant impact on the reaction products from guanidinium formate decomposition. The NH$_3$ yield was still >99% above 260°C, but started to decrease much earlier, if the temperature was reduced, e.g. only 87% at 230°C compared to 97% before the aging procedure. At the same time, the CO$_2$ yields were
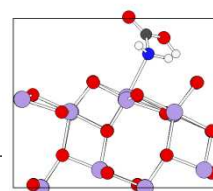
significantly lower than the NH_3 yields, while the overall carbon balance remained similar to the nitrogen balance. This already indicated the presence of significant amounts of carbon-containing side products from formate decomposition. Indeed, at temperatures above 260°C, CO was observed in increasing amounts, thereby replacing CO_2 as decomposition product of formic acid. Decreasing temperatures below 260°C yielded less CO, but led to formic acid emissions. As formic acid yields reached 5%, methanamide showed up at 1% yield. Even lower temperatures led to increasing formic acid emissions, but methanamide emissions halted at a maximum of 2% yield. During the entire experiment, HCN emissions were not detected.

Ammonium formate decomposition was also tested on the SO_2-aged 1.0% Au/TiO_2 catalyst, the results are shown in Figure 5-20.

Figure 5-20: AmFo 40 decomposition on 1.0% Au/TiO_2 after SO_2 aging (200 ppm at 400°C for 6 h). Gas feed: 5% H_2O, 10% O_2 and 85% N_2. GHSV = 19,900 h^{-1}.

While the NH_3-yield was unaffected in the temperature range of 180-320°C, the CO_2 yield changed compared to the fresh catalyst shown in Figure 5-8. With increasing temperature, CO_2 was replaced with CO in the product gas, at 320°C up to 34% CO were found.

The observation of increasing CO yields with higher temperatures points towards a different mechanism than CO oxidation to CO_2, as this reaction would be expected to be accelerated with increasing temperatures. CO formation is considered to derive from formic acid decomposition.

Methanamide decomposition was also tested on the S-poisoned Au-doped catalyst, the results are presented in Figure 5-21.

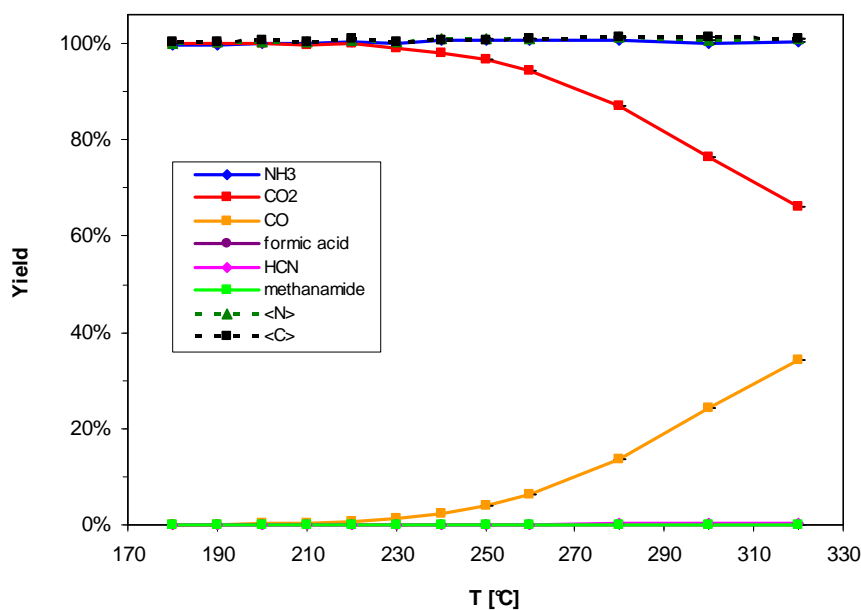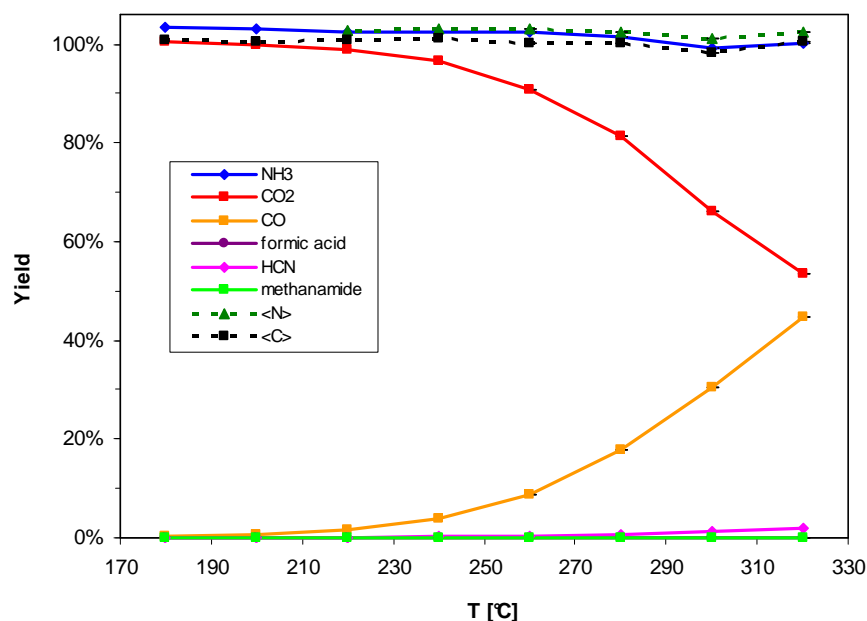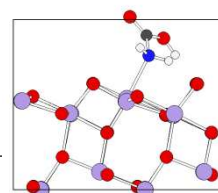**Figure 5-21: 80% Methanamide aqueous solution decomposition on 1.0% Au/TiO₂ after SO₂ aging (200 ppm at 400°C for 6 h). Gas feed: 5% H₂O, 10% O₂ and 85% N₂. GHSV = 19,900 h⁻¹.**

In the temperature range from 180-320°C NH_3-yields were after SO_2 aging still around unity. Similar to the experiment with AmFo, increasing temperatures caused substitution of CO_2 with CO, ramping up to 45% at

320°C. However, with methanamide, also HCN could be measured at high temperatures, amounting for up to 1.8% of the inserted nitrogen at 320%.

The cause for HCN emissions is the dehydration of methanamide at high temperatures, indicating that this process is faster than the hydrolysis of methanamide to yield NH_3 and formic acid and the subsequent formic acid decomposition.

Even though the catalyst showed visible deactivation in the SO_2 aging experiment, in contrast to the hydrothermal testing, the results are still surprisingly good, as methanamide and HCN are still largely suppressed after SO_2 poisoning. Contrary to known supported Au catalysts, the 1.0% Au/TiO_2 catalyst could withstand severe SO_2 poisoning conditions, except that part of the usually produced CO_2 is substituted by CO. As the amount of CO produced during the decomposition of the NH_3-precursor is very low, compared to the amount of CO contained in exhaust gas, the emission of CO as a decomposition product is not very critical concerning automotive emissions.

Another aspect concerning SO_2 poisoning is that during full load engine conditions very hot exhaust gas is produced, which leads to decomposition of the sulfates formed on the catalyst surface, thereby partially regenerating the catalyst's performance. This effect would also occur every time diesel particulate filter (DPF) regeneration is initiated by hot exhaust gas, which is intentionally produced by late fuel injection in the cylinders.

Concerning the processes taking place on the catalyst upon SO_2 poisoning, only qualitative remarks can be made. Since not only NH_3 yields, but also formic acid decomposition was affected by the poisoning procedure, there must have been an interaction between the deposited Au and SO_2. As the exact nature of the active site is unknown, it is not clear whether actually

the amphoteric TiO_2 support starts to form sulfate species on the surface, which interfere with the active sites, or Au is directly poisoned by the presence of SO_2 and, therefore, inhibited for formic acid decomposition. Interface sites, as active centers in the catalysis, could be affected by both routes. The fact that the deactivation did not fully inhibit the catalyst could also indicate a size-selective deactivation route.

Possibly, the deactivation process is not fully transforming all the active sites, because sufficient activity is still maintained to comply with the emission limits.

In order to shed more light onto the reactions involved in guanidinium formate's and the other NH_3-precursor compound's decomposition, and possibly detect intermediate species, experiments without O_2 were performed. The carrier gas entering the reactor consisted solely of nitrogen and water vapor. The resulting product gases plotted in Figure 5-22 are compared with Figure 5-19.
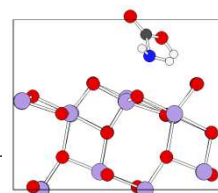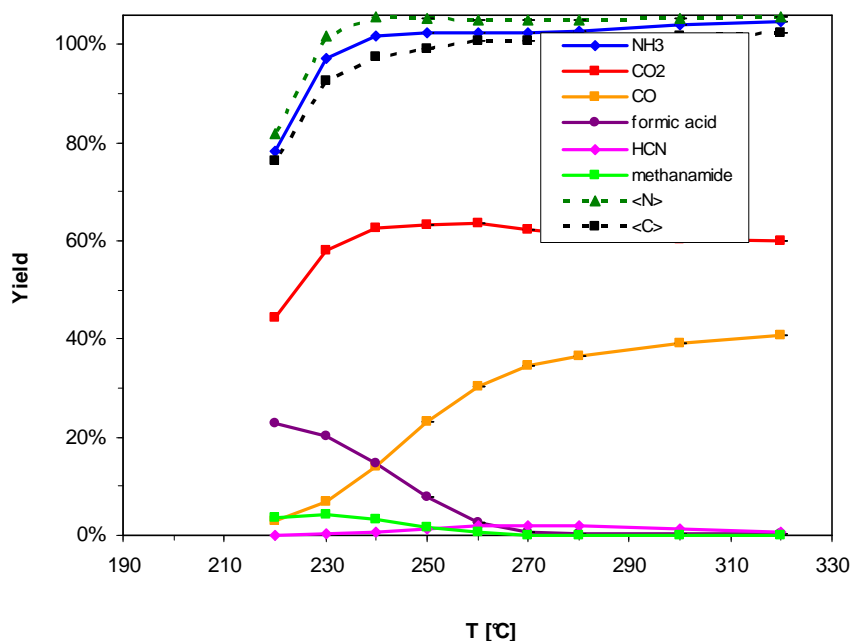
Figure 5-22: Decomposition of 60% guanidinium formate on 1.0% Au/TiO$_2$ under exclusion of O$_2$ (5% H$_2$O, 95% N$_2$, GHSV = 19,900h^{-1}).

While the decomposition of guanidine to ammonia and CO$_2$ seemed to progress similarly to the reaction with O$_2$, the formic acid decomposition was strongly affected. Only a small part of the formate ion was decomposed to CO$_2$, as deduced by subtracting the 50% yield due to guanidinium decomposition. The largest part of the contained carbon was emitted as CO at high temperatures, or as formic acid at low temperatures. At high temperatures, besides the substitution of CO$_2$ by CO, HCN could be detected in significant amounts up to a maximum of 2% yield around 270°C. At lower temperatures, the emission of formic acid caused the formation of methanamide, which increased with rising formic acid concentrations but leveled off at 4% yield.

O$_2$-free decomposition on the Au/TiO$_2$ catalyst was also performed with AmFo and methanamide. The results for AmFo are shown in Figure 5-23.
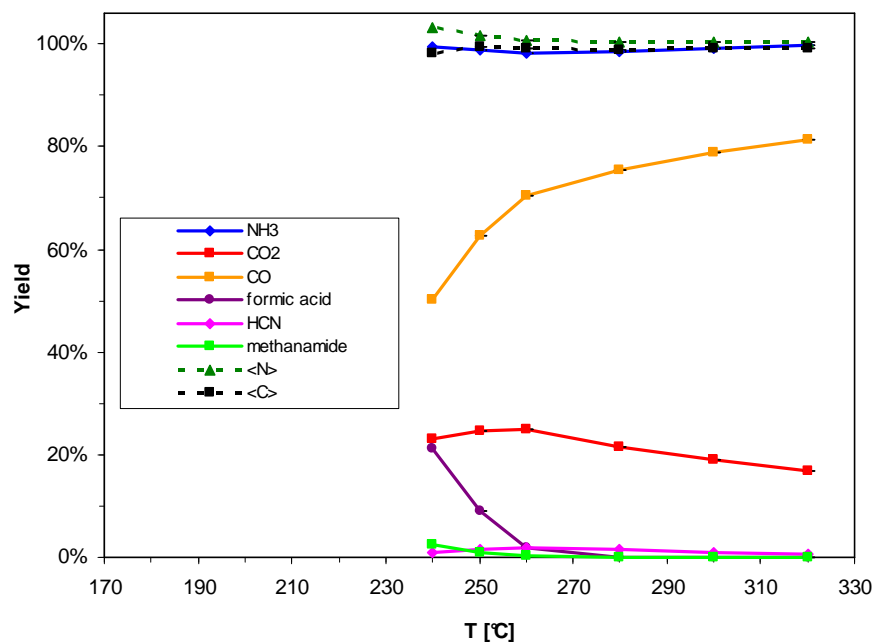
Figure 5-23: Decomposition of 40% ammonium formate solution on 1.0% Au/TiO$_2$ under exclusion of O$_2$ (5% H$_2$O, 95% N$_2$, GHSV = 19,900h^{-1}).

In comparison to Figure 5-8, the removal of O$_2$ during decomposition causes a strong decrease in CO$_2$ yield, which is mostly compensated by an increase of CO. But formic acid is also emitted at higher temperatures, at 250°C, 9% of the dosed formate was released as formic acid. Along with formic acid emissions, also emissions of methanamide were found to increase towards lower temperatures. HCN could also be measured with up to 2% at 260°C.

The decomposition of methanamide without O$_2$ is plotted in Figure 5-24, it should be compared with Figure 5-10 to evaluate the influence of O$_2$-free decomposition.
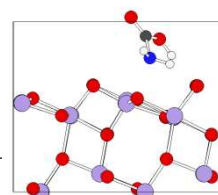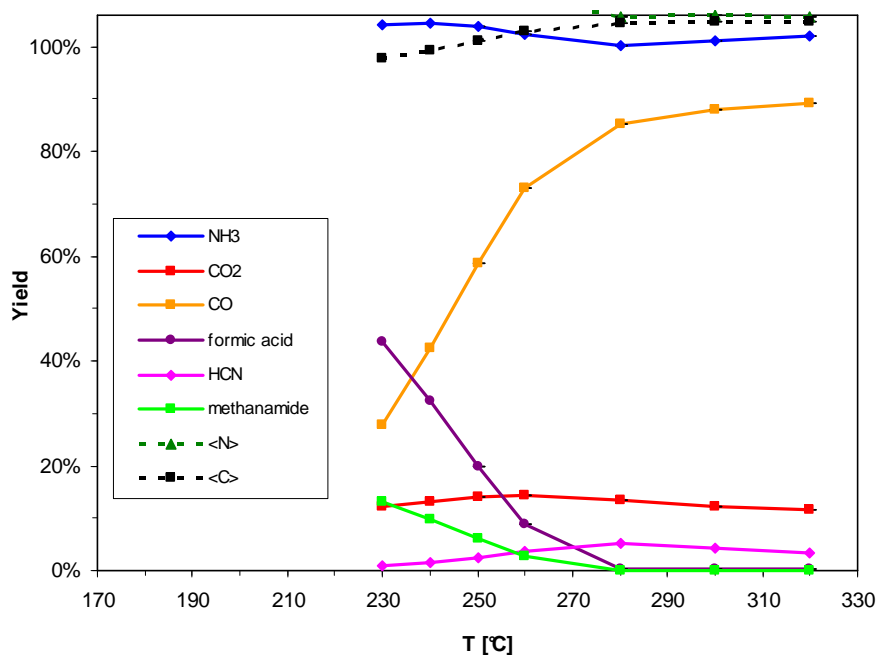
Figure 5-24: Decomposition of 80% methanamide solution on 1.0% Au/TiO$_2$ under exclusion of O$_2$ (5% H$_2$O, 95% N$_2$, GHSV = 19,900h^{-1}).

CO$_2$ yields were largely substituted by CO, but also relatively large amounts of HCN with up to 5% or methanamide-slip could be found in the entire temperature window. Formic acid was found to be the most dominant C-species at 230°C with 44% of the inserted methanamide.

Excluding O$_2$ from the carrier gas during decomposition appears to have the equivalent effect to removing the deposited Au, indicating a crucial role of O$_2$ in the involved reactions of formic acid decomposition. It should be noted, however, that the product distribution shown in previous figures will not be observed in the real-world application, because NO$_x$-containing exhaust gas typically contains significant amounts of O$_2$, e.g. ~10% O$_2$ in case of Diesel engine exhaust.

The water gas shift reaction should not be influenced by the absence of O$_2$. The produced CO should still be converted with H$_2$O to yield CO$_2$.

However, CO_2 evolved from formic acid only to a very small extent. Formic acid decomposition in general does not require O_2, but if the reaction mechanism involves a redox site, intermediately formed H_2 might be finally oxidized to H_2O. If formic acid decomposition was in fact progressing to CO and H_2O, the deposited Au might just have caused the rapid oxidation of CO to CO_2, thereby shifting the equilibrium to the product side leading to quick formic acid decomposition and thus preventing methanamide and HCN emissions.

In order to achieve the hydrolysis of guanidinium formate, TiO_2 is needed to release the NH_3 stored in guanidinium, while the deposition of Au on TiO_2 is required for the decomposition of formate to CO_2 in the presence of O_2.
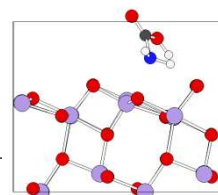
Experiments under O_2-free conditions were also performed with Pd-doped TiO_2. The results for decomposition of GuFo-solution are shown in Figure 5-25.
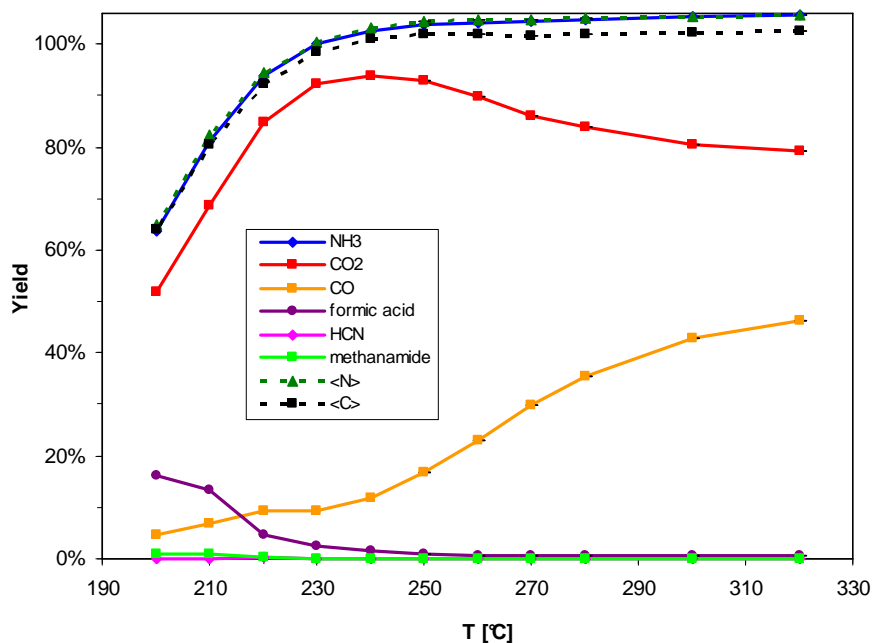

Figure 5-25: Decomposition of 60% guanidinium formate solution on 0.1% Pd/TiO₂ under exclusion of O₂ (5% H₂O, 95% N₂, GHSV = 14,800h⁻¹).

In contrast to Figure 5-7, there was no NH_3-oxidation detectable due to the removed O_2. Moreover, formic acid emissions were reduced, while HCN and methanamide were completely suppressed above 200°C. Besides these positive effects, the CO_2 yields also did not decrease as it is the case for the Au-doped catalysts under O_2-free conditions. CO_2 yields of >90% were not even achieved under presence of O_2 during decomposition on the same catalyst.

Figure 5-26 shows the decomposition of AmFo under O_2-free conditions on the 0.1% Pd-doped catalyst.
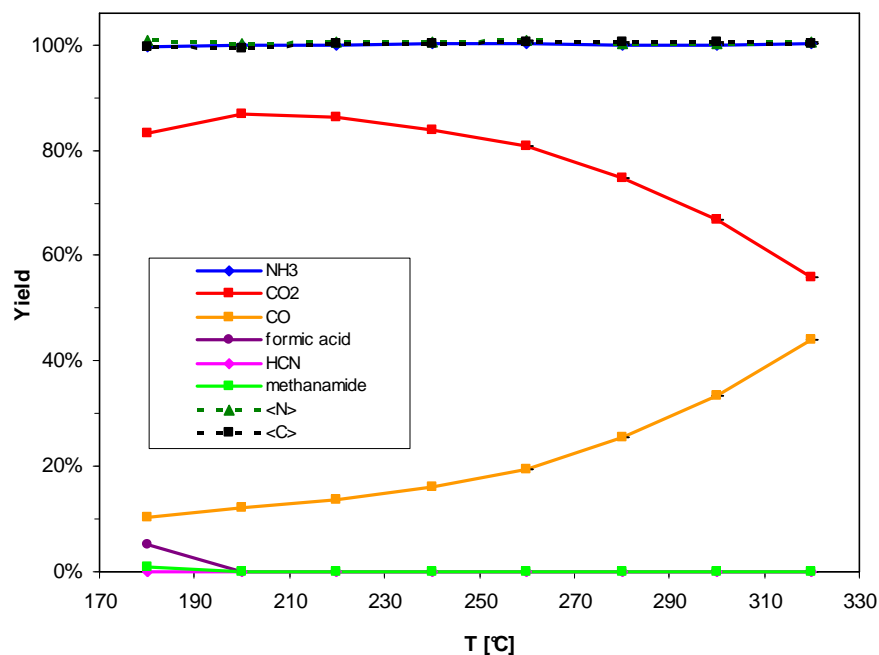
Figure 5-26: Decomposition of 40% ammonium formate solution on 0.1% Pd/TiO$_2$ under exclusion of O$_2$ (5% H$_2$O, 95% N$_2$, GHSV = 14,800h^{-1}).

The experiment is a variation of the one shown in Figure 5-9, in comparison, the absence of NH$_3$-oxidation is most prominent besides the partial substitution of CO$_2$ with CO. No HCN or methanamide are detected, formic acid is only present at 180°C with 5% of the overall yield. Figure 5-27 shows the decomposition of methanamide solution on the previously used Pd-doped catalyst under O$_2$-free conditions.
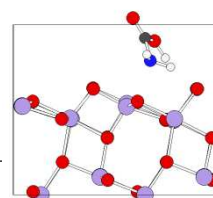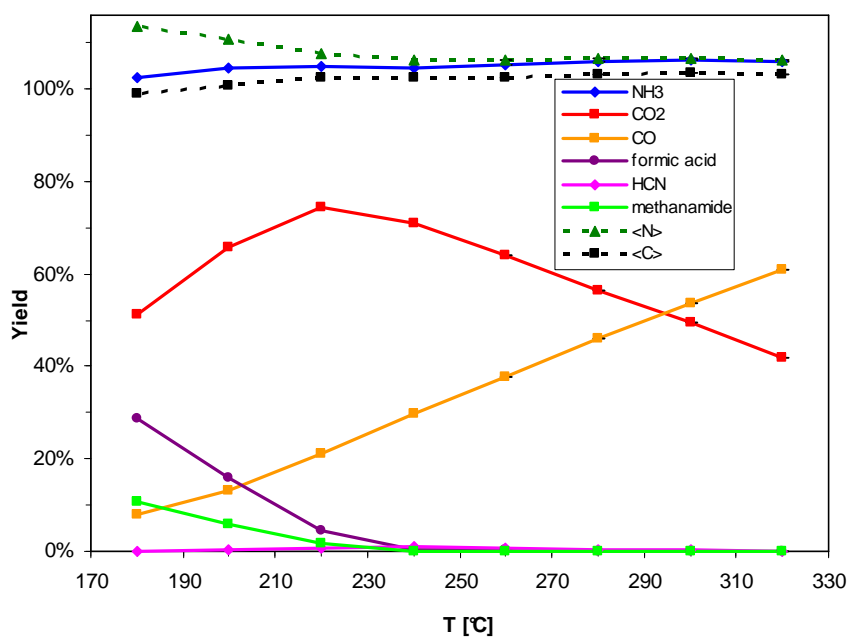
Figure 5-27: Decomposition of 80% methanamide solution on 0.1% Pd/TiO$_2$ under exclusion of O$_2$ (5% H$_2$O, 95% N$_2$, GHSV = 14,800h^{-1}).

Compared to Figure 5-11, again the absence of NH$_3$-oxidation is observed, but instead of solely obtaining CO$_2$ as a decomposition product, a mixture of CO$_2$, CO, formic acid and methanamide is obtained. In order to investigate whether the amount of deposited Pd on the catalyst influences the composition of the product gas, an experiment with a 1.0% Pd catalyst was performed (see Figure 5-28).
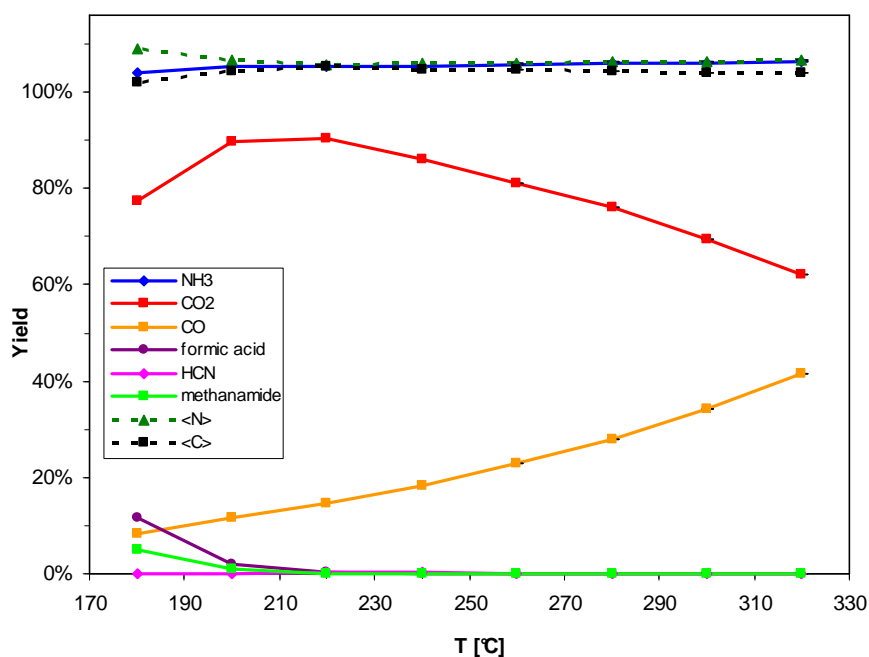
Figure 5-28: Decomposition of 80% methanamide solution on 1.0% Pd/TiO₂ under exclusion of O₂ (5% H₂O, 95% N₂, GHSV = 14,700h⁻¹).

Indeed, the increased amount of Pd causes an advantageous distribution of reaction products: Methanamide and formic acid are not detectable above 200°C, the remaining C-species were exclusively CO and CO_2. The ratio of CO_2 increased significantly, though at 320°C still 42% of CO is present.

O_2-free conditions during NH_3-precursor compounds decomposition on Pd-doped TiO_2 are found to be by far not as detrimental as the removal of O_2 is to Au-doped TiO_2. In contrast to any decrease, the exclusion of O_2 led to improved decomposition in the case of AmFo and GuFo.

As the formic acid decomposition or water gas shift reactions are considered to be independent from the removal of O_2, only the CO oxidation would be affected. Indeed, increased amounts of CO are determined in all O_2-free experiments. However, the reduced emission of formic acid in the case of GuFo and AmFo decomposition must be
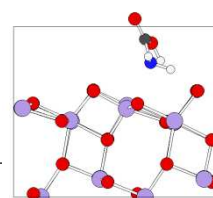
attributed to an increased formic acid decomposition reaction. Formic acid decomposition either partially proceeds to H_2 and CO_2, or the water gas reaction is very efficient under the experimental conditions, as the CO_2 formation cannot be attributed to other reactions under O_2-free conditions. However, the good decomposition of NH_3-precursor compounds on Pd-doped TiO_2 under O_2-free conditions is of no practical relevance, as real Diesel exhaust gas always contains O_2 in significant amounts.

5.4. Conclusion

Au/TiO_2 was determined to be an excellent catalyst for the decomposition of guanidinium formate and related NH_3-precursor compounds. The combination of TiO_2, which catalyzed the hydrolysis of guanidinium, and the deposited Au, which rapidly decomposed formate to CO_2, yielded a suitable product gas mixture for SCR applications consisting solely of NH_3 and CO_2. The introduction of Au to the hydrolysis catalyst did not cause oxidation of the desired reaction product NH_3. While the decomposition of guanidinium required water as a reactant, formate decomposition needed the presence of O_2.

It was shown that high surface area TiO_2 anatase of large grain size with high surface roughness was a suitable support for the deposition of nanodispersed Au. Even though the Au/TiO_2 catalyst was sintered above the Tammann temperature of Au, the Au cluster size growth was limited to approximately 20 nm. The observed catalytic activity of Au for the decomposition of formic acid remained unaffected by the hydrothermal treatment, indicating the active site was not heavily influenced by the aging procedure. This could be explained by the already rather large particles prior to the aging, which contained a comparable number of interface sites

like the large particles after sintering, or by the catalytic activity due to large Au clusters, which were present in both, the fresh and the aged sample.

SO_2 poisoning had a significant effect on catalytic activity, though it was not able to fully impair the catalyst's activity for formate decomposition. In the intended temperature operation range the SO_2 poisoning only caused a partial substitution of the reaction product CO_2 by CO.

Pd-doped TiO_2 also produced methanamide- and HCN-free NH_3-precursor decomposition gas mixtures. However, the desired NH_3 was oxidized at elevated temperatures, rendering the catalyst unsuitable for commercial applications. Under O_2-free conditions, NH_3 oxidation could be avoided, and formic acid decomposition was even improved.

In conclusion, the presented Au/TiO_2 catalyst proved to be highly active while showing unique selectivity for formate decomposition without NH_3 oxidation. The high activity was even maintained after severe aging conditions, which were comparable to long-term operation of a catalyst in exhaust gas aftertreatment applications. Therefore, the presented catalyst was transferred to our project partners and was tested in a prototype exhaust gas aftertreatment system of a Diesel engine.

The Pd/TiO_2 catalyst remained an interesting option for NH_3-precursor compound decomposition under O_2-free conditions, such as the ones applied in Chapter 6: "High-pressure liquid-phase decomposition ".
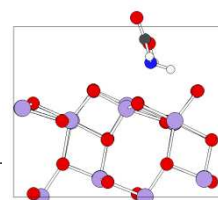
6. High-pressure liquid-phase decomposition

6.1. Introduction

Selective catalytic reduction (SCR) of NO_x with ammonia (NH_3) is a widespread technique for the elimination of harmful NO_x emissions from lean combustion sources. [91] In mobile applications the required NH_3 must be stored and released from NH_3-precursor compounds due to safety regulations. Reliable release of the NH_3 from the precursor compounds without the formation of harmful or undesired side products is becoming increasingly difficult as the thermal energy contained in the exhaust gas is constantly reduced.

Hydrolysis of the precursor in an external device operating independently of the exhaust gas temperature could provide gaseous NH_3 even at exhaust gas temperatures significantly lower than those required for the reliable evaporation of aqueous urea solution sprayed into the main exhaust duct. [85] Also, solutions of alternative NH_3-precursor compounds would become an option to produce gaseous NH_3. [165]

In this chapter, results on the generation of gaseous NH_3 from aqueous urea solution or aqueous methanamide solution by the catalytic decomposition in the liquid phase under elevated pressure and temperature are presented.

Urea decomposition in the liquid phase under elevated pressure has previously been considered for the treatment of wastewater. [323]

6.2. Experimental

The experimental setup is described in section "2.1.4 High-pressure reactor", the catalytic materials used in the reactor are listed in Table 6-1.
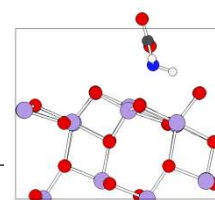
As NH_3-precursor solutions either 32.5% urea aqueous solution or 40% methanamide aqueous solution were used.

Table 6-1: List of catalytic materials inserted into the high-pressure reactor.

Material	Producer	Shape	Size	Amount	BET surface
TiO_2 (anatase)	Porzellanfabrik Frauenthal	crushed monolith	240-270 µm	9.51 g	70 m^2/g
ZrO_2	unknown	cylindrical pellets	2.9 · 3.2 mm	16.42 g	33 m^2/g
γ-Al_2O_3	Zeochem AG Uetikon	powder	0.8-1.0 mm	7.57 g	243 m^2/g
1.5% Au/TiO_2	in-house (doping at PSI)	400 cpsi monolith	7.5 · 125 mm	3.87 g	100 m^2/g

Au/TiO_2 was prepared by the deposition-precipitation procedure described in section "2.2.4 Preparation of noble metal-doped catalysts" using a cut-out TiO_2 monolith from a sample provided by Porzellanfabrik Frauenthal GmbH, which was loaded with 1.5% of gold relative to the TiO_2 mass and fitted into the reactor tube. The other catalysts, which were used for the decomposition of urea solution, were filled into the reactor without prior processing.

6.3. Results

The amount of NH_3 from decomposition and the amount of emitted NH_3-precursor compounds during the experiments are plotted in Figure 6-1. Both, decomposition of urea solution on catalysts or in the empty reactor and the decomposition of methanamide solution on Au/TiO_2 are shown.
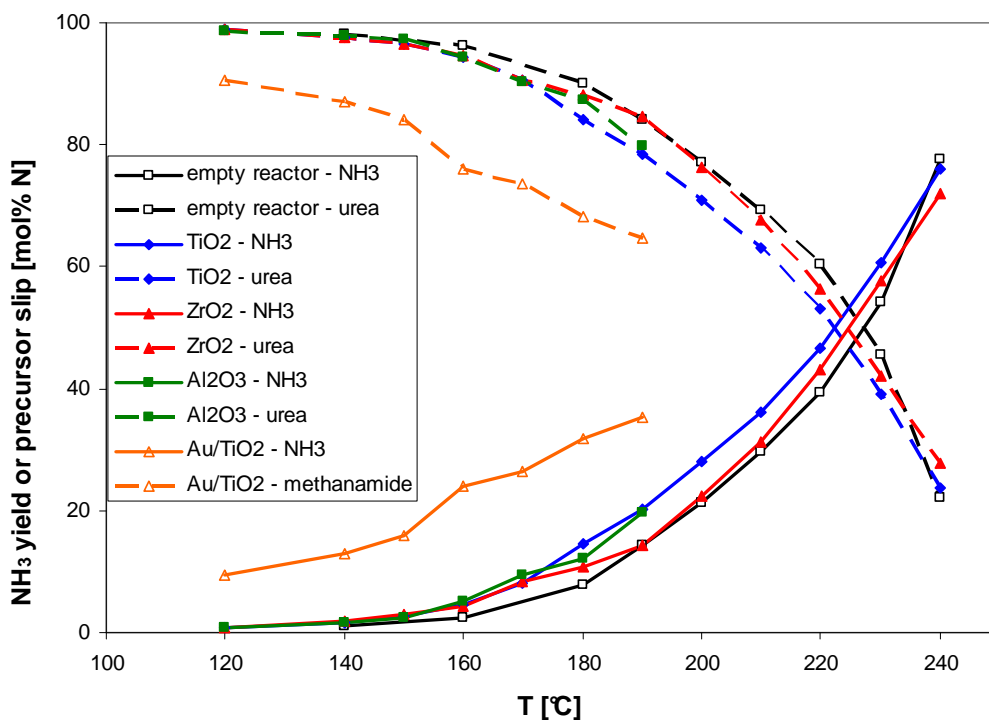
Figure 6-1: NH₃-yields and precursor slip during decomposition of urea or methanamide solution under pressure.

The amount of unconverted NH_3-precursor and yielded NH_3 evolve in opposite directions and add up to around 100%, indicating only a small amount of side product formation. Figure 6-2 shows all additionally detected compounds containing nitrogen, i.e. any side products reducing the yield of NH_3 from conversion of the NH_3-precursors. In case of methanamide solution no products containing nitrogen besides NH_3 or methanamide could be found. During decomposition of methanamide solution at 150°C 80% H_2, 20% CO_2 and 0.1% CO could be detected in the gas-phase. NH_3 could also be measured in trace amounts of approximately 60 ppm in the gas phase, indicating an efficient absorption of NH_3 in water. The obtained H_2 suggests decomposition of the intermediate formic acid to H_2 and CO_2 rather than H_2O and CO. [**324**]
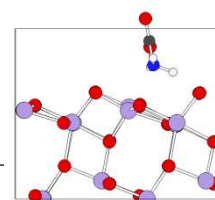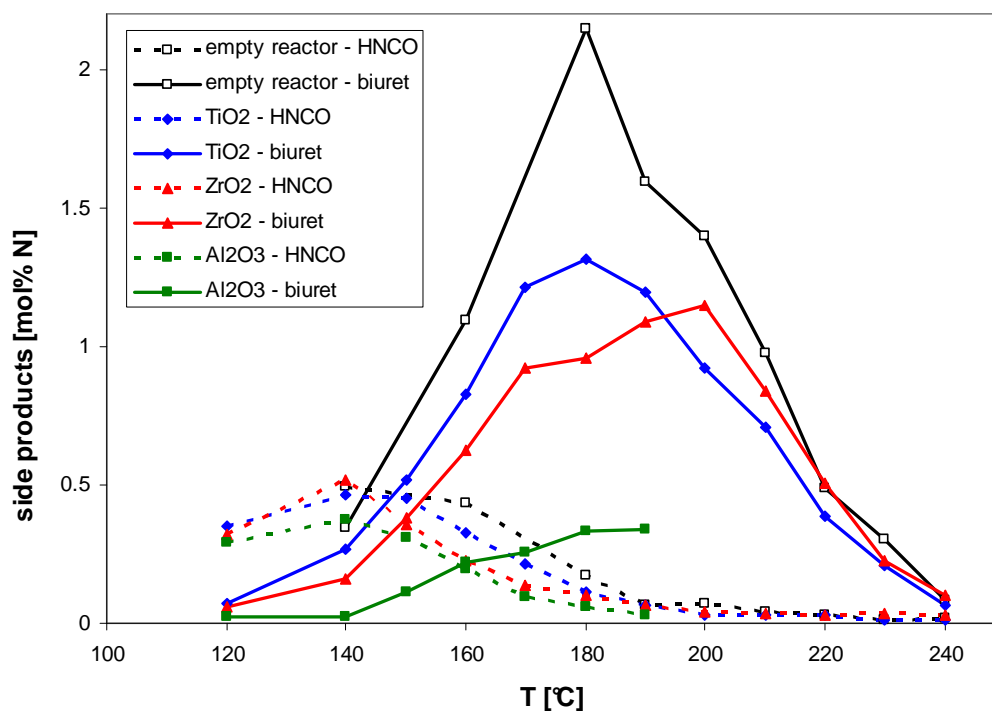
Figure 6-2: Side product formation from decomposition of urea solution under pressure.

The most striking feature of Figure 6-1 and Figure 6-2 is that the results of all urea decomposition experiments are quite similar, including the experiment without catalyst in the reactor. This observation is in contrast to the decomposition in the gas phase, which is negligible without catalyst up to 200°C, but shows conversions larger than 90% with any of the tested catalysts.

In order to compare liquid phase and gas phase decomposition, pseudo first-order rate constants according to 6-1 were calculated and compared with literature values. The Arrhenius plot for liquid phase decomposition is shown in Figure 6-3.

$$k = -\frac{V^*}{W}\ln(1-X) \quad [\frac{cm^3}{g \cdot s}] \qquad \textbf{6-1}$$

V^* = *volumetric flow through reactor*; W = *catalyst weight*; X = *NH$_3$-precursor conversion*
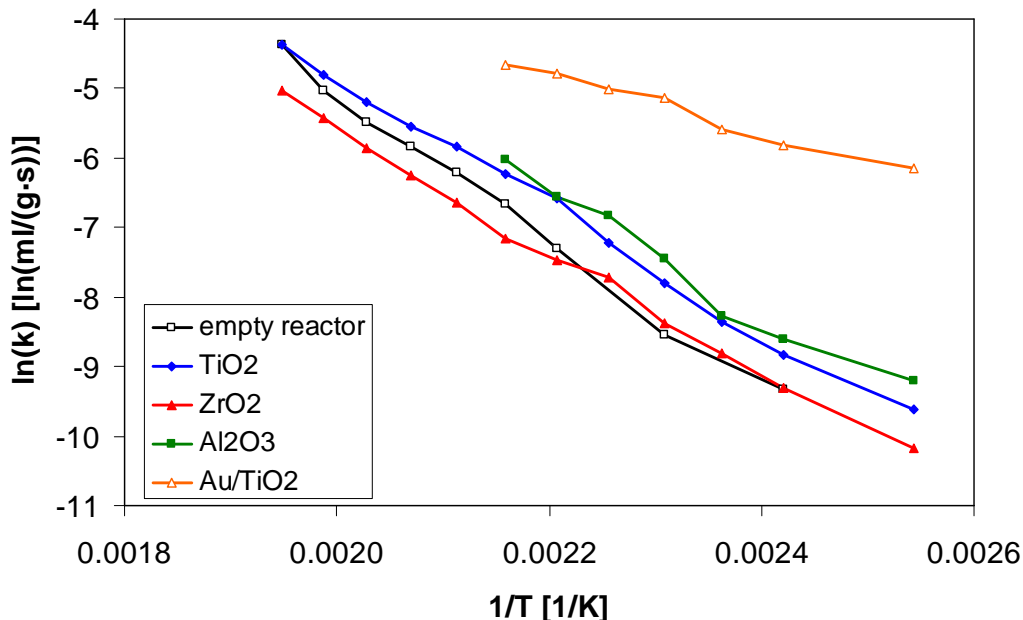
Figure 6-3: Arrhenius plot of decomposition in the liquid phase. Apparent activation energies (E$_A$) for the hydrolysis reaction are 87 kJ/mol (empty reactor), 75 kJ/mol (TiO$_2$), 72 kJ/mol (ZrO$_2$), 72 kJ/mol (Al$_2$O$_3$) and 34 kJ/mol (Au/TiO$_2$).

If compared with values for the gas phase decomposition of urea or HNCO on these catalytic materials, [**325,224**] the activation energies for urea hydrolysis are similar, while the pre-exponential factors are smaller by two orders of magnitude. In contrast to the gas phase decomposition though, the entire volumetric flow consists of aqueous urea, while it mostly consists of carrier gas for gas phase decomposition. Therefore, the smaller reaction rates can be overcompensated by the much smaller reactor volume for liquid phase decomposition.

The low activation energy of 34 kJ/mol for methanamide decomposition could point towards a diffusion limitation in the liquid phase. As a 400 cpsi extruded TiO$_2$ monolith with a pitch of 1.27 mm rather than a packed bed
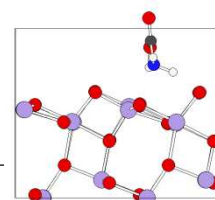
was used for the experiment, the maximum diffusion distance of 0.635 mm could indeed be too long for the low diffusion rates in the liquid phase. Consequently, superior catalytic decomposition could be feasible when using a more dense catalyst in the reactor.

6.4. Conclusion

The decomposition of urea in the liquid phase was – in contrast to the decomposition in the gas phase – not accelerated significantly by any of the tested catalytic materials. Comparison of the rate constants for urea decomposition on hydrolysis catalysts in the liquid phase with values from the gas phase show that gas phase decomposition proceeds approximately 100 times faster. However, the reactor size is much more compact for the liquid phase, thereby overcompensating the low reaction rates.

The decomposition of alternative NH_3-precursor compounds, which require a catalyst for successful release of stored NH_3 could profit from decomposition in the more concentrated liquid phase which also provides a large excess of the necessary reactant H_2O.

Consequently, the presented result could lead to the development of a new method to reliably provide gaseous NH_3 from NH_3-precursor compound solutions without the formation of side products, enabling direct injection into the main exhaust duct upstream of an SCR catalyst. [326,327]

7. *Enhanced-SCR* with NH$_4$NO$_3$

7.1. Introduction

Selective catalytic reduction (SCR) of NO$_x$ with NH$_3$ has become the most widely used exhaust aftertreatment method for the removal of NO$_x$ emissions from combustion processes of both stationary and mobile sources. [91] For mobile sources such as Diesel-engine powered vehicles, aqueous urea solution (AdBlue®) has been introduced to provide a safe precursor for onboard generation of NH$_3$ gas. [120,110]

Diesel engine exhaust gas usually contains mostly NO and a much lesser amount of NO$_2$. However, the Diesel Oxidation Catalyst (DOC) in the exhaust gas duct close to the exhaust manifold acts to oxidize some of the NO to NO$_2$. [328]

$$2\,NO\,+\,O_2\,\rightleftharpoons\,2\,NO_2 \qquad\qquad \textbf{7-1}$$

Besides the oxidation of undesired HC and CO, the NO oxidation is an important task of the DOC, as it enables the *fast-SCR* reaction. While pure NO will be reduced according to 7-2, an equimolar mixture of NO and NO$_2$ will be reduced by reaction 7-3, which is significantly faster and, therefore, called *fast-SCR*. [86]

$$4\,NO\,+\,O_2\,+\,4\,NH_3\,\longrightarrow\,4\,N_2\,+\,6\,H_2O \qquad \textbf{7-2}$$

$$2\,NO\,+\,2\,NO_2\,+\,4\,NH_3\,\longrightarrow\,4\,N_2\,+\,6\,H_2O \qquad \textbf{7-3}$$
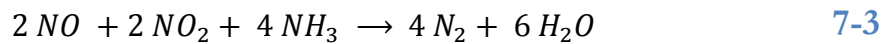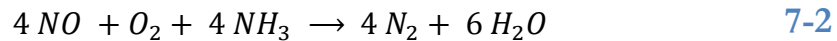
Besides these two reactions, the less desirable *NO$_2$-SCR* reaction also occurs in the case that *fast-SCR* is no longer possible, due to a lack of NO. [87]

$$6\,NO_2\,+\,8\,NH_3\,\longrightarrow\,7\,N_2\,+\,12\,H_2O \qquad \textbf{7-4}$$
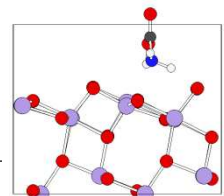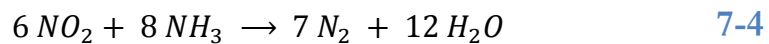
The reaction is less desired, as the reduction of pure NO_2 consumes 1.33 equivalents of NH_3, not just 1 as it is the case for *standard-SCR* and *fast-SCR*.

The NO oxidation on the DOC needs sufficiently high temperatures for the light-off in reaction 1-7. For example, the reaction will start around 150°C, and an equimolar ratio of NO and NO_2 is reached at 250°C (see Figure 7-1), but the temperatures are also dependent on the size of the DOC. For temperatures from 250°C to 400°C more NO_2 than NO is obtained. For higher temperatures, the thermodynamic equilibrium restricts the maximum concentration of NO_2 to be lower than the NO concentration. [328] Also, the space velocities and reactant concentrations experienced during the dynamic operation of the catalyst vary widely, leading to irregular catalytic conversion.
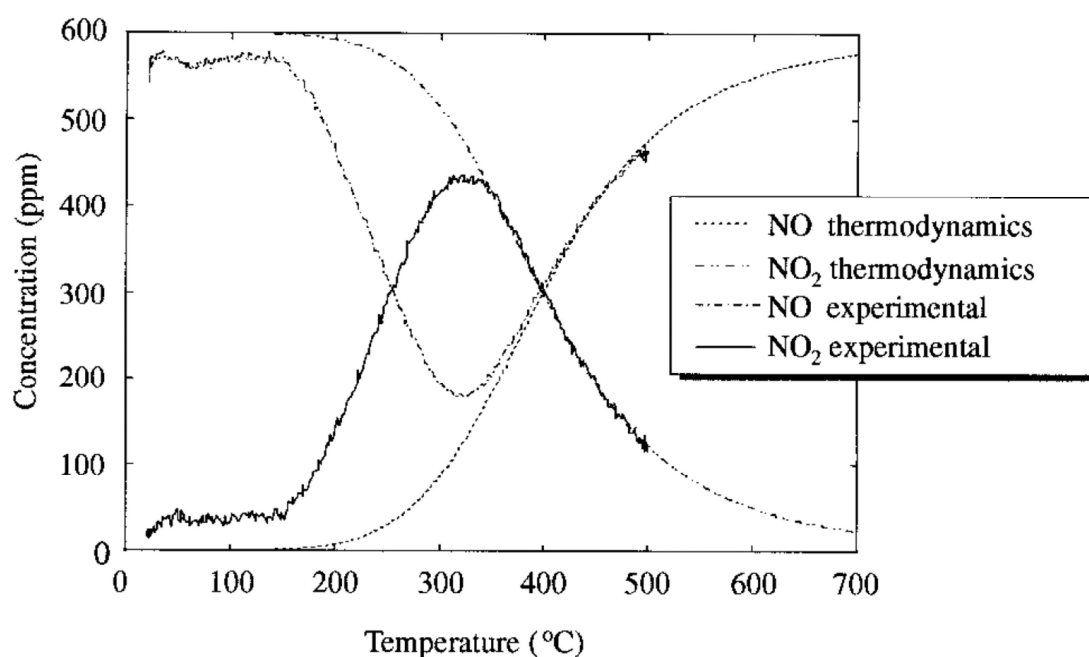
Figure 7-1: Oxidation of 600 ppm NO on a Pt-containing Diesel oxidation catalyst (reprinted with permission from reference [328]).

Forzatti et. al presented a novel method to create conditions similar to a NO/NO$_2$ gas mixture in the exhaust gas by adding ammonium nitrate (NH$_4$NO$_3$) to the aqueous urea solution used in mobile SCR applications. [**329**] The added NH$_4$NO$_3$ is decomposed in the exhaust to yield nitric acid (HNO$_3$), which oxidizes NO to yield NO$_2$. This solution has the advantage of providing NO$_2$ at low temperatures, and in exactly the ratios necessary for *fast-SCR* conditions.

The main reactions of this *enhanced-SCR* method are shown in 7-5 to 7-9. [**330**]

$$NH_4NO_3 \rightleftharpoons NH_3 + HNO_3 \qquad \text{7-5}$$

$$HNO_3 + NO \longrightarrow NO_2 + HONO \qquad \text{7-6}$$

$$HONO + NH_3 \longrightarrow NH_4NO_2 \qquad \text{7-7}$$

$$NH_4NO_2 \longrightarrow N_2 + 2\ H_2O \qquad \text{7-8}$$

$$NO + NO_2 + 2\ NH_3 \longrightarrow 2\ N_2 + 3\ H_2O \qquad \text{7-9}$$
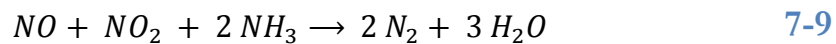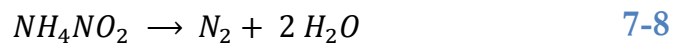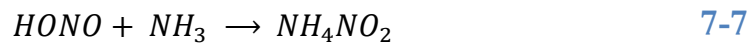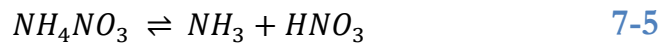
The overall reaction can be formulated as in 7-10:

$$2\ NO + NH_4NO_3 + 2\ NH_3 \longrightarrow 3\ N_2 + 5\ H_2O \qquad \text{7-10}$$
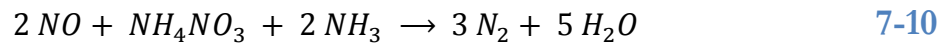
Forzatti et al. proposed a new concept for SCR catalysis, where optimal *fast-SCR* conditions could be achieved for NO$_2$-free NO$_x$-containing exhaust gas through the addition of NH$_4$NO$_3$ to AdBlue®. [**329**]

With our experimental setup [**260**] we were able to test for the first time whether the injection of an AdBlue®/NH$_4$NO$_3$-mixture to a solely NO-based NO$_x$-containing model exhaust gas flow results in equally good DeNO$_x$ rates on commercial SCR catalysts as does the dosing of AdBlue® to equimolar NO/NO$_2$ mixtures. Besides testing of *enhanced-SCR* performance under realistic conditions on commercial SCR catalysts, the knowledge of the role of NH$_4$NO$_3$ in the SCR mechanism could also be extended.
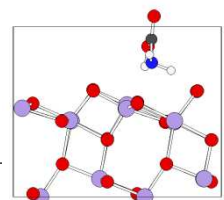
7.2. Experimental setup

Experimental investigations on the SCR catalysts were performed in our experimental setup for the investigation of NH_3-precursor compound solutions. [260] Commercial catalysts were obtained as samples from industry, an 1.9% V_2O_5 containing extruded honeycomb catalyst (400 cpsi) was obtained from Porzellanfabrik Frauenthal GmbH, while commercial Fe- or Cu-exchanged zeolite catalysts coated on cordierite honeycombs (400 cpsi) were obtained from Daimler AG. Core samples were cut out from the provided catalyst samples without further modification. The exact composition of the catalysts was not disclosed by either company. The vanadia-based catalyst contained mainly TiO_2 anatase, doped with WO_3 for increased acidity and thermal durability, and SiO_2 for structural stabilization. [227] The Fe-zeolite was a typical commercial type used in cars which are currently offered on the market. The Cu-zeolite showed high low-temperature activity and excellent stability during hydrothermal aging conditions, as typical for the state of the art chabazite-based Cu-zeolites which are commercially produced. [246,331] All catalyst samples were provided in large blocks, shaped to fit into the commercial application. For the experimental investigations small catalyst core samples of 40 mm length and approximately 18 mm diameter were cut out and fitted into the 20.4 mm diameter reactor. The overall gas flow was adjusted in all experiments to reach a Gas Hourly Space Velocity (GHSV) of 50,000 h^{-1}.

For the comparison of AdBlue® and AdBlue®/NH_4NO_3 solution or NH_3-gas in SCR performance, a constant temperature of 200°C was used for all catalysts. The relatively high space velocity and low temperature enables the observation of differences in catalytic activity, which would not be possible if conversion is constantly very high. In this way, the effect of NH_4NO_3

addition could thus be evaluated much better. The model exhaust gas composition used during SCR investigations included 1,000 ppm NO_x, 5% H_2O, 10% O_2 and balance N_2. Depending on the experiment, NO_x were either pure NO or an equimolar mixture of NO and NO_2 (abbreviated as NO/NO_2). The water vapor concentration was constantly corrected with the amount of dosed water via the NH_3-precursor solution, so a concentration of 5% H_2O was present as catalyst feed. In the case of NH_3-gas dosing for the SCR reaction, deionized water was sprayed onto the mounted catalyst, while the NH_3 was already included in the carrier gas. The AdBlue® and AdBlue®/NH_4NO_3 solutions were prepared using solid urea, NH_4NO_3 salt and deionized water. In addition a non-stoichiometric solution of urea and NH_4NO_3 was also prepared, denoted as Forzatti-sltn., because the solution represents the ratios used by Forzatti et al. in the previous publications. [329,332] The solution contains 0.68 molar equivalents of NH_4NO_3 relative to urea, rather than 1. The motivation in using such a mixture, will be explained in the discussion part.

Product gases were quantified by the previously presented multi-component gas analysis method using a ThermoFisher Antaris IGS FTIR spectrometer with 32 scans/spectrum at a resolution of 0.5 cm^{-1}.

7.3. Results and discussion

7.3.1. NH_3-slip/DeNO$_x$ measurements

The most meaningful and also relatively simple method to compare SCR activities is to record NH_3-slip/DeNO$_x$ curves. [228] These plots do not only demonstrate the SCR activity of a catalyst, but also give valuable information about the realistic DeNO$_x$ efficiency achieveable when complying with NH_3 emission restrictions such as e.g. 10 ppm for
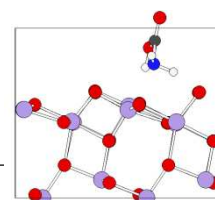
EURO VI. [**333**] In such a curve, the measured NH_3 slip after the SCR catalyst is plotted versus the achieved $DeNO_x$ efficiency. Ideally, the curve will remain flat on the abscissa until full $DeNO_x$ conversion. After this, the additionally produced NH_3 gas slips through the catalyst unconverted. Kinetics will determine whether the dosed reactants are converted successfully. This leads to an earlier increase of NH_3-slip in the case kinetics are not sufficiently high. In reality, uneven distribution of NH_3-precursor and as a consequence NH_3-gas will also lead to an earlier deviation from 0 ppm NH_3 slip, preventing the achievement of 100% $DeNO_x$. Finally, NO_x formation from excess NH_3 can cause a decline in $DeNO_x$ activity at very high dosage rates. [**228**]

In Figure 7-2 all the recorded NH_3-slip/$DeNO_x$ curves on the vanadia-based SCR catalyst are shown for easy comparison.
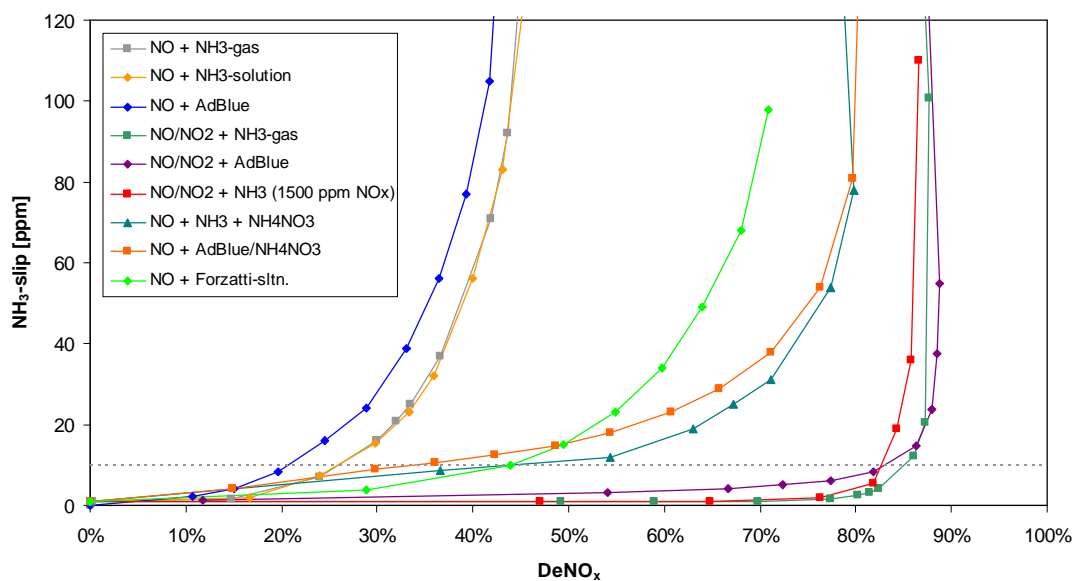
Figure 7-2: NH_3-slip/$DeNO_x$ curves for various NH_3-precursor solutions or NH_3-gas during SCR on a commercial vanadia-based SCR catalyst (50,000 h^{-1}; 1,000 ppm NO_x; 200°C).

There are three main sets of curves in the plot, each consisting of three individual curves. One set contains the *standard-SCR* curves, one the *fast-SCR* curves and the one in between contains the *enhanced-SCR* curves.

The set of *standard-SCR* curves contains two almost identical graphs, they are from SCR using either NH_3-gas or NH_3 aqueous solution. The perfect match between these two curves demonstrates that NH_3-gas or NH_3-solution are equally good NH_3 sources for the SCR process. This result is not surprising, as there is no catalytic process necessary to evaporate the NH_3-solution to yield NH_3-gas. Consequently, the following experiments for metal-exhanged zeolite SCR catalyst no longer featured a curve for NH_3-solution. The curve showing *standard-SCR* with AdBlue® is slightly shifted to lower $DeNO_x$ values for specific NH_3-slip concentrations. As the spray distribution can be considered to be homogeneous (compare Chapter 3: Setup for investigations on NH_3-precursor), the deviation of the AdBlue® curve is considered to result from the additional decomposition of urea, which must proceed in addition to the SCR reaction on the SCR catalyst. [85] At higher temperatures and/or lower space velocities this effect could no longer be observed.

The set of curves containing *fast-SCR* were acquired using either NH_3-gas or AdBlue®. Here, the conversions achieved with NH_3-gas could be reproduced with AdBlue® as well. The higher $DeNO_x$ rates due to the much faster SCR reaction enabled the efficient decomposition of AdBlue® to NH_3 without affecting SCR activity. A third curve is depicted, it shows the SCR of 1,500 ppm rather than 1,000 ppm of NO_x with NH_3-gas. This measurement was performed to check to what degree the higher $DeNO_x$ load on the SCR catalyst would result in lower SCR performance. While the addition of NH_4NO_3 will cause the formation of *fast-SCR* conditions from
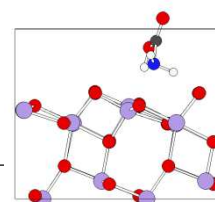
pure NO exhaust, it will at the same time increase the overall NO_x amount which needs to be reduced by 50%. Therefore, the depicted curve with 1,500 ppm NO_x was measured to provide an identical catalyst SCR load for comparison of *enhanced-SCR* with actual *fast-SCR* conditions.

However, from the application point of view, the reduction of the NO_x contained in the produced exhaust gas is most important, rather than the reduction of NO_x which contain to one third NO_x which were created by feeding a compound to the exhaust gas. $DeNO_x$ efficiencies were, therefore, referenced to the NO_x contained in the gas mixture prior to dosing of the NH_3-precursor compound. Luckily, the 1,500 ppm NO_x curve is only slighty shifted to lower values of $DeNO_x$ efficiency compared to the 1,000 ppm NO_x curve, so the difference can be considered to be almost negleglible under the chosen experimental conditions.

The third set of curves contains the experiments involving the addition of NH_4NO_3 to the model exhaust gas mixture. SCR was performed using either urea dissolved along with NH_4NO_3 in water, or by NH_3-gas and NH_4NO_3 addition. Either the equimolar solution of urea and NH_4NO_3 (AdBlue®/NH_4NO_3), or the 0.68 molar equivalent solution of NH_4NO_3 and urea (Forzatti-sltn.) was used. The measurements using NH_3-gas or AdBlue® in combination with NH_4NO_3 are quite similar, though not completely identical. While the maximum $DeNO_x$ values achieved are equal, the NH_3-slip at lower $DeNO_x$ rates is higher by about 5 ppm for the AdBlue®/NH_4NO_3 solution. The substoichiometric solution shows slightly lower NH_3-slip at $DeNO_x < 50\%$ than AdBlue®/NH_4NO_3, but it will only reach higher $DeNO_x$ rates with NH_3-slip concentrations well above the 10 ppm limitation. The lower $DeNO_x$ rates are due to the lowered amount

of NH_4NO_3, which was not sufficient to allow complete *enhanced-SCR* conditions.

Overall, the comparison of all NH_3-slip/$DeNO_x$ curves show that at the permitted maximum NH_3 slip of 10 ppm, *standard-SCR* efficiency is below 25%, while *fast-SCR* shows around 85% efficiency. *enhanced-SCR* with an equimolar solution was around 35%, while the substoichiometric solution could reach up to 44%. The proposed *fast-SCR* conditions could by far not be met using the *enhanced-SCR* method. The addition of NH_4NO_3 could not even produce half the increase in $DeNO_x$ as an NO/NO_2 gas mixture in the exhaust gas (would be at 55% $DeNO_x$). The observed NH_3-slip was significantly larger than in comparable experiments with NO/NO_2 gas mixtures, and the NH_3 emissions were accompanied by HNO_3 found in the gas phase. HNO_3 emissions are not immediately affected by emission control legislation for mobile sources, but should in general be avoided, if possible, due to its corrosive properties. N_2O emissions were below a concentration of 0.5 ppm, so they could be neglected in these measurements.

In Figure 7-3, all components resulting from reaction of different reducing agents with the model exhaust gas on the vanadia-based SCR catalyst are shown at an NH_3-slip of 10 ppm, or at maximum $DeNO_x$ efficiency. From the amount of inserted NO_x and reducing agent, the balance nitrogen was calculated. It consists of N-compounds which could not be quantified, i.e. gaseous N_2 and NH_4NO_3 which was deposited on the catalyst surface.
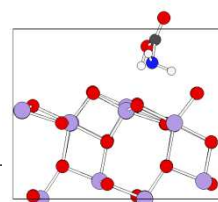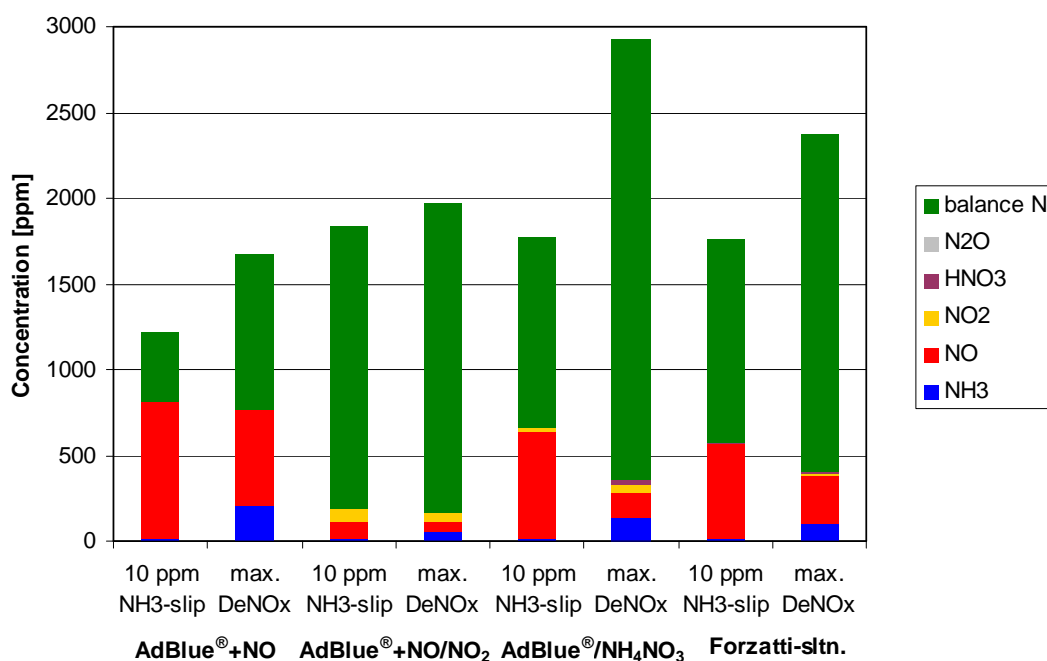
Figure 7-3: Reaction product distribution during SCR using different reducing agents on commercial vanadia-based catalyst. The product gas composition at either 10 ppm NH$_3$-slip or maximum DeNO$_x$ rates is shown.

Comparison of the product distributions at 10 ppm NH$_3$-slip yields a similar picture as the NH$_3$-slip/DeNO$_x$ curves, but indicates also the relative quantities of NO and NO$_2$ in the unconverted NO$_x$, and the formation of side-products. However, in Figure 7-3 there are no side products resolved at 10 ppm NH$_3$-slip, because the concentrations are too low. An interesting detail in the graph is the similar NO$_x$ concentration when using the Forzatti-solution and the stoichiometric AdBlue$^®$/NH$_4$NO$_3$ solution, even though the amount of *fast-SCR* is limited to 68% in case of the Forzatti-solution. This gives an indication of inhomogeneous NH$_4$NO$_3$ decomposition, which results in increased NH$_3$ emissions and prevents achieving high DeNO$_x$ at a given NH$_3$-slip limit.

The product distributions at maximum DeNO$_x$ values provide data on the components that are emitted from incomplete reaction. In addition, the

maximum achievable conversion is given – bearing in mind, that the overall sum of nitrogen will automatically be 1.5 times higher for the stoichiometric NH_4NO_3/urea solution and 1.33 times higher for the substoichiometric solution.

When using the NH_4NO_3-containing solutions, the amount of NO_x at maximum $DeNO_x$, is significantly lower than in the 10 ppm NH_3-slip scenario. This observation proves that much higher $DeNO_x$ rates are feasible using AdBlue[®]/NH_4NO_3 – even values comparable to NO/NO_2 are reached. The large difference between the maximum $DeNO_x$ rates and the one at low NH_3-slip is due to the insufficient utilization of NH_4NO_3 in the *enhanced-SCR* mechanism, as indicated by the emitted NH_3 and HNO_3. The conversion of NH_4NO_3 is significantly increased when supplied in substoichiometric amounts as in the Forzatti-solution. Here HNO_3 emissions were much lower, though also less $DeNO_x$ was achieved.

The emission of gaseous HNO_3 is partially caused by a slower oxidation of NO by HNO_3 than the transport of gaseous HNO_3 by the carrier gas, due to the vapor pressure of HNO_3. When excess NH_3 is present, the acid HNO_3 could also reform NH_4NO_3, rather than react with NO. [**334,335**] In the salt NH_4NO_3, both NH_3 and HNO_3 are stabilized as ionic compounds, which decreases their reactivity. If HNO_3 does not react with NO, then SCR will need to proceed via the *standard-SCR* route, which as seen from the curves for *standard-SCR*, is significantly less efficient under the experimental conditions.

From the measured compounds in the product gas, the contribution of *standard-SCR* could be determined. For the calculation, reactions 7-5 to 7-9 need to be considered, in addition to the SCR reactions, because the removal of NO can also be due to the oxidation to NO_2 by HNO_3.
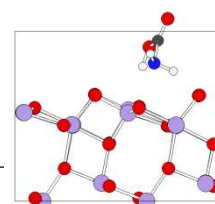
First, the amount of NO which is actually reduced to N_2 is derived from the inserted NO and the NO and NO_2 after the SCR reaction. The NO_2 concentration had to be substracted due to reaction 7-6.

$$[NO_{red.\ to\ N_2}] = [NO_{in}] - [NO_{out}] - [NO_{2\ out}] \qquad \textbf{7-11}$$

From the dosed amount of NH_4NO_3 and the measured HNO_3 and NO_2 emissions, the contribution of *fast-SCR* could be derived. The difference between inserted NH_4NO_3 and emitted HNO_3 had to be multiplied by two, because each HNO_3 caused one equivalent of NO_2, but additionally consumed one equivalent of NO for NO_2 production. The measured NO_2 emissions had to be multiplied by two as not only the reduction of one NO molecule was left out, but also the formation of NO_2 decreased the NO concentration.

It must be mentioned that equation 7-12 is based on the assumption of reaction 7-5, i.e. the decomposition of NH_4NO_3 is a precondition. In case NH_4NO_3 is just deposited on the catalyst surface, a higher contribution of *fast-SCR* than actually occurring will be estimated from the calculations. Thus, the calculation provides an upper bound of the actual contribution of *fast-SCR*.

$$SCR_{fast} = \frac{2\ ([NH_4NO_{3\ in}] - [HNO_{3\ out}]) - 2\ [NO_2]}{[NO_{red.\ to\ N_2}]} \qquad \textbf{7-12}$$

After calculating the contribution of *fast-SCR*, the remaining SCR activity was attributed to *standard-SCR*. The results for the NH_4NO_3-containing solutions are plotted in Figure 7-4.
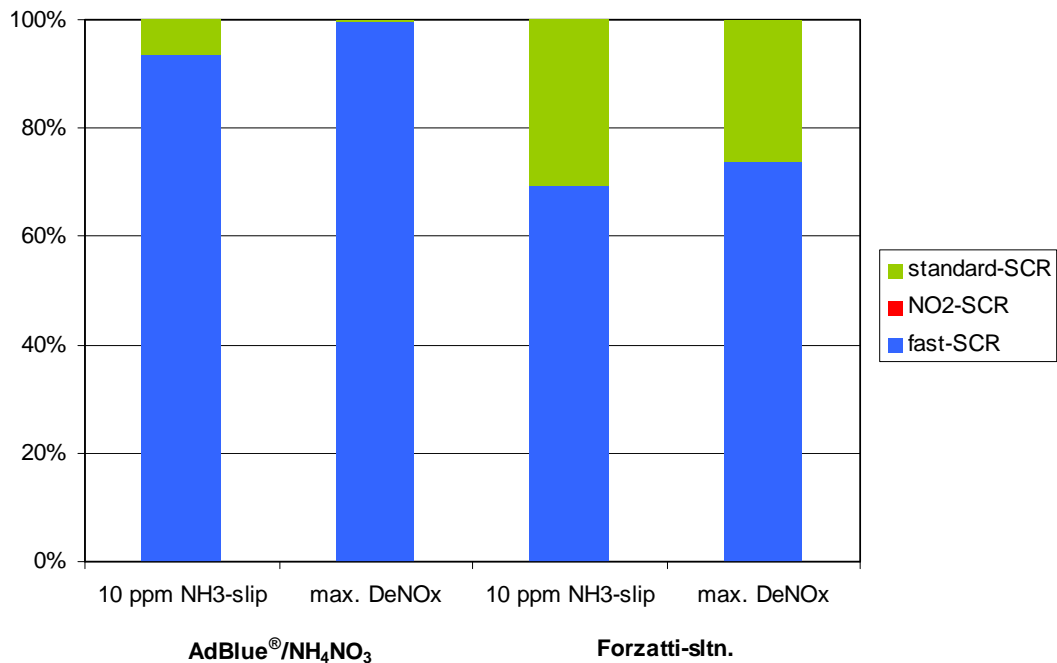
Figure 7-4: Contributions of different SCR reactions to overall DeNO$_x$ activity on commercial vanadia-based catalyst.

In case of the stoichiometric AdBlue$^®$/NH$_4$NO$_3$ solution, the contribution of *standard-SCR* is around 7% at 10 ppm NH$_3$-slip. The substoichiometric Forzatti-solution showed at the same NH$_3$-slip a *standard-SCR* contribution of 31%. At the maximum DeNO$_x$ values, only *fast-SCR* occurred using the stoichiometric solution, while still 26% *standard-SCR* remained using the substoichiometric solution. As the solution was overdosed relative to the NO in the gas flux, the amount of *fast-SCR* derived from NH$_4$NO$_3$ addition was no longer restricted to 68%. The amount of *fast-SCR* due to NO oxidation on the catalyst can also contribute to *fast-SCR*, but it was determined to be below 2% in an experiment of dosing NO and determining the emitted NO$_2$, without reducing agent.

Considering that there was no contribution of the *standard-SCR* reaction at all under NO/NO$_2$ gas mixture conditions, the *standard-SCR* contribution at 10 ppm NH$_3$-slip for the AdBlue$^®$/NH$_4$NO$_3$ solution and the Forzatti
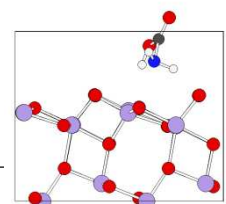
solution also provides an indication that in-situ production of NO_2 did not proceed completely.

The efficiency of NO_2 generation from NH_4NO_3 dosage can be calculated using formula 7-13.

$$\eta_{NO_2-gen.} = \frac{([NH_4NO_{3\,in}] - [HNO_{3\,out}])}{[NH_4NO_{3\,in}]} \qquad \text{7-13}$$

The analysis yields an efficiency around 98% for both solutions with any deviation to 100% being due to HNO_3 emissions. The build-up of NH_4NO_3 on the catalyst surface could not be deduced from the recorded emissions in the gas phase at the reactor outlet. The NO_2 generation efficiency gave only the formation of NO_2 from HNO_3, which, in the case of quantitative NH_4NO_3 decomposition, is identical to the generation from NH_4NO_3.

Reducing the ratio of NH_4NO_3 to urea is expected to also reduce the overall $DeNO_x$ efficiency, because it results in a higher contribution of *standard-SCR*. However, in the case of the vanadia-based SCR catalyst, the substoichiometric solution reached a higher $DeNO_x$ value at 10 ppm NH_3-slip, possibly due to the relatively lower deposition of NH_4NO_3 on the catalyst. Of course, the maximum $DeNO_x$ rates using the stoichiometric solution were again higher, because *fast-SCR* was not limited by a substoichiometric amount. Even the overdosing of the substoichiometric solution could not catch up with the $DeNO_x$ values of the stoichiometric solution.

However, it remains an important conclusion that NH_4NO_3 deposition on the catalyst is causing lower $DeNO_x$ rates than expected. Moreover, the dissociation of NH_4NO_3 independent of the active site for SCR caused the emission of NH_3 and HNO_3, leading to early NH_3 breaktrough. This effect

can be further aggravated by the transport of NH_4NO_3 aerosols through the first section of the SCR catalyst, as the decomposition of the aerosols in an end section of the catalyst could release NH_3 and HNO_3 without the possibility of reacting with NO.

As previously mentioned, the acquisition of NH_3-slip/$DeNO_x$ curves was not performed with a vanadia-based SCR catalyst, but was also carried out with a commercial metal-exchanged zeolite catalysts. The results for the Fe-exchanged zeolite catalyst are plotted in Figure 7-5.
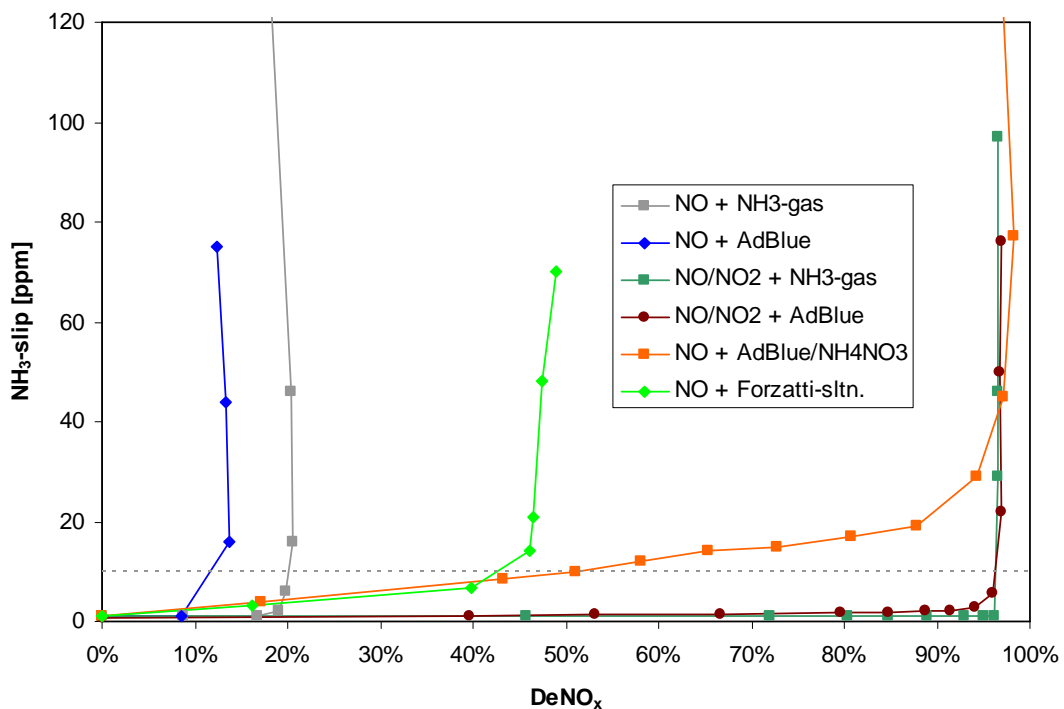
Figure 7-5: NH_3-slip/$DeNO_x$ curves for various NH_3-precursor solutions or NH_3-gas during SCR on a commercial Fe-exchanged zeolite SCR catalyst (50,000 h^{-1}; 1,000 ppm NO_x; 200°C).

Even though the overall picture changed, concerning the $DeNO_x$ values at 10 ppm NH_3-slip again three sets of curves are observed. At low $DeNO_x$, the measurements in which only *standard-SCR* proceeds are found, while the *fast-SCR* measurements are located at very high $DeNO_x$ rates.
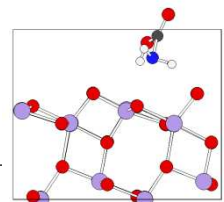
Intermediate between these two are the measurements in which NH_4NO_3 was dosed.

When NO was dosed as the only NO_x species, SCR using NH_3-gas resulted in almost double $DeNO_x$ efficiencies, if compared to AdBlue® dosing. This can be explained by the very low $DeNO_x$ rates below 20%, which further influence the hydrolysis of urea on the SCR catalyst, as the excess urea could condensate in the zeolite pores. In comparison, this effect was less relevant on the vanadia-based catalyst, due to the absence of small pores.

The very good agreement between *fast-SCR* using NH_3-gas and AdBlue®, conclusively demonstrates that AdBlue® dosing achieves identical $DeNO_x$ values of 96% at 10 ppm NH_3-slip, provided the catalytic activity is high.

$DeNO_x$ rates at 10 ppm NH_3-slip using solutions with added NH_4NO_3 were around 42% for the substoichiometric solution and around 50% for the stoichiometric solution. With the stoichiometric solution much higher maximum $DeNO_x$ rates could be achieved, though the NH_3-slip was far above the limit in this case. Interestingly, with the substoichiometric solution, $DeNO_x$ rates kept increasing, as overdosage led to a smaller gap in the stoichiometry and enabled higher contributions of *fast-SCR*. These effects are illustrated in Figure 7-6, which shows the outlet concentrations of gaseous compounds.
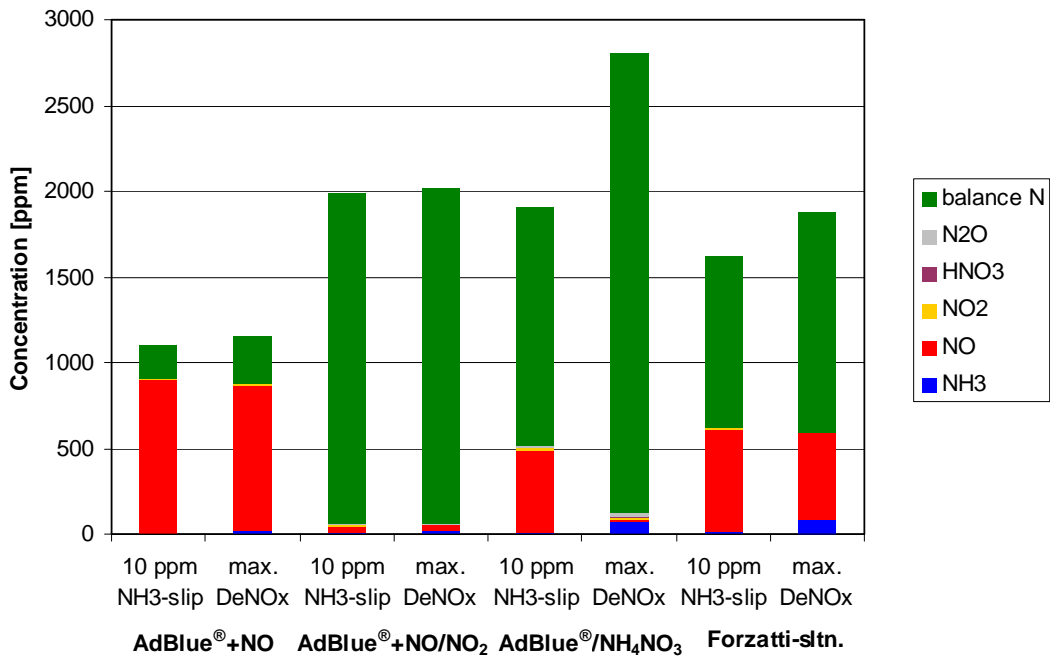
Figure 7-6: Reaction product distribution during SCR using different reducing agents on commercial Fe-exchanged zeolite catalyst. The product gas composition at either 10 ppm NH₃-slip or maximum DeNOₓ rates is shown.

The composition and quantity of compounds emitted at 10 ppm slip provide similar insights as the NH_3-slip/$DeNO_x$ curves: *standard-SCR* shows high amounts of NO, while with NO/NO_2 dosing only residual NO_x are observed. NH_4NO_3 addition leads to NO_x emissions that are about half of those obtained during *standard-SCR* alone.

The product concentrations at maximum $DeNO_x$ levels are interesting – dosing of AdBlue®/NH_4NO_3 solution led to less NO_x than reduction of a NO/NO_2 gas mixture. The effect can be explained by the excess dosage of urea and NH_4NO_3, which leads to full conversion of NO. However, due to the NH_4NO_3 decomposition not being restricted to proceed at the SCR active site, this excess is required for the high $DeNO_x$ rates. The NH_3 released from NH_4NO_3 in distance of the SCR site will cause the observed early NH_3-slip. This restricts the $DeNO_x$ rates achieved in NH_3-slip
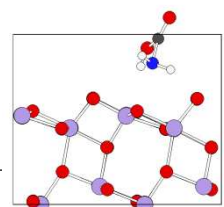
regulated applications. Combining the Fe-exchanged zeolite with an NH_3 oxidation catalyst could provide a possibility to utilize the high potential $DeNO_x$ efficiency. However, the emission of side products from such a combined system resulting from overdosage must also be monitored, as N_2O and HNO_3 should also not be emitted in amounts higher than 10 ppm. The amount of HNO_3 was lower than in the experiments with the vanadia-based SCR catalyst, but on the Fe-exchanged zeolite SCR catalyst, N_2O could also be found as a side product. The source of N_2O could be the decomposition of NH_4NO_3 as shown in 7-14. [336,337]

$$NH_4NO_3 \rightarrow N_2O + 2\,H_2O \qquad\qquad \text{7-14}$$
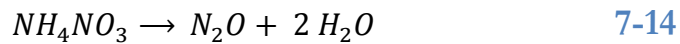
However, as there were no N_2O emissions detected in the experiments using the vanadia-based catalyst at the same temperature, and as NH_4NO_3 decomposition to N_2O is a mainly temperature-controlled process, this route is not considered likely. Instead, the alternative NO_2-SCR reaction was assumed to produce the N_2O according to 7-15. [338]

$$2\,NO_2 + 2\,NH_3 \rightarrow N_2 + N_2O + 3\,H_2O \qquad\qquad \text{7-15}$$
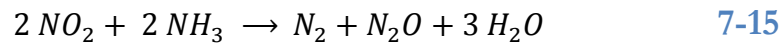
This SCR reaction is known to proceed on metal-exchanged zeolites, and results in N_2O emissions, especially in case of NO_2/NO ratios larger than unity, as NO_2-SCR is slower than *fast-SCR*. [339,340] Assuming measured N_2O evolved from reaction 7-15, the contribution of NO_2-SCR to the reduction of NO can be calculated according to 7-16.

$$SCR_{NO_2} = \frac{2[N_2O]}{[NO_{red.\ to\ N_2}]} \qquad\qquad \text{7-16}$$

Here, the definition for the amount of NO which was reduced to N_2 had to be extended according to 7-17, to also include the NO consumed in NO_2-SCR due to the previous generation of NO_2 via 7-6.

$$[NO_{red.\ to\ N_2}] = [NO_{in}] - [NO_{out}] - [NO_{2\ out}] - 2[N_2O] \qquad\qquad \text{7-17}$$

The contribution of *NO_2-SCR* for NO reduction at 10 ppm NH_3-slip was very low, with 1.0% in case of the stoichiometric solution and 0.6% for the substoichiometric solution. The contribution of *standard-SCR* was much higher for both solutions, with 23% and 42%, respectively. The calculated NO_2 generation from HNO_3 was very efficient at 99% for both runs.

For the calculation of the contribution of *fast-SCR*, equation 7-18 had to be introduced to include a term for N_2O emissions.

$$SCR_{fast} = \frac{2\,([NH_4NO_{3\,in}] - [HNO_{3\,out}]) - 2\,[NO_2] - 4[N_2O]}{[NO_{red.\,to\,N_2}]} \qquad \textbf{7-18}$$

At maximum $DeNO_x$, the amount of *standard-SCR* changed, in case of the stoichiometric solution down to 13%, for the substoichiometric solution it was slightly increased to 44%. The maximum *fast-SCR* contribution of 56% at maximum $DeNO_x$ for the substoichiometric solution is below the theoretical limit of 68%. When considering *fast-SCR* from NO oxidation on the catalyst, which could amount for up to 4% $DeNO_x$, the amount of *fast-SCR* from NH_4NO_3 is even further reduced. The contributions of the individual SCR reactions for the two solutions at 10 ppm NH_3-slip and maximum $DeNO_x$ can be seen in Figure 7-7.
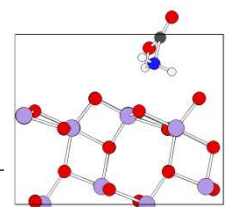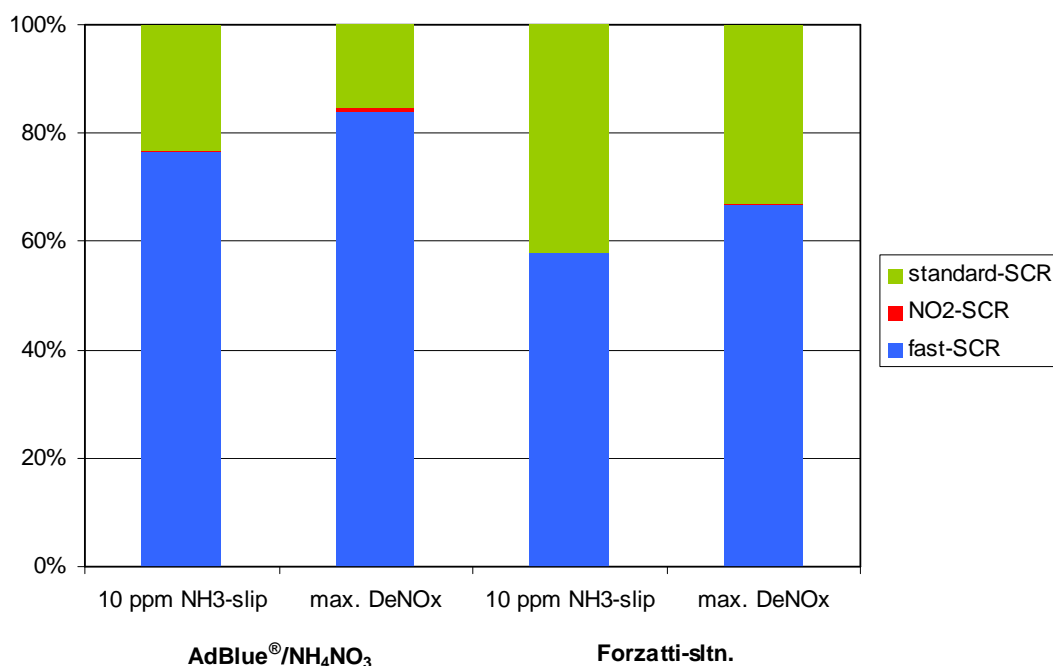
Figure 7-7: Contributions of different SCR reactions to overall DeNO$_x$ activity on commercial Fe-exchanged zeolite catalyst.

The high amount of *standard-SCR* also leads to the assumption that *standard-SCR* was directly competing with the reduction of HNO$_3$ by NO. Compared to gas-phase *fast-SCR*, which was shown to be much faster than *standard-SCR*, NO$_2$ formation from NH$_4$NO$_3$ is the additional step in *enhanced-SCR* that can become rate-determining.

Consequently, the advantage of NH$_4$NO$_3$ addition would become less pronounced when the *standard-SCR* mechanism is competitive with HNO$_3$ reduction. This insight should also be kept in mind when discussing the results for the Cu-exchanged zeolite SCR catalyst which are shown in Figure 7-8.
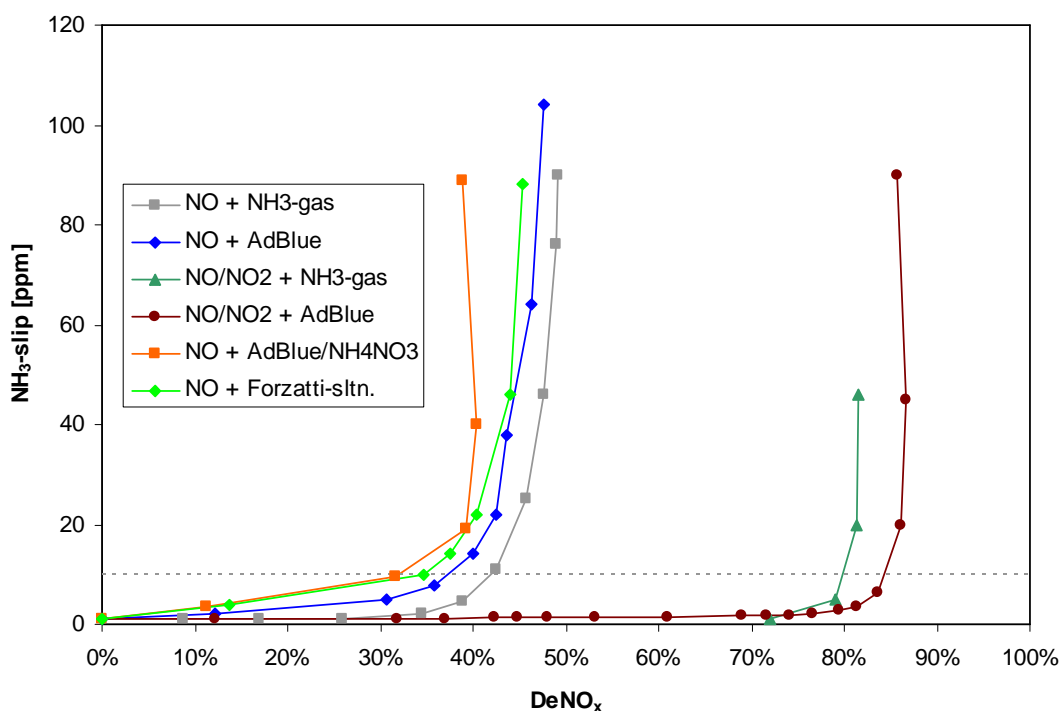
Figure 7-8 NH_3-slip/$DeNO_x$ curves for various NH_3-precursor solutions or NH_3-gas during SCR on a commercial Cu-exchanged zeolite SCR catalyst (50,000 h^{-1}; 1,000 ppm NO_x; 200°C).

The obtained results differ from the previous ones, as there seem to be only two sets of curves, one for the *fast-SCR* at high $DeNO_x$ rates, and all others at moderate $DeNO_x$ efficiencies.

For the *fast-SCR* curves, it is note-worthy to see that NO/NO_2 was reduced more efficiently by AdBlue® than by NH_3-gas (85% versus 80%). The hydrolysis reaction seemed to positively influence the *fast-SCR* reaction on the catalyst, or the catalytic activity with NH_3-gas was reduced due to the immediate exposure of the active Cu-sites to NH_3 rather than the successive release of NH_3 from urea. The formation of urea aerosols which were decomposing within the catalyst channels also caused a more uniform utilization of the overall catalyst volume for the SCR reaction.
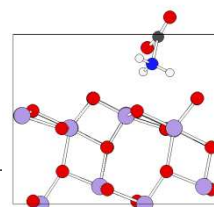
In contrast, *standard-SCR* using AdBlue® was again slightly less efficient than using NH_3-gas, but compared to *standard-SCR* on Fe-exchanged zeolite, the $DeNO_x$ rate of approximately 40% was significantly higher.

The low $DeNO_x$ rates achieved at 10 ppm NH_3-slip for NH_4NO_3 solutions are unexpected, with 34% for the substoichiometric solution and 32% for the stoichiometric solution. The maximum achievable $DeNO_x$ rates were even more different, with the substoichiometric solution performing better than the stoichiometric, though both remained below the results achieved with pure AdBlue®.

These observations are illustrated in Figure 7-9, which shows the product gas compositions at 10 ppm NH_3-slip and at the maximum achieved $DeNO_x$ activity.
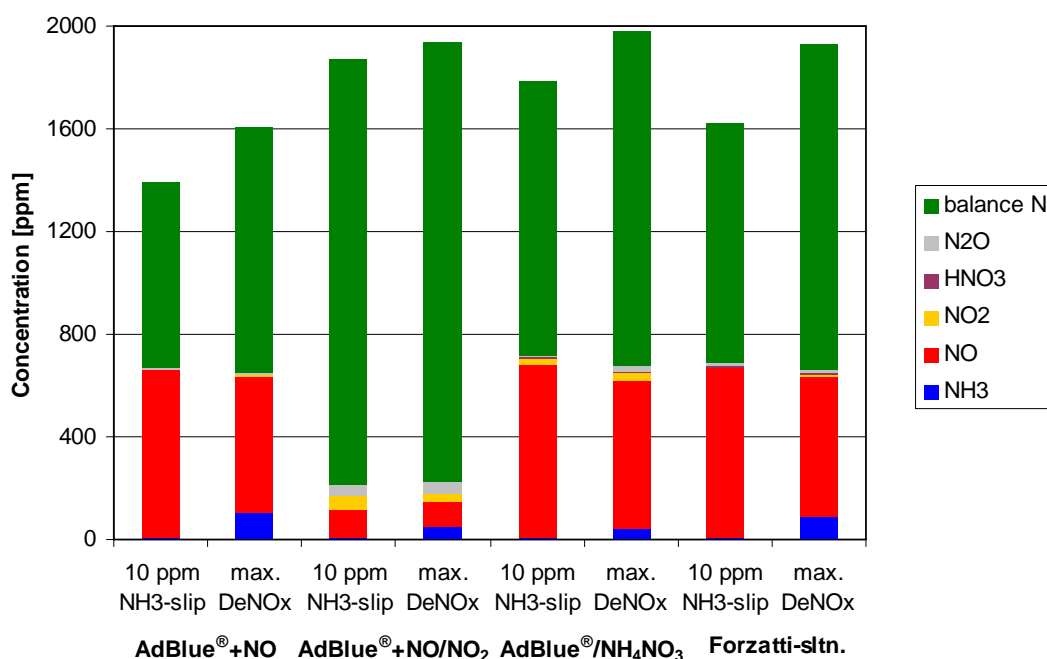
Figure 7-9: Reaction product distribution during SCR using different reducing agents on commercial Cu-exchanged zeolite catalyst. The product gas composition at either 10 ppm NH_3-slip or maximum $DeNO_x$ rates is shown.

With restricted NH_3-slip, NO_x emissions from *standard-SCR* using just AdBlue® and NO are equal to those obtained for NH_4NO_3 dosing. In the case of the stoichiometric solution, some of the NO_x is NO_2. For the substoichiometric solution only NO is measured, although the substoichiometric solution caused higher N_2O emissions. This result is in sharp contrast to theoretic expectations, as NH_4NO_3 addition brings no advantage for NO reduction. The NO/NO_2 experiment also caused relatively high amounts of NO_2 and N_2O, indicating incomplete *fast-SCR* conversion.

At maximum $DeNO_x$ conditions, all experiments except those with NO/NO_2 showed comparable NO_x concentrations in the product gas. As NH_3-slip no longer restricted $DeNO_x$ efficiency, the experiment indicated that any amount of added NH_4NO_3 would not cause any advantage compared to pure AdBlue®.

The absence of any beneficial effect from NH_4NO_3-addition needed to be inspected in detail, using the previously introduced formulae. The efficiency of NO_2 formation from HNO_3 was 98% for both stoichiometries of NH_4NO_3, based on the recorded HNO_3 emissions. *NO_2-SCR* consuming the produced NO_2 from NO amounted for 4.3% and 3.9% of the NO reduction for the stoichiometric and substoichiometric solution at 10 ppm NH_3-slip, respectively. The calculation of the contribution of *standard-SCR* in both scenarios was subject to errors. From inserting the concentrations in the introduced formulae, the amount of *standard-SCR* was calculated to be about 33% for the substoichiometric solution, and non-existent in case of the stoichiometric solution. Here, the deposition of dosed NH_4NO_3 on the catalyst surface must be assumed, as the $DeNO_x$ efficiencies when using NH_4NO_3-addition were lower than without addition. The
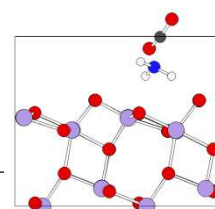
stoichiometric NH_4NO_3 addition even yielded the lowest $DeNO_x$ rates of all measured samples. As NO/NO_2 was efficiently reduced by AdBlue®, not the SCR reaction, but the production of NO_2 from NH_4NO_3 was limiting $DeNO_x$ performance. NH_4NO_3 build-up in the small zeolite pores seems to be the cause for the low $DeNO_x$ rates, which were at best similar to those for *standard-SCR*. The *standard-SCR* reaction was proceeding to a higher degree when less NH_4NO_3 was dosed, as in the case for the substoichiometric addition. Figure 7-10 shows the calculated contributions of the individual $DeNO_x$ reactions.
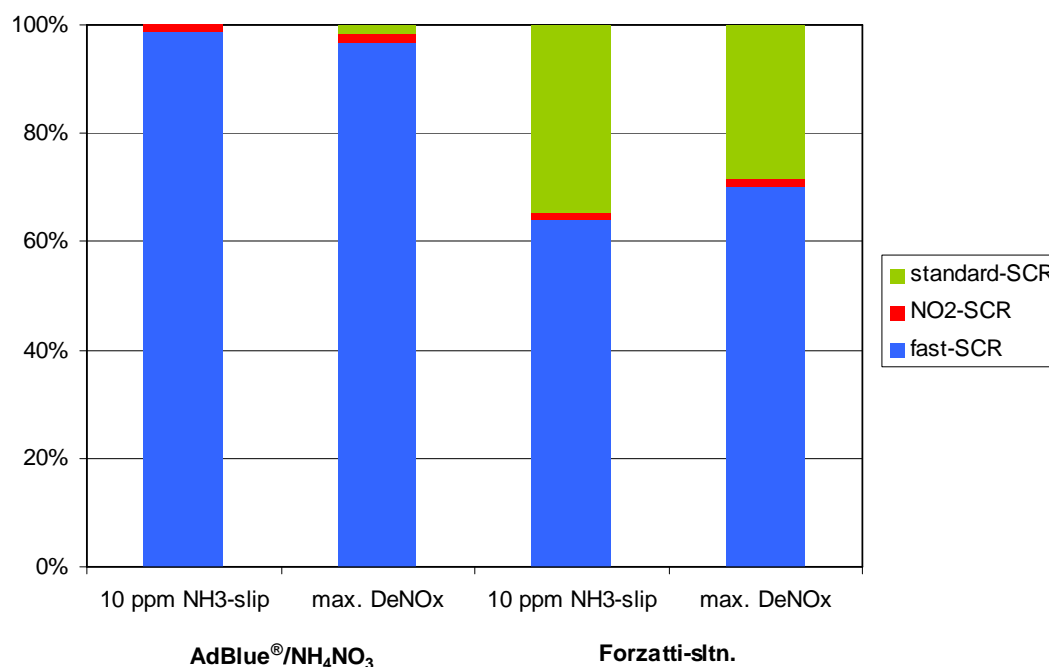
Figure 7-10: Contributions of different SCR reactions to overall DeNO$_x$ activity on commercial Cu-exchanged zeolite catalyst.

At maximum $DeNO_x$ the contribution of *fast-SCR* was basically identical to the used stoichiometry, i.e. 100% or 68% for the stoichiometric solution and the substoichiometric solution, respectively. At the same time, however, $DeNO_x$ conversions matching pure *standard-SCR* were observed, indicating no *fast-SCR* contribution. As previously mentioned, the

deposition of NH_4NO_3 on the catalyst surface causes an apparent contribution to *fast-SCR*. There seemed to be quantitative deposition of NH_4NO_3 on the catalyst causing apparent full utilization of the introduced *fast-SCR* agent. Partial decomposition of the accumulated NH_4NO_3 via reaction 7-14 to yield N_2O caused the apparent *NO_2-SCR* activity.

These observations lead to the conclusion that NH_4NO_3 addition on commercial Cu-exchanged zeolite could even cause a decrease in $DeNO_x$ efficiency, by restricting NO reduction to the *standard-SCR* pathway, and blocking some of the catalytic sites for NO reduction by NH_4NO_3.

In summary, on all SCR catalysts, the stoichiometric addition of NH_4NO_3 did not give the results expected from SCR of a NO/NO_2 gas mixture. Actually, the substoichiometric dosage of NH_4NO_3 appears the more attractive approach. In order to determine the optimum stoichiometry for NH_4NO_3 addition, a series of experiments was performed.

7.3.2. Determination of the optimum NO/NO_2 ratio

Experiments were performed using a 20% NH_4NO_3 solution. The overall amount of NO_x and NH_3 was kept constant by reducing NO and NH_3 in the gas mixture as NH_4NO_3 dosing increased. For comparison, a mixture of NO and NO_2 was also dosed and reacted with NH_3 gas. The dosing of NH_3 and NO_x was kept constant at $\alpha = 1$ during alteration of the NO_2/NO_x ratio (α defined according to 2-1). The calculated $DeNO_x$ rates were then plotted versus the used NO_2/NO_x ratios in the feed gas, or as theoretically obtained from the addition of NH_4NO_3. The curve for NH_4NO_3-solution was plotted twice, once according to the general $DeNO_x$
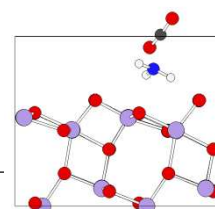
formula given by equation 2-2, and the second time only the NO-based DeNO$_x$ was calculated according to formula 7-19.

$$DeNO_{x\,(NO-based)} = \frac{NO_{(in)} - (NO_{(out)} + NO_{2\,(out)} + 2\,N_2O_{(out)})}{NO_{(in)}} \quad \textbf{7-19}$$

The advantage of formula 7-19 is in distinguishing the actual increase in conversion of inserted NO from an artificial increase in DeNO$_x$-efficiency due to reduced dosing of NO. In the case of significant deposition of NH$_4$NO$_3$ on the catalyst surface, the NH$_4$NO$_3$-based NO$_x$ which are not leaving the reactor due to deposition on the catalyst, falsify the calculated DeNO$_x$ values.

First, the results for the vanadia-based SCR catalyst are shown in Figure 7-11.

Figure 7-11: DeNO$_x$ efficiency in dependence of NO$_2$/NO$_x$ ratio on a commercial vanadia-based SCR catalyst (50,000 h^{-1}; 1,000 ppm NO$_x$; 1,000 ppm NH$_3$; 200°C).

The NO$_2$/NO$_x$ ratio with NO$_2$ gas showed maximum DeNO$_x$ efficiencies at exactly 0.5, as expected from the established *fast-SCR* stoichiometry. If the NO$_2$ was not dosed as gas but had to be formed from NH$_4$NO$_3$, then

the maximum remained at this position. This supported the *enhanced-SCR* mechanism as previously described. Beyond the dosage of NH_4NO_3 to supply equimolar amounts of NO_2 and NO at 0.5, the $DeNO_x$ rates decreased all the way to approximately 50% at a NO_2/NO_x ratio of 1.

The double equimolar dosing rate of NH_4NO_3 theoretically gives a pure NO_2 gas flow, which needs to be reduced via *NO₂-SCR* according to reaction 7-4 or 7-15. As reaction 7-15 produced N_2O, it could be quantified easily. At pure NO_2 feed conditions, only 0.5% of the NO_2 reacted via 7-15, the remaining part was reduced according to 7-4. The two *NO₂-SCR* routes are characterized by different stoichiometries for the reaction of NO_2 with NH_3. The stoichiometry of reaction 7-4 limits the maximum achievable NO_x conversion to 75%, while reaction 7-15 could still reach 100% NO_x conversion. Therefore, the 30% of observed overall $DeNO_x$ corresponds to 40% of the maximum NO_x conversion according to 7-4, making the vanadia-based SCR catalyst a moderately efficient *NO₂-SCR* catalyst in a non-ideal stoichiometric SCR reaction.
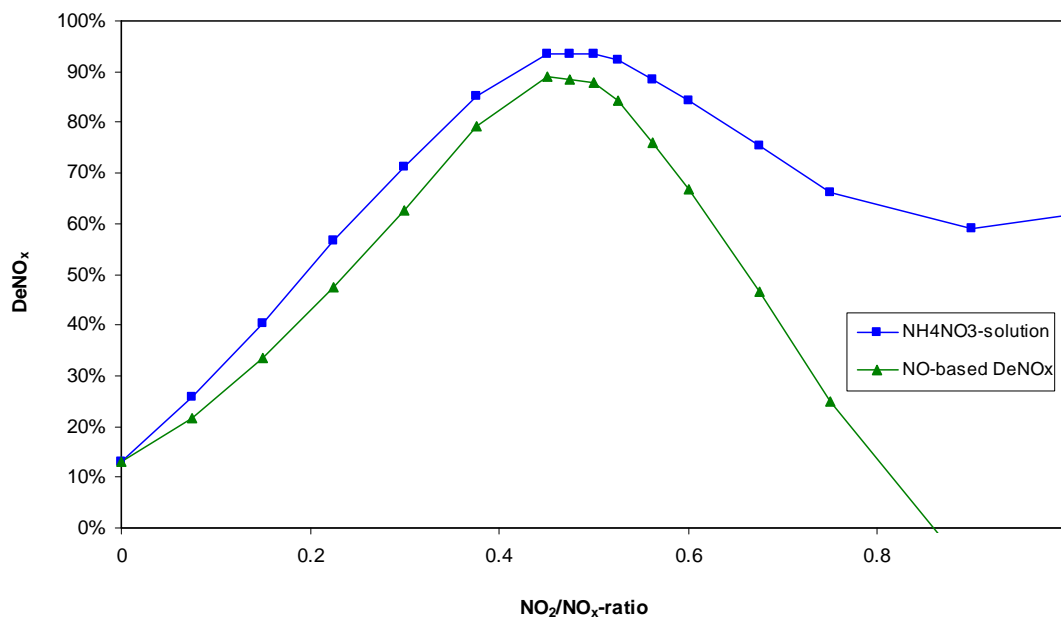
Figure 7-12: DeNO$_x$ efficiency in dependence of NO$_2$/NO$_x$ ratio on a commercial Fe-exchanged SCR catalyst (50,000 h^{-1}; 1,000 ppm NO$_x$; 1,000 ppm NH$_3$; 200°C).

Changing the percentage of NO$_2$ through NH$_4$NO$_3$ addition yielded a clear optimum at the theoretically predicted equimolar ratio of 0.5 on the Fe-exchanged zeolite catalyst. At higher ratios, N$_2$O emissions indicated the occurrence of *NO$_2$-SCR*, in accordance to 7-15, with a maximum contribution of 4.3% DeNO$_x$. However, the calculated NO-based DeNO$_x$ activity was negative, so the efficiency of the non-equimolar *NO$_2$-SCR* could not be calculated.

A discussion concerning the observed negative value at high NO$_2$/NO$_x$ ratio is included in the next section "7.3.4. Discussion of the NH$_4$NO$_3$-decomposition mechanism".

For now, it should just be noted that at NO$_2$/NO$_x$ ratios close to unity, NO-based DeNO$_x$ falls below the apparent DeNO$_x$ efficiency. This can be attributed to the deposition of NH$_4$NO$_3$ on the catalyst surface, which is incorrectly attributed to a DeNO$_x$ activity in the standard DeNO$_x$ formula.

Last, the Cu-exchanged zeolite catalyst was tested with different NO_2/NO_x ratios from NO/NO_2 gas mixtures or variations in NH_4NO_3 dosing rates.
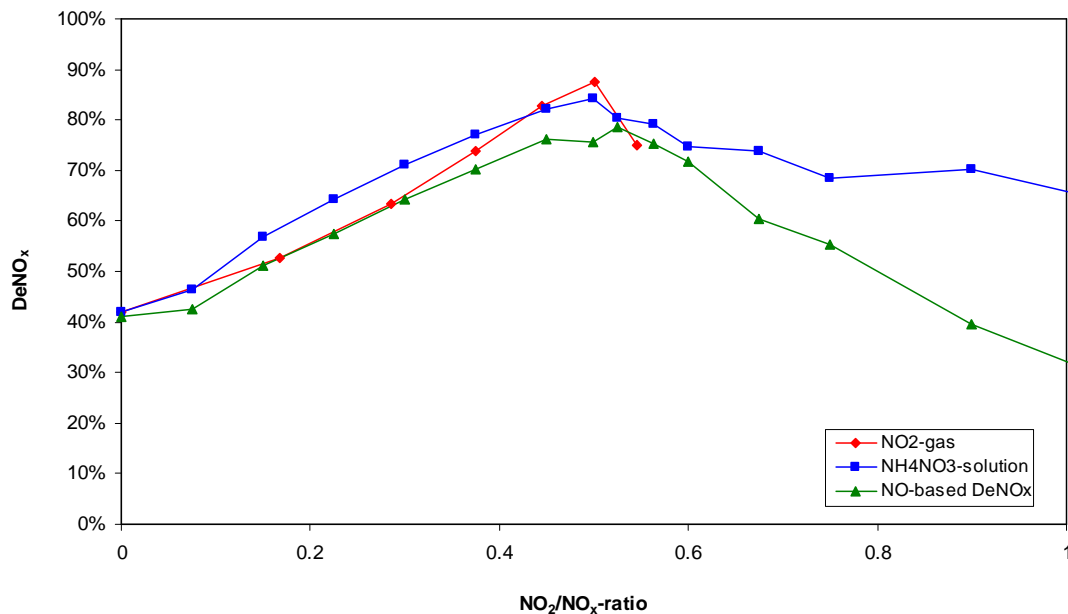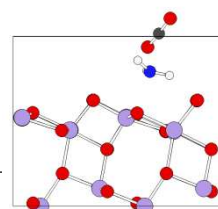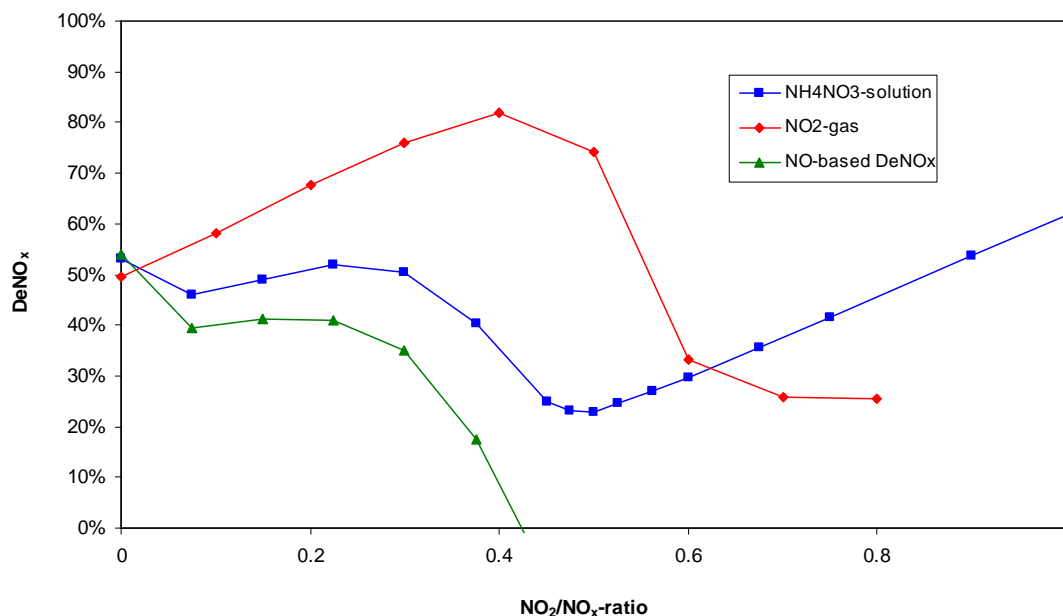

Figure 7-13: DeNOₓ efficiency in dependence of NO_2/NO_x ratio on a commercial Cu-exchanged SCR catalyst (50,000 h⁻¹; 1,000 ppm NOₓ; 1,000 ppm NH₃; 200°C).

The variation of NO_2-gas dosing showed a linear increase in $DeNO_x$ efficiency up to 0.4, at the ideal ratio of 0.5, $DeNO_x$ already started to decrease. Higher NO_2 concentrations led to lower $DeNO_x$ rates. Again, N_2O was determined in the product gas, though the maximum concentrations were determined around NO_2/NO_x ratios of 0.5 with a contribution of up to 3.4% $DeNO_x$. *NO₂-SCR* yielding N_2O decreased to less than 1% $DeNO_x$ above a NO_2/NO_x ratio of 0.6. The observed 25% $DeNO_x$ were, therefore, related to *NO₂-SCR* with an efficiency around 33%. Thus, the Cu-exchanged zeolite seemed to catalyze *NO₂-SCR* very inefficiently.

If NH_4NO_3 is added to create NO_2 by reduction of HNO_3 with NO, then the achieved $DeNO_x$ rates behaved significantly differently. Using the regular formula, the conversion remained around 50% up to a ratio of 0.3,
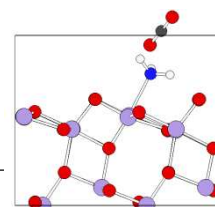
then DeNO$_x$ efficiency decreased to a minimum at 0.5. From the minimum, a constant increase in DeNO$_x$ all the way to pure NO$_2$ feedstock was observed. However, the calculation of NO-based DeNO$_x$ for the same measurement yielded DeNO$_x$ conversions in better agreement with the experiment: After an initial decrease to 40% this value was maintained up to a NO$_2$/NO$_x$ ratio of about 0.3, then DeNO$_x$ fell to a value of -18% at the optimum *fast-SCR* ratio of 0.5 and remained there up to higher ratios. Again, an explanation for this result shall be given in the next chapter.

NO$_2$-SCR yielding N$_2$O only played a minor role, with a maximum DeNO$_x$ contribution of 1.5% at a NO$_2$/NO$_x$ ratio of 0.3, and below 0.2% DeNO$_x$ at NO$_2$/NO$_x$ ratios larger than 0.5.

The decrease in DeNO$_x$ efficiency with increasing dosage of NH$_4$NO$_3$ could, as previously mentioned, be explained as the blockage of sites for *standard-SCR*. In the curve showing the DeNO$_x$ conversion according to the classic formula 2-2, after the miniumum at stoichiometric conditions, the efficiencies increased linearly with NO$_2$-content. However, in this range, 90% of the dosed NO could still be found in the product gas, even though up to 62% DeNO$_x$ was calculated at double-stoichiometric NH$_4$NO$_3$-addition. The remaining 10% NO were converted to NO$_2$, which could still be measured at the reactor outlet, without significant reductions. The concentration of emitted HNO$_3$ rose steadily from NO$_2$/NO$_x$ ratio of 0.5 to 1.0, but only to a maximum of 35 ppm. Therefore, a large build-up of NH$_4$NO$_3$ on the catalyst surface can be considered, which is further supported by the emissions of NH$_3$-slip, which match the sum of all detected NO$_x$ plus HNO$_3$. The plot of NO-based DeNO$_x$ activity illustrates how the apparent increase in DeNO$_x$ activity is actually just caused by the reduced NO dosing and the deposition of the substitute NO$_x$

as NH_4NO_3 on the catalyst surface. Instead of showing higer $DeNO_x$ efficiency, the catalyst becomes completely inactivated for any $DeNO_x$ activity due to the almost complete deposition of NH_4NO_3 on the surface.

In short, the seemingly linear increase in $DeNO_x$ efficiency with higher NH_4NO_3 dosing was in fact due to the reduced dosing of NO-gas and the build-up of NH_4NO_3 on the catalyst. The "missing" NO_x at the reactor outlet were then turned into a $DeNO_x$ activity by using the simple NO_x conversion equation 2-2. The actual $DeNO_x$ activity is considered to have vanished at this point due to catalyst deactivation by the physical blockage of active sites by NH_4NO_3-formation.

7.3.3. Temperature screening for *enhanced-SCR*

As all experiments were performed at a constant temperature of 200°C, a quick test was chosen to see to what extent the observed effects could be generalized to other operation temperatures. The overproportional dosage of reducing agent solution was also investigated.

In detail, the stoichiometric or substoichiometric NH_4NO_3-solution was dosed at α = 1.2 into a model gas containing 1,000 ppm of NO, while the temperature was scanned from 375°C to 175°C.

The results for the vanadia-based SCR catalyst are shown in Figure 7-14.
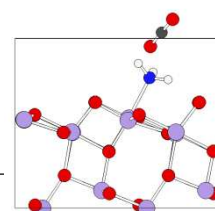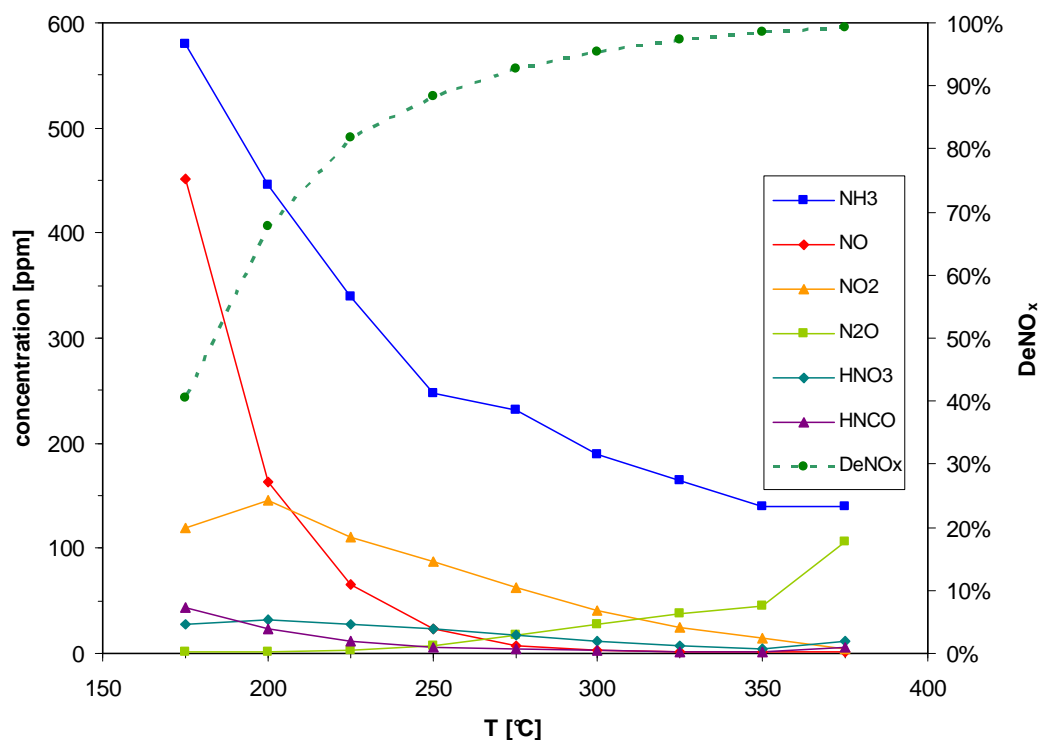
Figure 7-14: DeNO$_x$ efficiencies and product gas composition during dosage of a stoichiometric NH$_4$NO$_3$-urea solution on a vanadia-based SCR catalyst at various temperatures (50,000 h^{-1}; 1,000 ppm NO; 600 ppm urea; 600 ppm NH$_4$NO$_3$).

As the temperature is decreased from 375°C, DeNO$_x$ efficiency also decreases. In accordance with the decrease in DeNO$_x$, the NH$_3$-slip increased from 140 ppm at 375°C. The reason why 99.3% DeNO$_x$ is reached, even though 12 ppm HNO$_3$ and 106 ppm N$_2$O are emitted, is that they are not included in the NO$_x$ balance as defined in emission control legislation. [26] As long as N$_2$O is not specifically regulated by legislation or included in NO$_x$, even such high concentration would be tolerated, though it is generally known that N$_2$O posses a global warming potential of 310 equivalents of CO$_2$. [229] Evolution of N$_2$O proceeded at these high temperatures by the direct decomposition of NH$_4$NO$_3$ according to reaction 7-14. As the temperature decreases, N$_2$O emissions sharply decrease, at 250°C less than 10 ppm are measured. HNO$_3$ reduction is quite

efficient, at 350°C an optimum of 99% is reached, the worst conversion at 200°C still amounts to 94%. NO_2 and NO emission suggest, that above 200°C, NO_2 was quickly generated from NH_4NO_3 causing an excess compared to NO. The excess was possible as the dosing of the reducing agent solution was set at $\alpha = 1.2$. Thus, *fast-SCR* proceeded with NO being the limiting reactand, while at 175°C the high NO concentration without a similar increase in HNO_3 emissions points towards a deposition of NH_4NO_3 on the catalyst surface. Of course, the deposition of NH_4NO_3 on the catalyst surface caused a strong decline in $DeNO_x$ efficiency.

Considering that the addition of NH_4NO_3 is meant to enhance low-temperature $DeNO_x$, the high temperature for the deposition of NH_4NO_3 on the catalyst is restricting the low-temperature enhancement to a minimum of around 200°C. However, 200°C are currently no longer considered to be a very low temperature for Diesel exhaust and SCR aftertreatment systems dealing with the reduction of NO_x. The overdosing of NH_4NO_3/AdBlue® caused formation of N_2O above 300°C, and emission of HNO_3 below. But excess NH_4NO_3 also reacted with NO to form above-stoichiometric amounts of NO_2 that could no longer be consumed in *fast-SCR*. Thus, the overdosing of NH_4NO_3/AdBlue® will not only lead to an NH_3-slip, but also to additional NO_x formation, depending on the temperature range.

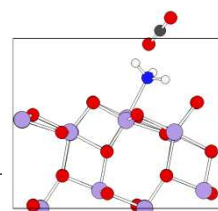The same experiment was also perfomed with the Fe-exchanged zeolite SCR catalyst, the result is presented in Figure 7-15.
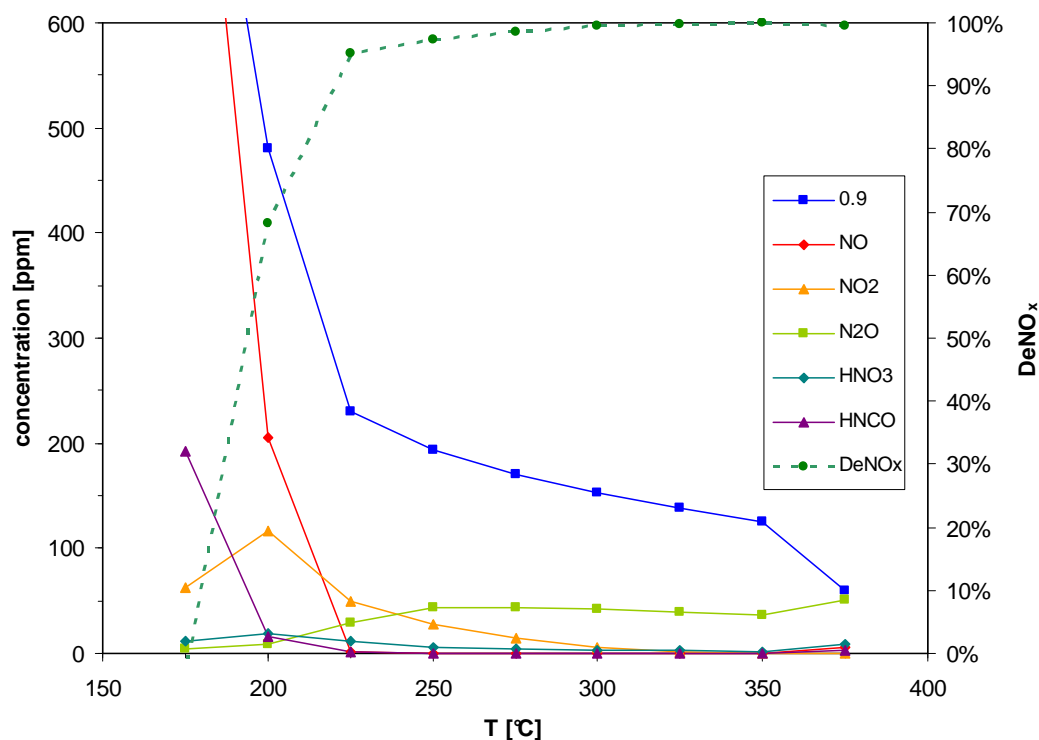
Figure 7-15: DeNO$_x$ efficiencies and product gas composition during dosage of a stoichiometric NH$_4$NO$_3$-urea solution on a Fe-exchanged zeolite SCR catalyst at various temperatures (50,000 h^{-1}; 1,000 ppm NO; 600 ppm urea; 600 ppm NH$_4$NO$_3$).

In comparison to the results for the vanadia-based catalysts, DeNO$_x$ efficiency is improved significantly down to 225°C, however, below 225°C DeNO$_x$ rates decrease dramatically to 0% at 175°C. Likewise, the NH$_3$-slip and NO-emissions increase at the low temperature end. As NO emissions were not present above 225°C, full conversion by *fast-SCR* is assumed to have occurred. Excess NO$_2$ from reaction with the excess NH$_4$NO$_3$ was also emitted, but most of the dosed nitrate was rather found as N$_2$O at the reactor outlet. The high NH$_3$-slip indicated that N$_2$O was mostly formed by direct NH$_4$NO$_3$ decomposition according to 7-14. The reaction became less pronounced at lower temperatures. At 175°C even HNCO emissions of 192 ppm could be detected, pointing towards an insufficient hydrolysis of urea. In combination with the high emission of other components, and the

low $DeNO_x$ rates, it is concluded that the fine pores of the Fe-exchanged zeolite were obstructed by NH_4NO_3 salt formation, which completely quenched SCR and furthermore hindered urea hydrolysis.

Last, the effect of NH_4NO_3 dosing on the commercial Cu-exchanged zeolite catalyst was investigated within the temperature range. The results are shown in Figure 7-16.
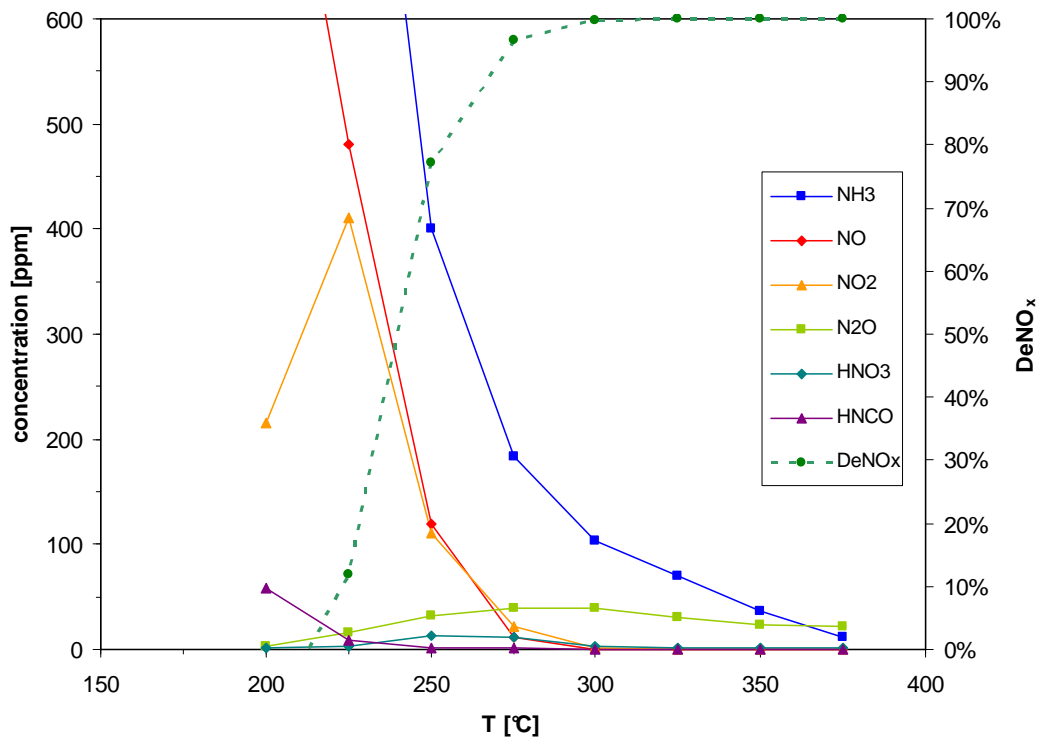
Figure 7-16: $DeNO_x$ efficiencies and product gas composition during dosage of a stoichiometric NH_4NO_3-urea solution on a Cu-exchanged zeolite SCR catalyst at various temperatures (50,000 h^{-1}; 1,000 ppm NO; 600 ppm urea; 600 ppm NH_4NO_3).

First, one realizes that the lowest temperature which was tested was no longer 175°C, because already at 200°C $DeNO_x$ activity on the catalyst ceased. Again, like on the Fe-exchanged zeolite catalyst, the drop from very good conversions above 95% to zero was very steep, in this case from 275°C to 200°C. NO and NO_2 emissions followed the same pattern, though in different direction, going from zero to several hundred ppms
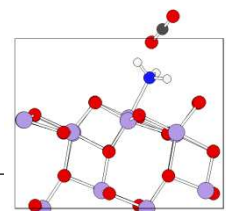
from 300°C to 225°C. The NH_3-slip was almost zero at 375°C, it gradually increased with lower temperatures, even though $DeNO_x$ remained at 100%. At 375°C, overdosage led only to minimal emissions of NH_3 and N_2O, which indicated NH_3 oxidation to N_2 by the catalyst. At its maximum, N_2O reached concentrations of 40 ppm. The N_2O formation went to zero as 200°C was reached, but at this temperature $DeNO_x$ activity vanished completely, and even 58 ppm of HNCO were detected. Again, the HNCO indicated insufficient urea hydrolysis, as the entire catalyst was inactivated by the deposited NH_4NO_3.

From the experiments with varying NO_2/NO_x ratios, however, it was seen that higher $DeNO_x$ rates on the Cu-exchanged zeolite catalyst could be reached if NH_4NO_3 dosing was halted.

7.3.4. Discussion of the NH_4NO_3-decomposition mechanism

The *enhanced-SCR* mechanism proposed by Forzatti et al. is part of the general *fast-SCR* mechanism proposed by them and others previously. [341,335,342,330]

In this mechanism, NO_2 first forms N_2O_4 which then disproportionates with water to HONO and HNO_3 (reactions 7-20 and 7-21). HONO then forms NH_3NO_2 (7-22), which decomposes to yield N_2 according to reaction 7-8, while HNO_3 starts to enter the reaction network as in reaction 7-6.

$$2\ NO_2\ \rightleftharpoons\ N_2O_4 \qquad\qquad \textbf{7-20}$$

$$N_2O_4\ +\ H_2O\ \longrightarrow\ HONO\ +\ HNO_3 \qquad\qquad \textbf{7-21}$$

$$HONO\ +\ NH_3\ \longrightarrow\ NH_4NO_2 \qquad\qquad \textbf{7-22}$$
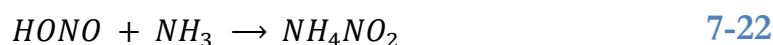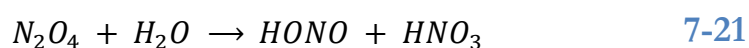
Thus, the addition of NH_4NO_3 is considered to be a shortcut to *fast-SCR*, because reactions 7-20 and 7-21 are no longer necessary.

The reaction of HNO_3 with NO, according to 7-6, represents an elegant mechanism that transforms HNO_3 into HONO, an indirect precursor of N_2 and, thus, already virtually reduces one NO_x to N_2. At the same time, NO is oxidized to NO_2, which is thought to be the rate-determining step in *standard-SCR*. [343]

However, an alternative route for the reaction of NH_4NO_3 exists, which was discussed in previous works on elucidating the *fast-SCR* mechanism. [87] HNO_3 reduction with NO does not proceed all the way to HONO, but only to NO_2 as shown in reaction 7-23.

$$2\ HNO_3 + NO\ \rightarrow\ 3\ NO_2 + H_2O \qquad\qquad \text{7-23}$$
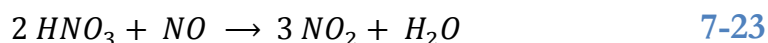
HNO_3 and NO comproportionate to NO_2, which needs to be converted in the *fast-SCR* according to 7-9, rather than already converting half of the NO_x to the labile HONO species. Overall, the stoichiometry of inserted NO, dosed NH_4NO_3 and NH_3 necessary for reduction is maintained, but in this mechanism the inserted NH_4NO_3 generates more interaction than just oxidizing NO to NO_2, while being transformed to NH_4NO_2 and decomposing to N_2.

As the performed experiments were focused on observing whether NH_4NO_3 addition in general is beneficial for NO reduction, and determining the optimum parameters for this reaction, no detailed investigations concerning the reaction mechanism were performed. However, during evaluation of the experiments which were concerned with the optimum NO_2/NO_x ratio, some surprising results were obtained, while considering the *enhanced-SCR* mechanism as introduced in 7-6 to 7-8. Calculation of $DeNO_x$ using formula 7-19 yielded negative values, as there were more NO_x coming out of the reactor than inserted. If NH_4NO_3 decomposition proceeded only by reactions 7-6 to 7-8, then even
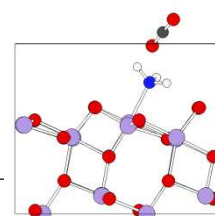
incomplete decomposition should not have caused the observed results, because the concentration of HNO_3 was not considered in formula 7-19. Thus, the measurements were evaluated assuming the mechanism 7-23 for the reaction of HNO_3 from NH_4NO_3 dissociation. $DeNO_x$ was calculated according to formula 4-3.

$$DeNO_{x\,(NO-based')} = \frac{NO_{(in)} - (NO_{(out)} + \frac{NO_{2\,(out)}}{3} + \frac{2\,N_2O_{(out)}}{3})}{NO_{(in)}} \quad \textbf{7-24}$$

The calculated alternative NO-based $DeNO_x$ activities for the experiments using the Fe-exchanged zeolite and the Cu-exchanged zeolite are plotted along with previously calculated $DeNO_x$ activities.

The results for the Fe-exchanged zeolite are shown in Figure 7-17.

Figure 7-17: DeNO$_x$ efficiency in dependence of NO$_2$/NO$_x$ ratio on a commercial Fe-exchanged SCR catalyst, calculated considering different NH$_4$NO$_3$ decomposition mechanisms (50,000 h^{-1}; 1,000 ppm NO$_x$; 1,000 ppm NH$_3$; 200°C).

Up to an NO_2/NO_x ratio of 0.4, the mechanism considered for the calculation is not relevant, as both mechanisms will provide an identical curve. Above this ratio, the alternative NH_4NO_3 decomposition meachnism

will show a slightly higher increase to the equimolar ratio at 0.5. The main difference, however, is the much steeper decrease of $DeNO_x$ activity exhibited by the regular formula, which extends all the way to negative values. The alternative mechanism calculation will only result in a minimum value of 40% $DeNO_x$ for the theoretically pure NO_2 feed. From this value, 4.3% *NO_2-SCR* $DeNO_x$ according to 7-15, can be substracted, as calculated from the measured N_2O emissions. The remaining NO_x conversion is assumed to be *NO_2-SCR* according to reaction 7-4. From the stoichiometry, an efficiency of 47% in this SCR reaction is calculated, which is in good agreement with published works on the efficiency of Fe-exchanged zeolite in this reaction. [**343**]

The experiment using Cu-exchanged zeolite was also re-evaluated considering the alternative NO-based $DeNO_x$, the result is shown in Figure 7-18.
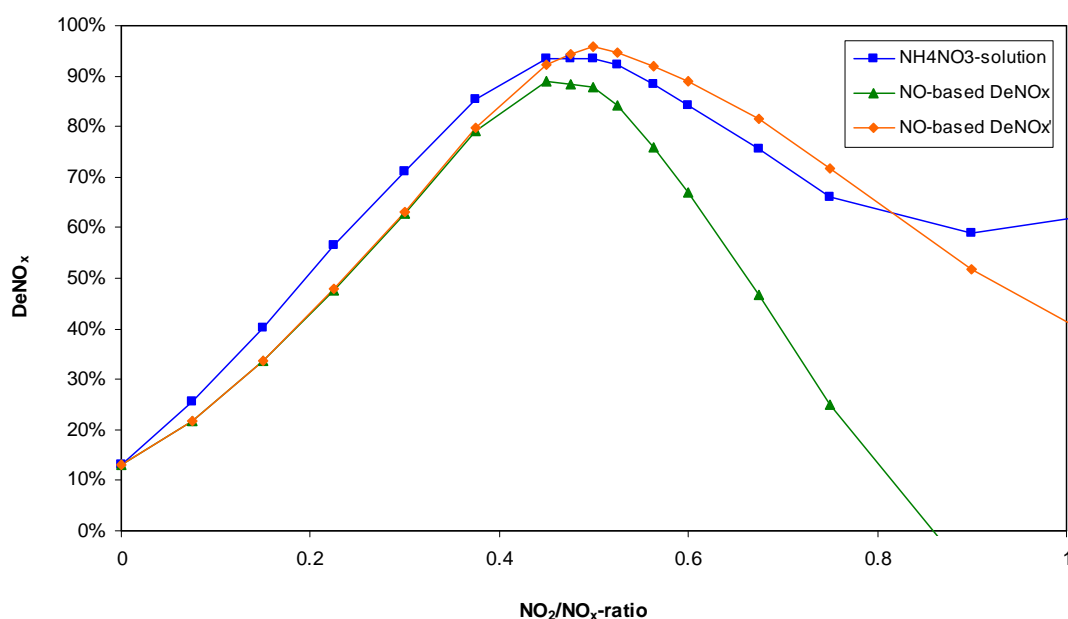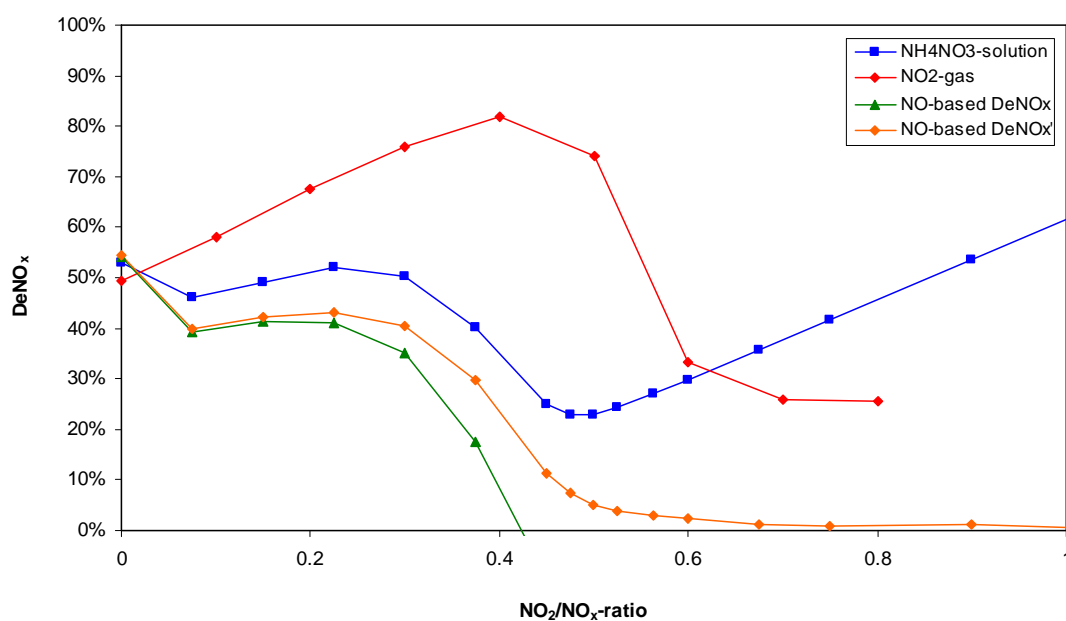

Figure 7-18: DeNO_x efficiency in dependence of NO_2/NO_x ratio on a commercial Fe-exchanged SCR catalyst, calculated considering different NH_4NO_3 decomposition mechanisms (50,000 h^{-1}; 1,000 ppm NO_x; 1,000 ppm NH_3; 200°C).
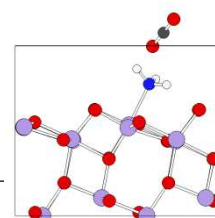
Up to an NO_2/NO_x ratio of 0.2 the deviations between the two reaction mechanisms are very small, but increasing the ratio results in a much smaller decrease in $DeNO_x$ for the alternative mechanism. In fact, the curve calculated considering the alternative mechanism leads to an asymptotic decrease towards 0% $DeNO_x$ activity, rather than to negative values as for the other mechanism. The calculated $DeNO_x$ activity according to the alternative mechanism is, therefore, assumed to actually display the real $DeNO_x$ activity.

From these results, it can be concluded that the alternative mechanism, as described in 7-23, is by far the dominant route for NH_4NO_3 processing on the catalyst. These results provide new insight into the *fast-SCR* mechanism, because this alternative route has not been considered in recent works. [**343,341,330**]

The fact that the alternative mechanism is dominant could also explain why NH_4NO_3 addition did not lead to a shortcut in the *fast-SCR* mechanism, just an upstream reaction converting part of the NO to NO_2. Where this reaction did not proceed efficiently, like on Cu-exchanged zeolite, the overall observed $DeNO_x$ activity was the same as regular *standard-SCR*.

7.4. Conclusion

Experiments concerning the combined dosing of NH_4NO_3 and urea on commercial SCR catalysts were made, in order to investigate the recently presented *enhanced-SCR* under realistic conditions. NH_4NO_3 addition in stoichiometric amounts did not show a boost in $DeNO_x$ activity comparable to *fast-SCR*, for any of the catalysts. While a beneficial effect was observed for the case of the vanadia-based and Fe-exchanged zeolite

catalysts, the Cu-exchanged zeolite catalyst actually showed decreasing $DeNO_x$ performance when NH_4NO_3 was dosed.

From experiments concerning the determination of the optimum amount of NH_4NO_3 addition, it could be clearly shown that the *enhanced-SCR* mechanism is not relevant. Instead, an alternative mechanism previously proposed as a route for *fast-SCR* dominates.

These results for commercial catalysts will most likely lead to several additional experiments on determining the mechanism of NH_4NO_3 addition on model catalysts, because it is so closely related to the *fast-SCR* mechanism, which is of high relevance for commercial SCR systems.
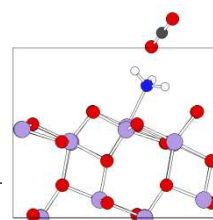
8. Summary and Outlook

8.1. Summary

This thesis consists of the following subprojects: Developing and testing of an experimental setup for the investigation of NH_3-precursor compound solutions, exploring the decomposition pathways for guanidinium formate, developing and testing of a noble metal-doped catalyst for the efficient decomposition of guanidinium formate and related compounds, presenting a novel approach for the decomposition of NH_3-precursor compound solutions in the liquid phase, and studying the effect of ammonium nitrate addition to AdBlue® to increase low-temperature SCR.

Testing of the constructed setup revealed that near-ideal conditions for the investigation of NH_3-precursor solutions were achieved, which allowed the investigation of solutions containing urea, guanidinium formate, ammonium formate, methanamide and ammonium nitrate in this thesis. The setup has also been used extensively in works on the urea decomposition mechanism and its possible side products.

Guanidinium formate decomposition pathways were explored by TPD experiments and DFT calculations. From the experiments, the final reactions products are obtained. The DFT calculations were restricted to a crystal surface of titanium dioxide in the anatase phase, without kinks or defects, and to reactions considered realistic based on the measured experimental reaction products. A gap remains between the experimentally determined reaction products and the reaction mechanism proposed by DFT simulations, because the proposed mechanisms cannot be proved directly by current experimental observations.
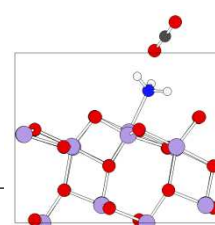
Au/TiO$_2$ was shown to efficiently decompose guanidinium formate to ammonia and carbon dioxide, without the formation of toxic side products or ammonia oxidation. The high efficiency of the catalyst is due to good formic acid decomposition activity. Formic acid decomposition requires the presence of oxygen. Without it, formic acid decomposition will be reduced and proceeds mainly to carbon monoxide. Oxygen participation was, thus, concluded to be not only restricted to carbon monoxide oxidation on the Au/TiO$_2$ catalyst. Palladium-doped catalysts were shown to be only a good alternative to gold-doped catalysts under oxygen-free conditions, as ammonia oxidation could then be eliminated. The Au/TiO$_2$ catalyst was transferred to the research project partners, and after its successful investigation on a Diesel test stand, it was transferred to a company offering exhaust aftertreatment solutions in retrofit applications.

Decomposition of urea solution in the liquid phase showed only slight acceleration of the hydrolysis reaction by commercial catalyst materials. From the calculated activation energies, mass transfer limitations are excluded. However, even with uncatalyzed urea decomposition, the overall size of the system is very compact compared to conventional spray decomposition setups. For alternative NH$_3$-precursor materials requiring decomposition catalysts the system could become very interesting as a compact converter unit. In particular, the evolving of hydrogen from the decomposition of formic acid derived compounds is an attractive product.

The addition of ammonium nitrate proposed recently to create *fast-SCR* similar conditions, was shown not to meet the theoretical expectations on commercial SCR catalysts. In some cases the addition of ammonium nitrate even had a detrimental effect on SCR performance. From experiments

dealing with the optimum dosage of ammonium nitrate, evidence of a currently overlooked reaction mechanism for *fast-SCR* were identified.

8.2. Outlook

The presented experimental setup is currently used for investigations on the urea decomposition mechanism for a parallel PhD thesis. The publication of the experimental setup also led to an assignment from industry to measure isocyanic acid emissions during SCR with AdBlue®. In the near future, other commercial measurement assignments regarding the decomposition of AdBlue®, in combination with SCR on industrial catalysts, could follow. Certainly, the setup will remain an important element for the follow-up PhD thesis, dealing with noble metal doped catalysts for the decomposition of formic acid derived compounds.

The modeling of the reaction mechanism considered exclusively a pure TiO_2 (anatase) catalyst. The later developed Au/TiO_2 catalyst with significantly improved decomposition activity is an interesting follow-up project. However, DFT simulations will need to be combined with experiments targeting the detailed investigation of the reaction mechanism, in order to provide conclusive proof for certain reaction mechanisms. Similar works on Au/TiO_2 catalysts for carbon monoxide oxidation indicate that DFT results are very susceptible to the various simplifications assumed in the calculations, which leads to a continuing discussion concerning the active site in catalysis.

A follow-up project on the decomposition of NH_3-precursor compounds would certainly feature works on noble metal-doped decomposition catalysts. The observed high selectivity and activity of Au/TiO_2 even after hydrothermal aging still remains to be fully understood. The combination
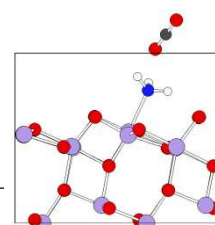
of experiments in the laboratory setup and sophisticated analytical techniques, such as HAADF-STEM, would provide a deeper understanding of the structure-function relationship of the catalyst. Characterization of the catalyst under operating conditions using e.g. X-ray absorption spectroscopy (XAS) could eventually also yield information about the active species involved in the catalytic decomposition reaction. This could be used to prepare even more active and/or stable catalysts, by (i) replacing the titanium dioxide support structure with other hydrolysis active materials such as aluminum oxide, (ii) choosing gold alloys like gold/palladium as noble metal dopant or (iii) trying even core-shell catalysts consisting of an outer gold shell layer with a platinum metal group core. After successful testing under realistic conditions with model Diesel exhaust gas, the newly developed catalysts could again be transferred to the industrial project partners with the aim of eventually leading to improved alternative NH_3-precursor based systems for mobile applications.

Decomposition of NH_3-precursor compounds under elevated pressure would lead not only to a compact system to provide the necessary reducing agent for SCR, but in case of simultaneous hydrogen production, the product gas could be used for other applications as well. By further reforming the produced ammonia to hydrogen, the proposed NH_3-precursor compounds would suit as hydrogen storage compounds. Without reforming of ammonia, the product gas is still a highly energetic gas mixture which can be burnt for propulsion or power generation. Similar solutions were proposed in the past, some have been successfully employed in niche markets, but the simplicity of the system in this thesis could provide additional opportunities.

The mainly empirical works on *enhanced-SCR* provided valuable information about the applicability in commercial systems, but also led to a reconsideration of the currently proposed reaction mechanism for *fast-SCR* in general. These indications could lead to novel experiments focusing on the detailed examination of the SCR reaction by researchers in this field. The constructed experimental setup provides the unique opportunity to also conduct experiments with dosing of urea, ammonium nitrate or nitric acid solutions during SCR in model exhaust gas in order to test various hypotheses.
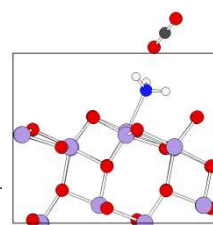
9. References

[1] R. N. Colvile, E. J. Hutchinson, J. S. Mindell, and R. F. Warren, *Atmos. Environ.*, *35*, 2001, pp. 1537-1565.

[2] R. J. Laumbach and H. M. Kipen, *J. Allergy Clin. Immun.*, *129*, 2012, pp. 3-13.

[3] F. J. Kelly and J. C. Fussell, *Clin. Exp. Allergy*, *41*, 2011, pp. 1059-1071.

[4] W. Grünert, H. Papp, C. Rottländer, and M. Baerns, *Chem. Tech-Leipzig*, *47*, 1995, pp. 205-216.

[5] M. V. Twigg, *Appl. Catal. B-Environ.*, *70*, 2007, pp. 2-15.

[6] S. Carli and B. Heller, "Messung der Partikelanzahl für Euro 5 - eine Herausforderung?" *9. FAD-Konferenz: Herausforderung - Abgasnachbehandlung für Dieselmotoren*, Dresden, 2011.

[7] L.-E. Schulte, "Euro VI für Nutzfahrzeugmotoren - Ein neuer Ansatz im Genehmigungsverfahren für Nutzfahrzeugmotoren" *9. FAD-Konferenz: Herausforderung - Abgasnachbehandlung für Dieselmotoren*, Dresden, 2011.

[8] M. Mehring, *Composition and reactivity analysis of diesel soot with advanced FTIR spectroscopy and a new TG-FTIR system at the example of the oxidation with O2, NO2 and H2SO4 and the SCR reaction with NOx and NH3.* ETH Zürich: Diss. ETH No. 19993, 2011.
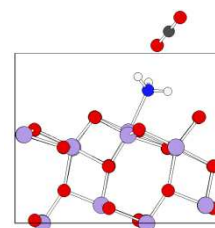
[9] Y. B. Zeldovich, *Acta Physiochem. USSR*, *21*, 1946, pp. 577-656.

[10] K. Saito and S. Ichihara, *Catal. Today*, *10*, 1991, pp. 45-56.

[11] D. Hofmann, B. Mencher, W. Häming, and W. Hess, "Grundlagen des Ottomotors" in *Bosch Grundlagen Fahrzeug- und Motorentechnik*. Wiesbaden: Vieweg+Teubner Verlag, 2011, pp. 44-59.

[12] K. C. Taylor, *Catal. Rev.*, *35*, 1993, pp. 457-481.

[13] T. Raatz, "Grundlagen des Dieselmotors" in *Bosch Grundlagen Fahrzeug- und Motorentechnik*. Wiesbaden: Vieweg+Teubner Verlag, 2011, pp. 14-31.

[14] H. Schulz, G. Bandeira De Melo, and F. Ousmanov, *Combust. Flame*, *118*, 1999, pp. 179-190.

[15] M. M. Maricq, D. H. Podsiadlik, D. D. Brehob, and M. Haghgooie, *SAE technical paper*, 1999-01-1530.

[16] D. Dahl, I. Denbratt, and L. Koopmans, *SAE technical paper*, 2008-01-0426.

[17] R. van Basshuysen, *Gasoline engine with direct injection*. Wiesbaden: Vieweg+Teubner Verlag, 2009.

[18] K. Epping, S. Aceves, R. Bechtold, and J. Dec, *SAE technical paper*, 2002-01-1923.

[19] S. M. Aceves et al., *SAE technical paper*, 2004-01-1910.

[20] S. Hemdal, M. Andersson, P. Dahlander, R. Ochoterena, and I.

Denbratt, *Int. J. Engine Res.*, *12*, 2011, pp. 549-563.

[21] H. Tschoeke et al., "Diesel engine exhaust emissions" in *Handbook of Diesel engines*. Berlin: Springer-Verlag, 2010, pp. 417-485.

[22] "Key Events in the History of Air Quality in California" 06.02.2012 [Online]. URL: http://www.arb.ca.gov/html/brochure/history.htm.

[23] "Euro 1 standards" *Official Journal of the European Union*, 1991, p. Regulation No. 91/441/EEC.

[24] "Euro 2 standards" *Official Journal of the European Union*, 1994, p. Regulation No. 94/12/EC.

[25] "Euro 3/4 standards" *Official Journal of the European Union*, 1998, p. Regulation No. 98/69/EC.

[26] "Euro 5/6 standards" *Official Journal of the European Union*, 2007, p. Regulation No. 715/2007.

[27] "Emission Standards: Europe: Heavy-Duty Diesel Truck and Bus Engines" 01.09.2009 [Online]. URL: http://dieselnet.com/standards/eu/hd.php.

[28] R. F. Sawyer, *J. Expo. Sci. Env. Epid.*, *20*, 2010, pp. 487-488.

[29] T. Johnson, *SAE technical paper*, 2012-01-0368.

[30] G. Greeves, I. M. Khan, and G. Onion, "Effects of Water Introduction on Diesel Engine Combustion and Emissions" *16th Symposium (International) on Combustion*, Pittsburgh, PA, USA, 16 1977,
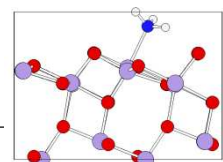
pp. 321-336.

[31] T. V. Johnson, *Int. J. Engine Res.*, *10*, 2009, pp. 275-285.

[32] A. Traebert, L. Zimmermann, R. Frey, and T. Johansson, "Investigation of a Combined Exhaust After-Treatment System for Commercial Vehicles" , Berlin, Germany, 2010.

[33] P. Granger and V. I. Parvulescu, *Chem. Rev.*, *111*, 2011, pp. 3155-3207.

[34] S. Ichihara et al., *SAE technical paper*, 1994-940928.

[35] J. G. Nunan, W. B. Willianson, H. J. Robota, and M. G. Henk, *SAE technical paper*, 1995-950258.

[36] Bosch Media Service. "Bosch Spare Parts Range Offers the Right Oxygen Sensor for Almost Every Vehicle "14.09.2010 [Online]. URL: http://www.bosch-presse.de/presseforum/details.htm?txtID=4797&tk_id=109.

[37] M. V. Twigg et al., *SAE technical paper*, 2002-01-0351.

[38] M. V. Twigg, *Philos. T. R. Soc. A*, *363*, 2005, pp. 1013-1033.

[39] M. V. Twigg, *Catal. Today*, *163*, 2011, pp. 33-41.

[40] P. N. Hawker, *Platinum Metals Rev.*, *39*, 1995, pp. 2-8.

[41] A. P. E. York et al., *SAE technical paper*, 2005-01-0954.

[42] B. J. Cooper and J. Thoss, *SAE technical paper*, 1989-890404.

[43] R. Allansson et al., *SAE technical paper*, 2004-01-0072.

[44] J. Kitagawa, T. Hijikata, and S. Yamada, *SAE technical paper*, 1991-910136.

[45] M. Khair, *SAE technical paper*, 2003-01-2303.

[46] W. A. Cutler et al., *SAE technical paper*, 2007-01-1268.

[47] L. J. Gill, P. G. Blakeman, M. V. Twigg, and A. P. Walker, *Top. Catal.*, *28*, 2004, pp. 157-164.

[48] W. Bögner et al., *Appl. Catal. B-Environ.*, *7*, 1995, pp. 153-171.

[49] G. Centi and S. Perathoner, "Chapter 1 Introduction: State of the art in the development of catalytic processes for the selective catalytic reduction of NOx into N2" in *Past and Present in DeNOx Catalysis - From Molecular Modelling to Chemical Engineering.* Amsterdam, Netherlands: Elsevier, 2007, pp. 1-23.

[50] S. Matsumoto, *Catal. Today*, *29*, 1996, pp. 43-45.

[51] W. S. Epling, L. E. Campbell, A. Yezerets, N. W. Currier, and J. E. Parks, *Catal. Rev.*, *46*, 2004, pp. 163-245.

[52] S. Matsumoto, *Catal. Surv. Jpn.*, *1*, 1997, pp. 111-117.

[53] S. Poulston and R. R. Rajaram, *Catal. Today*, *81*, 2003, pp. 603-610.

[54] J. G. E. Cohn, "Method of removing nitrogen oxides from gases" US3118727, 12.10.1956.
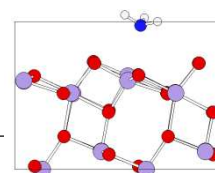
[55] J. G. E. Cohn, "Method of selectively removing oxides of nitrogen from oxygen-containing gases" US2975025, 05.11.1957.

[56] M. Huuhtanen, T. Maunula, and R. L. Keiski, *Stud. Surf. Sci. Catal.*, *158*, 2005, pp. 1867-1874.

[57] S. Niemi et al., *SAE technical paper*, 2009-01-2880.

[58] H. Hirabayashi et al., *SAE technical paper*, 2011-01-1277.

[59] A. Lahougue et al., *SAE technical paper*, 2011-01-2092.

[60] Y. F. Tham, J.-Y. Chen, and R. W. Dibble, *P. Combust. Inst.*, *32*, 2009, pp. 2827-2833.

[61] X. Shi et al., *J. Environ. Sci.*, *20*, 2008, pp. 177-182.

[62] E. Frank, H. Oguz, and W. Weisweiler, *Chem. Eng. Technol.*, *6*, 2003, pp. 679-683.

[63] P. Granger et al., *Top. Catal.*, *39*, 2006, pp. 65-76.

[64] J. H. Jones, J. T. Kummer, K. Otto, M. Shelef, and E. E. Weaver, *Environ. Sci. Technol.*, *9*, 1971, pp. 790-798.

[65] R. Burch, P. J. Milington, and A. P. Walker, *Appl. Catal. B-Environ.*, *4*, 1994, pp. 65-94.

[66] M. Richter, R. Fricke, and R. Eckelt, *Catal. Lett.*, *94*, 2004, pp. 115-118.

[67] E. Kondratenko, V. A. Kondratenko, M. Richter, and R. Fricke, *J.*

Catal., *239*, 2006, pp. 23-33.

[68] K.-I. Shimizu and A. Satsuma, *Appl. Catal. B*, *77*, 2007, pp. 202-205.

[69] R. Fricke, M. Richter, R. Eckelt, and D. Captain, "Selective catalytic reduction of nitrogen oxides with ammonia and oxygen, useful for purifying stationary or mobile engine exhaust gas and waste gas from nitric acid manufacture, uses added hydrogen and catalyst containing silver" DE10261817, 19.12.2002.

[70] A. N. Rollinson, G. L. Rickett, A. Lea-Langton, V. Dupont, and M. V. Twigg, *Appl. Catal. B-Environ.*, *106*, 2011, pp. 304-315.

[71] R. Lan, J. T. S. Irvine, and S. W. Tao, *Int. J. Hydrogen Energy*, *37*, 2012, pp. 1482-1494.

[72] M. V. Twigg and I. C. Wishart, "The use of urea in catalytic production of hydrogen" GB2458994, 11.04.2008.

[73] Z. Liu and S. I. Woo, *Cataly. Rev.*, *48*, 2006, pp. 43-89.

[74] S. Hu et al., *Atmos. Environ.*, *43*, 2009, pp. 2950-2959.

[75] D. M. Chapman, *Appl. Catal. A-Gen.*, *392*, 2011, pp. 143-150.

[76] M. M. Shafer et al., *Environ. Sci. Technol.*, *46*, 2012, pp. 189-195.

[77] Z. Liu, N. Ottinger, and C. Cremeens, *SAE technical paper*, 2012-01-0887.

[78] G. Cavataio et al., *SAE technical paper*, 2007-01-1575.
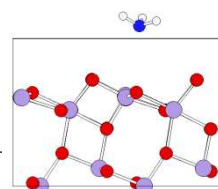
[79] R. Q. Long and R. T. Yang, *J. Catal.*, *201*, 2001, pp. 145-152.

[80] S. Brandenberger, *Selektive katalytische Reduktion (SCR) von NO mit NH3 über Fe-ZSM-5: Identifizierung der aktiven Zentren, hydrothermale Desaktivierung und Stabilisierung.* Thesis No. 18867: ETH Zürich, 2010.

[81] T. V. Johnson, *SAE technical paper*, 2011-01-0304.

[82] X. Hou, W. Epling, S. Schmieg, and W. Li, *SAE technical paper*, 2011-01-1138.

[83] D. M. Chapman et al., *SAE technical paper*, 2010-01-1179.

[84] J. Girard, C. Montreuil, J. Kim, G. Cavataio, and C. Lambert, *SAE technical paper*, 2008-01-1029.

[85] M. Koebel, M. Elsener, and M. Kleemann, *Catal. Today*, *59*, 2000, pp. 335-345.

[86] A. Kato et al., *J. Phys. Chem.-US*, *85*, 1981, pp. 4099-4102.

[87] M. Koebel, G. Madia, and M. Elsener, *Catal. Today*, *73*, 2002, pp. 239-247.

[88] F. Klingstedt, K. Arve, K. Eränen, and D. Y. Murzin, *Accounts. Chem. Res.*, *39*, 2006, pp. 273-282.

[89] M. Folic, L. Lemus, I. Gekas, and A. Vressner, "Selective Ammonia Slip Catalyst Enabling Highly Efficient NOx Removal Requirements of the Future" *US DOE "Directions in Engine Efficiency and Emissions Research (DEER) Conference"*, Detroit, MI, USA, 2010.

[90] K. Kamasamudram, C. Henry, and A. Yezerets, "N2O Emissions from 2010 SCR Systems" *US DOE "Directions in Engine Efficiency and Emissions Research (DEER) Conference"*, Detroit, MI, USA, 2011.

[91] S. Roy, M. S. Hegde, and G. Madras, *Appl. Energ., 86*, 2009, pp. 2283-2297.

[92] Y. Nakabayashi, H. Yugami, and K. Mouri, "Development of Flue Gas Treatment in Japan" *Proceedings of the Joint Symposium on Stationary Combustion NOx Control Volume III*, Denver, CO, USA, 1980.

[93] J. E. Cichanowicz and L. J. Muzio, "Twenty-Five Years of SCR Evolution: Implications For US Application And Operation" *Proceedings of the U.S EPA-DOE-EPRI Combined Power Plant Air Pollutant Control Mega Symposium and The A&WMA Specialty Conference on Mercury Emissions: Fate, Effects, and Control*, Chicago, IL, USA, 2001.

[94] S. C. Stultz, "Nitrogen Oxides Control" in *Steam - its generation and use Edition: 41*. Charlotte, NC, USA: The Babcock & Wilcox Company, 2005, pp. 34-1 - 34-15.

[95] J. D. Mobley, "Assessment of NOx Flue Gas Treatment Technology" *Proceedings of the Joint Symposium on Stationary Combustion NOx Control Volume III*, Denver, CO, USA, 1980.

[96] E. Hums, *Catal. Today, 42*, 1998, pp. 25-35.

[97] J. E. Cichanowicz, L. J. Muzio, and M. C. Hein, "The First 100 GW of SCR in the U.S. - What Have We Learned?" *Proceedings of the U.S EPA-DOE-EPRI-A&WMA Power Plant Air Pollutant Control Mega*

Symposium, Baltimore, MD, USA, 2006.

[98] X. Guo, C. Bartholomew, W. Hecker, and L. L. Baxter, *Appl. Catal. B-Environ.*, *92*, 2009, pp. 30-40.

[99] Y. Wada and K. Yamatsuta, "Treating exhaust gases contg. nitrogen oxide(s) - by adding granules of cyanuric acid, urea or ammonium cpd., and an organic cpd. having nitrile gp." JP54028771, 08.08.1977.

[100] R. A. Perry and D. L. Siebers, *Nature*, *324*, 1986, pp. 657-658.

[101] R. A. Perry, *J. Chem. Phys.*, *82*, 1985, pp. 5485-5488.

[102] R. A. Perry, "NO reduction using sublimation of cyanuric acid" US4731231, 05.05.1986.

[103] R. A. Perry, "System for NO reduction using sublimation of cyanuric acid "US4800068, 23.03.1987.

[104] R. A. Gardner-Chavis and M. P. May, "Catalytic decomposition of cyanuric acid and use of product to reduce nitrogen oxide emissions" US5087431, 20.09.1990.

[105] D. L. Siebers and J. A. Caton, *Combust. Flame*, *79*, 1990, pp. 31-46.

[106] J. A. Caton and D. L. Siebers, *Combust. Sci. Technol.*, *65*, 1989, pp. 277-293.

[107] Wolfgang Held and Axel König, "Verfahren und Vorrichtung zur Reduktion von Stickoxiden" DE3642018, 09.12.1986.

[108] Wolfgang Held, Axel König, and Lothar Puppe, "Verfahren zur

Reduktion von in Abgasen enthaltenen Stickoxiden mittels eines zeolithhaltigen Katalysators" DE3830045, 03.08.1988.

[109] W. E. Bowers, "Reduction of nitrogen-based pollutants through the use of urea solutions containing oxygenated hydrocarbon solvents" US4719092, 04.10.1985.

[110] Wolfgang Held, Axel König, Thomas Richter, and Lothar Puppe, "Catalytic NOx Reduction in Net Oxidizing Exhaust Gas" *SAE technical paper*, 1990-900496.

[111] E. Jacob, "Process and device for selective catalytic NOx reduction in exhaust gases containing oxygen" EP487886, 29.11.1990.

[112] D. Fromm and D. Lützow, *Chem. unserer Zeit*, *13*, 1979, pp. 78-81.

[113] A. M. Bernhard, D. Peitz, M. Elsener, and O. Kröcher, *Top. Catal.*, *submitted*, 2012.

[114] W. Weisweiler and F. Buchholz, *Chem. Ing. Tech.*, *73*, 2001, pp. 882-887.

[115] S. Käfer, W. Müller, A. Herr, and A. Lacroix, "Process and assembly to release urea pellets to automotive exhaust gases at a controlled rate regulated by a rotating disc with compressed air supply" DE10251498, 04.11.2002.

[116] W. Müller, A. Herr, S. Käfer, A Lacroix, and E. Jacob, "SCR using solid urea" *Proceedings of the 3rd Internation Exhaust Gas and Particulate Emissions Forum*, Sinsheim, Germany, 2004.

[117] E. Jacob, W. Müller, A. Herr, S. Käfer, and A. Lacroix, "Process and apparatus for producing ammonia" DE10206028, 14.02.2002.

[118] H. Dismon, A. Köster, R. Lappan, M. Nowak, and W. Müller, "Vorrichtung zur Reduktion von Stickoxiden im Abgas von Brennkraftmaschinen" DE102006004170, 27.01.2006.

[119] J. F. T. Berliner, *Ind. Eng. Chem.*, *28*, 1936, pp. 517-522.

[120] "Diesel engines — NOx reduction agent AUS 32 — Part 1: Quality requirements" in *International Standard 22241-1.*, 2006-10-15.

[121] J. Thompson, J. Op De Beeck, E. Joubert, and T. Wilhelm, *SAE technical paper*, 2008-01-1181.

[122] "Diesel engines - NOx reduction agent AUS 32 - Part 3: Handling, transportation and storage" in *International Standards ISO 22241-3.*, Feb. 2008-02-15.

[123] P. L. T. Gabrielsson, *Top. Catal.*, *28*, 2004, pp. 177-184.

[124] F. F. Mao and C. G. Li, "Urea-Ethanol-Water Solution Properties for Diesel NOx Control Using Urea" *Presentations of the 6th Diesel Engine Emissions Reduction (DEER) Workshop*, San Diego, CA, USA, 2000.

[125] C. Lambert, C. Montreuil, and J. Vanderslice, *SAE Technical Paper*, 2003-01-0775.

[126] A. Solla et al., *SAE technical paper*, 2005-01-1856.

[127] R. K. Lyon, "Method for the reduction of the concentration of NO in combustion effluents using ammonia" US3900554, 16.03.1973.

[128] A. Marko et al., "Verfahren und Vorrichtung zur selektiven katalytischen NOx-Reduktion" DE19728343, 03.07.1997.

[129] M. Koebel and M. Elsener, *Ind. Eng. Chem. Res.*, *37*, 1998, pp. 3864-3868.

[130] Timo Nissinen and Jari Kukkonen, "Catalytic process for reducing nitrogen oxides in flue gases and reducing agent composition" FI2004000057, 04.02.2004.

[131] T. Highfield, "Lower Freezing DEF For Higher NOx Reduction Attainment" *Presentations of the Directions in Engine-Efficiency and Emissions Research (DEER) Conference*, Detroit, MI, USA, 2011.

[132] "Kemira and Terra Environmental Technologies Inc. signed license agreement of Kemira's Denoxium" 11.09.2008 [Online]. URL: http://www.kemira.com/en/media/whatsup/Pages/KemiraTerra Denoxium.aspx.

[133] S. Y. Lee and S. W. Baek, *Ind. Eng. Chem. Res.*, *50*, 2011, pp. 8285-8294.

[134] R. Gassen, H. Gohr, N. Muller, and J. Vehlow, *Z. Werkstofftechnik*, *17*, 1986, pp. 218-225.

[135] M. M. Singh and A. Gupta, *Mater. Chem. Phys.*, *46*, 1996, pp. 15-22.

[136] S. K. Singh, A. K. Mukherjee, and M. M. Singh, *Can. Metall. Quart.*,

50, 2011, pp. 186-194.

[137] I. Sekine and A. Chinda, *Corrosion*, *40*, 1984, pp. 95-100.

[138] I. Sekine, S. Hatakeyama, and Y. Nakazawa, *Corros. Sci.*, *27*, 1987, pp. 275-288.

[139] I. Sekine and K. Momoi, *Corrosion*, *44*, 1988, pp. 136-142.

[140] I. Sekine, A. Masuko, and K. Senoo, *Corrosion*, *43*, 1987, pp. 553-560.

[141] O. Kröcher, M. Elsener, and E. Jacob, "Neue Reduktionsmittel für die Low NOx-SCR-Technik / New reducing agents for the low-NOx SCR technology" *Proceedings of the 5th International Exhaust Gas and Particulate Emissions Forum*, Ludwigsburg, Germany, 2008.

[142] G. L. Kennedy, *Crit. Rev. Toxicol.*, *31*, 2001, pp. 139-222.

[143] T. H. Dresser, E. R. Rivera, F. J. Hoffmann, and R. A. Finch, *J. Appl. Toxicol.*, *12*, 1992, pp. 49-56.

[144] P. A. Fail, J. D. George, T. B. Grizzle, and J. J. Heindel, *Reprod. Toxicol.*, *12*, 1998, pp. 317-332.

[145] B. R. Ramachandran, A. M. Halpern, and E. D. Glendening, *J. Phys. Chem. A*, *102*, 1998, pp. 3934-3941.

[146] G. Fulks et al., "A Review of Solid Materials as Alternative Ammonia Sources for Lean NOx Reduction with SCR" *SAE technical paper*, 2009-01-0907.

[147] H. A. Irazoqui and M. A. Isla, *Ind. Eng. Chem. Res.*, *32*, 1993, pp.

2671-2680.

[148] C. B. Sclar and L. C. Carrison, *Science*, *14*, 1963, pp. 1205-1207.

[149] M. Krüger, P. Nisius, V. Scholz, and A. Wiartalla, *MTZ Worldwide Edition*, 2003-06.

[150] M. Tatur, D. Tomazic, F. Lacin, H. Sullivan, and A. Kotrba, "Solid SCR Demonstation Truck Application" *Directions in Engine-Efficiency and Emissions Research Conference*, Dearborn, MI, USA, 2009.

[151] F. Lacin et al., *SAE technical paper*, 2011-01-2207.

[152] E. Lepinasse and B. Spinner, *Int. J. Refrig.*, *17*, 1994, pp. 309-322.

[153] T. Vegge et al., "Indirect Hydrogen Storage in Metal Ammines, Part 4: Chemically Bound Hydrogen Storage" in *Solid-State Hydrogen Storage: Materials and Chemistry*. Cambrige, UK: Woodhead Publishing Limited, 2008, pp. 533-564.

[154] T. D. Elmøe et al., *Chem. Eng. Sci.*, *61*, 2006, pp. 2618-2625.

[155] C. Y. Liu and K.-I. Aika, *B. Chem. Soc. Jpn.*, *77*, 2004, pp. 123-131.

[156] T. Johannessen, C. H. Christensen, J. K. Nørskov, U. Quaade, and R. Z. Sørensen, "High density storage of ammonia" WO2006081824, 03.02.2005.

[157] T. Johannessen et al., *SAE Technical paper*, 2008-01-1027.

[158] T. Johannessen, "Next generation SCR system for fuel-efficient NOx reduction" *IQPC Conference Selective Catalytic Reduction*,

Wiesbaden, Germany, 2011.

[159] "Navistar to Invest in Danish Technology Company" 21.12.2009 [Online]. URL: http://media.navistar.com/index.php?s=43&item=343.

[160] T. Johannessen, "Compact ammonia storage systems for fuel-efficient NOX emissions reduction" *CTI conference on SCR Systems*, Stuttgart, Germany, 2010.

[161] D. Nicosia, I. Czekaj, and O. Kröcher, *Appl. Catal. B-Environ.*, *77*, 2008, pp. 228-236.

[162] F. Tang, B. Xu, H. Shi, J. Qiu, and Y. Fan, *Appl. Catal. B-Environ.*, *94*, 2010, pp. 71-76.

[163] C. H. Christensen et al., *J. Mater. Chem.*, *15*, 2005, pp. 4106-4108.

[164] "RÖMPP Online" 01.03.2002 [Online]. URL: http://www.roempp.com/prod/.

[165] O. Kröcher, M. Elsener, and E. Jacob, *Appl. Catal. B-Environ.*, *88*, 2009, pp. 66-82.

[166] "Kennwerte von Ottokraftstoffen und ihre Bedeutung" *DIN EN 228*, 2008-11.

[167] G. L. Gist and J. R. Burg, *Toxicol. Ind. Health*, *13*, 1997, pp. 661-714.

[168] E. Jacob, "Ammoniakvorläufersubstanz und Verfahren zur selektiven katalytischen Reduktion von Stickoxiden in

sauerstoffhaltigen Abgasen von Fahrzeugen" DE102005059250, 12.12.2005.

[169] T. Günther, B. Mertschenk, and B. Schulz, "Guanidine and derivatives" in *Ullmann's Encyclopedia of Industrial Chemistry*. Weinheim: Wiley-VCH, 2006, pp. 175-188.

[170] B. S. Schulz, "Physikalisch- chemische Eigenschaften" *NORA Projektreffen*, Trostberg, Germany, 2008.

[171] O. Kröcher et al., "Guanidiniumformiat als neues Reduktionsmittel für die Low NOx-SCR-Technik" *Proceedings of the 2nd Conference MinNOx - Minimization of NOx Emissions Through Exhaust Gas Aftertreatment*, Berlin, 2008.

[172] M. Koebel and E. O. Strutz, *Ind. Eng. Chem. Res.*, *42*, 2003, pp. 2093-2100.

[173] A. Strecker, *Liebigs Ann. Chem.*, *118*, 1861, pp. 151-177.

[174] G. W. Watt and R. G. Post, *Ind. Eng. Chem.*, *45*, 1953, pp. 846-849.

[175] J. S. Blair and J. M. Braham, *Ind. Eng. Chem.*, *16*, 1924, pp. 848-852.

[176] E. Erlenmeyer, *Liebigs Ann. Chem.*, *146*, 1868, pp. 258-260.

[177] R. N. Shreve and R. P. Carter, *Ind. Eng. Chem.*, *36*, 1944, pp. 423-426.

[178] J. H. Paden, K. C. Martin, and R. C. Swain, *Ind. Eng. Chem.*, *39*, 1947, pp. 952-958.

[179] K. Sugino and M. Yamasita, *J. Soc. Chem. Ind. Japan Suppl.*, *45*, 1942,

pp. 1-2.

[180] E. Baumann, *Ber. Dtsch. Chem. Ges.*, *7*, 1874, pp. 1766-1773.

[181] J. Volhard, *J. Prakt. Chem.*, *9*, 1874, pp. 6-30.

[182] H. Gockel, *Angew. Chem.-Ger. Edit.*, *48*, 1935, p. 430.

[183] "49.1 Guanidin - Bildung und Darstellung "in *Beilsteins Handbuch der Organischen Chemie.* Berlin: Springer, 1941, pp. 4. Ergänzungswerk, Band 3, 466-470.

[184] R. Klinger, *Ein Beitrag zur Chemie der Guanidine.* Leipzig: PhD thesis, 1926.

[185] W. J. Jones, *T. Faraday Soc.*, *55*, 1959, pp. 524-531.

[186] W. Marckwald and F. Struwe, *Ber. Dtsch. Chem. Ges.*, *55*, 1922, pp. 457-463.

[187] T. Yamada, X. Liu, U. Englert, H. Yamane, and R. Dronskowski, *Chem. Eur. J.*, *15*, 2009, pp. 5651-5655.

[188] H. Mark and K. Weissenberg, *Z. Phys.*, *16*, 1923, pp. 1-22.

[189] S. J. Angyal and W. K. Warburton, *J. Chem. Soc.*, 1951, pp. 2492-2494.

[190] C. C. Angell et al., *T. Faraday Soc.*, *53*, 1957, pp. 589-600.

[191] E. P. Hunter and S. G. Lias, *J. Phys. Chem. Ref. Data*, *27*, 1998, pp. 413-656.

[192] E. D. Raczynska et al., *J. Phys. Org. Chem.*, *16*, 2003, pp. 91-106.

[193] J. W. Otvos and J. T. Edsall, *J. Chem. Phys.*, *7*, 1939, p. 632.

[194] D. Halverson, *Rev. Mod. Phys.*, *19*, 1947, pp. 87-131.

[195] R. Mecke and W. Kutzelnigg, *Spectrochim. Acta, 16*, 1960, pp. 1225-1230.

[196] L. Kellner, *P. R. Soc. London*, *177*, 1941, pp. 456-475.

[197] J. D. Dunitz, *X-ray Analysis and the Structure of Organic Molecules.* Ithaca, NY, USA: Cornell University Press, 1979.

[198] M. S. Lehmann, J. J. Verbist, W. C. Hamilton, and T. F. Koetzle, *J. Chem. Soc. Perk. T. 2*, 1973, pp. 133-137.

[199] C. S. Frampton, C. C. Wilson, N. Shankland, and A. J. Florence, *J. Chem. Soc. Faraday T.*, *93*, 1997, pp. 1875-1879.

[200] K. M. Barkigia, L. M. Rajkovic-Blazer, M. T. Pope, E. Prince, and C. O. Quicksall, *Inorg. Chem.*, *19*, 1980, pp. 2531-2537.

[201] A. Gobbi and G. Frenking, *J. Am. Chem. Soc.*, *115*, 1993, pp. 2362-2372.

[202] B. Amekraz et al., *New J. Chem.*, *20*, 1996, pp. 1011-1021.

[203] G. A. Olah, A. Burrichter, G. Rasul, M. Hachoumy, and G. K. S. Prakash, *J. Am. Chem. Soc.*, *119*, 1997, pp. 12929-12933.

[204] S. Lapange, *Physicochemical aspects of protein denaturation.* New York:

Wiley, 1978.

[205] J. L. England and G. Haran, "Role of Solvation Effects in Protein Denaturation: From Thermodynamics to Single Molecules and Back" in *Annual Review of Physical Chemistry*. Palo Alto, CA, USA: Annual Reviews, 2011, pp. 257-277.

[206] Y. Nozaki and C. Tanford, *J. Biol. Chem.*, *245*, 1970, pp. 1648-1672.

[207] J. P. Greenstein, *J. Biol. Chem.*, *125*, 1938, pp. 501-513.

[208] A. Ulas, G. A. Risha, and K. K. Kuo, *Fuel*, *85*, 2006, pp. 1979-1986.

[209] M. Ichino, T. Yokoyama, S. Oda, and Y. Iwai, *Nippon Kagaku Kaishi*, *3*, 2002, pp. 281-288.

[210] K. Engelen and M. H. Lefebvre, *Propell. Explos. Pyrot.*, *27*, 2002, pp. 290-299.

[211] R. S. Damse and A. K. Sikder, *J. Hazard. Mater.*, *166*, 2009, pp. 967-971.

[212] R. S. Damse, N. H. Naik, M. Ghosh, and A. K. Sikder, *J. Propul. Power*, *25*, 2009, pp. 249-256.

[213] R. Sivabalan, M. B. Talawar, and N. Senthilkumar, *J. Therm. Anal. Calorim.*, *78*, 2004, pp. 781-792.

[214] N. Fischer, D. Izsak, T. M. Klapotke, S. Rappenglück, and J. Stierstorfer, *Chem.-Eur. J.*, *18*, 2012, pp. 4051-4062.

[215] Y. I. Rubtsov, A. I. Kazakov, D. B. Lempert, and G. B. Manelis,

Russ. J. Appl. Chem., *77*, 2004, pp. 1083-1091.

[216] M. R. Udupa, *Thermochim. Acta*, *53*, 1982, pp. 383-385.

[217] W. W. Wendlandt, M. Kasper, and S. Bellamy, *Thermochim. Acta*, *75*, 1984, pp. 239-244.

[218] J. Bell, *J. Chem. Soc.*, 1928, pp. 2074-2077.

[219] M. P. Fülscher and E. L. Mehler, *Theochem-J. Mol. Struc.*, *165*, 1988, pp. 319-327.

[220] I. Rozas, I. Alkorta, and J. Elguero, *Org. Biomol. Chem.*, *3*, 2005, pp. 366-371.

[221] S. Orihara, A. Yamamoto, and K. Ishida, "Urea water and denitrification apparatus using the same" JP2007145796, 14.06.2007.

[222] R. K. Graupner, J. D. Hultine, and J. A. Van Vechten, "Guanidine based composition and system for same" WO2005108289, 03.05.2005.

[223] W. R. Epperly et al., "Multi-stage process for reducing the concentration of pollutants in an effluent" US5057293, 23.05.1989.

[224] P. Hauck, A. Jentys, and J. A. Lercher, *Appl. Catal. B-Environ.*, *70*, 2007, pp. 91-99.

[225] H. L. Fang and H. F. M. DaCosta, *Appl. Catal. B-Environ.*, *46*, 2003, pp. 17-34.

[226] G. Piazzesi, *The Catalytic Hydrolysis of Isocyanic Acid (HNCO) in the*

Urea-SCR Process. ETH Zurich: Ph.D. Thesis No. 16693, 2006.

[227] G. Madia, M. Elsener, M. Koebel, F. Raimondi, and A. Wokaun, *Appl. Catal. B-Environ.*, *39*, 2002, pp. 181-190.

[228] O. Kröcher, *Stud. Surf. Sci. Catal.*, *171*, 2007, pp. 261-289.

[229] P. Forster, V. Ramaswamy, and et al., "Changes in Atmospheric Constituents and in Radiative Forcing" in *Climate Change 2007: The Physical Science Basis. Contribution of Working Group I to the Forth Assessment Report of the Intergovernmental Panel on Climate Change.* Cambridge: Cambridge University Press, 2007, p. 212.

[230] M. Casapu et al., *J. Phys. Chem. C*, *114*, 2010, pp. 9791-9801.

[231] M. Casapu et al., *Appl. Catal. B-Environ.*, *103*, 2011, pp. 79-84.

[232] F. D. Liu, W. P. Shan, X. Y. Shi, C. B. Zhang, and H. He, *Chinese J. Catal.*, *32*, 2011, pp. 1113-1128.

[233] E. R. Becker and H. J. Jung, "Selective catalytic reduction catalyst consisting of iron sulfate, ceria and alumina" US4798817, 13.06.1986.

[234] H. J. Jung, "Selective catalytic reduction catalyst consisting essentially of nickel and/manganese sulfate, ceria and alumina" US4780445, 24.04.1984.

[235] K. Adelmann, N. Söger, L. Mussmann, M. Pfeifer, and G. Jeske, "Vanadium-free catalyst for selective catalytic reduction and process

for its preparation" US2010034717, 23.10.2006.

[236] N. Apostolescu et al., *Appl. Catal. B-Environ.*, *62*, 2006, pp. 104-114.

[237] K. Adelmann et al., "Exhaust gas purification system for the treatment of engine exhaust gases by means of SCR catalyst" US2011146237, 11.04.2008.

[238] C. Narula, X. Yang, P. Bonnesen, and E. Hagaman, *SAE technical paper*, 2011-01-1330.

[239] N. V. Heeb et al., *Environ. Sci. Technol.*, *41*, 2007, pp. 5789-5794.

[240] A. Mayer, N. Heeb, J. Czerwinski, and M. Wyser, *SAE technical paper*, 2003-01-0291.

[241] T. V. Johnson, *Platinum Metals Rev.*, *54*, 2010, pp. 216-222.

[242] C. A. Laroo, C. R. Schenk, L. J. Sanchez, and J. McDonald, *Environ. Sci. Technol.*, *45*, 2011, pp. 6420-6428.

[243] Z. G. Liu, J. C. Wall, P. Barge, M. E. Dettmann, and N. A. Ottinger, *Environ. Sci. Technol.*, *45*, 2011, pp. 2965-2972.

[244] P. J. Andersen et al., "Transition Metal/Zeolite SCR Catalysts" WO2008132452, 26.04.2007.

[245] I. Bull et al., "Copper CHA zeolite catalysts" WO2008106519, 27.02.2007.

[246] H.-X. Li, W. E. Cormier, and B. Moden, "High silica chabazite for selective catalytic reduction, methods of making and using same"

US2010092362, 26.03.2007.

[247] J. H. Kwak, R. G. Tonkyn, D. H. Kim, J. Szanyi, and C. H. F. Peden, *J. Catal.*, *275*, 2010, pp. 187-190.

[248] S. T. Korhonen, D. W. Fickel, R. F. Lobo, B. M. Weckhuysen, and A. M. Beale, *Chem. Commun.*, *47*, 2011, pp. 800-802.

[249] J. Luo et al., *SAE technical paper*, 2012-01-1096.

[250] G. C. Bond and P. Sermon, *J. Chem. Soc. Chem. Comm.*, 1973, pp. 444-445.

[251] M. Haruta, T. Kobayashi, H. Sano, and N. Yamada, *Chem. Lett.*, *16*, 1987, pp. 405-408.

[252] B. Nkosi, N. J. Coville, and G. J. Hutchings, *J. Chem. Soc. Chem. Comm.*, 1988, pp. 71-72.

[253] R. Zanella, L. Delannoy, and C. Louis, *Appl. Catal. A*, *291*, 2005, pp. 62-72.

[254] M. Daté, M. Okumura, S. Tsubota, and M. Haruta, *Angew. Chem. Int. Ed.*, *43*, 2004, pp. 2129-2132.

[255] A. S. K. Hashmi and G. J. Hutchings, *Angew. Chem. Int. Edit.*, *45*, 2006, pp. 7896-7936.

[256] A. A. Herzing, C. J. Kiely, A. F. Carley, P. Landon, and G. J. Hutchings, *Science*, *321*, 2008, pp. 1331-1335.

[257] O. Vaughan, *Nat. Nanotechnol.*, *5*, 2010, pp. 5-7.

[258] M. Ojeda and E. Iglesia, *Angew. Chem. Int. Edit.*, *48*, 2008, pp. 4800-4803.

[259] C. Rice et al., *J. Power Sources*, *111*, 2002, pp. 83-89.

[260] D. Peitz, A. Bernhard, M. Elsener, and O. Kröcher, *Rev. Sci. Instrum.*, *82*, 2011, p. 084101.

[261] D. Peitz, T. Todorova, O. Kröcher, A. Wokaun, and B. Delley, *J. Phys. Chem. C*, *115*, 2011, pp. 1195-1203.

[262] M. Koebel, M. Elsener, and G. Madia, *SAE technical paper*, 2001-01-3625.

[263] M. Koebel and M. Elsener, *J. Chromatogr. A*, *689*, 1995, pp. 164-169.

[264] J. P. Perdew, K. Burke, and M. Emzerhof, *Phys. Rev. Lett.*, *77*, 1996, pp. 3865-3868.

[265] B. Delley, *J. Chem. Phys.*, *92*, 1990, pp. 508-517.

[266] B. Delley, *J. Chem. Phys.*, *113*, 2000, pp. 7756-7764.

[267] B. Delley, *Phys. Rev. B*, *66*, 2002, p. 155125.

[268] N. Govind, M. Petersen, G. Fitzgerald, D. King-Smith, and J. Andzelm, *Comp. Mater. Sci.*, *28*, 2003, pp. 250-258.

[269] K. Fukui, *Accounts Chem. Res.*, *14*, 1981, pp. 363-368.

[270] C. Gonzalez and H. B. Schlegel, *Chem. Phys.*, *90*, 1989, pp. 2154-2161.

[271] "Messen der Ammoniak-Konzentration, Indophenol-Verfahren," 1974.

[272] A. M. Bernhard, I. Czekaj, M. Elsener, A. Wokaun, and O. Kröcher, *J. Phys. Chem. A*, *115*, 2011, pp. 2581-2589.

[273] O. Kröcher and M. Elsener, *Appl. Catal. B-Environ.*, *92*, 2009, pp. 75-89.

[274] S. Tsubota, M. Haruta, T. Kobayashi, A. Ueda, and Y. Nakahara, *Stud. Surf. Sci. Catal.*, *63*, 1991, pp. 695-704.

[275] M. Devadas, O. Kröcher, and A. Wokaun, *React. Kinet. Catal. L.*, *86*, 2005, pp. 347-354.

[276] J. J. Benbow, L. W. Lord, and D. J. Heath, "Support and catalyst" GB1385907, 07.05.1971.

[277] S. Brunauer, P. H. Emmett, and E. Teller, *J. Am. Chem. Soc.*, *60*, 1938, pp. 309-319.

[278] G. Stokes, *T. Cambridge Philos. Soc.*, *9*, 1851, pp. 8-106.

[279] O. Reynolds, *Philos. T. Roy. Soc. A*, *174*, 1883, pp. 935-982.

[280] M. Kleemann, M. Elsener, M. Koebel, and A. Wokaun, *Ind. Eng. Chem. Res.*, *39*, 2000, pp. 4120-4126.

[281] M. Eichelbaum, A. B. Siemer, R. J. Farrauto, and M. J. Castaldi,

Appl. Catal. B-Environ., *97*, 2010, pp. 98-107.

[282] S. D. Yim et al., *Ind. Eng. Chem. Res.*, *43*, 2004, pp. 4856-4863.

[283] E. Seker, N. Yasyerli, E. Gulari, C. Lambert, and R. H. Hammerle, *J. Catal.*, *208*, 2002, pp. 15-20.

[284] H. Ström, A. Lundström, and B. Andersson, *Chem. Eng. J.*, *150*, 2009, pp. 69-82.

[285] F. Birkhold, U. Meingast, P. Wassermann, and O. Deutschmann, *Appl. Catal. B-Environ.*, *70*, 2007, pp. 119-127.

[286] W. Schreier, *Gefahrst. Reinhalt. L.*, *69*, 2009, pp. 25-30.

[287] G. Piazzesi, M. Devadas, O. Kröcher, M. Elsener, and A. Wokaun, *Catal. Commun.*, *7*, 2006, pp. 600-603.

[288] S. Chen and Y. Lu, *Spectrochim. Acta. B*, *43*, 1988, pp. 287-291.

[289] K. Avila et al., *Science*, *333*, 2011, pp. 192-196.

[290] V. Thomsen, D. Schatzlein, and D. Mercuro, *Spectroscopy*, *18*, 2003, pp. 112-114.

[291] C. Arrouvel, M. Digne, M. Breysse, H. Toulhoat, and P. Raybaud, *J. Catal.*, *222*, 2004, pp. 152-166.

[292] T. Bredow and K. Jug, *Surf. Sci.*, *327*, 1995, pp. 398-408.

[293] A. Fahmi and C. Minot, *Surf. Sci.*, *304*, 1994, pp. 343-359.

[294] A. Beltran, J. R. Sambrano, M. Calatayud, F. R. Sensato, and J. Adres, *Surf. Sci.*, *490*, 2001, pp. 116-124.

[295] A. Vittadini, A. Selloni, F. P. Rotzinger, and M. Grätzel, *Phys. Rev. Lett.*, *81*, 1998, pp. 2954-2957.

[296] M. Nilsing, S. Lunell, P. Persson, and L. Ojamäe, *Surf. Sci.*, *582*, 2005, pp. 49-60.

[297] I. Onal, S. Soyer, and S. Senkan, *Surf. Sci.*, *600*, 2006, pp. 2457-2469.

[298] M. Posternak, A. Baldereschi, and B. Delley, *J. Phys. Chem. C*, *113*, 2009, pp. 15862-15867.

[299] I. Czekaj, O. Kröcher, and G. Piazzesi, *J. Mol. Catal. A-Chem.*, *280*, 2008, pp. 68-80.

[300] I. Czekaj, G. Piazzesi, O. Kröcher, and A. Wokaun, *Surf. Sci.*, *600*, 2006, pp. 5158-5167.

[301] A. N. Alexandrova and W. L. Jorgensen, *J. Phys. Chem. B*, *111*, 2007, pp. 720-730.

[302] K. Sagarik and S. Chaiyapongs, *Biophys. Chem.*, *117*, 2005, pp. 119-140.

[303] Y. J. Zheng and R. L. Ornstein, *J. Am. Chem. Soc.*, *118*, 1996, pp. 11237-11243.

[304] E. P. Kirpichev, L. V. Titov, Yu. I. Rubtsov, and L. A. Gavrilova, *Russ. J. Phys. Chem. (Engl. Transl.)*, *42*, 1968, pp. 269-270.

[305] H. G. M. DeWit, J. C. Van Miltenburg, and C. G. DeKruif, *J. Chem. Thermodyn.*, *15*, 1983, pp. 651-663.

[306] M. W. Chase, *J. Phys. Chem. Ref. Data*, *27*, 1998, pp. 1-30.

[307] J. Lelieveld et al., *Science*, *304*, 2004, pp. 1483-1487.

[308] A. Boddien et al., *Science*, *333*, 2011, pp. 1733-1736.

[309] B. Loges, A. Boddien, H. Junge, and M. Beller, *Angew. Chem. Int. Edit.*, *47*, 2008, pp. 3962-3965.

[310] C. Fellay, P. J. Dyson, and G. Laurenczy, *Angew. Chem. Int. Edit.*, *47*, 2008, pp. 3966-3968.

[311] M. Haruta, *Nature*, *437*, 2005, pp. 1098-1099.

[312] W. Yan, S. M. Mahurin, Z. Pan, S. H. Overbury, and S. Dai, *J. Am. Chem. Soc.*, *127*, 2005, pp. 10480-10481.

[313] Y. Tai et al., *Appl. Catal. A*, *268*, 2004, pp. 183-187.

[314] B. K. Min, W. T. Wallace, and D. W. Goodman, *J. Phys. Chem. B*, *108*, 2004, pp. 14609-14615.

[315] A. M. Venezia et al., *Appl. Catal. A*, *310*, 2006, pp. 114-121.

[316] R. Zanella, V. Rodríguez-Gonzáles, Y. Arzola, and A. Moreno-Rodriguez, *ACS Catal.*, *2*, 2012, pp. 1-11.

[317] D. Peitz, M. Elsener, and O. Kröcher, *Abstr. Pap. Am. Chem. S.*, *242*, 2011, pp. 33-FUEL.

[318] M. Comotti, C. D. Pina, R. Matarrese, and M. Rossi, *Angew. Chem. Int. Edit.*, *43*, 2004, pp. 5812-5815.

[319] G. C. Bond and D. T. Thompson, *Gold Bull.*, *33*, 2000, pp. 41-52.

[320] A. K. Sinha, S. Seelan, S. Tsubota, and M. Haruta, *Angew. Chem. Int. Edit.*, *43*, 2004, pp. 1546-1548.

[321] Y. Liu, C.-J. Jia, J. Yamasaki, O. Terasaki, and F. Schüth, *Angew. Chem. Int. Edit.*, *49*, 2010, pp. 5771-5775.

[322] Y. Cheng, C. Montreuil, G. Cavataio, and C. Lambert, *SAE technical paper*, 2008-01-1023.

[323] M. Okazaki and T. Funazukuri, *J. Mater. Sci.*, *43*, 2008, pp. 2316-2322.

[324] J. M. Trillo, G. Munuera, and J. M. Criado, *Catal. Rev.*, *7*, 1972, pp. 51-86.

[325] A. M. Bernhard, D. Peitz, M. Elsener, A. Wokaun, and O. Kröcher, *in preparation*, 2012.

[326] M. Elsener, O. Kröcher, D. Peitz, and A. Bernhard, "Ammonia generator converting liquid ammonia precursor solutions to gaseous ammonia for DeNOx-applications using selective catalytic reduction of nitrogen oxides" EP11153417, 04.02.2011.

[327] M. Elsener, O. Kröcher, D. Peitz, and A. Bernhard, "Ammonia generator converting liquid ammonia precursor solutions to gaseous ammonia for DeNOx-applications using selective catalytic reduction

of nitrogen oxides" 2011P01935WO, 27.01.2012.

[328] L. Olsson et al., *J. Phys. Chem. B*, *103*, 1999, pp. 10433-10439.

[329] P. Forzatti, I. Nova, and E. Tronconi, *Angew. Chem. Int. Edit.*, *48*, 2009, pp. 8366-8368.

[330] P. Forzatti, I. Nova, E. Tronconi, A. Kustov, and J. R. Thøgersen, *Catal. Today*, *184*, 2012, pp. 153-159.

[331] S. J. Schmieg et al., *Catal. Today*, *184*, 2012, pp. 252-261.

[332] P. Forzatti, I. Nova, and E. Tronconi, *Ind. Eng. Chem. Res.*, *49*, 2010, pp. 10386-10391.

[333] European parliament and council, "Regulation (EC) No 595/2009" *Official Journal of the European Union*, 2009.

[334] M. J. Li, J. Henao, Y. Yeom, E. Weitz, and W. M. H. Sachtler, *Catal. Lett.*, *98*, 2004, pp. 5-9.

[335] C. Ciardelli, I. Nova, E. Tronconi, D. Chatterjee, and B. Bandl-Konrad, *Chem. Comm.*, 2004, pp. 2718-2719.

[336] J. H. MacNeil, H. T. Zhang, P. Berseth, and W. C. Trogler, *J. Am. Chem. Soc.*, *119*, 1997, pp. 9738-9744.

[337] J. C. Oxley, J. L. Smith, E. Rogers, and M. Yu, *Thermochim. Acta*, *384*, 2002, pp. 23-45.

[338] A. Grossale, I. Nova, and E. Tronconi, *J. Catal.*, *265*, 2009, pp. 141-

147.

[339] A. Grossale, I. Nova, and E. Tronconi, *Catal. Today*, *136*, 2008, pp. 18-27.

[340] M. Colombo, I. Nova, and E. Tronconi, *Catal. Today*, *151*, 2010, pp. 223-230.

[341] A. Savara, M. J. Li, W. M. H. Sachtler, and E. Weitz, *Appl. Catal. B-Environ.*, *81*, 2008, pp. 251-257.

[342] I. Nova, C. Ciardelli, E. Tronconi, D. Chatterjee, and B. Brandl-Konrad, *Catal. Today*, *114*, 2006, pp. 3-12.

[343] M. Iwasaki and H. Shinjoh, *Appl. Catal. A-General*, *390*, 2010, pp. 71-77.

List of publications

Peer-reviewed articles

C. Gerhart, H.-P. Krimmer, B. Hammer, B. Schulz, O. Kröcher, D. Peitz, T. Sattelmayer, P. Toshev, G. Wachtmeister, A. Heubuch, E. Jacob, Development of a 3rd Generation SCR NH$_3$-Direct Dosing System for Highly Efficient DeNO$_x$, *SAE Technical Paper Series* 2012-01-1078.

D. Peitz, A. Bernhard, M. Elsener, O. Kröcher, Laboratory test reactor for the investigation of liquid reducing agents in the selective catalytic reduction of NO$_x$, *Rev. Sci. Inst.* **2011**, *82*, 084101.

D. Peitz, T. Todorova, O. Kröcher, A. Wokaun, B. Delley, Guanidinium Formate Decomposition on the (101) TiO$_2$-Anatase Surface: Combined Minimum Energy Reaction Pathway Calculations and Temperature-Programmed Decomposition Experiments, *J. Phys. Chem. C* **2011**, *115*, 1195–1203.

Patent applications

D. Peitz, O. Kröcher, Catalyst for the conversion of liquid ammonia precursor solutions to gaseous ammonia avoiding the formation of undesired side products, *European Patent application EP12152814*, **2012**.

M. Elsener, O. Kröcher, D. Peitz, A. Bernhard, Ammonia generator converting liquid ammonia precursor solutions to gaseous ammonia for DeNO$_x$ applications using selective catalytic reduction of nitrogen oxides, *European Patent application EP11153417,* **2011**.

Also published as

M. Elsener, O. Kröcher, D. Peitz, A. Bernhard, Ammonia generator converting liquid ammonia precursor solutions to gaseous ammonia for DeNO$_x$ applications using selective catalytic reduction of nitrogen oxides, *International Patent application 2011P01935WO,* **2012**.

Talks

D. Peitz, Catalytic decomposition of guanidinium formate for onboard ammonia gas production, independent of engine operation*, 9. FAD-Konferenz „Herausforderung Abgasnachbehandlung für Dieselmotoren"*, Dresden, Germany, November 3rd–4th **2011**.

D. Peitz, Guanidinium formate as a novel ammonia precursor for NO$_x$ abatement using selective catalytic reduction in mobile applications, *ACS National Meeting*, Denver, Colorado, USA, August 28th–September 1st **2011**.

D. Peitz, Investigation of guanidinium formate as novel ammonia precursor compound for selective catalytic reduction of NO$_x$, *18th International Symposium Transport and Air Pollution*, Dübendorf, Switzerland, May 18th–19th **2010**.

Poster presentations (selected)

D. Peitz, M. Elsener, O. Kröcher, Catalytic decomposition of guanidinium formate as novel ammonia precursor for selective catalytic reduction of NO$_x$, 45. Jahrestreffen Deutscher Katalytiker, Weimar, Germany, March 14th–16th, **2012**.

D. Peitz, M. Elsener, O. Kröcher, NH_3 generation by decomposition of guanidnium formate on noble metal-doped TiO_2-catalysts, *1ˢᵗ Swiss Heterogeneous Catalysis Meeting*, Grindelwald, Switzerland, June 16ᵗʰ–17ᵗʰ **2011**.

D. Peitz, O. Kröcher, M. Elsener, Guanidinium formate as novel ammonia precursor compound for the selective catalytic reduction of NO_x in engine exhaust gas, *2010 Fall Meeting of the Swiss Chemical Society*, ETH Zurich, Switzerland, September 16ᵗʰ **2010**.

D. Peitz, O. Kröcher, M. Elsener, Guanidinium formate as novel ammonia precursor compound for mobile SCR applications, *2ⁿᵈ International Symposium on Air Pollution Abatement Catalysis*, Cracow, Poland, September 8ᵗʰ–11ᵗʰ **2010**.

D. Peitz, O. Kröcher, M. Elsener, NO_x Reduction in Diesel Exhaust Gas by Guanidinium Salts, *119ᵗʰ BASF International Summer Courses*, Ludwigshafen, Germany, July 27ᵗʰ–August 6ᵗʰ **2010**.

Curriculum vitae

Name: Daniel Peitz

Date of birth: 20.07.1983

Place of birth: Nuremberg, Germany

Nationality: German

Professional education

08/2008 – 07/2012   PhD thesis in the Catalysis for Energy Group of the Paul Scherrer Institute in Villigen, Switzerland under the supervision of Prof. Dr. A. Wokaun at ETH Zurich

10/2007 – 06/2008   Master thesis in the group of Prof. Dr. M. Prato of the Università degli studi di Trieste, Italy and in the group of Prof. Dr. D. M. Guldi of the University of Erlangen-Nuremberg

10/2006 – 10/2007   Master studies of Molecular Nano Science at the University of Erlangen-Nuremberg

06/2006 – 08/2006   Bachelor thesis in the group of Prof. Dr. D. M. Guldi of the University of Erlangen-Nuremberg

10/2003 – 06/2006   Bachelor studies of Molecular Science at the University of Erlangen-Nuremberg